The isotropy of the Universe as seen through galaxy clusters

Dissertation
zur
Erlangung des Doktorgrades (Dr. rer. nat.)
der
Mathematisch-Naturwissenschaftlichen Fakultät
der
Rheinischen Friedrich-Wilhelms-Universität Bonn

von
Konstantinos Nikolaos Migkas
aus
Thessaloniki, Griechenland

Bonn, 09.02.2021

Angefertigt mit Genehmigung der Mathematisch-Naturwissenschaftlichen Fakultät der Rheinischen Friedrich-Wilhelms-Universität Bonn

1. Gutachter:	Prof. Dr. Thomas H. Reiprich
2. Gutachter:	Prof. Dr. Cristiano Porciani
Tag der Promotion:	08.06.2021
Erscheinungsjahr:	2021

To Eftychia, Mom, Dad, and my Home.

"Cosmologists are often in error, but never in doubt"
- Lev Landau

Abstract

The cosmological principle (CP) postulates that the Universe is isotropic and homogeneous. This implies that the Universe has the same expansion rate toward every direction and holds similar amounts of matter when averaged over sufficiently large scales. The CP is a fundamental building block of the standard cosmological model and is broadly taken as an axiom in extragalactic astronomy. However, its observational foundation remains uncertain. Multiple studies that tested the CP have been conducted in the past, frequently returning controversial results. Since each methodology suffers from certain limitations and potential biases, it is crucial to develop several independent tests to scrutinize the CP further. Galaxy clusters can be an excellent probe of cosmic isotropy. They are the largest, gravitationally bound systems in the Universe, and they contain up to thousands of galaxies and vast amounts of dark matter. Their intracluster medium (ICM) is filled with hot ionized plasma that strongly emits X-ray radiation. This work aims to apply a novel, powerful test for the CP using galaxy clusters. Specifically, I use their so-called scaling relations (SCs) to probe the isotropy of the local Universe. This work consists of two projects.

In the first project, I focus on the tight correlation between the X-ray luminosity $L_{\rm X}$ and the temperature T of galaxy clusters. To estimate $L_{\rm X}$ from the measured X-ray flux, one needs to assume the values of the cosmological parameters, such as the expansion rate of the Universe, H_0. On the other hand, the T measurement is nearly free of cosmological assumptions. I exploit this property to draw conclusions about cosmic isotropy by investigating the directional behavior of the $L_{\rm X} - T$ relation. If H_0 is spatially constant and no previously undetected, X-ray absorbing gas and dust clouds exist, then $L_{\rm X} - T$ should be statistically similar toward all directions. To constrain the $L_{\rm X} - T$ relation I use a homogeneously selected galaxy cluster sample with 313 objects. Their temperatures, metallicities, and redshifts were measured, using observations from the Chandra and XMM-Newton telescopes. Further corrections in the publicly available $L_{\rm X}$ values were also performed to better account for the X-ray absorption, point source contamination, and merging clusters. By scanning the extragalactic sky, it is shown that $L_{\rm X} - T$ manifests a strongly anisotropic behavior at a $\gtrsim 4\sigma$ confidence level. The apparently preferred axis lies toward the Galactic coordinates $(l, b) \sim (280^\circ, -20^\circ)$. A large variety of potential systematic biases that could result in artificially observed anisotropies is inspected, including X-ray absorption effects. None of these tests reveal any significant bias in the anisotropy detection. To further check the consistency of the results, I repeat the analysis with two other, completely independent cluster samples. Both samples exhibit a similar $L_{\rm X} - T$ anisotropy. When all three samples are combined, they result in 842 individual clusters. Their joint analysis further amplifies the statistical significance of the observed anisotropy, boosting it to a $\sim 5\sigma$ level. The most anisotropic direction is $(l, b) \sim (303^\circ, -27^\circ)$ with a H_0 variation of $\sim 15\%$ across the sky, in agreement with several past studies, conducted with different probes. A conclusive answer on the origin of this anisotropy, however, could not be given yet.

In the second project, I attempt to decisively identify the origin of the apparent anisotropies. To do so, I use three more cluster properties; the total integrated Compton parameter $Y_{\rm SZ}$, the infrared luminosity of the brightest cluster galaxy, and the X-ray half-light radius of the clusters. All three are nearly free of absorption issues. This allows for the construction of 10 multiwavelength SCs, through

which essential information on the nature of the cluster anisotropies can be obtained. Five of these SCs are presented in the literature for the first time. I make use of nearly 570 individual clusters and I employ advanced statistical tools to robustly assess the statistical significance of the results. Low-scatter SCs that are sensitive *only* to unknown X-ray absorption issues (e.g., $L_{\rm X} - Y_{\rm SZ}$) and not to H_0 spatial variations or bulk flows, do not show any significant anisotropies. Therefore, the scenario of excess X-ray absorption biasing the results is strongly disfavored. Next, I exploit SCs that only trace cosmological phenomena and do not suffer from absorption issues (e.g., $Y_{\rm SZ} - T$). Nearly the same anisotropies are detected as in the $L_{\rm X} - T$ relation, with a higher statistical significance due to the reduced scatter of the new SCs. This result supports the notion that the observed anisotropies are of cosmological origin. When all available information is combined, a 9% anisotropy in H_0 is robustly detected toward $(l, b) \sim (280^{\circ}, -15^{\circ})$, rejecting the CP at a 5.4σ confidence level. Comparisons with isotropic Monte Carlo simulations confirm the high statistical significance of the detected anisotropy. Additional tests show that numerous, generally known biases, do not alleviate the observed tension. An alternative explanation to the H_0 anisotropy would be the existence of a $\sim$ 900 km/s bulk flow (coherent peculiar motion of clusters toward a specific direction), extending out to $\gtrsim$ 500 Mpc. This would also contradict the CP, since such a motion would require a large-scale matter inhomogeneity, inconsistent with the concordance cosmology predictions.

Since a cornerstone of concordance cosmology is in doubt, more tests are needed to provide a definite answer. Forthcoming morphological parameters of the used clusters will help reduce the scatter of the relations and provide more precise results. The upcoming eROSITA All-Sky Survey will also allow for anisotropy studies with many more clusters at greater distances. This is a necessity in order to distinguish between a cosmological anisotropy and a bulk flow.

Contents

CHAPTER 1

Introduction

The term "cosmology" comes from the Greek words κόσμος(=the physical world) and λόγος(=logic and speech). It refers to the quest of humanity to understand the mechanisms of the world as a whole through reasoning. Throughout history, humankind tried to grasp the origin of the cosmos ever since the first civilizations emerged. To reach the level of understanding we now possess about the Universe, we stood on the shoulders of our ancestors. Hence, a brief journey through the history of astronomy and cosmology is entailed.

1.0.1 Brief History of Astronomy and Cosmology

1.0.1.1 Prehistory and Classical Antiquity

The first attempts to explain the sky phenomena were mixed with myth and religion. The focal point of the interaction of ancient cultures with the Universe was the solar system and the brightest stars in the night sky. After all, the naked eye was the only astronomical instrument people possessed. In the beginning and according to our findings, people expressed their "awareness" of the cosmos through cave paintings; the oldest ones possibly date back to the Palaeolithic period (e.g., Krupp, 1994; Sweatman et al., 2018). Later on and during the Bronze and Iron Ages, identifying and describing regularities on the appearance of celestial bodies was the main objective. Changes in the sky were associated with different weather and physical phenomena, timing, sailing, and agricultural activities. For instance, based on observations of the Moon and the Sun, the 365-day calendar was first established in ancient Egypt (2nd millennium BC) to predict the annual flooding of the Nile, which provided the nation with a surpass of food supplies (e.g., Parker, 1974). No interpretative efforts for these phenomena are known to have been made up to then. The given explanations were mostly related to the actions of divine beings. For example, ancient Egyptians related the spring equinox and the winter solstice, nine months apart, with the rebirth and renewal of the self-creating god Ra, who ruled the entire created world. This implied a self-creating and eternal Universe for the ancient Egyptians. Both the Mayans and people of ancient India also tracked the movement of the heavenly bodies to keep time and create calendars while attributing all sky objects and motions to deities (e.g. Ruggles, 2005).

The transition of astronomy into a science took place in Mesopotamia after the 8^{th} century BC. Babylonians recognized and recorded the periodicity of astronomical effects, such as eclipses and planetary motions. These records are the oldest scientific documents that we know of. Based on these recordings, the 18-year Saros cycle of lunar eclipses was documented for the first time by the people of Mesopotamia (.) They were also the first to apply mathematics and construct coherent and internally logical arithmetic models of the solar system with predictive power (e.g., calculating the apparent motion

of Jupiter in the sky). These models were mainly used to forecast catastrophic events and notify the king and the country. The first documentation of the well-known Halley's comet was also possibly provided by the Babylonians (Stephenson et al., 1985). The sexagesimal system was also introduced in Mesopotamia, where numerous star catalogs were compiled. The engagement of the Babylonians with the cosmos, however, followed an empirical approach. An explanatory, theoretical model did not accompany it since they did not seek a cause for their observations. Their cosmological view, although not much is known, possibly referred to a multilevel Universe consisting of a plurality of heavens and earths. This sole system was portrayed to revolve with no specific center necessarily existing (e.g., Steele, 2015).

Arguably the most remarkable contributions to cosmology and astronomy in ancient times came from Greece (the next paragraphs have been compiled from various sources, mostly from Greek textbooks such as Spandagos 2004, and the original manuscripts; for a review in English see for example Heath 1932 or Dicks 1971). Ancient Greeks developed the first scientific cosmological models, and cosmology, alongside astronomy, advanced to a highly sophisticated level. They were aware of the work of Babylonians, on which they built to some extend. However, they mainly explored their own ideas, which were accompanied by geometrical models and universal laws explaining their observations. The study of the cosmos was approached based on evidence and reasoning, relied on mathematics (and especially geometry, which progressed significantly in ancient Greece), and flourished through exchanging ideas. For example, there was significant development on understanding the nature of our planet between the 5^{th} and 3^{rd} century BC. The first reference to a spherical Earth was documented after observing a lunar eclipse, the nature of eclipses was accurately described, and the rotation of the Earth around its axis was suggested. Furthermore, ancient Greeks measured the Earth's axial tilt (although Chinese astronomers have already measured this in 1100 BC, Wittman 1979), and its axial precession was discovered and estimated for the first time. They also accurately calculated the circumference of the Earth, and they predicted the existence of falling meteors on Earth, attributing it to "heavenly objects loosening or tearing apart" (e.g., Bailey et al., 1986). Many ancient Greek philosophers (a term that also encompassed scientists back then) contributed to these discoveries, but particularly Anaxagoras, Eratosthenes, and Hipparchus stood out. The latter introduced the apparent magnitude as a measure for the brightness of stars, which is used until today.

The cosmological perception of ancient Greeks initially consisted of the solar system and the "sphere of motionless stars." In the 6^{th} century BC, Pythagoras first argued that the motions of all celestial objects obey specific numerical laws. Following the Pythagorean perception, Philolaus described a spherical Universe where the six known planets (including the Earth), the Moon, the Sun, and the sphere of stars, revolved around a "central fire." His theory implied that the apparent motion of heavenly bodies was, at a large degree, caused by the motion of the observer. It is believed that this is the oldest mention in a nongeocentric Universe. Others later discredited Philolaus' theory since this presumed central fire was not observed. Leucippus and Democritus suggested that everything in the Universe was made by small, unbreakable pieces of matter, the "atoms" (Greek for "cannot be split"), and every material is the result of the same atoms structured in different ways. Later, Anaximandros was probably the first to describe the Earth, Sun, and Moon system based on mathematics. At the same time, around 380 BC, Eudoxus and Callopus attempted to explain the planets' motions by creating the first three-dimensional geocentric model. The most widely accepted model of the Universe in ancient Greece was developed by Aristotle, who expanded the work of Eudoxus, Empedocles, and his teacher Plato. According to Aristotle, Earth was in the center of the cosmos, which was composed of 55 concentric terrestrial spheres interconnected. Celestial bodies were attached to them and rotated with different velocities. The region below the Moon consisted of four fundamental elements: Earth, water, air, and fire. It could change and decay over time. The rest of the Universe consisted of a fifth element, aether (i.e., quintessence), and was considered eternally unchanged. The notion of "space" did not exist beyond the final sphere of fixed

stars. The "prime unmoved mover" (πρώτον κινούν ακίνητον), a supernatural entity, was considered to be responsible for the eternal movement of the outer sphere with a constant angular velocity, while this motion propagated to the rest of the spheres. The positions of the celestial objects in Aristotle's model are displayed in the left panel of Fig. 1.1.

The most accurate cosmological model of ancient times was developed by Aristarchus, who was not a supporter of Aristotle's ideas. Aristarchus first proposed the heliocentric system, with the planets of the solar system in orbit around the Sun (e.g., Heath et al., 1913). Supporting Anaxagoras' previous ideas, Aristarchus also suspected that the stars were simply other suns but at much greater distances. He explained their apparent motion as a result of the continuous rotation of the Earth. This model implied that stellar parallaxes should be observed due to the Earth's motion. However, none was detected due to the naked eye's limited resolution (75 times larger than the parallax of the closest star). This lack of evidence was considered to disproof Aristarchus' model at the time, who, however, explained this by postulating that the stars were at infinite distance. Another implication of Aristarchus' model that was also not observed at the time was that objects falling to Earth should be swept westward. Eventually, this model was disregarded by ancient Greeks, although Seleucious explored it further later on.

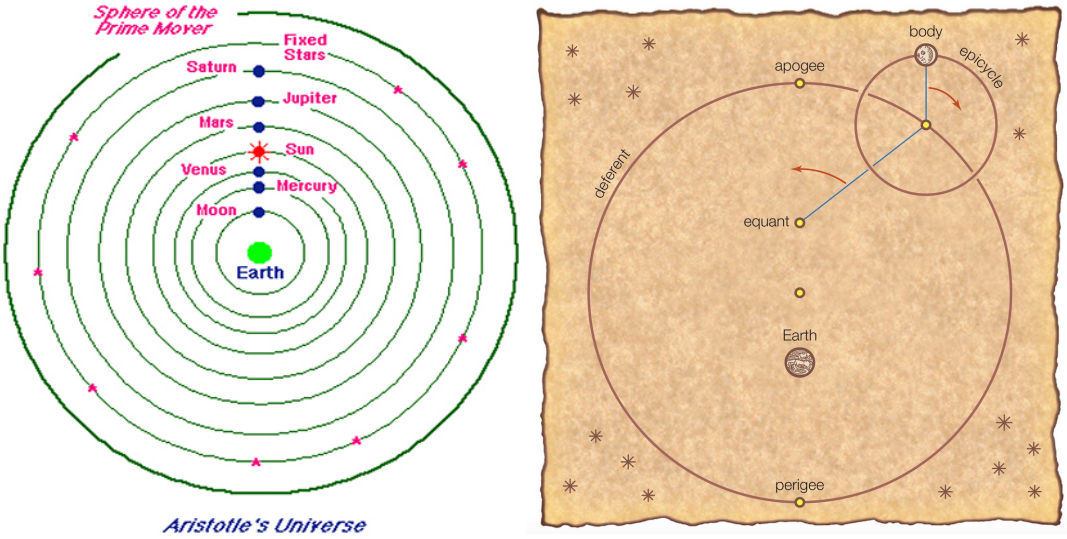

Figure 1.1: The Aristotelian geocentric Universe (left) and the Ptolemaic epicycle model (right). Images taken from Kolata (2015) and `https://www.britannica.com/science/equant` respectively.

The geocentric model prevailed, but its weaknesses, such as the unexplained retrograde motion of planets and their time-varying brightness, still had to be accommodated. The use of *epicycles* was initially proposed and developed by Appolonius and Hipparchus. It is believed that the latter also had a crucial contribution to the development of the Antikythera Mechanism, which was the first analog computer in history. The mechanism was able to predict some planetary motions, eclipses, moon phases, and other phenomena (Freeth et al., 2008). Three centuries later, the idea of epicycles was further formalized and established by Ptolemy, writer of the Almagest, a grand treatise on the geocentric cosmology, epicycles, and the entire solar system. Epicycles were circular orbits followed by planets. These circles (and not the planets) were bound to eccentric orbits around the Earth, following concentric spheres called *deferents*, centered slightly away from the Earth at the *eccentric*. The center of epicycles had a constant angular velocity compared to the *equant*, the antipodal point of Earth with respect to the eccentric. The mechanism of epicycles is illustrated in Fig. 1.1 (right panel). The exceptionally accurate predictions of planetary motions by the Babylonians were of great value for constructing the epicycle model. The

Ptolemaic cosmological model had great explanatory power and lasted for more than 1500 years.

Throughout the centuries, various other cultures made significant contributions to astronomy. For instance, in ancient China, various star catalogs and maps were composed, and the mechanism behind solar eclipses was proposed. Moreover, Jupiter's satellite Ganymede was probably detected for the first time and several supernovae explosions were recorded, including the very first one in 185 AD. Finally, in the medieval Middle East, a description of the Andromeda galaxy and the Large Magellanic Cloud was given, the magnitude and color of many stars were cataloged, a refinement of the Ptolemaic model took place, and natural philosophy was distinguished by scientific astronomy. However, not much progress in cosmology was made until the Copernican Revolution.

1.0.1.2 Renaissance and Enlightenment

The next substantial change in the standard cosmological theory came in the 16^{th} century from Copernicus. He formalized the heliocentric system, removing the Earth from the center of the Universe. Within the next century, the observations of Galileo and Brahe (who, however, developed his own, different model), the three laws of planetary motion from Kepler, and Newton's theory of gravity came to existence (see, e.g., Taton, 1989, for a review). These helped to consolidate the heliocentric theory and place it on a solid theoretical foundation. Newton realized that the Sun did not stand still at the center of the world but orbited the common gravity center of all solar system objects. Despite some existing opposition mostly arising from the Catholic Church, heliocentrism became the standard model of the Universe since it was in perfect agreement with all the observational data. Using a recent invention, the telescope, the Milky Way was resolved into faint stars, and many previously invisible ones were also discovered. Kepler argued for a finite Universe, while astronomers such as Digges and Bruno postulated the spatial infinity of the Universe and favored that the stars were nothing more than distant suns. Given the support by other scientists such as Descartes, this idea was also standardized by the end of the 17^{th} century. Furthermore, Newton introduced the first form of the *Cosmological Principle*, the focal point of this dissertation. In his Philosophiae Naturalis Principia Mathematica, he asserted that the physical laws uniformly extend to all scales.

In the late 18^{th} century, the idea that the Universe extends much further than previously thought started to establish. Kant and Lambert argued for a hierarchically structured, static Universe, where the Milky Way was a disc of stars initially formed from a large gas cloud (nebula), and that probably there are numerous other such clouds in the Universe. Herschel provided the first quantitive estimates of the size and shape of the cosmos by mapping our Galaxy using star counts, while together with Messier, they discovered many more nebulae. Some of them were shown to have spiral shapes.

1.0.1.3 20^{th} century: A Larger, Expanding Universe

Cosmology took its modern scientific form after the beginning of the 20^{th} century. By then, the Universe was still believed to be static and composed only of our Galaxy. In 1915, Einstein published his work on General Relativity (GR), showing the Universe to be a dynamical system that must either expand or contract (Einstein, 1916). Preferring to force a static solution of his (field) equations, he later added the infamous *cosmological constant* Λ. Based on these equations, De Sitter described an empty, expanding Universe (de Sitter, 1916a; de Sitter, 1916b; de Sitter, 1917). The work of Friedmann, Lemaître, Robertson, and Walker (FLRW) resulted in another solution of Einstein's field equations, namely the FLRW metric and the Friedmann equations (Friedmann, 1922; Lemaıtre, 1931a; Robertson et al., 2017; Walker, 1937). These described an isotropic, homogeneous, and expanding Universe filled with matter, radiation, and other components. Nearly 100 years later, Friedmann equations are still the foundation of

our standard cosmological model.

The plethora of observational developments in the first decades of that century served as the pillar on which modern cosmology was (and still is) based. A key element was the realization by Leavitt that some stars with varying brightness, called Cepheids, exhibit a clear correlation between their periodicity and their absolute luminosity (Leavitt et al., 1912). This made them *standard candles* (objects with a known intrinsic luminosity, used to determine cosmological distances). Cepheids were later discovered in the Andromeda nebula by Hubble, who determined its distance. He concluded that the Andromeda nebula could not be a part of the Milky Way since it lay too far away (E. P. Hubble, 1929). Thus, it had to be another, separate galaxy. For the first time in human history, it was strictly evident that the Universe extends well beyond the Milky Way. Meanwhile, Slipher measured for the first time the redshifts[1] of 41 spiral galaxies (still believed to be nebulae by that time). Converting them into a velocity, he demonstrated that most of these objects were moving away from Earth (Slipher, 1917). Hubble estimated the distances of 24 more galaxies moving away from us, using Cepheids, among other methods. He then plotted the radial velocities of these galaxies (obtained by Slipher) against their distances (E. Hubble, 1929). Hubble discovered that the further away a galaxy is, the faster it is moving away from us. This correlation was later named as the *Hubble's law*, and is expressed as

$$v = H_0 \times D \tag{1.1}$$

where v is the radial, recession velocity of a galaxy in km/s, D is its distance in Mpc (1 Mpc=3.26 million light-years), and H_0 is the Hubble constant. The latter expresses the expansion rate of the Universe and is measured in units of velocity per distance (km/s/Mpc). His famous plot is shown in Fig. 1.2.

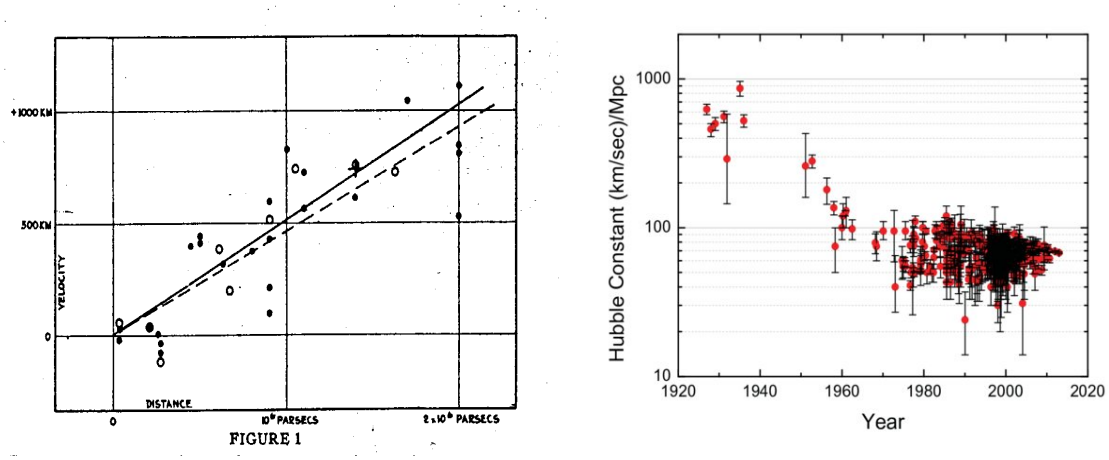

Figure 1.2: *Left panel*: Original Hubble's diagram of E. Hubble (1929). Full dots and solid line represent the case where all galaxies are considered individually, while the empty circles and dashed line represent the results after binning the galaxies into groups. The cross represents the mean result of 22 galaxies that were not analyzed individually. *Right panel*: Evolution of H_0 measurements with time (taken from Pritychenko 2015). During the last decade, the scatter has been significantly decreased.

It is worth to note that Lemaître also provided observational evidence for this correlation, independently

[1] The observed shift of the emitted photon energies (spectrum) of a celestial object towards lower energies, due to the expansion of the space between the observer and the object or due to the Doppler effect.

of Hubble and around the same time[2]. In 2018, the International Astronomical Union voted for renaming the Hubble law to *Hubble-Lemaître* law. Both Lemaître and Hubble obtained a much larger expansion rate of the Universe (625 and 500 km/s/Mpc respectively) than the currently accepted one ($\sim$ 70 km/s/Mpc). This was due to vastly underestimating the distances of the studied galaxies. The established expansion of the Universe led Einstein to abandon the cosmological constant Λ from his equations.

1.0.1.4 Establishing modern cosmology: Big Bang, Dark Matter, and Dark Energy

In the first half of the 20$^{\text{th}}$ century, the cosmological community was divided about the dynamical evolution of the Universe, and numerous models were proposed. However, two models stood out in terms of popularity: the Big Bang model and the Steady-State model. The former was formulated by Lemaître (Lemaıtre, 1931b), and described a Universe that had a beginning in time, has gone through an ultradense and hot state in the past, and expands forever. This Universe obeys the Cosmological Principle, being homogeneous and isotropic. This means that an observer will measure the same cosmic properties at a given time, no matter where they are placed or towards where they look. On the other hand, the Steady-State model was developed by Hoyle, Bondi and Gold (Hoyle, 1948; Bondi et al., 1948), and described an expanding Universe with infinite age, where the matter density remains constant by continuous creation of matter. This would mean that the Universe looks the same at any given time, obeying the *perfect* Cosmological Principle.

During the 1950s and 1960s, the Big Bang model prevailed due to the overwhelming observational evidence. For instance, the existence of very distant, radio-loud quasars falsified the Steady State model. The most crucial verification of the Big Bang model was the discovery of the Cosmic Microwave Background (CMB) in 1964 by Penzias and Wilson (Penzias et al., 1965). The CMB is the relic radiation of a very early stage of the Universe, when the density and temperature of the cosmic plasma are very high. The CMB can be observed in the microwave frequencies. Its existence was predicted by Gamow, Alpher, and Bethe (Gamow, 1946; Alpher et al., 1948) as a direct consequence of the Big Bang model, while it was inconsistent with the Steady State model. From that point on, the Big Bang model has been generally accepted by astronomers as the standard model of cosmology.

The existence of the mysterious *dark matter* was another significant development in cosmology during this time. Astronomers realized that the amount of luminous matter did not correspond to the total matter that should exist to explain various observations, assuming of course that GR is the correct theory of gravity at all cosmological scales. Therefore, much more matter should be present in the Universe, which we can simply not see. Speculations about invisible matter have been made since ancient times. The first scientific arguments based on observations started to appear in the 19$^{\text{th}}$ century by Bessel, Le Verrier, Secchi, and others (see Bertone et al., 2018, for a review on the history of dark matter). In these cases, the missing matter was revealed to be very faint (dark) stars and planets, or dark gas and dust clouds. The first attempts to quantify the total dark matter within our Galaxy came from Kelvin, who studied the velocity dispersion of stars. Based upon his work, Poincaré (who probably came up with the term "dark matter" even though many times it is credited to Zwicky), Föpic, Kapteyn, Oort, and Jeans further studied the amounts of total matter in the Milky Way. They mostly concluded that a considerable amount of dark matter exists, but probably less than the visible matter. They considered this dark matter's nature to be that of ordinary matter that does not emit sufficient light and not some form of exotic matter.

In 1933, Zwicky carried out the most influential and robust estimation of dark matter amounts until

[2] Hubble published his results for the first time in 1924 in The New York Times, in a non-peer-reviewed article. Lemaître published his peer-reviewed article in 1927 but written in French and in a low impact journal, while Hubble published his findings in a peer-reviewed journal in 1929. Two years later, Lemaître republished his article in English, in a higher profile journal (Lemaıtre, 1927).

then. He firstly measured the apparent velocity dispersion of several galaxy members of the Coma cluster of galaxies (Zwicky, 1933). Zwicky then applied the virial theorem (which relates the kinematic energy of galaxies to the total gravitational potential energy of a system) and determined the total mass of the Coma cluster. By also estimating the mass of the visible matter (i.e., via the total light it emits), he concluded that the unseen mass was hundreds of times larger than the matter that could be observed. Three years later, Smith presented similar findings by studying the Virgo cluster.

Nevertheless, some ambiguity around this topic remained for the next few decades. Nearly 40 years later, more compelling evidence came to light in favor of large amounts of unseen matter in spiral galaxies. Rubin and Ford studied the rotational curves of such galaxies out to large radii and saw that they do not decline, as expected, if no additional mass existed (Rubin et al., 1978). This could be reconciled with the standard gravity theory only if a spherical dark matter halo surrounded the visible parts of the galaxies. Within the next decades, independent analyses using various methodologies (e.g., gravitational lensing) confirmed the need for dark matter, which appeared to be ~ 5 times more abundant than visible matter. The remaining question was the nature of this excess matter. This debate was later settled by observing the CMB anisotropies in greater detail, the Big Bang Nucleosynthesis predictions, and the observed cosmic abundances of heavy elements. Dark matter cannot be ordinary, baryonic matter from which our everyday cosmos is built of. It has to be an exotic, nonbaryonic form of matter. To this day, the exact nature of dark matter remains unknown.

The next major addition to the standard cosmological model was the exponential expansion of space in the very early stages of the Universe after the Big Bang. This phase is simply referred to as *inflation*. Inflation was introduced as a solution to several cosmological problems (Guth, 1981; Linde, 1982; Starobinsky, 1982). Such problems were the inability to detect magnetic monopoles and to explain the observed flatness of space and the horizon problem (which referred to the surprising, large-scale isotropy of the CMB). Guth, Linde, and Starobinsky were awarded the 2014 Physics Nobel prize for their contributions to the theory of inflation.

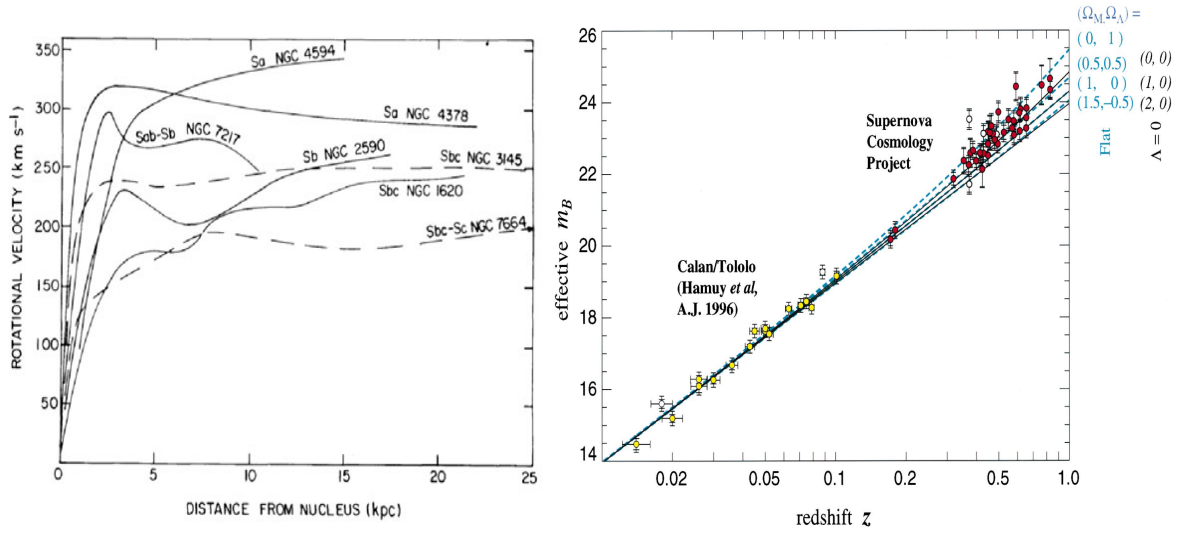

Figure 1.3: *Left panel*: Dark matter evidence from rotation curves of seven galaxies as presented in Rubin et al. (1978). They do not decrease with radius as expected from standard gravity theories if no dark matter existed. *Right panel*: Dark energy evidence from the apparent brightness of 42 SNIa as a function of redshift, as presented in Perlmutter et al. (1999). SNIa are further away than they should be in a matter-dominated Universe with no dark energy. The notations of the plot will be explained in the next section.

The final, and arguably most important, element added in the standard cosmological model is the so-called *dark energy*. After the 1980s, the predominant cosmological model dictated that we live in a spatially flat Universe, where 95% of its total mass-energy component is in the form of dark matter, while the rest 5% is baryonic matter. However, many inconsistencies started to accumulate between observations and theoretical predictions. For example, fewer cluster halos than expected from the structure formation models were found (e.g., Davis et al., 1985; Bahcall et al., 1992), the baryonic content of clusters pointed toward a low-density Universe (e.g., White et al., 1993), the measured Hubble constant was larger than what was needed to reconcile the model with the estimated age of the Universe (e.g., Huchra, 1992), and the observed peculiar velocity field of galaxies deviated from the model expectations (e.g., Peebles, 1984; Efstathiou et al., 1992; Kofman et al., 1993). To reconcile with these findings, many studies considered that the cosmological constant Λ might be positive rather than zero. In other words, a form of vacuum energy, imprinted in the fabric of space, might exist. The definitive evidence of Λ being positive came by Riess et al. (1998) and Perlmutter et al. (1999). The two independent studies used supernovae of type Ia (SNIa, considered to be standard candles) to trace the expansion of the Universe out to large cosmic distances. Both studies found that distant SNIa appeared fainter than expected. This could be explained only if the expansion of the Universe is accelerating instead of decelerating as previously thought. For this to be possible within the FLRW framework, a substance with the properties of Λ should drive cosmic expansion. This substance was named dark energy and accounts for $\sim 70\%$ of the entire mass-energy density of the cosmos. It is postulated to act opposite to gravity, "pushing" the Universe to grow faster. This discovery established the Lambda Cold Dark Matter (ΛCDM) model as the concordance model in cosmology. Riess, Perlmutter, and Schmidt were awarded the Nobel Prize in Physics in 2011 for proving the accelerating expansion of the Universe. Unfortunately, the nature of dark energy remains completely unknown to this day.

Since then, the growth of the science of cosmology has been stunning. Multiple experiments that cover the entire electromagnetic spectrum have been employed to help us put tight constraints in almost all cosmological parameters. In the 21st century we entered the era of *precision* cosmology. Does this mean we have figured out the Universe? Far from it. First and foremost, the nature of dark matter and dark energy, which together constitute $> 95\%$ of the Universe, remains completely unknown. Aside from this, ΛCDM has been proven to be a tremendously successful model, but some discrepancies persist. The most well known is the so-called *Hubble tension* (e.g., Mörtsell et al., 2018). This refers to the fact that the current expansion rate of the Universe, i.e., H_0, as inferred from the *early* Universe measurements (e.g., the most precise CMB measurements), strongly disagrees with the local, *late* Universe measurements (e.g., SNIa). A similar tension exists between the CMB predictions and the observed matter structure measurements in terms of the amplitude of the matter power spectrum (e.g., Douspis et al., 2019; G. W. Pratt et al., 2019). The understanding of the exact physical processes that led to the early inflation period is still lacking. Last but not least, several indications about a cosmic anisotropy have been recently emerged. These anisotropies refer either to a spatially varying expansion rate of the Universe due to primordial effects or large, coherent motions of galaxies and galaxy clusters (called *bulk flows*), which are inconsistent with the predictions of ΛCDM. This is the focus of this dissertation, and further discussions can be found in Chapters 3 and 4.

1.0.2 The standard cosmological model

Our cosmological model is founded on two fundamental pillars; the validity of the Cosmological Principle (CP) and general relativity (GR) being the correct theory of gravity. CP states that there is no special place or direction in the Universe, which is statistically homogeneous and isotropic on sufficiently large scales. Consequently, its measured properties depend only on the radial distance from an observer. Moreover,

GR is assumed to govern the gravitational interactions of matter on all cosmic scales.

1.0.2.1 Dynamical evolution, cosmological parameters, and distances

In GR, the three-dimensional space can be merged with time into one four-dimensional continuum, called *spacetime*. By assuming the CP, the FLRW metric can be defined by solving Einstein's field equations. Simply put, this metric describes the distance between two fixed points in spacetime, and it keeps "stretching" due to the expansion of the Universe. The change in the proper distance of two points due to space expansion is proportional to the dimensionless *cosmic scale factor* $a(t)$, where t is the cosmic time. For the present time t_0, the scale factor is normalized to unity, i.e., $a(t_0) = 1$. The general form of the FLRW metric given in spherical coordinates is

$$\mathrm{d}s^2 = c^2\mathrm{d}t^2 - a(t)^2\left[\mathrm{d}r^2 + f_K^2(r)\left(\mathrm{d}\theta^2 + \sin^2\theta\,\mathrm{d}\phi^2\right)\right], \tag{1.2}$$

where c is the speed of light, r is the comoving radial coordinate, and (θ, ϕ) are the angular coordinates. The function $f_K(r)$ is the comoving radial distance and is given by

$$f_K(r) = \begin{cases} K^{-\frac{1}{2}}\sin\left(K^{\frac{1}{2}}r\right) & (K > 0) \\ r & (K = 0) \\ (-K)^{-\frac{1}{2}}\sinh[(-K)^{\frac{1}{2}}r] & (K < 0), \end{cases} \tag{1.3}$$

where $K \propto \mathrm{length}^{-2}$ expresses the geometry of the Universe. The case with $K > 0$ corresponds to a hyperspherical, finite Universe ("closed"), which will eventually recollapse under its self-gravity. On the other hand, $K < 0$ describes a spatially infinite one with constant negative curvature ("open") that will expand forever. The standard cosmological model, however, dictates that we live in a Euclidean-space, infinite Universe ("flat") with $K = 0$, which will also expand forever.

Photons emitted with a frequency ν_e from an astrophysical source, travel through spacetime along light rays (i.e., null geodesics, $\mathrm{d}s = \mathrm{d}\theta = \mathrm{d}\phi = 0$). Based on Eq. 1.2, one can show that they are subject to time dilation. The latter is manifested as a decrease in their observed frequencies ν_0. This shift can also be expressed in terms of the scale factor at the time of the photon emission, as $\dfrac{\nu_e}{\nu_0} = a(t)^{-1}$. The redshift z of a luminous source is defined as the relative change in the frequency of photons and thus it can be related to the scale factor as:

$$z = \frac{\nu_e - \nu_0}{\nu_0} = \frac{1}{a(t)} - 1. \tag{1.4}$$

Thus, for the present time $z = 0$, while z increases with the distance of an object, since the emitted light needs more time to reach us and suffers a more severe time dilation. For instance, if we observe the light emitted from a galaxy when the Universe was half its current size, $a(t) = 0.5$, we will measure $z = 1$. This relation holds for all cosmological models.

Moreover, the expansion rate of the Universe at any point of cosmic time can be defined in terms of $a(t)$. This is known as the *Hubble parameter* $H(t)$ and reads as

$$H(t) = \left(\frac{\dot{a}}{a}\right); \quad H(t_0) = H_0 = a(\dot{t}_0). \tag{1.5}$$

The second part describes the expansion rate of the Universe today, namely the Hubble constant H_0, which is arguably the most important cosmological parameter. As discussed above, its exact value is a topic of intense discussion in modern cosmology (Hubble tension), but it seems to lie between 67 and 75

km/s/Mpc (Riess, 2019). Moreover, from Eq. 1.4 and 1.5, it is evident that the Hubble parameter can be expressed as a function of redshift as well, i.e., $H = H(z)$. This is the most common form in modern cosmology since z is a direct observable, while a and t are not.

The dynamical evolution of the Universe is described by the two Friedmann equations (see Sect. 1.0.1.3). These relate $a(t)$ and its time derivatives $a\dot{(t)}$ and $a\ddot{(t)}$ to the contents of the Universe as follows:

$$\begin{aligned} \left(\frac{\dot{a}}{a}\right)^2 &= \frac{8\pi G\rho(t)}{3} - \frac{Kc^2}{a^2} \\ \frac{\ddot{a}}{a} &= -\frac{4\pi G}{3}\left[\rho_{\mathrm{tot}}(t) + \frac{3P}{c^2}\right], \end{aligned} \tag{1.6}$$

where G is the gravitational constant. Here ρ_{tot} and P correspond respectively to the total mass-energy density and pressure of all components. These components are handled as homogeneous perfect fluids in the Friedmann equations.

There is a certain critical value ρ_{crit} of the total density for every cosmic time, which defines a spatially flat Universe with $K = 0$. Combining Eq. 1.5 and 1.6, one finds that

$$\rho_{\mathrm{crit}}(t) = \frac{3H(t)^2}{8\pi G} = \rho_{\mathrm{crit},0}E(t)^2, \tag{1.7}$$

where $\rho_{\mathrm{crit},0} = \dfrac{3H_0^2}{8\pi G} \approx 9.5 \times 10^{-30}$ g/cm^3 the critical density today (for $H_0 = 70$ km/s/Mpc) and $E(t) = \dfrac{H(t)}{H_0}$ the evolution of the Hubble parameter. A higher total density $\rho_{\mathrm{tot}} > \rho_{\mathrm{crit}}$ would result in $K > 0$ and a closed Universe, while for $\rho_{\mathrm{tot}} < \rho_{\mathrm{crit}}$ the spatial curvature would be negative ($K < 0$) and the Universe would be an open one.

There are several components in the Universe that contribute to the total density. The most crucial ones are the baryonic matter (ρ_{b}), dark matter (ρ_{CDM}), dark energy (ρ_{DE}, which in the case of vacuum energy reduces to ρ_Λ), and at a lesser degree, radiation (ρ_{r}). A brief description of each component is given below.

- **Radiation**: Radiation is composed of relativistic, nearly massless particles. Currently, only CMB photons are believed to contribute to the radiation component. Relativistic neutrinos can also contribute to ρ_{r}. However, neutrinos are currently nonrelativistic since they have a small but nonzero mass. In the very early stages of the Universe, neutrinos were relativistic due to their high temperatures and small masses, thus contributed to ρ_{r}. The exact moment of this transition is uncertain due to the unknown neutrino mass. As later discussed, the effects of the radiation in the dynamical evolution of the cosmos are completely negligible for the vastly largest part of the Universe's age.

- **Baryonic matter**: Baryonic matter makes up for the ordinary, luminous matter of the cosmos known to us, protons and neutrons. In cosmology, however, baryons are more loosely defined to include all atomic matter, ignoring the minimal contribution of electrons (which are leptons) to the total mass. Therefore, ρ_{b} include the planets, stars, neutron stars, black holes, gas, and dust of the Universe.

- **Dark matter**: Dark matter is nonbaryonic matter that does not emit, absorb, or reflect electromagnetic radiation. It is believed to barely interact with baryonic matter (if any) and be collisionless. Its existence is inferred through its strong gravitational interaction with baryons and light. The

true nature of dark matter remains one of the biggest mysteries in modern physics. Two main subdivisions of dark matter exist, the hot (HDM) and cold (CDM) species. HDM consists of particles with relativistic velocities and low masses, such as neutrinos. HDM smooths out the small-scale structures in the early Universe, allowing large-scale structures to rise first. CDM comprises nonrelativistic, massive particles that collapse under gravity and favor the creation of small-scale structures before large-scale ones. Observations (e.g., large-scale structure of matter) support that CDM accounts for the vast majority of dark matter in the Universe. Weakly interacting massive particles (WIMPs) are the prime candidate for dark matter (e.g., Jungman et al., 1996), however experiments designed to detect them have failed to do so (e.g., Aprile et al., 2018). Several other dark matter candidates exist, with arguably the most popular being axions (e.g., Marsh, 2016).

- **Dark energy**: Dark energy is the hypothetical, homogeneous, perfect fluid that drives the Universe's accelerated expansion ($\ddot{a}$), having a negative pressure and counteracting the self-gravity of matter. The nature of dark energy is unknown, as is its behavior with time. In the standard cosmological model, dark energy is often identified as the cosmological constant Λ, or interchangeably as vacuum energy. The latter is the energy of space, motivated by fluctuations of the ground state of quantum fields.

Baryons and dark matter can be combined into one component, "matter" (ρ_m), since they both interact through gravity and have the same effects on the dynamics of the Universe. Hence, one can write $\rho_\mathrm{tot} = \rho_\mathrm{m} + \rho_\mathrm{DE} + \rho_\mathrm{r}$. The density parameters $\Omega_i = \dfrac{\rho_i}{\rho_\mathrm{crit}}$ denote the relative contribution of each component with respect to the critical density. As a result,

$$\Omega_\mathrm{tot} = \frac{\rho_\mathrm{tot}}{\rho_\mathrm{crit}} = \frac{\rho_\mathrm{m} + \rho_\mathrm{DE} + \rho_\mathrm{r}}{\rho_\mathrm{crit}} = \Omega_\mathrm{m} + \Omega_\mathrm{DE} + \Omega_\mathrm{r}. \tag{1.8}$$

By plugging 1.5, 1.7, and 1.8 into 1.6, we get

$$\Omega_\mathrm{m} + \Omega_\mathrm{DE} + \Omega_\mathrm{r} + \Omega_\mathrm{K} = 1, \tag{1.9}$$

where $\Omega_\mathrm{K} = -\dfrac{Kc^2}{a^2H^2}$ is the curvature density parameter. Here all the density parameters are functions of time. The relation between the density ρ and the pressure P of each component is characterized by the *equation of state* (EOS)

$$P = w\rho c^2, \tag{1.10}$$

where w is the dimensionless EOS parameter of each component. By plugging the EOS into the second Friedmann equation in 1.6, and solving the differential equation one finds how the different densities evolve with cosmic time, or equivalently the scale factor a. For a constant w, this reads:

$$\rho = \rho_0 a^{-3(w+1)}, \tag{1.11}$$

where ρ_0 is the density of a component today.

Baryonic and dark matter are both pressureless, with $w_\mathrm{m} = 0$. For radiation, the EOS can be found from thermodynamics to be $w_\mathrm{r} = 1/3$. For the curvature "density", the definition of Ω_K implies that $w_K = -1/3$. Finally, the exact EOS of dark energy is one of the most important questions in cosmology and a field of intense research. It is denoted as w_DE and it can be either a constant or a function of cosmic time, i.e., the scale factor [$w_\mathrm{DE}(a)$]. In the latter case, the second Friedmann equation has a more complex,

as does 1.11 consequently. In the limiting case that dark energy is in fact vacuum energy, then $w_\Lambda = -1$, and its density ρ_Λ remains constant throughout cosmic time.

Plugging the w_i values and Eq. 1.4 into Eq. 1.11 and dividing by Eq. 1.7, one obtains each density parameter as a function of redshift:

$$\Omega_\mathrm{m} = \Omega_{\mathrm{m},0}\frac{(1+z)^3}{E(z)^2},\quad \Omega_\mathrm{r} = \Omega_{\mathrm{r},0}\frac{(1+z)^4}{E(z)^2},\quad \Omega_K = \Omega_{K,0}\frac{(1+z)^2}{E(z)^2},\quad \Omega_\mathrm{DE} = \Omega_{\mathrm{DE},0}\frac{(1+z)^{[3(w_\mathrm{DE}+1)]}}{E(z)^2}. \quad (1.12)$$

Here the index "0" indicates the value of a parameter in the present era. The contribution of each species to the density sum rule 1.9 changes with time. The density parameter values have been well constrained through the years, via several different methods. Although there is some small scatter around their best-fit values, the generally accepted values are $\Omega_{\mathrm{m},0} \approx 0.3$, $\Omega_{\mathrm{r},0} \approx 9 \times 10^{-5}$, and $\Omega_{\mathrm{DE},0} \approx 0.7$ (note that many times the notation Ω_Λ is used instead, even when dark energy is not restricted to the cosmological constant case). The latest observations favor a rather flat Universe with $\Omega_{\mathrm{K},0} \leq 10^{-3}$ (Efstathiou et al., 2020; Planck Collaboration et al., 2020), although recently some contradicting results pointed towards a slightly positively curved Universe with $\Omega_{\mathrm{K},0} \approx -0.09$ (Di Valentino et al., 2020). Nonetheless, the general consensus still is that of $\Omega_{\mathrm{K},0} \approx 0$. From now on, the "0" index will be omitted in the density parameters, and the present time value will be implied, unless the dependance on z is explicitly showed.

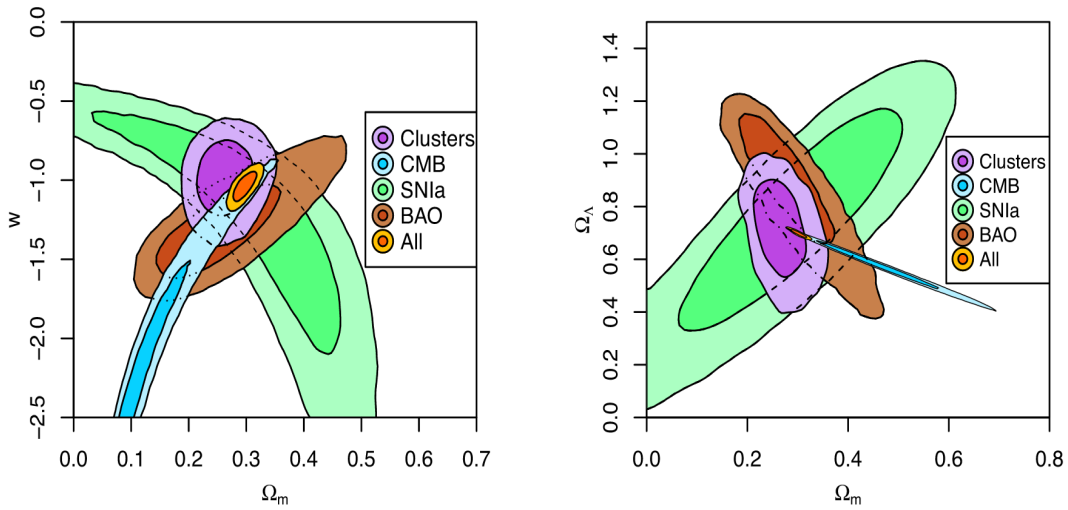

Figure 1.4: Cosmological parameter constraints on the matter and dark energy density (Ω_m and Ω_Λ respectively) and dark energy EOS (w) based on different probes. Each probe traces the underlying cosmology in a different manner and their combination provides tighter overall constraints. Agreement across independent methods solidifies the tested model, while possible discrepancies might reveal systematic biases in the analyses, or new physics that need to be added in the standard cosmological model. The image is adopted from Mantz et al. (2015).

For the EOS of dark energy there is higher uncertainty around its exact value, however most studies support a constant value of $w_\mathrm{DE} \approx -1$, which points towards vacuum energy as the origin of the accelerated expansion. This value also acts as a boundary between different possible explanations of dark energy and different final fates of the Universe. More negative values would imply that the density of dark energy *increases* as the Universe expands. This would lead to the so-called "Big Rip" scenario, where all matter is eventually ripped apart due to the extreme expansion of space. Examples of constraints on the above cosmological parameters are shown in Fig. 1.4.

Making use of Eqs. 1.4-1.12, the first Friedmann equation can be rewritten in its most commonly used

form:

$$H(z) = H_0 \sqrt{\Omega_{\rm r}(1+z)^4 + \Omega_{\rm m}(1+z)^3 + \Omega_K(1+z)^2 + \Omega_{\rm DE}(1+z)^{3(w+1)}} \Rightarrow$$
$$H(z) = H_0 E(z), \tag{1.13}$$

where $E(z) = \sqrt{\Omega_{\rm r}(1+z)^4 + \Omega_{\rm m}(1+z)^3 + \Omega_K(1+z)^2 + \Omega_{\rm DE}(1+z)^{3(w+1)}}$. Therefore, the Hubble parameter describes the expansion rate of the Universe at any time (through z) as a function of its contents and the EOS of dark energy. Furthermore, due to their very low density values, the contributions of radiation and curvature can be ignored, leaving us with $\Omega_{\rm DE} \approx 1 - \Omega_{\rm m}$. Also, in the case of ΛCDM, $w_{\rm DE} = -1$, and 1.13 reduces to a function of only two free parameters:

$$H(z) = H_0 \sqrt{\Omega_{\rm m}(1+z)^3 + (1-\Omega_{\rm m})}. \tag{1.14}$$

Using this formulation, one can determine the age of the Universe from Eq. 1.5, by integrating with respect to the scale factor, from the Big Bang ($a = 0$) to today ($a = 1$):

$$H(a) = \frac{{\rm d}a}{a{\rm d}t} \Rightarrow t_{\rm age} = \frac{1}{H_0} \int_0^1 \frac{{\rm d}a}{aE(a)} \tag{1.15}$$

This yields an age of ≈ 13.7 billion years according to ΛCDM.

In a dynamical Universe, there is no one unique meaning of distance between two objects. As light rays travel from a source to an observer, spacetime continuously evolves. There are however three main approaches that we can consider to define a cosmological distance, namely the *comoving distance* D_C, the *luminosity distance* D_L, and the *angular diameter distance* D_A. The last two can be obtained observationally by how bright or how large an object appears in the sky if we know these objects' intrinsic properties.

More specifically, the luminosity distance of a source is defined as

$$D_L = \sqrt{\frac{L}{4\pi f}}, \tag{1.16}$$

where L is the intrinsic luminosity of the source (emitted energy per time) and f is its flux (luminosity per surface area). The latter can be easily measured, while the former has to be known. If this is indeed the case, then D_L can be determined without assuming any cosmological model. The objects for which the intrinsic luminosity is known are called *standard candles*. The angular diameter distance of a source is defined as

$$D_A = \frac{R}{\Theta}, \tag{1.17}$$

where R is the physical extend of the object perpendicular to the line of sight, while Θ is the apparent angular size in the sky. These two distances, together with D_C, can also be estimated theoretically. These estimations are based solely on the measured redshift of an extragalactic object, the FLRW metric, and the Friedmann equations as follows.

D_C is defined within the comoving coordinate system of spacetime, and as such it does not change with time. It can be obtained from the FLRW metric in Eq. 1.2. Information travels in space in the form of light. As mentioned before, light rays follow null geodesics with ${\rm d}s = {\rm d}\theta = {\rm d}\phi = 0$. Also, let us consider a flat Universe (which will be used throughout this dissertation). Thus, Eq. 1.2 can be rewritten

as

$$a(t)\,\mathrm{d}r = -c\,\mathrm{d}t \Rightarrow r = \int_{t_{\rm em}}^{t_{\rm obs}} \frac{c}{a(t)}\mathrm{d}t, \tag{1.18}$$

where $t_{\rm em}$ is the time that a photon was emitted from a source, and $t_{\rm obs}$ the time it was detected by an observer. If consider ourselves as the observers, then $t_{\rm obs}$ =now, $a = 1$, and $z = 0$. Plugging 1.4 and 1.5 into Eq. 1.19, one can express the radial comoving distance $D_C \equiv r$ in terms of the cosmological redshift of a source z:

$$D_C = \frac{c}{H_0}\int_0^z \frac{\mathrm{d}z'}{E(z')}. \tag{1.19}$$

It can be shown (e.g., S. Weinberg, 1972; Amendola et al., 2010, among many others) that D_L and D_A relate to D_C and to each other as:

$$D_L = (1+z)\,D_C = (1+z)^2\,D_A. \tag{1.20}$$

This relation is independent of the assumed cosmological model. Accordingly, by measuring the cosmological redshift of a source through its observed spectrum, one can calculate the different types of distances of this source for any cosmological model.

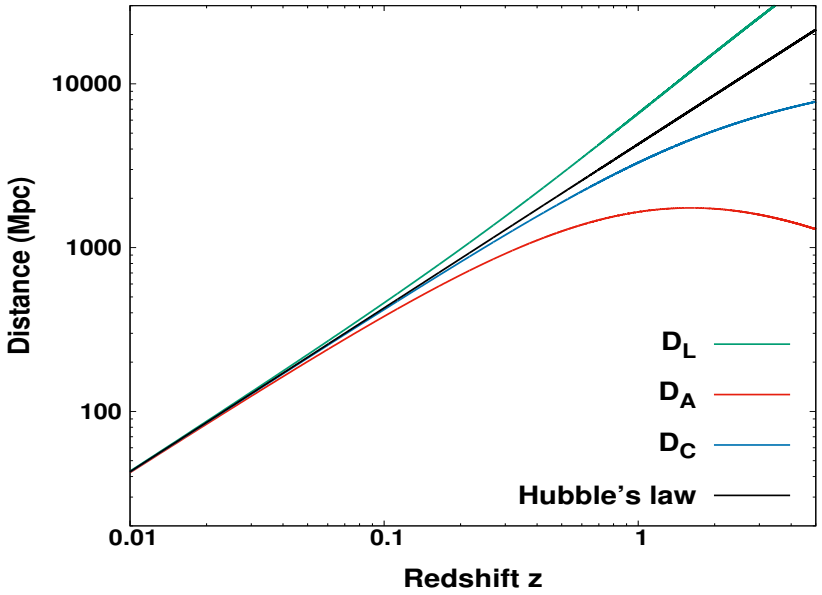

Figure 1.5: Cosmological distances as a function of redshift. The luminosity, angular diameter, and comoving distances are shown in green, red, and blue respectively. The Hubble-Lemaître law distance is shown in black (denoted as "Hubble's law" for convenience).

Fig. 1.5 compares the evolution of the three distances with z for the ΛCDM model. The pure Hubble-Lemaître law [Eq. 1.1] is also shown. It is clear that at low z, the different types of distances do not significantly deviate. This strongly changes with increasing z. D_A shows a counterintuitive behavior at $z \gtrsim 1.3$, where it starts to decrease again. Qualitatively, this happens because the Universe gets much smaller at high z, and an object of fixed size occupies a larger fraction of the overall space, which makes it appear larger in the sky.

Finally, one can compare an object's observed distance, which is determined independently of any

cosmological model, to the theoretically expected distance, which is based on the measured z. The cosmological parameter values that make the two distances match can then be obtained. Using a large number of extragalactic objects, one can obtain reliable estimates for the cosmological parameters. This is the standard methodology of how these values are constrained based on measured distances.

1.0.2.2 Growth of structures

In the Friedmann equations, the Universe is an entirely homogeneous place. The density of matter does not have a positional dependence, it is only a function of time. Of course, this is not a true description of the cosmos. The initial density perturbations created at the early cosmic times grow with time due to their self-gravity. This gravitational instability amplifies the matter structure formation, and, fortunately for us, planets, stars, galaxies, and clusters of galaxies are eventually created. The so-called "cosmic web" also consists of filaments and sheets of galaxies and gas and immense voids with very little dark and baryonic matter within them.

Overdense regions continuously accrete more mass from their surroundings, forming dark matter halos that trap baryons, eventually creating luminous objects. As these regions are created close to each other, they undergo mergers due to their gravitational attraction, forming even larger structures. This hierarchical structure formation from small overdensities to larger ones is called the *bottom-up* scenario. As argued before, this constitutes strong evidence that the dark matter is composed of massive, slow-moving particles instead of relativistic ones. In Fig. 1.6, an example of the cosmic web is shown as obtained by the Millennium simulation (Springel et al., 2005). The evolution of large-scale structure is clear with redshift and cosmic time.

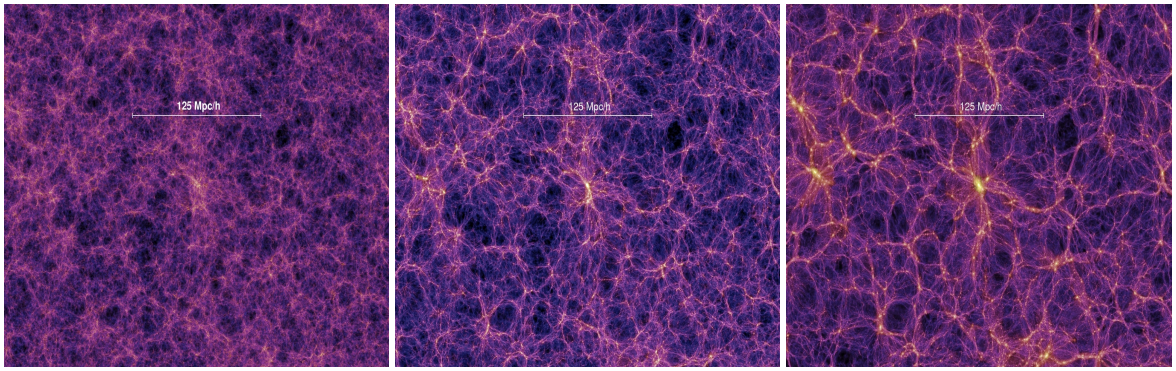

Figure 1.6: Example of large-scale structure evolution from the Millennium simulation at $z = 5.7$ (left), $z = 1.4$ (middle), and $z = 0$ (right). Each plot side is ≈ 400 Mpc.

The growth of structure formation can be studied analytically. Let us define the *density contrast* parameter δ:

$$\delta(r,t) = \frac{\rho(r,t) - \langle\rho(t)\rangle}{\langle\rho(t)\rangle}, \tag{1.21}$$

which compares the density $\rho(r)$ of a region with radius r with the mean density of the Universe $\langle\rho\rangle$. As long as density fluctuations are small ($\delta \ll 1$), one can use linear perturbation theory. Some other necessary (but reasonable) assumptions made are that dark energy is collisionless and homogeneous, that radiation is insignificant compared to the pressureless matter, and that the considered perturbations are much smaller than the horizon scale ($= c/H(z)$, ≈ 4 Gpc today) at a given time. Matter is also treated as a fluid. One can now use the well-known continuity, Euler, and Poisson equations (describing the

conversation of matter, momentum, and the gravitational potential respectively) and combine them with Eq. 1.21. Then, one determines the way that the density contrast of a region changes with time:

$$\ddot{\delta} + 2H\dot{\delta} - \frac{3H_0^2\Omega_{\rm m}}{2a^3}\delta = 0. \tag{1.22}$$

Here the expansion of the Universe factors in through the so-called the "Hubble drag", $2H\dot{\delta}$. This term tries to prevent the overdensities from collapsing into structures, acting as friction. Moreover, the $\frac{3H_0^2\Omega_m}{2a^3}\delta$ term results in an acceleration of the the collapse under the self-gravity of the spherical region. The time dependance $D_{\pm}(t)$ and the spatial dependance $\Delta_{\pm}(\mathbf{r})$ of Eq. 1.22 can be separated:

$$\delta(\mathbf{r}, t) = D_+(t)\,\Delta_+(\mathbf{r}) + D_-(t)\,\Delta_-(\mathbf{r}), \tag{1.23}$$

where the "+" and "−" solutions denote the growing and decaying solution, and are linearly independent. It can be shown that the decaying solution dies out quickly as the size of the Universe increases and only D_+ (hereafter D) survives. Now one can replace $\delta(\mathbf{r}, t)$ with $D(t)$ in Eq. 1.22, and solve the differential equation to find the redshift dependancy of D (in the case of $w_{\rm DE} = -1$). $D(z)$, which is called the *growth factor*, is normalized so $D(z = 0) = 1$ for $\Omega_{\rm m} = 1,\ \Omega_\Lambda = 0$ (called an Einstein-de Sitter, EdS, Universe) and is given by

$$D(z) = 2.5\ \Omega_{\rm m}\ E(z) \int_z^\infty \frac{(1 + z')}{E(z')^3}\ {\rm d}z'. \tag{1.24}$$

The growth factor does not depend on H_0, but it strongly depends on the density parameters. Also, $D(z)$ decreases with increasing z. This demonstrates that as the cosmic time passes, the density contrast of structures increases. Qualitatively, overdense regions with $\delta > 0$ will suffer a greater self-gravitation than a region with average density. The expansion of the overdense region then slows down compared to the average Hubble expansion, and δ increases further. Accordingly, underdense regions with $\delta < 0$ will expand faster due to the lack of self-gravity and they will become less dense with time.

A spherical overdensity reaches its maximum radius before it starts collapsing. This is called the *turnaround radius*. In linear perturbation theory and for a EdS model, the necessary density contrast for this to happen is $\delta_{\rm lin}^{\rm turn} \approx 1.06$, at any given cosmic time. In reality, however, the evolution of the density fluctuations is nonlinear. It can be found that the respective nonlinear turnaround density contrast is $\delta_{\rm nonlin}^{\rm turn} \approx 4.55$. Utilizing the virial theorem and energy conservation, one can find that a spherical overdensity will collapse and reach virial equilibrium when its radius is half of the turnaround radius. Subsequently, its density will increase by a factor of 8. The time needed for an overdensity to reach the turnaround point equals the time needed to collapse. Thus, for an EdS model, it can be easily shown that the average background density will decrease by a factor of 4 due to the Hubble expansion. Overall then, the nonlinear density contrast for a gravitationally bound structure will be amplified by 32 times, becoming $\delta_{\rm nonlin}^{\rm coll} \approx 178$ times denser than the rest of the Universe. This value will be much lower for a ΛCDM Universe; nevertheless a density contrast of 200 is still used to distinguish between collapsed halos (i.e., galaxy cluster halos) and the Hubble expansion. The properties of a halo within the sphere that its average density is 200 times larger than the average density of the Universe is denoted with a "200" subscript (e.g., M_{200} for the halo mass within the sphere with the virial radius R_{200}).

The study of the abundance of the gravitationally bound halos can unveil valuable information about cosmological parameters, such as $\Omega_{\rm m}$. One can measure the *halo mass function*, namely how many halos exist per mass and per redshift, and one can compare this to the theoretical expectation based on the growth of structure, which depends on the assumed cosmology (e.g., Reiprich et al., 2002; Schellenberger

et al., 2015). This method is independent of the geometrical tests, which study cosmological distances and thus provides a complementary and powerful test for any cosmological model.

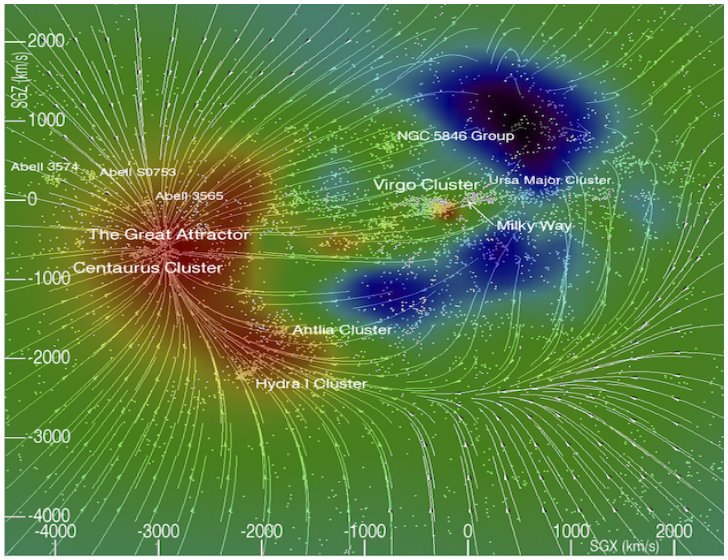

Figure 1.7: Peculiar velocity field (arrows) and matter density field (color coded) of the local Universe (~ 100 Mpc per plot side), taken by Courtois et al. (2013).

Since inhomogeneous structures arise at small scales, it is expected that gravitational attraction will vary in different directions. This would cause nearby galaxies and galaxy clusters to move towards their most massive neighbors due to this excess gravity. Their motion will be characterize by their *peculiar velocity* $\mathbf{v}$. Consequently, if one knows the density contrast field $\delta(\mathbf{x}, a)$ of a region, the peculiar velocity field $\mathbf{v}(\mathbf{x}, a)$ can be predicted. For the present epoch (a=1), the peculiar velocity field is given by

$$\mathbf{v}_{\mathrm{pec}}(\mathbf{x}) = \frac{\Omega_{\mathrm{m}}^{0.6}}{4\pi} H_0 \int \delta(\mathbf{x}') \frac{\mathbf{x}' - \mathbf{x}}{|\mathbf{x}' - \mathbf{x}|^3} \mathrm{d}^3 x'. \tag{1.25}$$

This theoretical prediction can also be used to put constraints on the cosmological parameters. One can compare this to the measured peculiar velocities of the galaxies in the local Universe. The peculiar velocities can be obtained by comparing their measured redshift with the cosmological redshift that they *should* have based on their distance, which can be measured independently of cosmology (e.g., standard candles). The radial peculiar velocity u_{pec} of a source directly relates to the redshift z_{pec} it causes due to the relativistic Doppler effect as

$$z_{\mathrm{pec}} = \sqrt{\frac{1 + u_{\mathrm{pec}}/c}{1 - u_{\mathrm{pec}}/c}} - 1. \tag{1.26}$$

A coherent motion of a sphere of galaxies and clusters towards a particular direction is called a *bulk flow*. A reconstruction of the peculiar velocity field and the matter over- and underdensities in the local Universe is displayed in Fig. 1.7. One can see that at the scales of the plot, a bulk flow of our local neighborhood towards the overdense region of the Great Attractor exists. This bulk flow is further amplified by the lack of gravity from the void in the opposite region.

1.0.2.3 Timeline of the Universe

The Universe came into existence $\approx$ 13.7 billion years ago with the hot Big Bang (BB), when all space, time, and energy were created from a cosmic singularity. The first $\approx 10^{-43}$ s (hereafter all time and temperature scales are considered to be approximate estimations) are characterized as the *Planck epoch*. Our physical theories for these times are largely undefined. However, it is believed that the four fundamental forces of nature (gravity, the strong and weak nuclear forces, and the electromagnetic force) were unified. By the end of the Planck epoch, the temperature of the Universe was $T_{\rm Uni} \approx 10^{32}$ K (10^{19} GeV equivalently in terms of particle energy). The *Grand Unification Epoch* (GUT) followed, with gravity becoming distinct from the other three forces unified under the hypothetical electronuclear force. At 10^{-38} s, when $T_{\rm Uni} \approx 10^{27}$ K, the strong nuclear force was also separated from the rest, releasing vast amounts of energy and marking the end of the GUT epoch. It is speculated that this led to a symmetry-breaking phase transition, favoring the production of matter over antimatter in the Universe. This process is called *baryogenesis*. The immense discharge of energy during this phase is believed to have led to the exponential expansion of the Universe by 26 orders of magnitude during the *inflation period*, which lasted from 10^{-36} s to 10^{-32} s after the BB. This rapid expansion is postulated to have magnified the initial density quantum fluctuations in the Universe over cosmic scales. This can explain the causal contact between widely separated regions in the later Universe. It also flattens out the curvature of spacetime, leading to a currently flat Universe, almost regardless of the initial conditions. After inflation, the *electroweak era* started and lasted until 10^{-12} s after the BB. During that time, the weak nuclear force decoupled from the electromagnetic force, while the hypothetical dark matter particles with masses of $\geq$ 100 GeV stop producing since cosmic temperature drops below that threshold. These particles also freeze-out, halting any interactions, halting most interactions with other particles, and they start forming a homogeneous background. Up to that point, no known baryons or hadrons have been formed. As the Universe cooled down to 1 GeV, it entered the *particle epoch*, when hadrons and baryons such as protons and neutrons were formed, followed by the formation of leptons, such as electrons and neutrinos. Annihilation of matter and antimatter took place, leaving a small surplus of matter (tracing back to the GUT epoch). As the particle epoch was coming to an end and the particle energies were $\sim$ 1.4 MeV, the timescale of the weak interactions between neutrinos and the rest of the particles became larger than the age of the Universe, and thus neutrinos stopped interacting with the other particles. Up to that point, neutrons and protons were in equilibrium through the (inverse) β decay. After the decoupling of neutrinos, inevitably, the inverse β decay (which converts protons into neutrons) could not continue, and neutrons could no longer be produced. At the same time, they continued to decay into protons, and as such, their abundance dropped significantly. Shortly after, electron-positron pairs could also not be created since the photon energies generally dropped below the electron rest mass ($\approx$ 0.5 MeV).

The *Big Bang Nucleosynthesis* (BBN) epoch started roughly one minute after the BB, when the temperature dropped below 10^9 K or 0.1 MeV. After that, the tail of photons' energy distribution did not surpass 2.22 MeV, which is the binding energy of the deuterium nucleus. Therefore, the latter started to form undisrupted by photons. The formation of helium nuclei followed, which bounded almost all the available neutrons. Some minimal amounts of lithium and beryllium were also formed, but no heavier elements. BBN lasted for roughly 10 minutes, and the standard cosmological model correctly predicts the final abundances of the produced elements. The BBN time is succeeded by the *plasma era*, where photons were coupled with baryons and electrons, interacting mostly through Compton scattering. No major events took place during that time, which lasted for 380, 000 years.

In the early Universe, there was a significantly higher number of photons than baryons. Neutral hydrogen had not yet formed. The electron binding energy of hydrogen is 13.6 eV. Until the temperature of the Universe dropped to $\sim$ 3500 K (or 0.3 eV), there was a sufficient number of photons in the tail

of the energy distribution to prevent electrons from getting (and staying) captured. As the Universe expanded and the temperature dropped below that threshold, electrons started coupling successfully with protons to form hydrogen. This process is called *recombination* and occurred at redshift $z \approx 1100$ and lasted for $\approx 40,000$ years. The density of free electrons rapidly decreased, and photons were able to stream freely to cosmic distances. This process produced the last scattering surface, and clearly, these photons are the most ancient light one can observe. Today we are indeed able to observe this surface in the form of the CMB, which has the spectrum of a perfect blackbody with a temperature of 2.73 K. From its small temperature fluctuations, we can infer that the density fluctuations at $z \approx 1100$ were in the order of $\delta \lesssim 10^{-4}$. These fluctuations were the seeds that would eventually cause the structure of the Universe to form.

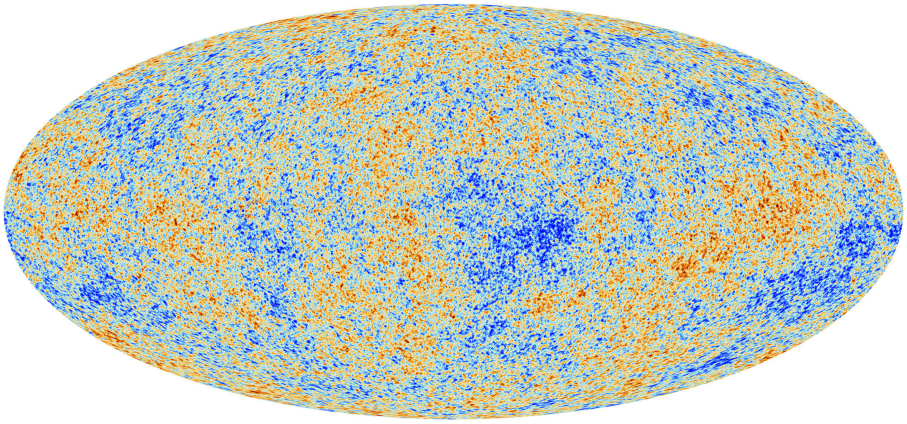

Figure 1.8: Temperature anisotropies in the CMB as observed by the *Planck* satellite (Planck Collaboration et al., 2014). The hotter temperatures are shown in red.

After recombination and until the first structures to appear, a few hundred million years passed. This period is referred to as the *dark ages*, due to the lack of astrophysical objects able to produce light (e.g., stars). The Universe was almost completely dark, with the only existing light to be the CMB photons and the 21 cm radiation emitted from neutral hydrogen. Roughly 300 Myr years after the BB, the first stars and galaxies started to form. As they started radiating energy, the produced photons started to ionize the intergalactic neutral gas once more. This time is referred to as *reionization* and is placed roughly at $z \approx 7.8$, 650 Myr after the BB (Planck Collaboration et al., 2020). From then on, the large-scale structure kept developing, with the first protocluster of galaxies arising shortly after. Due to the bottom-up scenario, however, the majority of galaxy clusters formed more recently, within the last 8 billion years ($z \lesssim 1$).

The timeline of the Universe can also be subdivided into epochs based on its dynamical behavior. The latter depends on which species (radiation, matter, or dark energy) dominated the total mass-energy density at any time. Using Eq. 1.12, one can equate the density parameters to determine the time that each component was more abundant than the rest. Doing so, the radiation-matter equality redshift is found:

$$\begin{aligned} \Omega_{\rm r}(z) = \Omega_{\rm m}(z) \;\Rightarrow\; \Omega_{\rm r}(1+z_{\rm rm,eq})^4 = \Omega_{\rm m}(1+z_{\rm rm,eq})^3 \\ \Rightarrow z_{\rm eq} \approx 3340 \quad \text{and} \quad t_{\rm eq} \approx 52000 \text{ years.} \end{aligned} \tag{1.27}$$

Thus, the *radiation-dominated era* ($\Omega_{\rm r} > \Omega_{\rm m}$) started after the BB and lasted until that time. In the very early Universe when $\Omega_{\rm r} \gg \Omega_{\rm m}$, the size of space was increasing with time as $a \propto t^{1/2}$, but the expansion was decelerating ($\ddot{a} < 0$). This can be seen by the two Friedmann equations, (Eq. 1.6). That era was

succeeded by the *matter-dominated era* ($\Omega_m > \Omega_r$, $\Omega_m > \Omega_{DE}$). Nearly 40 Myr after the BB, the radiation practically stopped influencing the dynamics of the Universe, since its density had dropped to negligible levels. Dark energy would still not emerge as a significant element of the Universe for a few billion years. Consequently, cosmic evolution strongly resembled that of an EdS model with $\Omega_m \approx 1$. Space expanded as $a \propto t^{2/3}$, still in a decelerating manner.

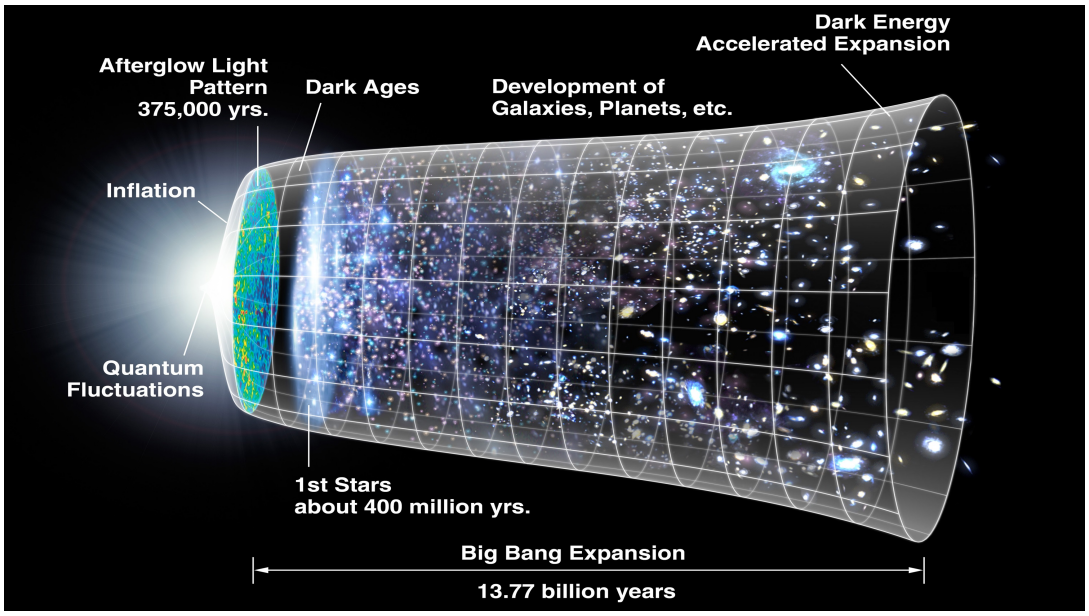

Figure 1.9: Timeline of the Universe (taken from `https://map.gsfc.nasa.gov/`).

Assuming $w_{DE} = -1$, the expansion of the Universe started accelerating ≈ 7 billion years ago ($z \lesssim 0.8$). Note that we are still in the matter-dominated era, but dark energy had already become the driving force of cosmic expansion. Following the same reasoning as in Eq. 1.27, one can compute when the *dark energy-dominated era* began. One finds that the density of dark energy surpassed that of matter during the last ≈ 3.7 billion years of the Universe, ($z \lesssim 0.33$). After Ω_m becomes negligible $\Omega_{DE} \approx 1$, the expansion will become exponential, $a \propto e^t$.

1.0.2.4 Cosmological Principle and the importance of testing it

The CP supports the lack of directionality in the Universe, and it is implied throughout the standard cosmological model. Cosmological parameters, and subsequently cosmic evolution, depend only on time. When one estimates the distance of an extragalactic source, only its redshift is taken into account and not its direction. In a nutshell, no primordial preferred axis is assumed to exist, and the expansion rate and contents of the Universe are taken to be statistically equivalent towards all directions. This property is called *isotropy* and plays a vital role in modern cosmological research.

Standard cosmology assumes the CMB rest frame to be the same as the matter rest frame; in other words, one should observe an isotropic behavior of the large-scale structure if one observes an isotropic CMB. When we do observe the CMB, a large dipole anisotropy in its temperature is found. This dipole anisotropy is believed to be caused purely by the Doppler shift of the CMB due to our random peculiar motion with respect to the Hubble expansion frame. We infer this motion to be 369 km/s towards the Galactic coordinates $(l, b) = (264^\circ, +48^\circ)$ and we properly Doppler-boost all the measured redshifts to account for that. Thus, we finally expect to see an isotropic Universe. However, the fact that the entire

CMB dipole is considered a result of our local motion is an assumption that we accept since, in principle, at least a part of this anisotropy could have a primordial origin. As such, the CMB and the large-scale structure might not share the same rest frame. This would constitute a violation of isotropy since a preferred axis would exist in the Universe.

A form of observed *anisotropy* can occur, however, even in an intrinsically isotropic Universe if strong bulk flows exist around the observer and not taken into account. This is due to the following reason. The observed redshift of a source is a combination of two phenomena; its cosmological redshift $z_{\rm cosm}$ due to the expansion of space and the redshift $z_{\rm pec}$ due to its peculiar motion with respect to the observer, which is caused by the Doppler effect. Under a bulk flow, extragalactic objects within a sky region have a $z_{\rm pec}$ that is systematically altering the overall measured z towards higher or lower values. If not corrected for, this phenomenon will result in inferring wrong cosmological redshifts for celestial objects, thus wrong distances and cosmological parameters. However, the standard cosmological model and CP predict that no significant bulk flows should exist at scales of $\gtrsim 200$ Mpc, simply because of the homogeneous distribution of matter (*homogeneity*). Simply put, the average peculiar velocity of such volumes compared to the CMB rest frame should be negligible. These predictions arise from the structure formation model and its application to reconstruct the peculiar velocity field (Eq. 1.25). Therefore, any possibly detected strong bulk flows that extend at larger scales would be in direct conflict with ΛCDM.

The importance of looking for deviations from isotropy in cosmological data lies in the three possible outcomes. Firstly, the CP can be independently confirmed by different methods, which will provide more concrete evidence about the validity of our cosmological theories. Secondly, a study might observe anisotropies, inconsistent with other studies. This could eventually reveal previously unknown systematic biases, affecting numerous other studies of similar methodologies. In the era of precision cosmology, a full understanding of systematics is critical. Thirdly, a repeating verification of observed anisotropies from independent studies could eventually lead to a major paradigm shift in our cosmological theories and force us to rethink how much we understand the Universe after all.

The hypothesis of isotropy has been scrutinized in the past, but with contradicting results. An extended discussion on previous studies can be found in Sects. 3.1, 3.9.1, 4.1, and 4.9.2.

1.0.3 Galaxy clusters

Clusters of galaxies are powerful tools to study a variety of extragalactic astrophysical topics. Their application to study the CP is the focus of this dissertation. The literature contains innumerable sources from which one can obtain information about galaxy clusters. For the following sections, Sarazin (1986), Rosati et al. (2002), Schuecker (2005), S. W. Allen et al. (2011), Kravtsov et al. (2012), Giodini et al. (2013) and and Reiprich et al. (2013) and references therein have been advised.

1.0.3.1 Definition and components

Galaxy clusters are the largest gravitationally bound systems in the Universe. They form at the overdense regions of the cosmic web, such as the intersections of filaments, where the most massive dark matter halos are found. They accrete mass from their surroundings, forming aggregates of galaxies and gas. Baryons are then trapped under the self-gravity of the dark matter halo, making clusters closed systems. After the collapse of matter slows down significantly and any merging processes halt, galaxy clusters are usually considered to be in virial and hydrostatic equilibrium (to first approximation). They are detached from the Hubble expansion, and they are generally defined within their R_{200} radius. The typical mass

of galaxy clusters is $10^{13} - 10^{15}$ $M_\odot$[3] and their typical diameter is $1 - 5$ Mpc. Clusters with masses of $\lesssim 10^{14}$ $M_\odot$ are usually referred to as *galaxy groups*, although their initial distinction was based on their galaxy number.

Galaxy clusters are built from four main components:

- **Galaxies**: First defined as accumulations of galaxies, clusters contain from a few, up to ~ 1000 luminous galaxy members (many more dwarf galaxies can be embedded). Clusters of galaxies with $\lesssim 50$ galaxies are categorized as galaxy groups. Overall, galaxies account only for the $\sim 5\%$ of the total mass of a galaxy cluster. Galaxies are the optical and infrared components of clusters. In general, elliptical galaxies are more abundant within galaxy clusters than in the less dense cosmic field. More elliptical galaxies are created within these dense environments for two reasons. Firstly, due to the frequent collisions between galaxies, which eventually transforms them into ellipticals. Secondly, due to the stripping of their gas and dust due to ram pressure, as they travel within the intracluster medium, following the gravitational well of the halo. Galaxy members exhibit typical velocity dispersions of $\sim 300 - 1200$ km/s. Their number density increases towards the cluster center, where ellipticals dominate the population. Towards the cluster outskirts, the fraction of spiral galaxies increases since these members have been captured by the cluster more recently. The Brightest Cluster Galaxy (BCG) is a characteristic property of galaxy clusters. It is usually found close to the cluster center, but its exact position depends on the dynamical state of the cluster. The vast majority of BCGs are giant elliptical galaxies that have devoured other galaxies in the past, and their size roughly scales with the cluster mass.

- **Intracluster medium**: Most of the baryonic matter in galaxy clusters ($\gtrsim 80\%$) is in the form of hot plasma distributed smoothly across the intracluster medium (ICM). Due to the halo's deep potential well, the gas falls rapidly toward the cluster center and releases gravitational potential energy. It then undergoes adiabatic compression and shock heating, increasing the ICM temperature to typical values of $k_B T \approx 1 - 10$ keV (in X-ray astronomy, usually the Boltzmann constant k_B is omitted, and particle energies are referred to as temperatures T), or $10^7 - 10^8$ K equivalently. ICM is collisionally ionized, consisting of free electrons and ions which follow a Maxwell-Boltzmann distribution. Hydrogen is the most abundant element in clusters (and in the Universe); therefore, most of the ICM ions are simply free protons. Ionized helium also contributes to the ICM, while a small fraction of heavier elements, generally referred to as "metals," also exists. The chemical enrichment of the ICM takes place mainly through supernova explosions, which eject their material out of the host galaxy. The fraction of metals in the ICM varies from $Z \sim 0.2\%$ to $Z \sim 1.5\%$, with the cluster centers being more metal-rich than the outskirts. These metallicities are expressed in terms of the solar metallicity $Z_\odot$, and so $Z \sim 0.1 - 1$ $Z_\odot$. Moreover, the hot plasma is optically thin with particle densities of $n_{\rm gas} \sim 10^{-3} - 10^{-1}/{\rm cm}^3$, increasing towards the center. The ICM accounts for $\sim 10 - 15\%$ of the total cluster mass and is the main X-ray component of clusters.

- **Dark matter**: The bulk of a cluster's total mass is in the form of dark matter ($\sim 80 - 85\%$). Since it does not interact with light, it is only detectable indirectly via its gravitational effects, such as the deflection of light from background galaxies (strong and weak gravitational lensing), the velocity dispersion of galaxies, and the effect it has in the equilibrium state of the ICM. The dark matter density follows a decreasing gradient from the cluster center to the outskirts.

- **Relativistic particles**: a tiny fraction of a cluster's energy is usually encompassed within charged

[3] The quoted typical ranges of cluster properties refer to the majority of clusters. Of course there are some clusters lying outside of these ranges.

particles with relativistic velocities that travel along the magnetic field lines of the cluster (e.g., Willson, 1970). Due to their acceleration, they emit synchrotron radiation. It is believed that these particles are accelerated in ICM shocks and by Active Galactic Nuclei (AGN) jets.

Figure 1.10: Overlaid X-ray (diffuse emission) and optical (individual galaxies) image of the Coma cluster. Taken from `https://www.esa.int/`.

1.0.3.2 Applications

Being at the crossroads of astrophysics and cosmology, galaxy clusters are excellent cosmic laboratories. Their different components are observed nearly throughout the full electromagnetic spectrum. As a result, they provide valuable insights to a wide variety of extragalactic physics problems.

Arguably the most important applications of galaxy clusters is putting constraints on cosmological parameters. The abundance of halos per mass and per redshift is very sensitive to the cosmological parameters as discussed in Sect. 1.0.2.2. Clusters can also trace the total mass of the Universe through their mass-to-light ratio. They can also be used to estimate the universal baryon density, since their contents are representative of the overall baryons-dark matter fraction of the cosmos. In addition, the luminous part of clusters can be utilized to trace the total matter power spectrum. The nature of dark matter, as well as alternative theories of gravity, can be tested through phenomena such as the Bullet cluster merger (e.g., Robertson et al., 2017). Dark energy can also be probed through the cluster turnaround density (Pavlidou et al., 2020).

Distance measurements can be achieved with galaxy clusters as well and the cosmological parameters can be constrained as discussed in previous sections. For instance, their gas mass fraction within a given aperture depends on the angular diameter distance. The latter can be also estimated observationally by combining microwave and X-ray observations of clusters, making them standard rulers, while the luminous part of clusters can be utilized to trace the total matter power spectrum. Scaling relations of galaxy clusters (which will be discussed in detail later) also allow for the observational estimate of the luminosity and angular diameter distances. Last but definitely not least, they can be used to test the isotropy of the Universe and the existence of large bulk flows.

Besides assessing the values of cosmological parameters, galaxy clusters address other interesting astrophysical topics as well. The metal enrichment and evolution of the Universe can be traced, since clusters trap their gas, and act as cosmic reservoirs. The distribution of metals help us draw conclusions on their origin and how they are ejected from the systems they were initially created in. The evolution of galaxies within clusters can be compared to that of the field, and the environmental effects can be assessed. Analysis of emission processes of chemical elements that take place only under extreme conditions can be of great value for atomic physics, while the physical properties of AGN can be correlated with those of the host cluster. Finally, the origin of large-scale magnetic fields can be studied through their extended diffuse synchrotron emission.

Of course the possible applications of galaxy clusters are only limited by the imagination of researchers.

1.0.3.3 X-ray emission of galaxy clusters

Galaxy clusters are the brightest extended X-ray sources in the extragalactic sky, showing diffuse emission. Three main processes that produce X-ray photons take place within the ICM; thermal bremsstrahlung emission (free-free), deexcitation emission (bound-bound), and recombination emission (free-bound). The overall emissivity ϵ_ν is defined as the luminosity $L = \mathrm{d}E/\mathrm{d}t$ (emitted energy per time), per volume V and per photon frequency ν:

$$\epsilon_\nu \equiv \frac{\mathrm{d}L}{\mathrm{d}V\mathrm{d}\nu} \tag{1.28}$$

The contribution to the total ϵ from every emission mechanism is described below.

Bremsstrahlung radiation occurs when a free electron is accelerated by the Coulomb field of an ion. A photon is emitted by this interaction at the expense of the total system's energy. The electron remains free afterward. The energy and the number of the induced photons depend on the kinetic energy and the electrons' density, and thus Bremsstrahlung radiation produces a continuum spectrum. For clusters with electron temperatures of $k_B T_\mathrm{e} \gtrsim 2$ keV and typical metal abundances of $\lesssim 1\ \mathrm{Z}_\odot$, Bremsstrahlung is the primary radiation mechanism due to the high kinetic particle energies. The emissivity of this process ϵ_ν^ff is expressed as a function of photon energy $h\nu$ (where h is the Planck's constant):

$$\begin{aligned} \epsilon_\nu^\mathrm{ff} = A(\mathrm{e}, m_\mathrm{e}, k_B)\, g_\mathrm{ff}(Z_\mathrm{i}, T_\mathrm{e}, \nu)\, \frac{Z_\mathrm{i}^2\, n_\mathrm{e}\, n_i}{T^{1/2}}\, e^{-\frac{h\nu}{k_B T_\mathrm{e}}} \Rightarrow \\ \epsilon_\nu^\mathrm{ff} \propto n_\mathrm{e}^2 T_\mathrm{e}^{-1/2} e^{-\frac{h\nu}{k_B T_\mathrm{e}}}, \end{aligned} \tag{1.29}$$

where A is a constant that depends on the absolute electron charge e, electron mass m_e, and on the Boltzmann constant k_B. Also, $g_\mathrm{ff} \sim 1$ is the so-called Gaunt factor, accounts for quantum effects, and has only a weak dependancy on T_e and ν. Finally, Z_i is the charge of the ions, and $n_{\mathrm{e},i}$ are the number densities of the electrons and ions respectively. It is evident that fewer photons are emitted with high energies ($h\nu \gtrsim 2$ keV) than with lower ones, showing an exponential cutoff in their energy distribution (i.e., spectrum). The emissivity of the high energy-end of the spectrum also increases with increasing T_e. By integrating over all photon energies, one can find that the *total* bremsstrahlung emissivity ϵ^ff of a fully ionized plasma can be approximated as

$$\epsilon^\mathrm{ff} \propto T_\mathrm{e}^{1/2} n_\mathrm{e}^2. \tag{1.30}$$

Therefore, the density of the ICM gas plays a key role for the X-ray luminosity of a massive galaxy cluster, while the temperature is also important.

Deexcitation emission occurs when an electron is bound to an atom and transitions to a lower energy

quantum state. The energy difference between these two bound states is released as a photon. This process produces photons with specific energies, leading to line emission. These spectral lines can broaden in the observed spectrum due to the Doppler shift of the photon energy, which originates from the gas motions within the ICM. Only metals contribute to line emission since the level transitions of hydrogen, helium, and lithium electrons emit photons with lower energies. The bulk contribution in the ICM emission lines comes from the iron L and K shell line complexes ($\sim$ 1 keV and $\sim$ 6.7 keV, respectively). Other significant lines come from oxygen ($\sim$ 0.7 keV), magnesium ($\sim$ 1.4 keV), silicon ($\sim$ 1.9 keV), sulphur ($\sim$ 2.6 keV), and other metals. Line emission is the dominant process for clusters with $k_B T_e \lesssim 2$ keV.

Recombination emission is produced when an ion captures a free electron and the residual energy is emitted as a photon. Since the exact photon energy depends on the electron's kinetic energy, this process results in continuum radiation. Recombination emission becomes important only for cooler clusters with $k_B T_e \lesssim 1.5$ keV and for high energy photons of $h\nu \gtrsim 3$ keV (e.g., Kaastra et al., 2008; Böhringer et al., 2010).

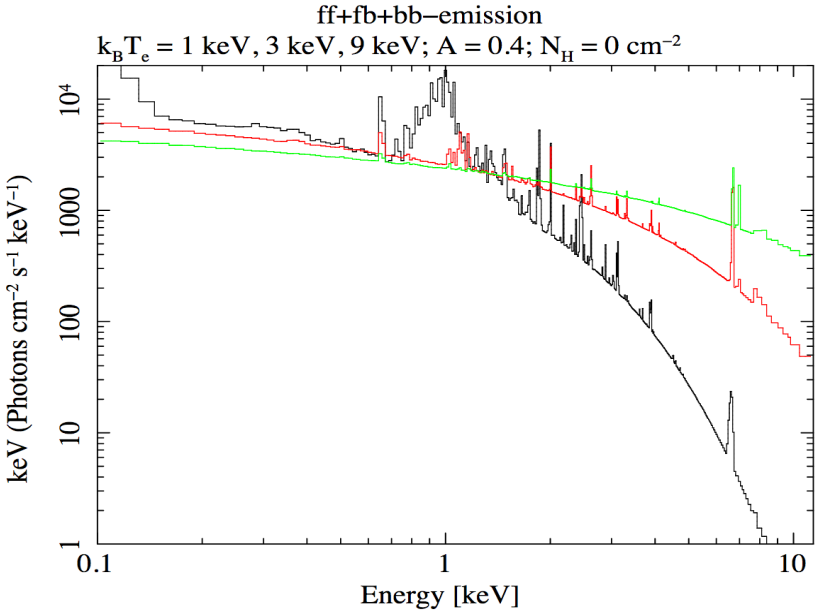

Figure 1.11: Galaxy cluster X-ray spectral models for three different electron temperatures; 1 keV (black), 3 keV (red), and 9 keV (green). All spectra have the same metallicity, density, and absorption. The spectra include bremsstrahlung, deexcitation, and recombination emission. Taken from Reiprich et al. (2013).

The total emissivity for ICM temperatures of $k_B T_e \lesssim 2$ keV, can be roughly approximated as

$$\epsilon \propto T_e^{-0.6} n_e^2. \tag{1.31}$$

The dependance of the emissivity on the electron temperature is opposite than for more massive clusters and the bremsstrahlung radiation (Eq. 1.30).

The final X-ray spectrum of a galaxy cluster is a combination of all these effects. Three X-ray model spectra are illustrated in Fig. 1.11. All three have the same metallicity (0.4 $Z_\odot$) and density, while they undergo no X-ray absorption. They show, however, three different ICM temperatures; 1 keV, 3 keV, and 9 keV. As expected, the most prominent characteristics of the spectra are clear. Hotter clusters show much higher emissivity at high photon energies and slightly fewer photons at low temperatures. Line

emission, while irrelevant for high electron temperatures, becomes important for low temperature clusters. Interestingly, the total emissivity within the 0.1-2.4 keV energy band and for clusters with $k_B T_e \gtrsim 2$ keV is rather insensitive to the temperature and depends mainly on the gas density:

$$\epsilon_{0.1-2.4\ \mathrm{keV}} \propto n_e^2. \tag{1.32}$$

The typical cluster X-ray luminosity within the 0.1-2.4 keV band is $L_X \sim 10^{42} - 10^{45}$ erg/s.

1.0.3.4 X-ray absorption

X-ray photons travel through the interstellar medium (ISM) of the Milky Way before they reach our telescopes. Heavy elements in the ISM can interact with these photons through photoelectric absorption. As a result, the observed X-ray spectrum is distorted compared to the emitted one. To avoid biased measurements of cluster properties, one has to account for this absorption. For that, the column density of metals along the line of sight of a cluster is needed, together with their absorption cross-section as a function of photon energy. However, it is not trivial to accurately quantify the metal abundance of every sky direction. Instead, the neutral hydrogen column density N_H is used as a proxy for the metal column density. N_H can be determined by 21-cm emission line radio observations, as done by the Leiden/Argentine/Bonn survey (LAB, Kalberla et al., 2005). By assuming the fraction of hydrogen and metals in the ISM to be that of the Sun, one can estimate the number of absorbing particles towards a line of sight. The solar metal abundance has been studied extensively in the past (e.g., Asplund et al., 2009). The photoelectric absorption cross-section as a function of the X-ray photon energy is displayed in Fig. 1.12. One sees that this cross-section is significantly larger for soft X-ray photons. The observed spectrum I_{obs} is then a function of the amount of hydrogen N_H, the cross-section $\sigma(E)$, and the emitted spectrum of the source I_{emit}:

$$I_{obs}(E) = e^{-\sigma(E) N_H} I_{emit}(E). \tag{1.33}$$

Moreover, it has been shown that the total hydrogen (neutral+molecular) column density N_{Htot} is a more accurate tracer of the true amount of absorbing material than neutral hydrogen alone. Although the amount of molecular hydrogen is difficult to be measured, several empirical methods have been employed to estimate N_{Htot}, such as the X-ray afterglow of gamma ray bursts and far-infrared all-sky maps (Willingale et al., 2013). In general, more molecular hydrogen is found in regions with more neutral hydrogen.

The main limitations of the methodology to trace the true X-ray absorption using the hydrogen as a proxy are fourfold. Firstly, radio surveys such as LAB have a limited spatial resolution, within which the true N_H can still slightly vary. Secondly, the solar chemical composition still encompasses some uncertainties that propagate in the X-ray absorption models. Thirdly, radio surveys detect hydrogen only within a certain velocity range of the gas and dust (e.g., $\sim \pm 400$ km/s). Absorbing material with velocities outside this range will not be detected, and accounted for. This is particularly important for the hydrogen outside of the Milky Way, but still in our cosmic neighbourhood, such us the Magellanic system (see an extended discussion of that in Sect. 3.6.3). Arguably the most important limitation, is the fact that the metallicity of the ISM is not spatially constant, as assumed to be. As a result, a fixed N_H does not always correspond to the same, true X-ray absorption. This can create biases that are discussed in detail in Sects. 3.6.3. Despite of these limitations, the absorption correction of X-ray data is crucial for the subsequent scientific conclusions. This can be seen from Fig. 1.13, where three X-ray model spectra are plotted for different (uncorrected) absorptions. Low energy photons ($E \lesssim 1$ keV) are severely absorbed, distorting the real spectrum of the source. At the same time, higher energy photons are not strongly affected by X-ray absorption.

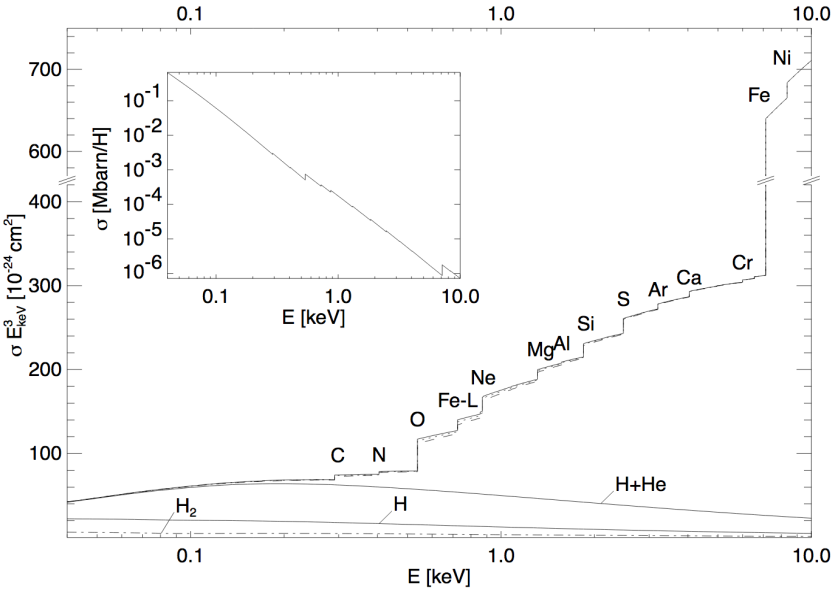

Figure 1.12: *Inner panel*: Photoelectric absorption cross section per hydrogen atom of the ISM (units: 1 Mbarn= 10^{-18} cm^2) as a function of the incoming X-ray photon energy. Solar metallicity of the ISM has been assumed. *Outer panel*: Same as the inner panel, after multiplying the cross-section with E^3 for display purposes, and showing the spectral positions of heavy elements. Taken from Wilms et al. (2000).

1.0.3.5 Sunyaev-Zeldovich effect

Space is filled with CMB photons with energies of ~ 0.2 meV. When these photons travel through the ICM of a cluster, a small fraction of them experience inverse-Compton scattering by the highly energetic, free electrons. Therefore, the photon energy is boosted, creating a unique distortion in the CMB spectrum toward the cluster sky position. This is the so-called Sunyaev-Zeldovich (SZ) effect, discovered by Sunyaev et al. (1970) and and Sunyaev et al. (1972), and is displayed in the left panel of Fig. 1.14. In the right panel of Fig. 1.14, one sees that the intensity of the CMB spectrum is amplified at $\gtrsim 217$ GHz frequencies by the SZ effect, and reduced at lower frequencies, as CMB photons shift to higher energies. In Fig. 1.15, the image of a galaxy cluster is displayed for different frequencies.

The exact intensity of the SZ effect is expressed by the Compton parameter y and depends on the state of the ICM, namely its gas density ρ and temperature T. With higher ρ, more photon "kicks" take place by electrons, while with higher T, these kicks transfer more energy to the CMB photons. This dependancy is given by Eq. 4.1 in Sect. 4.2.1, where more details on the technical aspect of this effect can be found. In brief, y increases with ICM density and clusters size, i.e., the mass of a cluster. It is also integrated over the entire solid angle of a cluster to give the *integrated* Compton parameter Y. For simplicity, one can think of this value as the microwave analog of a cluster's flux. Finally, Y is multiplied by D_A^2 in order to derive the intrinsic intensity of the SZ signal of a cluster $Y_{\rm SZ} = Y \times D_A^2$, known as the *total* integrated Compton parameter. This is eventually the value that scales with the other cluster properties, as I show in the second project of this dissertation, and in Sect. 1.0.3.6.

Finally, the SZ effect have two components. The *therma* component (tSZ), which is the one described until now, and the *kinetic* component (kSZ). The latter has a much lower amplitude than the tSZ effect, and usually its contribution can be ignored. kSZ is the result of the peculiar velocity of a cluster with respect to the CMB frame, which causes an average Doppler shift to the scattered photons. While the

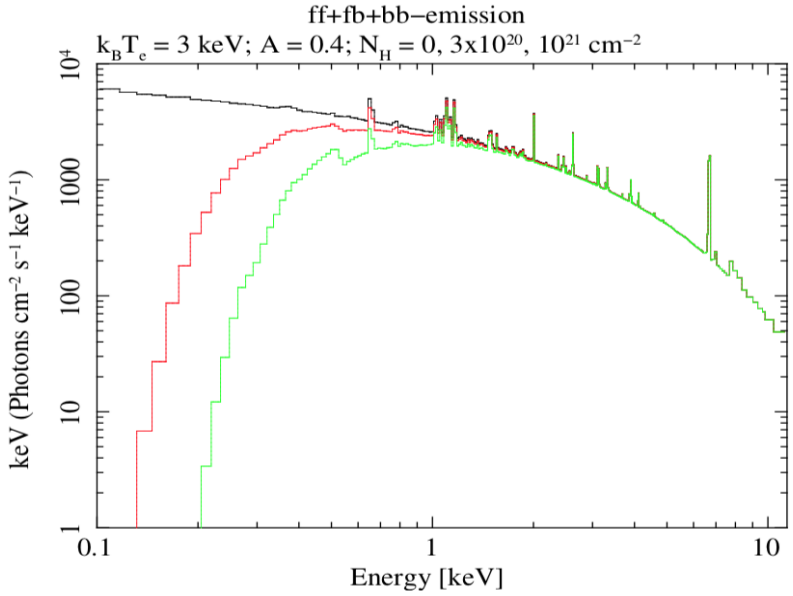

Figure 1.13: Galaxy cluster X-ray spectral models for three different hydrogen column densities (i.e., absorptions); no absorption (black), $3 \times 10^{20}/\mathrm{cm}^2$ (red), and $10^{21}/\mathrm{cm}^2$ (green). All spectra have the same metallicity, density, and temperature. The spectra include bremsstrahlung, deexcitation, and recombination emission. Taken from `https://astro.uni-bonn.de/~reiprich/`.

kSZ effect can be used to detect bulk flows, its weak signal requires the stacking of many clusters to detect the effect (see Sect. 4.9.2).

1.0.3.6 Scaling relations

One of the most fundamental aspects of galaxy clusters are their scaling relations (SCs). These express the correlation between several cluster properties as simple power laws. SCs are of paramount importance for cosmological studies and for understanding the physical processes taking place within clusters. For a review, see Giodini et al. (2013).

SCs were theoretically predicted by (Kaiser, 1986), under the so-called *self-similar model*, which adopted certain assumptions and simple mathematical formalisms. The main assumption is that the gravitational potential energy is the only energy transferred to the ICM during the collapse of a cluster. Furthermore, the density of the Universe changes as in Eq. 1.7, with $\rho \propto E(z)^2$. Since cosmic overdensities still need to reach a specific density contrast to collapse into clusters, halos that formed earlier in the Universe must be denser than collapsed halos today. This redshift evolution can be scaled appropriately with $E(z)$, and when one does so, then all clusters have the same mean (scaled) density. Considering all the simplifications of the self-similar model, one concludes that all clusters are scaled versions of each other, and have the same behavior despite their redshift or mass.

Based on that model, one can predict several SCs. For instance, one can relate the total cluster mass M_{500} within the R_{500} radius[4] with the gas temperature T. The mass is given by

$$M_{500} = \frac{4\pi}{3} 500 \, \rho_{\mathrm{crit},0} E(z)^2 R_{500}^3, \tag{1.34}$$

[4] As a reminder, this is the radius within which the mean density of the cluster is 500 times larger than the critical density of the Universe.

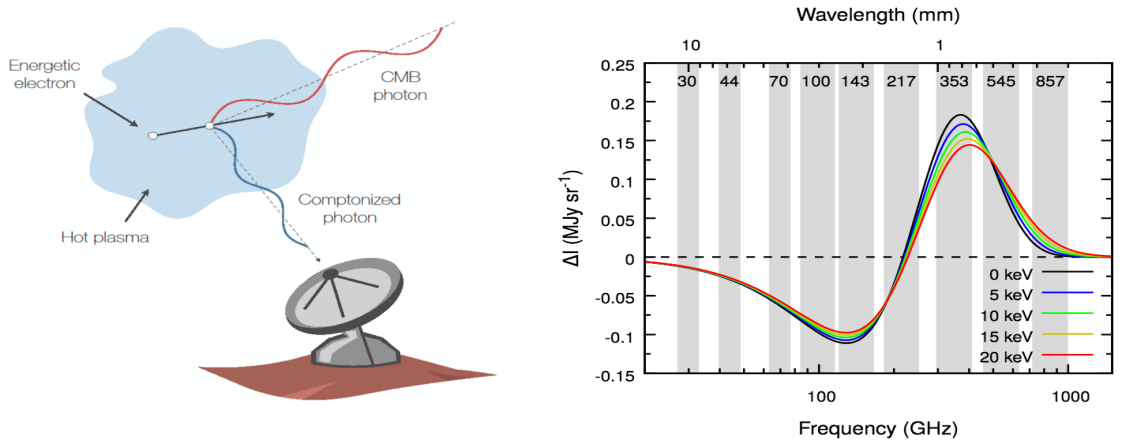

Figure 1.14: *Left panel*: Scattering of CMB photons from hot ICM electrons in the SZ effect (taken from `https://astro.uni-bonn.de/`. *Right panel*: Intensity difference of the CMB spectrum caused by the SZ effect, along the line of sight of a cluster. The spectral distortion is shown as a function of photon frequency, and for five different ICM temperatures. Taken from Erler et al. (2018).

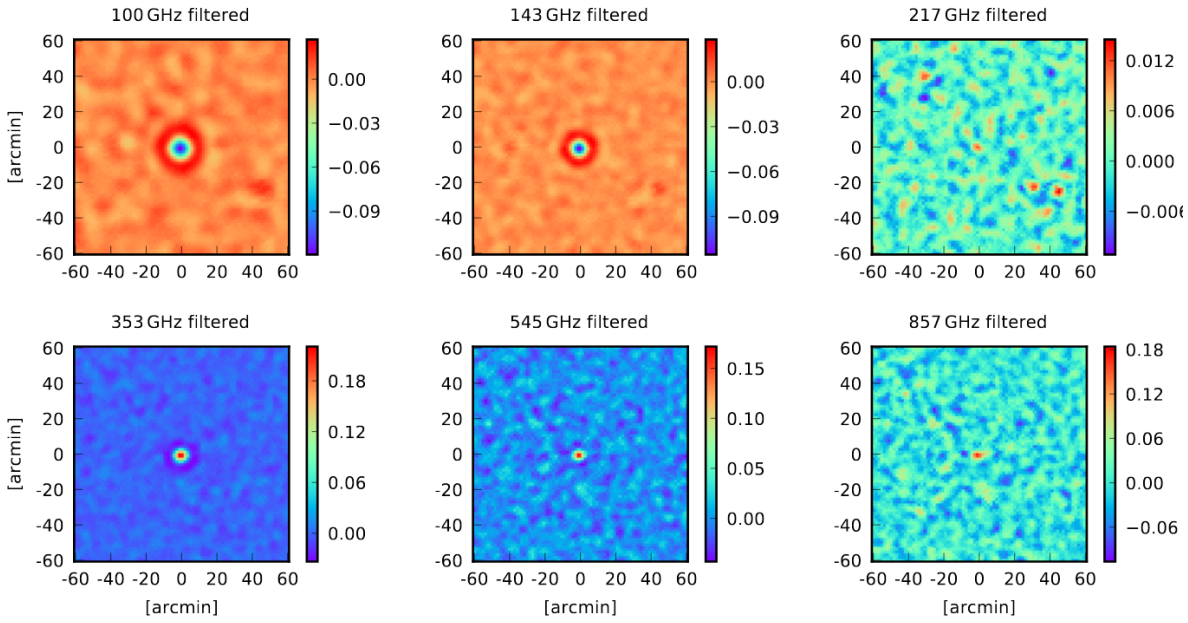

Figure 1.15: CMB maps towards the sky position of a galaxy cluster, at different frequencies. The temperature difference is shown color-coded (blue is cold). Taken from Erler et al. (2018).

where $\rho_{\mathrm{crit},0}E(z)^2$ is the critical density at the redshift z of the cluster. The choice of the density contrast radius (R_{500}) serves as an example, and this exercise can be repeated for any density contrast. Thus, from now on "500" will be omitted.

We can now assume that the ICM is in virial equilibrium and isothermal. Applying the virial theorem[5]

[5] $2K + U = 0$, where K is the thermal energy, or internal kinetic energy, of the gas, and U its gravitational potential energy.

to the cluster gas particles, we find that $T \propto \frac{M}{R}$. Plugging this into Eq. 1.34 it follows that

$$M \propto E(z)^{-1} T^{3/2}. \tag{1.35}$$

Hence, from the self-similar $M - T$ relation, one concludes that clusters with fixed mass are hotter in the past.

The X-ray luminosity-temperature $L - T$ relation can also be predicted according to the self-similar model. From Eq. 1.36, integrating over all frequencies, one can express the X-ray luminosity as a function of emissivity and volume V, i.e., radius: $L \propto \epsilon\, V \propto \epsilon\, R^3$. Plugging in Eq. 1.30, it follows that

$$L \propto n_{\rm e}^2\, T^{1/2}\, R^3 \propto \rho_{\rm gas}^2\, T^{1/2}\, R^3 \propto \frac{M_{\rm gas}^2}{R^6}\, T^{1/2}\, R^3, \tag{1.36}$$

where we used the proportionality between the number density of electrons and total gas density ($n_{\rm e} \propto \rho_{\rm gas}$) and the fact that $\rho_{\rm gas} \propto \frac{M_{\rm gas}}{R^3}$, where $M_{\rm gas}$ is the gas mass. Furthermore, $f_{\rm gas} \equiv \frac{M_{\rm gas}}{M}$ is the gas fraction. Plugging this, Eq. 1.34, and Eq. 1.35 into Eq. 1.36 one derives that

$$L \propto E(z)\, T^2, \tag{1.37}$$

where $f_{\rm gas}$ is ignored since it is constant in the self-similar model. Thus, the self-similar $L - T$ relation predicts that clusters with fixed temperatures were more luminous in the past (because they were denser). Note here that if one initially used the X-ray luminosity $L_{\rm X}$ within 0.1-2.4 keV, one would need to use Eq. 1.32 instead of Eq. 1.30. This would result in a less steep self-similar slope, $L_{\rm X} \propto E(z)\, T^{3/2}$.

The total integrated Compton parameter $Y_{\rm SZ}$ is another interesting quantity with important SCs for this work. It is easier to investigate the correlations of $Y_{\rm SZ}$ via its X-ray analog, $Y_{\rm X} = M_{\rm gas}\, T$. Therefore, $Y_{\rm X} \propto M\, T \propto E(z)^{-1} T^{3/2} T$. Since $Y_{\rm X} \propto Y_{\rm SZ}$, this rewrites as

$$Y_{\rm SZ} \propto E(z)^{-1}\, T^{5/2}. \tag{1.38}$$

Finally, one finds easily that

$$L_{\rm X} \propto E(z)^{8/5} Y_{\rm SZ}^{3/5}. \tag{1.39}$$

The SCs between many different properties can be predicted in a similar manner. Others however are not trivial to be formulated. For example, the optical and infrared luminosity of a cluster's BCG scales with the mass, X-ray luminosity, and temperature of that cluster. However, the exact nature of the BCG is not predicted by the self-similar model, and thus one does not know what to expect for the BCG scaling relations. Moreover, the X-ray half-light radius $R_{50\%}$ of a cluster (radius within half of the total flux is emitted) should scale with the other properties, but not in the same fashion as the absolute cluster radius, since it depends on several factors. Although possible, it can prove quite challenging to predict the scaling laws that govern the relation of $R_{50\%}$ with the other cluster properties. Finally, the observed scaling relations many times deviate from the self-similar expectations, due to the additional physical processes taking place within the ICM, such as AGN feedback and supernovae-driven winds. Discussions about previous observational studies on these SCs can be found in Sect. 4.4.

1.0.4 Morphology

One of the most frequent categorization of galaxy clusters is based on their dynamical state. Is a cluster *relaxed*[6] or *disturbed*? There is not one unique definition of relaxed and disturbed clusters. In principle, relaxed clusters have a nearly spherical and symmetric structure. They only show limited (if any) subclustering across their volume and they are in virial equilibrium. They have not undergone any merger activity in their recent past and they appear to have smooth density and surface brightness profiles, both increasing toward the cluster core. Due to their lack of interaction with other objects, the BCG is usually found in the bottom of the gravitational well, in the cluster center. This position usually coincides with the peak of the X-ray emission. Generally, relaxed clusters are a better representation of the idealized self-similar model. On the other hand, disturbed clusters usually show a more asymmetric, complex morphology. They are characterized by more and lumpier substructures which are probably the result of recent interactions with other galaxy clusters. Furthermore, their surface brightness profile is usually less peaked towards the core, i.e., a lower fraction of their total X-ray emission comes from the center of the cluster than for relaxed clusters.

Arguably the most common division of galaxy clusters is based on the state of their core region. *Cool-core* (CC) clusters are characterized by a very dense center and a strong central peak in their surface brightness profile. Their name originates from the fact that their temperature is lower towards their core than in its surroundings. Due to their high, central ICM density, CC show an enhanced emissivity in their cores, which makes them more luminous in X-rays than other types of clusters. *Noncool-core* (NCC) clusters on the other hand do not show a drop in their central temperature or such a strong central peak in their surface brightness profile. They also exhibit less dense cores than CC clusters. In Fig. 1.16, the X-ray images of relaxed, disturbed, CC and NCC clusters are displayed.

CC and NCC clusters can be divided based on several properties. For instance, the concentration parameter is widely used, which describes the fraction of X-ray emitting light of the very core, compared to the entire cluster (or a fixed fraction of the cluster). With a higher the concentration parameter, a cluster emits more X-ray photons from its center, which increases the probability that it is a CC cluster. One of the most efficient parameters to distinguish between CC and NCC clusters though is the cooling time $t_{\rm cool}$, which is the timescale on which the ICM cools down. $t_{\rm cool}$ is defined as the ratio of the internal energy density $u \propto n_{\rm e} T_{\rm e}$ and emissivity ϵ. For ICM temperatures of $T_{\rm e} \gtrsim 2$ keV, bremsstrahlung is the dominate emission process and $\epsilon \approx \epsilon^{\rm ff}$. In that case, the cooling time is a function of the electron density and temperature:

$$t_{\rm cool} \approx 91.5 \times \frac{10^{-3}\ {\rm cm}^{-3}}{n_{\rm e}} \left(\frac{T_{\rm e}}{10\ {\rm keV}} \right)^{1/2}\ {\rm Gyr}. \tag{1.40}$$

The ICM beyond the core of a cluster, almost always has $t_{\rm cool}$ larger than the age of the cluster, and hence the gas is not cooled down. Within the core however, due to the high $n_{\rm e}$, it is possible that there is enough time for the gas to cool. Strong CC clusters are usually defined as the ones with $t_{\rm cool} \leq 1$ Gyr, and NCC $t_{\rm cool} \geq 10$ Gyr, with the intermediate clusters labelled as weak CC clusters (D. S. Hudson et al., 2010). As CC clusters emit large amounts of energies, the kinetic energy of the particles decreases, resulting in a lower temperature in their centers. There are some mechanisms however that reheat the ICM around the core, such as AGN feedback (e.g., McNamara et al., 2007).

Finally, there is a strong correlation between the CC/NCC and relaxed/disturbed cluster divisions. More specifically, CC are more closely related to relaxed clusters, while NCC clusters are usually disturbed clusters (see Sect. 4.7.1).

[6] Some times relaxed clusters are referred to as *regular*.

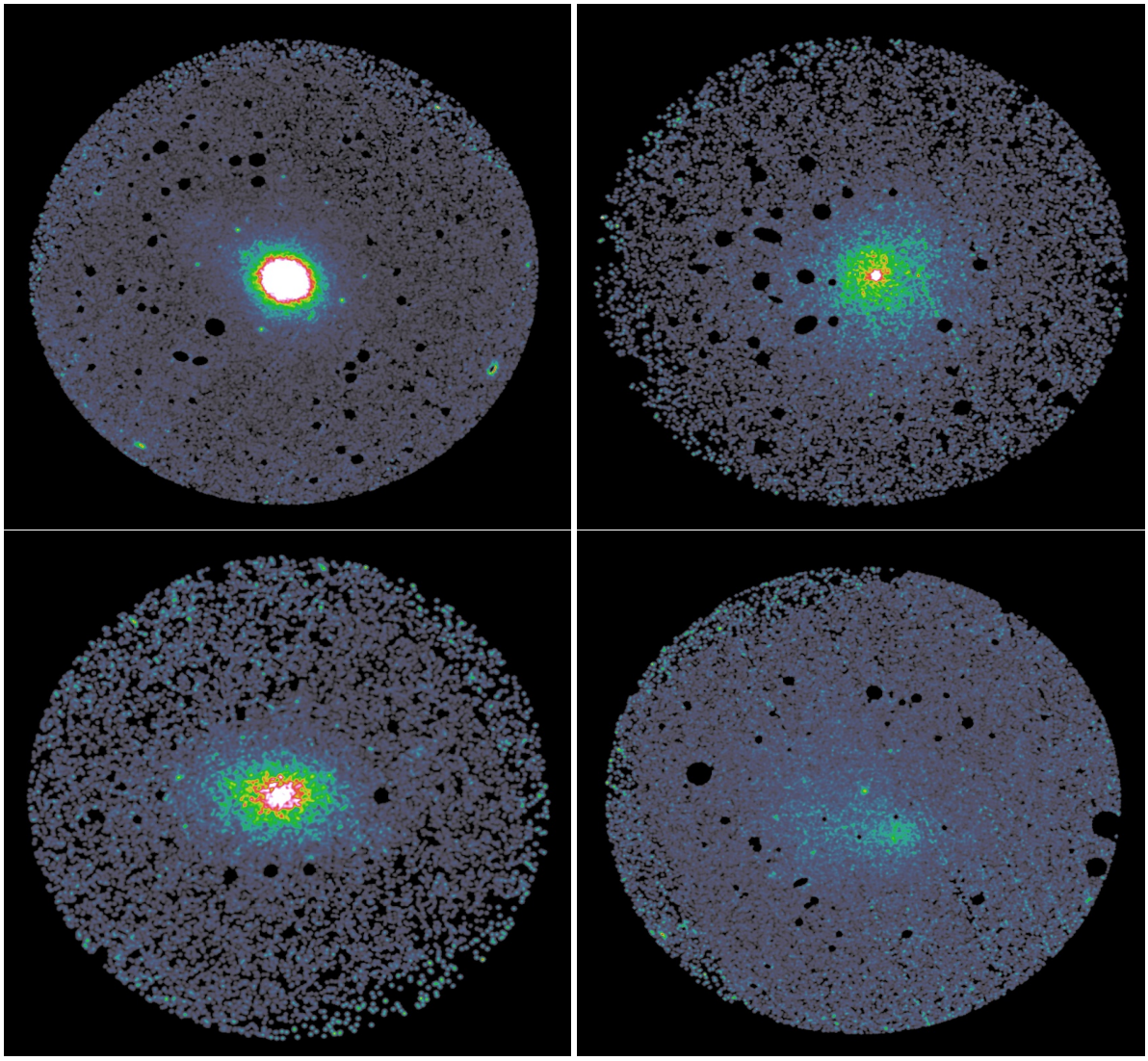

Figure 1.16: X-ray images in the 0.5-2 keV band from a relaxed, CC cluster (S1063, top left), a relaxed, but NCC cluster (A3301, top right), a slightly disturbed, NCC cluster (A0761, bottom left), and a highly disturbed, NCC cluster (A3570, bottom right). The clusters were observed by the XMM-Newton telescope. The count-rate (equivalent to X-ray flux) is shown color-coded, with the same range in all images.

1.0.5 Telescopes

Telescopes act as our eyes to the Universe. They are being used to observe various astrophysical objects in different wavelengths and obtain valuable data that help us constrain cosmological parameters. Here I give a brief summary of the telescopes that have been employed to obtain the data I use in this dissertation.

1.0.5.1 ROSAT

The RÖentgen SATellite (ROSAT) was an X-ray observatory developed by Germany, the United States, and the United Kingdom (Briel et al., 1996). It was launched in 1990 and put into a low Earth orbit, from where it operated until 1999. Two telescopes were placed on board of ROSAT; one designed for

the soft X-ray band (0.1-2.4 keV) and one for the extreme ultraviolet band (0.06-0.2 keV). The X-ray telescope consisted of two Position Sensitive Proportional Counters (PSPC) detectors and one High Resolution Imager detector. The data I use come solely from the PSPC detectors, and thus, hereafter, the reference to these detectors will be implied when "ROSAT" is referred. The spatial resolution of an X-ray telescope depends on several things, such as photon energy, off-axis angle of a source, etc., but in average, the spatial resolution[7] of ROSAT was $\lesssim 1$ arcmin at 1 keV. For the same photon energies, its spectral resolution was ~ 400 eV. Moreover, the field of view (FOV) had a $\approx 2^{\circ}$ diameter with a maximum on-axis effective area of ~ 250 cm^2 at 1 keV. Within half a year from its launch, ROSAT completed the first all-sky survey in the soft X-ray band, detecting $\sim 150,000$ X-ray sources. This allowed for the construction of multiple catalogs of galaxy clusters and point sources, which led to significant advancements in X-ray astrophysics. The primary cluster sample used in this dissertation was created based on this survey. Moreover, ROSAT performed pointed observations of X-ray sources as well.

1.0.5.2 XMM-Newton

The X-ray Multi-Mirror Mission (XMM-Newton) is the largest X-ray observatory developed and being operated by European Space Agency (ESA Jansen et al., 2001). It was launched in 1999 and placed at a highly elliptical orbit, moving between a medium and a high Earth orbit. XMM-Newton is equipped with three telescopes, each one nesting 58 mirror shells. It carries three European Photon Imaging Cameras (EPIC), which are at the prime focal point of each telescope. Two of them are Metal Oxide Semi-conductor (MOS1 and MOS2) CCD arrays. The third one is a p-n (PN) junction CCD array based on a newly developed CCD technology with a higher quantum efficiency. The EPIC system provides a large effective area of 2150 cm^2, which is one of the main strengths of XMM-Newton compared to other X-ray observatories. Its FOV is $30'$ while it covers a broad energy range of $0.2 - 12$ keV. Its spatial and spectral resolution are $\sim 14'$ and ~ 50 eV respectively, both at 1 keV. XMM-Newton has performed both full scans of parts of the sky and a plethora of pointed observations with a very high sensitivity. Furthermore, XMM-Newton offered for the first time the opportunity to simultaneously observe a source in X-rays and in optical and ultraviolet wavelengths due to its Optical Monitor (OM), which carries on board. Finally, it also carries two Reflection Grating Spectrometers (RGS), which can provide high-quality spectral information in the $0.4 - 2.5$ keV band, with a spectral resolution of < 5 eV at 1 keV energies.

1.0.5.3 Chandra

The Chandra X-ray telescope (named after Subrahmanyan Chandrasekhar) was designed and launched by NASA in 1999 (Weisskopf et al., 2000), under which still operates. It was placed at an elliptical, high Earth orbit and had two main operative instruments; the Advanced CCD Imaging Spectrometer (ACIS) and the High Resolution Camera (HRC). These two nest inside them a High and a Low Energy Transmission Grating (HETG and LETG), respectively. ACIS, which is the main instrument used to obtain the data used in this work, consists of 10 CCD chips with an operating energy range of 0.2-10 keV and a spectral resolution of ~ 100 eV (at 1 keV). It also has a total (not circular) FOV of 640 arcmin^2. ACIS maximum effective area reaches ~ 600 cm^2 at 1.5 keV. On the other hand, HRC consists of 2 microchannel plate detectors and can observe within the 0.1-10 keV band, with a total FOV of ~ 1400 arcmin^2 with an effective area of ~ 230 cm^2 at 1 keV. Chandra constituted a breakthrough for X-ray astronomy mostly due to its very low (yet unmatched) spatial resolution of $\approx 0.5''$. It conducted surveys

[7] The quoted spatial resolution for all X-ray instruments is the half-energy width (HEW).

on parts of the sky, while its focal point is pointed observations. All the above allowed Chandra to detect and identify X-ray point sources, such as AGNs, very efficiently. This remains its main advantage against other X-ray telescopes up to this day, while, of course, extended X-ray sources such as galaxy clusters are also studied by Chandra with high precision.

1.0.5.4 ASCA

The Advanced Satellite for Cosmology and Astrophysics (ASCA) was designed by Japan, with scientific payload contributions from the United States as well (Tanaka et al., 1994). ASCA was launched in 1993 and was placed at a nearly circular, low Earth orbit, from which it degraded with time. The satellite operated successfully until 2000. The main breakthrough of ASCA was the use of CCD detectors for the first time as the focal plane detectors in X-ray astronomy. These detectors were the Gas Imaging Spectrometer (GIS) and the Solid-State Imaging Spectrometer (SIS). ASCA consisted in total of four identical X-ray telescopes, each one equipped with an imaging spectrometer. ASCA provided an effective area of 350 cm^2, a FOV of $50'$ diameter (GIS), and a spectral resolution of $\sim$ 100 eV (SIS), all at 1 keV, while it had a rather poor spatial resolution of $3'$. Its covered energy range was 0.4-10 keV. ASCA's main objective during its seven and a half years of operation was conducting pointed observations.

Figure 1.17: Artists' impressions of the five telescopes: ROSAT (top left), XMM-Newton (top center), Chandra (top right), ASCA (bottom left), and Planck (bottom right). Credit for all the images: `https://www.nasa.gov/`).

1.0.5.5 Planck

The Planck space telescope was deployed by ESA to probe the CMB anisotropies with unprecedented accuracy (Tauber et al., 2010). It was launched in 2009 and placed at the second Lagrangian point

of the Sun-Earth system (L2), from where it operated until 2013, before the mission came to an end. Planck carried two instruments, the Low Frequency Instrument (LFI) and the High Frequency Instrument (HFI), covering a total of nine different frequencies within the 30-857 GHz range. The detectors of the instruments were kept at temperatures close to zero by an advanced cryogenic system. The spatial resolution of Planck decreased with frequency, going from $32'$ down to $5'$. Its primary objective was to perform an all-sky survey at the nine frequencies. It did so with unprecedented accuracy, completing five full scans with HFI and eight and a half scans with LFI. Planck's survey allowed cosmologists to study the very early stages of the Universe and further uncover the strengths and the weaknesses of the standard cosmological model.

CHAPTER 2

X-ray data reduction and spectral analysis

In this Chapter, I present the work I have conducted to reduce 100 XMM-Newton observations and extract the spectral information (temperature, metallicity, and redshift) for 91 galaxy clusters. These measurements are used in the next Chapters of this dissertation.

2.1 EPIC X-ray background

To obtain reliable cluster measurements from X-ray observations, one needs to properly treat the different background components that contaminate an XMM-Newton EPIC observation. As discussed below, some of the components are reflected and focused by the telescope's mirrors, while others penetrate the shielding and hit the detectors directly. The EPIC background can be separated into the particle background, the electronic noise, and the cosmic X-ray photon background (e.g., A. M. Read et al., 2003; Carter et al., 2007, and references therein).

Particle background

The particle background can be subdivided into soft-proton background and cosmic-ray-induced background. Soft protons originate from the Sun and are accelerated by magnetospheric reconnection events up to several hundred keV energies. They are trapped by the magnetosphere of our planet and are then captured by the grazing mirrors of XMM-Newton. They are highly variable (showing fluctuations up to 1000%) and unpredictable, contaminating up to 40% of the XMM-Newton's observation time. Generally, the frequency of these flares is crudely proportional to the distance of the Earth from the Sun. The intrinsic spectrum of the solar flares is a continuum, resembling a power law. However, when soft protons hit the detectors, they can cause fluorescence lines due to the interaction with the telescope's material. These particles need a narrow incidence angle to hit the detector by going through the entire telescope system. Thus, they occur mostly inside the FOV, similarly to X-ray photons, but with a flatter vignetting. Naturally, their intensity is much lower in the unexposed corners of the cameras (Kuntz et al., 2008). Soft protons are the primary contaminant in times of high background levels.

Moreover, internal cosmic ray induced events are produced from high-energy particles interacting with the detector and causing instrumental fluorescence lines. Also, these high energy particles might directly produce charge in the CCDs. They are less variable than soft protons, $\sim \pm 10\%$ during an observation. They cause a relatively flat continuum spectrum, unchanged at > 2 keV, with small fluctuations in the fluorescence lines. For instance, the Al-K line at 1.4865 keV appears in both MOS and PN, while the

Si-K at 1.7397 appears in MOS. The internal instrumental background caused by cosmic rays is not vignetted and has a strong presence in the unexposed corners.

Electronic noise

The electronic noise originates from bright pixels at low energies (< 0.3 keV), readout noise, and artificial low energy enhancements in the outer CCDs of the MOS detectors. The bright pixel component is relatively constant throughout an observation, while it can greatly vary between different observations. The artificial low energy enhancements are usually observed at < 0.5 keV and affect ∼ 20% of the observations. The cause of this enhancement remains ambiguous.

Cosmic X-ray photon background

This component has an astronomical origin, and it is independent of the used telescope. It can be subdivided into the soft X-ray and the hard X-ray background photons. Soft X-ray background photons mostly originate from the Local Hot Bubble and the Galactic disk and halo. The Local Hot Bubble (LHB) is considered to be a hot relic in our Galactic neighborhood dating to the last nearby supernova. LHB provides an explanation for the prevalent presence of the soft X-ray diffuse emission in our Galactic neighborhood, which peaks at ∼ 0.6 keV and becomes negligible at $\gtrsim$ 1 keV (e.g., Mernier et al., 2015). Moreover, the Galaxy's hot plasma shows a thermal diffuse X-ray emission that peaks at $E \sim 0.8$ keV and can be practically ignored after $\gtrsim$ 1.5 keV. Some emission lines are also seen in low energies. Both of these components are vignetted and constant with time. However, they can spatially vary up to ±35% for different sky coordinates. Some components with a minor contribution to the cosmic X-ray background might exist, such as the Solar Wind Charge Exchange, but due to their low energy produced photons and the weak emission are irrelevant to this analysis (e.g., Snowden et al., 2004). Finally, the hard cosmic X-ray background photons mainly originate from unresolved AGNs within the FOV. It is the dominant cosmic X-ray photon background component at $E \gtrsim 1$ keV (De Luca et al., 2004). It is vignetted and rather constant spatially.

2.2 XMM-Newton data reduction

To reduce the 100 XMM-Newton observations, I implemented an X-ray cluster reduction pipeline developed by Dr. Florian Pacaud, which was adjusted according to this work's needs. For clusters with multiple observations, the one with the longest exposure time was considered first. If the quality of he observation did not allow for a temperature measurements (according to the criteria presented below), then the observation with the second longest exposure time was considered, and so on. Throughout the data reduction, the XMMSAS v16.0.0 and HEASOFT v6.20 softwares were used.

Flare filtering

The XMM-Newton cluster observations data files (ODFs) were retrieved from the XMM-Newton archive[1]. Using the emchain and epchain task from XMMSAS, I generated calibrated event lists from the ODFs for the MOS and PN cameras, respectively. These event lists need to be cleaned from the time-varying, soft-proton solar flares which contaminate the observations. Therefore, the light curves (photon counts as a function of time intervals) of the three cameras are created within the 0.3-10 keV energy band. For

[1] http://nxsa.esac.esa.int/nxsa-web/#home

MOS1 and MOS2, the detected good events are binned per 52 s, and per 26 s for PN. The histogram of the counts per time bin is produced, and a Poisson function is fitted to it. All the events outside the 3σ range from the peak of the distribution are excluded. The remaining events are the good time intervals (GTIs), which are considered to be nearly free from any soft-proton contamination, although, in practice, a significant component of flares can survive the filtering. Depending on the observation, this process can reject almost all the observing time as contaminated, or none at all. Moreover, disagreements in the soft-proton contamination might appear between the MOS and the PN cameras due to their different sensitivities. In Fig. 2.1, the light curves of three clusters are displayed for MOS1 and PN. One sees that for the cluster A0500, $\sim$ 100% of the exposure time is characterized as GTI. For A3122, $\sim$ 70% of the total time is GTI, and thus this cluster can also be efficiently used. On the other hand, the MS1111.8 observation is completely contaminated by solar flares and, hence, useless.

After this flare filtering process, some leftover soft-proton contamination might still be present. To assess if the flared time intervals are successfully discarded, the so-called IN/OUT ratio is determined (De Luca et al., 2004). This is the ratio of the events that occurred within the FOV (IN) over the ones that occurred in the unexposed parts of the detectors (OUT), i.e., the corners. The IN/OUT ratio is estimated two times, one before the flare filtering and one after, only for the GTIs ($\mathrm{IN/OUT_{GTI}}$). For the IN events, the 10 arcmin around the center are excluded, and only the photons with $\geq$ 6 keV are considered for MOS, and $\geq$ 5 keV for PN. This ensures that any contribution from the observed source, the Galaxy, or from unresolved AGNs is eliminated due to the low effective area of the detectors so far away from their center and for such high photon energies. Consequently, the observed counts can only be induced by soft protons and cosmic rays. On the other hand, the OUT counts are obtained when the filter wheel of the detectors is closed. Soft protons and X-ray photons cannot penetrate it and can only hit the corners of the detectors. They do not reach the telescope's focal plane in that case. Therefore, the collected counts are produced only by cosmic rays. As a result, an IN/OUT ratio significantly higher than unity (> 1.3, De Luca et al. 2004) indicates that soft protons strongly contaminate the event lists. This is many times the case before the flare filtering. For example, the IN/OUT ratio for A3122 before filtering is 2.9 and 2.1 for MOS1 and PN, respectively. For the filtered GTIs, the IN/OUT ratio should be ≤ 1.15 to consider an event list cleaned from solar flares.

Based on that process, one can characterize each XMM-Newton observation and evaluate if it can be further used. Certain conditions are established in order for a detector's GTI to be used as a *good* observation. These are:

- No significant residual soft-proton contamination should exist, i.e., $\mathrm{IN/OUT_{GTI}} \leq 1.15$.
- The only exception is if $1.15 < \mathrm{IN/OUT_{GTI}} \leq 1.2$ for a detector (e.g., PN), but $\mathrm{IN/OUT_{GTI}} \leq 1.15$ for the other two detectors (e.g., MOS1 and MOS2).
- The GTI should be at least $\geq$ 30% of the total exposure time.
- The GTI should be at least $\geq$ 4 ks.

If at least one of these conditions is not met, then the specific detector is discarded from the following analysis. If no detector meets these thresholds, then the entire observation is discarded. Finally, many times the longest cluster observation had a usable GTI for one or two detectors, but more than one pointed observation existed for that cluster. In that case, I repeated the flare filtering for the next longest observation as well and decided which one provided the best data.

I repeated this process for 45 XMM-Newton observations in total. 55 additional observations by Dr. Florian Pacaud and Dr. Miriam Ramos-Ceja.

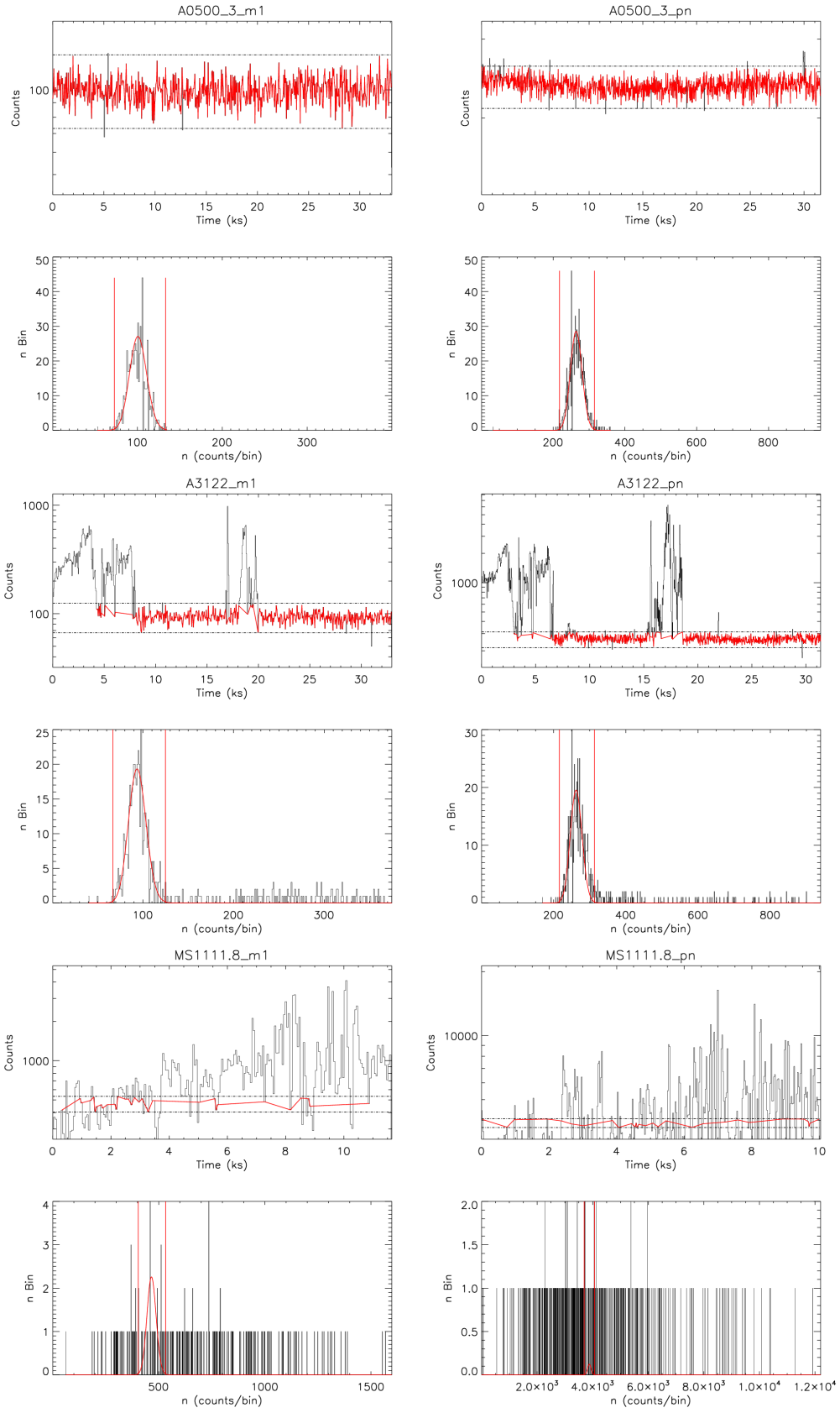

Figure 2.1: Detected counts per time bins for A0500 (top), A3122 (middle), and MS1111.8 (bottom). In the bottom part of each plot the respective histogram of the counts per bin is shown.

Anomalous state and out-of-time events

Next, I perform some diagnostics to identify noisy CCD behavior that might interfere with the following analysis. A pattern of such problems, the so-called *anomalous state*, has been found in the past for the MOS detectors (and not the PN), and appropriate test were developed (Kuntz et al., 2008). Anomalous state results in an increased background level at energies below 1 keV. To identify the problematic detector chips, I implement the Kuntz & Snowden test. The hardness ratio of the count-rate (2.5-5.0 keV)/(0.4-0.8 keV) is plotted against the 0.3-10.0 keV count-rate. Low values for this ratio (abnormally increased signal in the 0.4-0.8 keV band) indicate the presence of the anomalous state, and the chips that suffer from this are excluded from the rest of the processing. Fig. 2.2 displays the anomalous state of CCD 5 of the MOS2 detector for the A1631 cluster (left) and the lack of any such problems in the MOS1 camera for the A1918 cluster. After excluding the events coming from the problematic CCDs, new, clean event lists are generated.

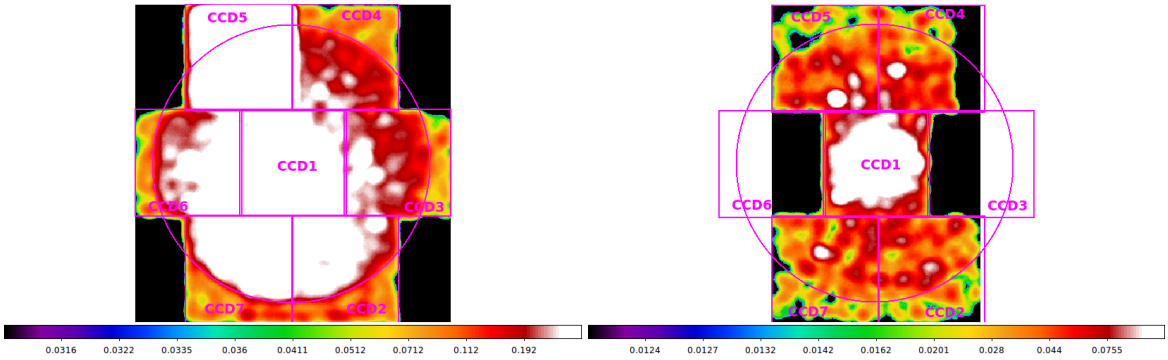

Figure 2.2: Anomalous state affecting the 5th CCD of the MOS2 camera of the A1631 observation (left), while the A1918 observation does not show any anomalous behavior for MOS1 (right).

Another instrumental artifact is the out-of-time events (OOT) coming from the PN detector, the CCDs of which show a fast readout time. As a result, besides the actual integration interval, photons are also registered during the readout of the CCDs. Obtaining the list of these events, they are then added to the instrumental background and eventually subtracted from the clean event lists.

Masking of point sources and substructures

When extracting and modeling the clusters' spectra, one needs to consider only the photons emitted from the cluster and not from other sources. In every XMM-Newton frame, however, tens of point sources lie within the FOV, in their vast majority being AGNs. These need to be masked, and their photons need to be discarded from the later-derived spectra. To do so, the images of the three EPIC detectors are coadded and corrected for the spatially varying exposure time across the FOV. The biggest effect of the time exposure correction is that it removes the apparent gaps in the coadded images caused by the physical gaps between the different chips. Afterward, a two-step procedure follows. Firstly, the coadded image in the 0.5-2 keV band is used by the pipeline to identify and mask point sources, as described in Pacaud et al. (2006). In a nutshell, a wavelet-based source-detection algorithm is employed, which removes the noise, and the sources become clearly distinct. The source catalog from the filtered image is then extracted using the SEXTRACTOR software (Bertin et al., 1996). The detected sources are masked, and the photons from their sky positions are discarded.

Not all point sources are detected by this procedure, however. To ensure that the point source contamination is entirely eliminated, I visually inspected the coadded image in the soft 0.5-2 keV band

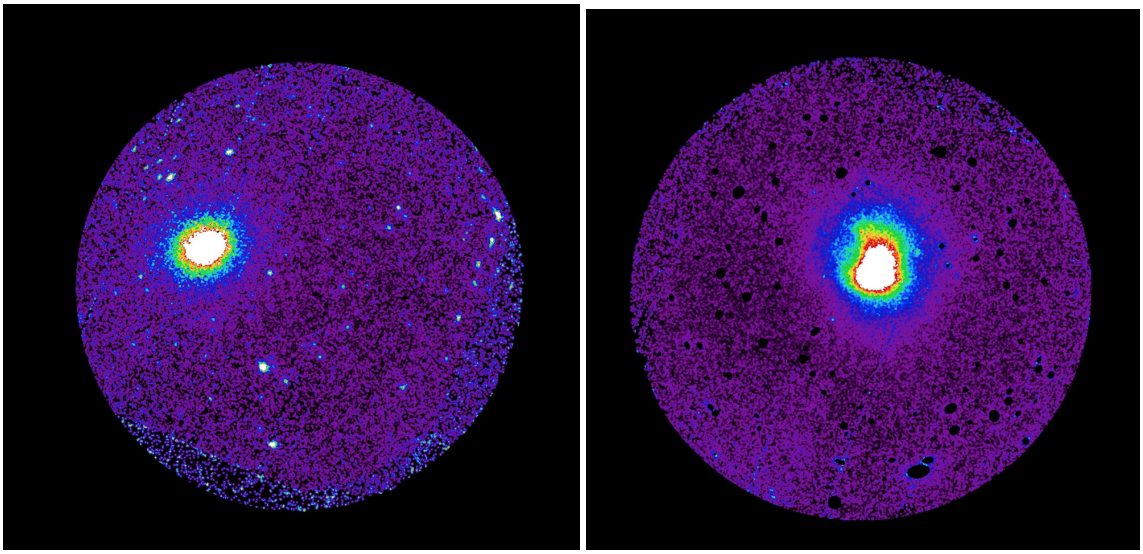

Figure 2.3: Cleaned, exposure time-corrected X-ray images in the 0.5-2 keV band of RBS1842 before masking (left) and of A2443 after masking (right).

the hard 2-10 keV band. AGNs are more luminous in the hard band while the cluster's brightness dims, and thus the hard band offers a better insight into the point source population within the FOV. I manually masked all the remaining AGNs, stars, and extended substructures that might interfere with the cluster's spectral analysis later on for all 100 XMM-Newton observations. The images of two clusters, RBS1842 and A2443, are displayed in Fig. 2.3, before and after the masking.

Instrumental background correction

The instrumental background must be subtracted from the clean images before one extracts the spectrum. For that, I utilize the filter wheel closed (FWC) observations, which are dominated by the instrumental background. The FWC observations have a different exposure time from CCD to CCD and from the main observation. They also show a different particle background level. For that, FWC observations were renormalized to match the background level of the cluster exposure. This is done independently for every CCD of the EPIC system by using the events from their unexposed corners, following Kuntz et al. (2008). For the central CCDs without unexposed corners, the rescaling factor is assessed from the corners of the neighboring CCDs. The count-rate within the 2.5-5 keV (MOS and PN) and the 8-9 keV (MOS) energy bands is considered for this calibration to avoid certain fluorescence lines that appear in the detectors. The derived instrumental background level is then reprojected to the main observation frame and is subtracted from the images. Finally, to account for an imperfect instrumental background subtraction, Gaussian emission lines are included during the spectral fitting to model the possible residuals. The instrumental background image of A2377 is displayed in Fig. 2.4 as an example.

Cluster center

The cluster centers are needed to determine the region around it from which the spectra are extracted. I considered the X-ray emission peak as the center. The clean, background-subtracted, coadded image of the cluster is used in the 0.4-1.25 keV energy band. The image is first smoothed by a Gaussian function with a full width half maximum (FWHM) of 75 arcsec, worsening its resolution intentionally, and an

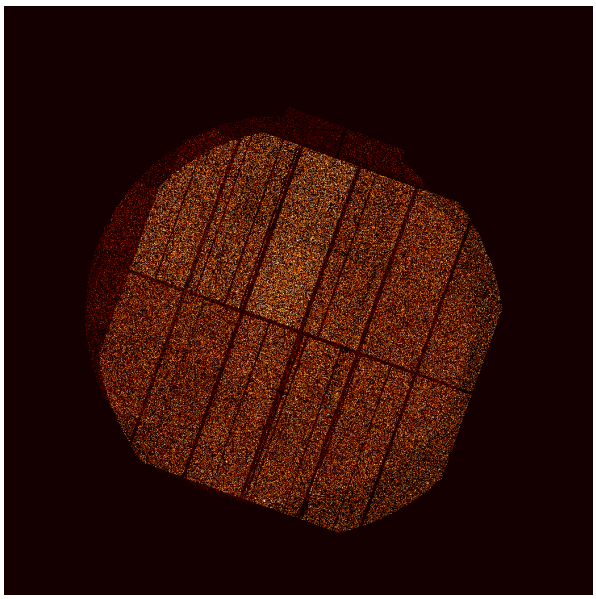

Figure 2.4: Instrumental background of the A2377 observation. Note the detector gaps that are obvious before the exposure time correction is applied.

initial X-ray peak is determined. This is done to ensure that the X-ray peak is not selected based on a single hot pixel or a poorly removed AGN. The resolution is then iteratively improved in small steps to look for a more precise peak location within a box of side ten times the previous FWHM. This is done until a final resolution of 7.5 arcsec is reached. The brightest X-ray pixel's coordinates are then assigned as the cluster's center.

I performed all the intermediate parts from the flare filtering to here for 76 XMM-Newton observations, while Dr. Miriam Ramos-Ceja reduced the rest 24 observations.

Spectra extraction

The spectrum of a region is the number of observed photons (or counts) as a function of the photon energy bin. For every cluster, I extracted three spectra; the astrophysical background spectrum, the spectrum within $< 0.2\ R_{500}$ (cluster core), and the spectrum from the $0.2 - 0.5\ R_{500}$ annulus. The selection of the regions from which the background spectra were extracted are described in Sect. 3.3. These regions are plotted in Fig. 2.5 for three clusters with different apparent R_{500} values.

For every spectral extraction, the photon redistribution matrix file (RMF) and ancillary response file (ARF) are generated. The RMF contains information about the detector's response as a function of energy. In other words, it gives the probability of assigning a photon to a given energy channel as a function of the captured photon's energy. The ARF defines the instrument's quantum efficiency across the FOV as a function of photon energy averaged over time. The RMF and ARF files are generated for every detector separately and used to properly calibrate the detected spectra to obtain the true spectra emitted from the source. Each spectrum is then binned according to the photon energies. Every bin contains at least 25 photons, so the χ^2 minimization can be used when fitting the appropriate models to the data.

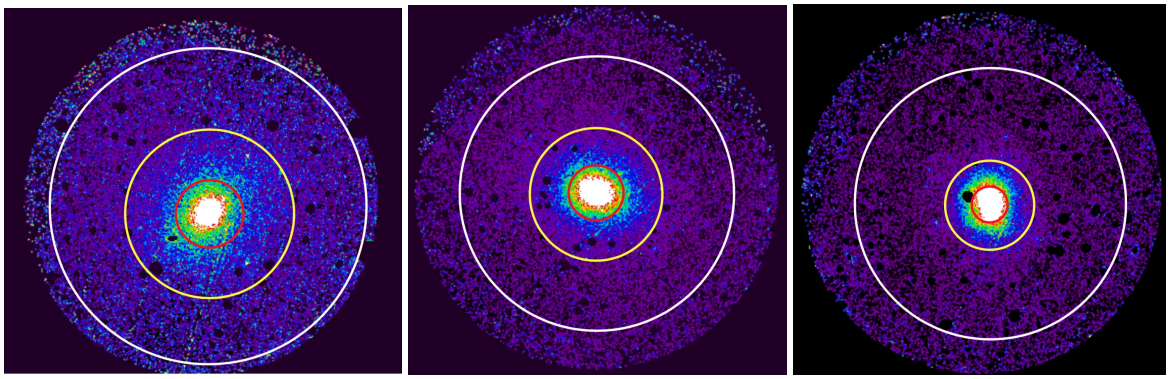

Figure 2.5: Cleaned, exposure time-corrected X-ray images in the 0.5-2 keV band of S0555 (left), A3104 (middle), and A0022 (right). The red circle corresponds to the 0.2 R_{500} radius, the yellow circle corresponds to the 0.5 R_{500} radius, and the region outside the white circle corresponds to the background region. The white circle marks the 0.9 R_{500}, R_{500}, and 1.6 R_{500} radius respectively.

2.3 Spectral fitting

By fitting the X-ray spectrum of the ICM, one can constrain several cluster properties, such as the temperature, metallicity, and redshift. The temperature T can be found by the height of the high energy, exponential cutoff of an X-ray spectrum, as shown in Fig. 1.11. The width of the emission lines is also affected. The metallicity Z can be constrained by the amplitude of the emission lines, while the redshift z by their observed energy shift.

For the spectral analysis, the XSPEC v12.9.1 software was used (K. A. Arnaud, 1996). The model that accounts for the X-ray emission of collisionally-ionized diffuse gas is the so-called *apec* model, and is a function of T, Z, z, and the normalization $a_{\rm apec}$ (in units of cm^{-5} which will be implied from now on). The latter is simply the integral of the ICM particle density squared over the emitting volume and scaled by the source's distance. $a_{\rm apec}$ was usually left free to vary (as a nuisance parameter) since it is of no interest for this analysis. However, its value was checked for all fits to ensure that it did not return erratic values, which could jeopardize the reliability of the fits. Moreover, the so-called *phabs* model accounts for the photoelectric X-ray absorption. Its only free parameter is the $N_{\rm H}$, while the metal abundances and cross sections are adopted from Asplund et al. (2009). The so-called *pow* model describes a power-law emission coming from AGNs. It depends on the spectral power index β and its normalization $a_{\rm pow}$ (measured in photons/keV/cm^2/s at 1 keV, from now on the units will be implied). Finally, the "gaussian" components account for various emission lines, coming from recombination or deexcitation emission or residual instrumental fluorescence lines.

The 0.7 – 7 keV part of each spectrum was used for the fitting. This was done to be consistent with the Chandra measurements, where the same energy range was used. That way, one avoids a stronger dependence of T on the exact absorption correction, which mostly affects low energies (Fig. 1.13). Also, the Ni, Cu, and Zn fluorescence lines in the PN detector within the 7.4-9 keV energy range are avoided. The fitted model to each extracted spectrum is:

$$\begin{aligned} \text{model} = & A \times [apec_1 + phabs \times (apec_2 + pow + apec_3) + \text{gaussian} + \text{gaussian} + \\ & + B \times phabs \times apec_4 \end{aligned} \tag{2.1}$$

The different components of this model are described below:

- **A**, **B**: normalization constants for the calibration of the background and the cluster emission

models.

- **apec$_1$**: accounts for the X-ray emission from the LHB, which is the least important component of the photon background for this analysis due to the selected energy range $0.7 - 7$ keV for fitting the spectrum. For the emission of the LHB, we adopt $T = 0.099$ keV, $Z = 1$ Z$_\odot$, and $z = 0$. At start, $a_{\rm apec}$ was set to 1.7×10^{-6}.

- **phabs**: accounts for the absorption from the Galaxy. The input, fixed $N_{\rm Htot}$ value was adopted from Willingale et al. (2013) as already mentioned before.

- **apec$_2$**: accounts for the diffuse X-ray emission of the Galaxy. I used $T = 0.225$ keV (McCammon et al., 2002), $Z = 1$ Z$_\odot$, and $z = 0$. Initially, $a_{\rm apec}$ was set to 7.3×10^{-7}.

- **pow**: accounts for the continuum emission of unresolved AGNs. I fixed its spectral power index to $\beta = 1.45$ (De Luca et al., 2004). The normalization was initially set to $a_{\rm pow} = 5 \times 10^{-7}$.

- **apec$_3$**: accounts for the residual cluster emission in the background spectrum (when relevant). Its redshift is kept fixed to the cluster's known redshift. Its normalization was kept fixed to zero when no residual cluster emission was expected in the background region (see Sect. 3.3 for more details). Otherwise, T, Z, and $a_{\rm apec}$ were initially kept fixed to some expected values based on the a-priori known properties of each cluster.

- **gaussian**: accounts for two fluorescence lines; the Al K-alpha line at 1.4865 keV and the Si K-alpha line at 1.7397 keV.

- **apec$_4$**: accounts for the ICM cluster emission.

One needs to constrain the background components first, and its spectrum was fitted in the beginning. For that, I set $B = 0$ to ignore the cluster's main emission since it is irrelevant for the background spectrum. At first, all parameters were kept frozen except for $a_{\rm pow}$ which is the only component that affects the high energies. After it was constrained, it was frozen to its best-fit value. Next, when applicable, the $apec_3$ component was fitted (T, Z, and $a_{\rm apec}$), and then kept fixed to its best-fit solution. Following the same reasoning, the gaussian instrumental lines and the normalizations of the $apec_2$ and $apec_1$ components were constrained.

Next, the cluster properties need to be obtained. For that, the spectrum from the $0.2 - 0.5\ R_{500}$ annulus was used. The photons coming from this region originate both from the cluster's emission and the background. Consequently, the entire model from Eq. 2.1 is fitted. The obtained best-fit values for the background components were used as starting points, and they were allowed to vary within a restricted range. The $apec_4$ model is left completely free to vary and its T, Z, and $a_{\rm apec}$ are constrained. If any spectral fitting returned $\chi^2 > 1.3$, the initial values of the normalization were shifted to ensure they do not bias the result. Eventually, observations that returned a worse fit than this threshold were discarded.

From that procedure, I obtained the T and Z values for the 91 clusters which I use in this dissertation's projects. 76 of them are used as the default values for the respective clusters, while the rest 15 are used for comparison purposes with Chandra temperatures (see Sect. 3.11). On top of these results, I also constrained z and $N_{\rm H}$ based on the X-ray cluster spectra. For that, the spectra from the cluster cores ($< 0.2\ R_{500}$) were included in the model as an extra *apec* component with independent T and Z. Additionally, z and $N_{\rm H}$ were left free to vary but they were linked between the $< 0.2\ R_{500}$ and the $0.2 - 0.5\ R_{500}$ spectra, and the background spectra. Overall, the X-ray z was constrained for all 76 clusters, while $N_{\rm H}$ was constrained for 44 clusters (more details are given when these measurements

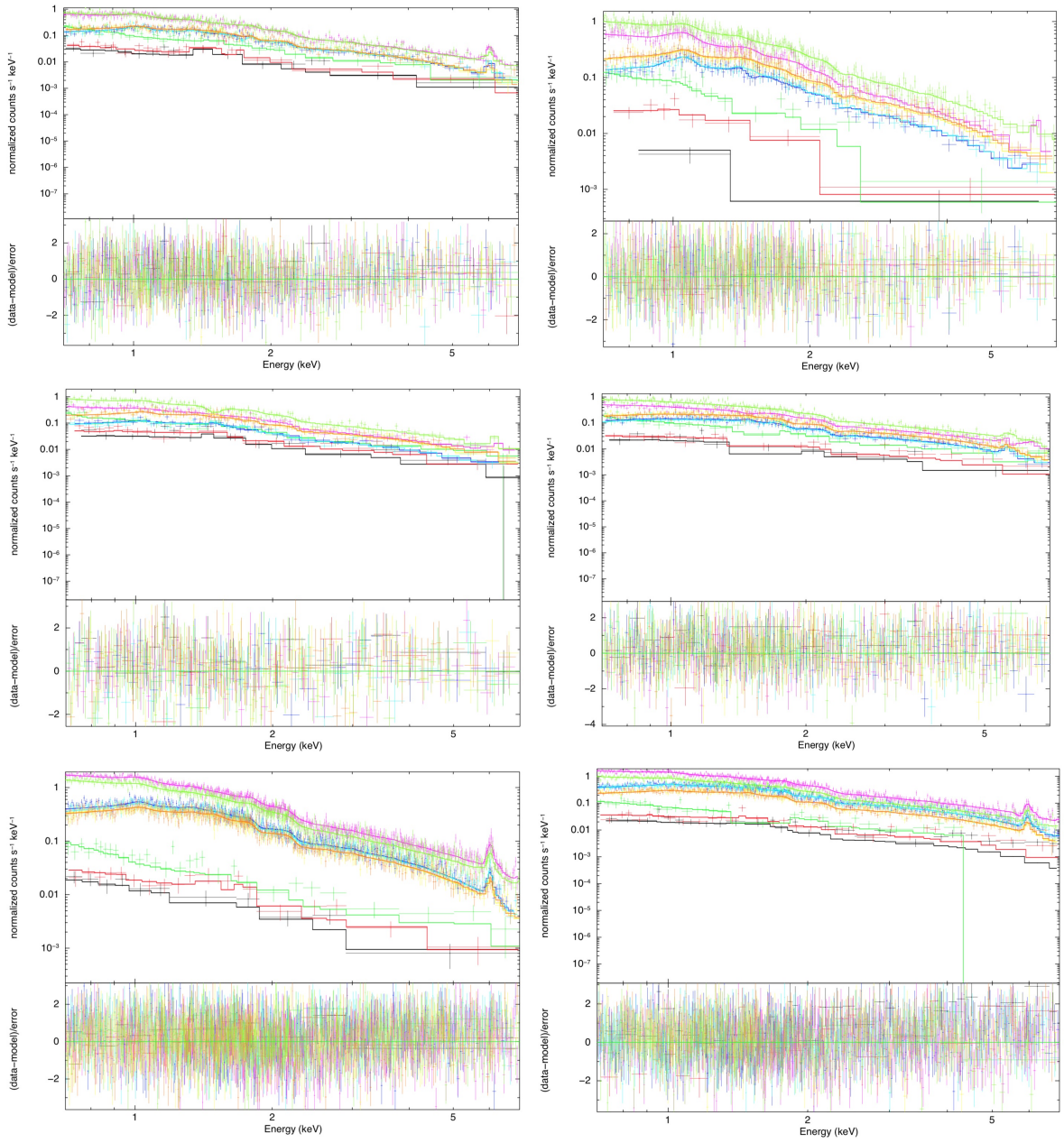

Figure 2.6: X-ray spectra in the 0.7 – 7 keV energy band for six clusters; starting from left to right and from top to bottom (like reading), A0458, A0602, A1205, A1451, A2811, and A2941. In every plot, the two highest spectra correspond to the PN spectra for the $< 0.2\ R_{500}$ and $0.2 - 0.5\ R_{500}$ regions, respectively. The next four spectra correspond to the MOS detectors for the two regions. Finally, the three bottom spectra correspond to the background obtained from MOS1 (red), MOS2 (black), and PN (deep green).

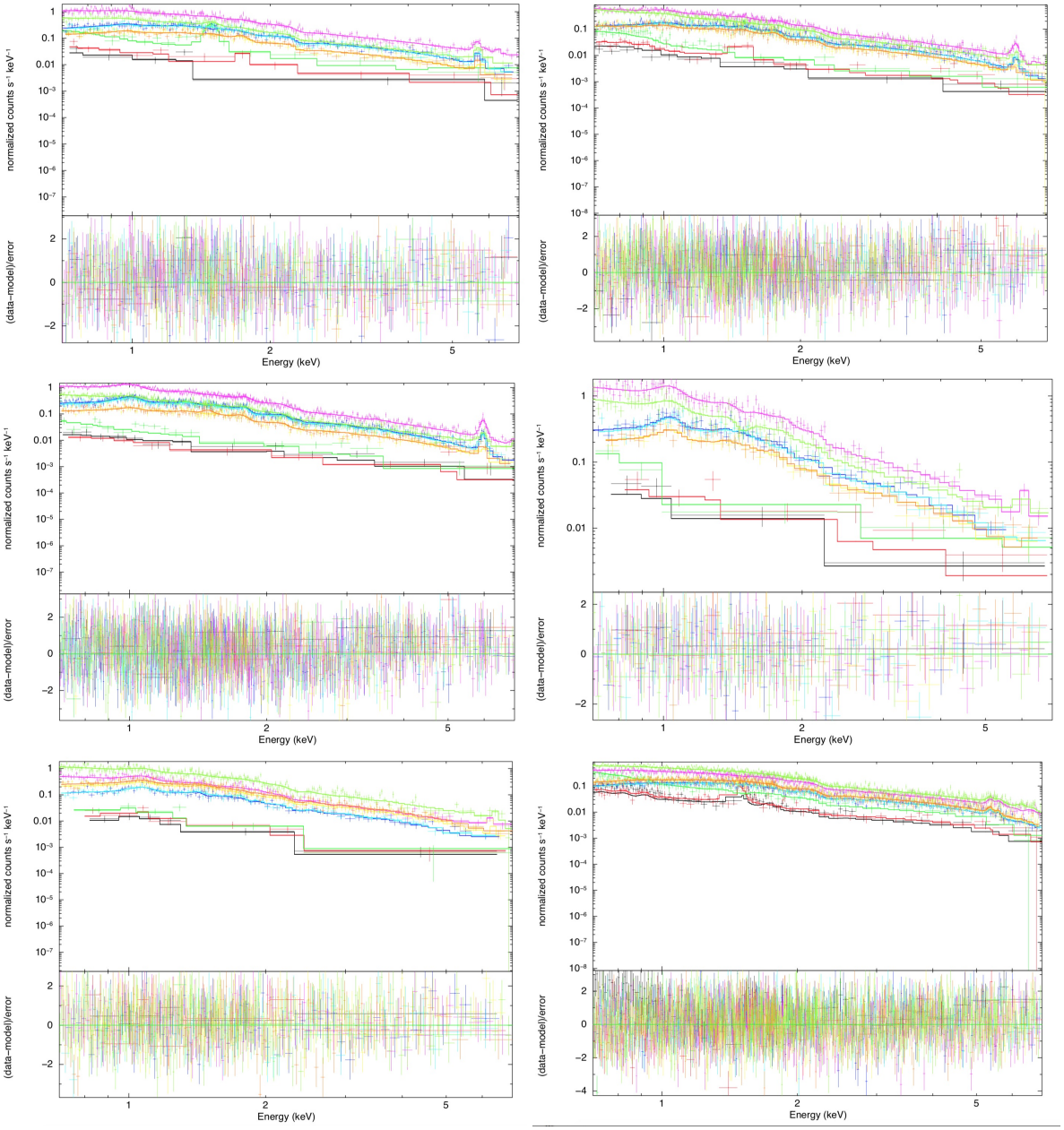

Figure 2.7: Same as in Fig. 2.6, for A3396, A3694, A3814, A4010, PegasusII, and RXCJ13144-2515.

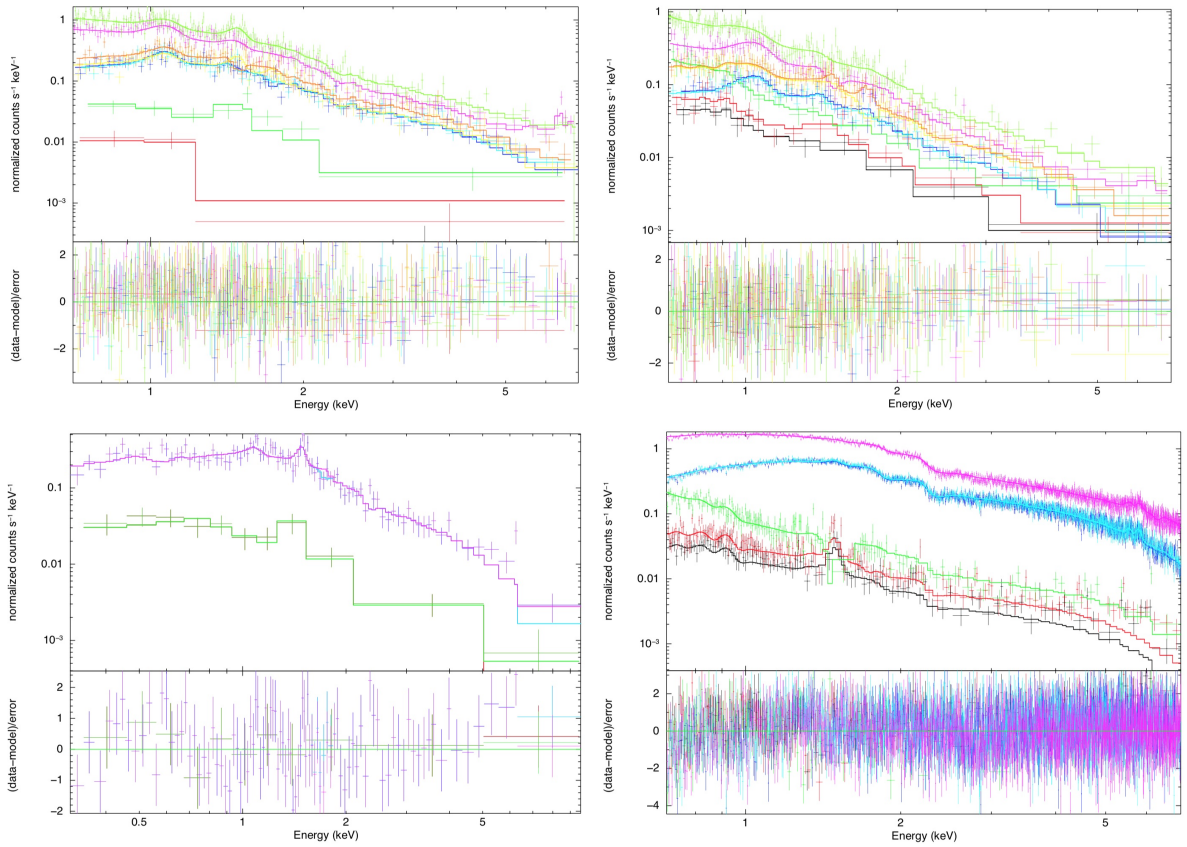

Figure 2.8: *Top panel*: Same as in Fig. 2.6 for NGC1650 and RXCJ13534-2753. *Bottom panel*: Same as in Fig. 2.6, but only for the $0.2-0.5\,R_{500}$ and the background regions. On the left, the MOS1 and MOS2 spectra of the A0076 cluster are displayed (the fewest counts of all analyzed clusters). On the right, the spectra from the A2163 cluster (the hottest cluster used in this work) are shown, from all three detectors.

are used later in Chapters 3 and 4). In Figs. 2.6, 2.7, and 2.8 (top panels), the spectra from both cluster regions and their background regions are displayed for 14 clusters, as an example. Clusters of different temperatures, metallicities, fluxes and exposure times are considered in order to give a representative picture of the spectral analysis process. In the bottom panels of Fig. 2.8, the spectra only from the $0.2-0.5\,R_{500}$ regions and the background are plotted for two clusters with opposite observation qualities. A0076 has a very low GTI (4.1 ks) with a few detected counts, and the PN camera is excluded due to a hight IN/OUT ratio after the filtering. Its constrained T has a 29% uncertainty. On the other hand, the observation of A2163 has a quite high GTI (98 ks), with many detected photons, and low IN/OU ratios after the filtering for all three cameras. It is the hottest cluster within this work, and one of the hottest clusters known ($T \sim 15-19$ keV, depending on the telescope). Its best-fit T as given by the displayed fit has an uncertainty of only 1.3%.

CHAPTER 3

Probing cosmic isotropy with a new X-ray galaxy cluster sample through the $L_X - T$ scaling relation

This Chapter presents the first project of my thesis. I probe the isotropy of the X-ray luminosity-temperature relation of galaxy clusters and attempt to draw conclusions on possible spatial variation of the cosmic expansion rate. The spectral information for the clusters observed by Chandra was provided by Dr. Gerrit Schellenberger. This Chapter has been published as Migkas et al. (2020) (Migkas, K., Schellenberger, G., Reiprich, T. H., Pacaud, F., Ramos-Ceja, M.E., and Lovisari, L., 2020, A&A, 636, A15) with the journal Astronomy & Astrophysics (link: `https://doi.org/10.1051/0004-6361/201936602`, Bibcode: 2020A&A...636A..15M).

Abstract

The isotropy of the late Universe and consequently of the X-ray galaxy cluster scaling relations is an assumption greatly used in astronomy. However, within the last decade, many studies have reported deviations from isotropy when using various cosmological probes; a definitive conclusion has yet to be made. New, effective and independent methods to robustly test the cosmic isotropy are of crucial importance. In this work, we use such a method. Specifically, we investigate the directional behavior of the X-ray luminosity-temperature ($L_X - T$) relation of galaxy clusters. A tight correlation is known to exist between the luminosity and temperature of the X-ray-emitting intracluster medium of galaxy clusters. While the measured luminosity depends on the underlying cosmology through the luminosity distance D_L, the temperature can be determined without any cosmological assumptions. By exploiting this property and the homogeneous sky coverage of X-ray galaxy cluster samples, one can effectively test the isotropy of cosmological parameters over the full extragalactic sky, which is perfectly mirrored in the behavior of the normalization A of the $L_X - T$ relation. To do so, we used 313 homogeneously selected X-ray galaxy clusters from the Meta-Catalogue of X-ray detected Clusters of galaxies (MCXC). We thoroughly performed additional cleaning in the measured parameters and obtain core-excised temperature measurements for all of the 313 clusters. The behavior of the $L_X - T$ relation heavily depends on the direction of the sky, which is consistent with previous studies. Strong anisotropies are detected at a $\gtrsim 4\sigma$ confidence level toward the Galactic coordinates $(l, b) \sim (280^\circ, -20^\circ)$, which is roughly consistent with the results of other probes, such as Supernovae Ia. Several effects that could potentially explain these

strong anisotropies were examined. Such effects are, for example, the X-ray absorption treatment, the effect of galaxy groups and low redshift clusters, core metallicities, and apparent correlations with other cluster properties, but none is able to explain the obtained results. Analyzing 10^5 bootstrap realizations confirms the large statistical significance of the anisotropic behavior of this sky region. Interestingly, the two cluster samples previously used in the literature for this test appear to have a similar behavior throughout the sky, while being fully independent of each other and of our sample. Combining all three samples results in 842 different galaxy clusters with luminosity and temperature measurements. Performing a joint analysis, the final anisotropy is further intensified ($\sim 5\sigma$), toward $(l, b) \sim (303^\circ, -27^\circ)$, which is in very good agreement with other cosmological probes. The maximum variation of D_L seems to be $\sim 16 \pm 3\%$ for different regions in the sky. This result demonstrates that X-ray studies that assume perfect isotropy in the properties of galaxy clusters and their scaling relations can produce strongly biased results whether the underlying reason is cosmological or related to X-rays. The identification of the exact nature of these anisotropies is therefore crucial for any statistical cluster physics or cosmology study.

3.1 Introduction

The isotropy of the Universe on sufficiently large scales is a fundamental pillar of the standard model of cosmology. The most important consequence of isotropy is that the expansion rate of the Universe as well as the physical properties of all astronomical objects must be the same regardless of the direction in the sky. Due to the high significance of this hypothesis, it is necessary that it is robustly scrutinized and tested against different cosmological probes using the latest data samples.

What was initially introduced as a repercussion of general relativity and the Friedmann-Lemaître-Robertson-Walker (FLRW) metric was later supported by observations. The most crucial of them is arguably the cosmic microwave background (CMB) as observed by Cosmic Background Explorer (*COBE*, Efstathiou et al., 1992), the Wilkinson Microwave Anisotropy Probe (*WMAP*, Bennett et al., 2013), and the *Planck* (Planck Collaboration et al., 2016) telescopes. CMB shows a remarkable isotropy at small angular scales (high multipoles), whilst some anisotropies are still present in lower multipoles. The most prominent one is the so-called CMB dipole which, if one assumes its purely kinematic origin, is caused by the Doppler shift due to the motion of our Solar System with respect to the CMB rest frame. This indicates that the Solar System moves toward the Galactic coordinates $(l, b) \sim (264^\circ, +48^\circ)$ with a peculiar velocity of ~ 370 km/s (Kogut et al., 1993; Fixsen et al., 1996) with respect to the CMB rest frame. Another anisotropic feature present in the CMB is the dipole power asymmetry detected in both *WMAP* and *Planck* with a significance of $\sim 2 - 3.5\sigma$ toward $(l, b) \sim (230^\circ, -20^\circ)$ (Eriksen et al., 2004; Hanson et al., 2009; Bennett et al., 2011; Akrami et al., 2014; Planck Collaboration et al., 2014; Planck Collaboration et al., 2016). Its nature still remains relatively unclear. The interpretation of the significance of these results differ between papers. Other potential challenges for the isotropy of the Universe found in the CMB is the parity asymmetry, $\sim 3\sigma$ toward $(l, b) = (264^\circ, -17^\circ)$ and the unexpected quadrupole-octopole alignment and the existence of the Cold Spot at $(l, b) = (210^\circ, -57^\circ)$ (Tegmark et al., 2003; Vielva et al., 2004; Kim et al., 2010; Aluri et al., 2012; Cai et al., 2014; Planck Collaboration et al., 2014; Planck Collaboration et al., 2016; Schwarz et al., 2016).

The CMB is a great tool to study the behavior of the early Universe. However, it can be quite challenging to extract information about the directional behavior of the late Universe based on that probe. This problem intensifies when one considers that according to ΛCDM the late Universe is dominated by dark energy whose effects are not directly present in the CMB spectrum. Moreover, since the nature of dark energy is still completely unknown, one can only make assumptions about the isotropic (or not) behavior of dark energy. Consequently, it becomes clear that other cosmological probes, at much lower

redshifts than the CMB, are needed in order to search for possible anisotropies in the late Universe. There are indeed many probes that have been used for such tests.

For instance, Type Ia Supernovae (SNIa) have been extensively used to test the isotropy of the Hubble expansion with many results reporting no significant deviation from the null hypothesis (Lin et al., 2016; Andrade et al., 2018; Sun et al., 2018; Y.-Y. Wang et al., 2018). Other studies however, claim to detect mild-significance anisotropies in the SNIa samples that more often than not approximately match the direction of the CMB dipole (Schwarz et al., 2007; Antoniou et al., 2010; Colin et al., 2011; Mariano et al., 2012; Kalus et al., 2013; Appleby et al., 2015; C. A. P. Bengaly J. et al., 2015; Javanmardi et al., 2015; Migkas et al., 2016; Colin et al., 2017). Generally, the reported results from SNIa strongly depend on the used catalog. Moreover, the robustness of SNIa as probes for testing the isotropy of the Universe based on the current status of the relative surveys has been recently challenged (Colin et al., 2017; Beltrán Jiménez et al., 2015; Rameez, 2019). This is mainly because of the highly inhomogeneous spatial distribution of the data (most SNIa in the latest catalogs lie close to the CMB dipole direction), their sensitivity to the applied kinematic flow models which readjust their measured heliocentric redshifts, as well as the assumptions that go into the calibration of their light curves.

Other probes that have been used to pinpoint possible anisotropies or inconsistencies with the ΛCDM model are the X-ray background (Shafer et al., 1983; Plionis et al., 1999), the distribution of optical (Javanmardi et al., 2017; Sarkar et al., 2019) and infrared galaxies (Yoon et al., 2014; Rameez et al., 2018), the distribution of distant radio sources (Condon, 1988; Blake et al., 2002; Singal, 2011; Rubart et al., 2013; Tiwari et al., 2015; C. A. P. Bengaly et al., 2018; Colin et al., 2018; C. A. P. Bengaly et al., 2019), GRBs (Řıpa et al., 2017; Andrade et al., 2019), peculiar velocities of galaxy clusters (Kashlinsky et al., 2008; Kashlinsky et al., 2010; Watkins et al., 2009; Kashlinsky et al., 2011; Atrio-Barandela et al., 2015) and of SNIa (Appleby et al., 2015) etc. While some of them find no statistically significant challenges for the null hypothesis of isotropy, others provide results which are unlikely to occur within the standard cosmological model framework. The use of standard sirens for such tests in the future has also been proposed (**cai**).

Since the outcome of the search for a preferred cosmological direction remains ambiguous, new and independent methods for such tests should be introduced and applied to the latest data samples. In Migkas et al. (2018) (hereafter M18), the use of the directional behavior of the galaxy cluster X-ray luminosity-temperature relation is described as a cosmological probe. It is well-known that galaxy clusters are the most massive gravitationally bound systems in the universe, strongly emitting X-ray photons due to the large amounts of hot gas they contain ($\sim 10\%$ of their total mass) in their intra-cluster medium (ICM). Their physical quantities follow tight scaling relations, for which Kaiser (1986) provided mathematical expressions. Specifically, the correlation between the X-ray luminosity ($L_{\rm X}$) and the ICM gas temperature (T) of galaxy clusters is of particular interest since it can be used to trace the isotropy of the Universe, which is a new concept for such cosmological studies. The general properties of the $L_{\rm X} - T$ scaling relation have been extensively scrutinized in the past by several authors (e.g., Vikhlinin et al., 2002; Pacaud et al., 2007; G. W. Pratt et al., 2009; Mittal et al., 2011; Reichert et al., 2011; Hilton et al., 2012; Maughan et al., 2012; Bharadwaj et al., 2015; Lovisari et al., 2015; Giles et al., 2016; Zou et al., 2016; Migkas et al., 2018; Ebrahimpour et al., 2018).

In a nutshell, the gas temperature, the flux and the redshift of a galaxy cluster do not require any cosmological assumptions in order to be measured [1]. Using the flux and the redshift together with the luminosity distance, through which the cosmological parameters come into play, one can obtain the

[1] Only indirectly when the selection of the cluster relative radius within which the used spectra are extracted is based on a cosmological distance, such as the X-ray luminosity-mass scaling relation ($L_{\rm X} - M$) and the conversion of the radius from Mpc to arcmin, where the luminosity and angular diameter distances enter. Nevertheless, even in these cases, the dependence happens to be very weak.

luminosity of a cluster. The luminosity however can also be predicted (within an uncertainty range) based on the cluster gas temperature. Hence, adjusting the cosmological parameters, one can make the two luminosity estimations match. This can be repeatedly applied to different sky patches in order to test the consistency of the obtained values as a function of the direction. The full detailed physical motivation behind this is discussed in M18. There, it is shown that the directional behavior of the normalization of the $L_X - T$ relation strictly follows the directional behavior of the cosmological parameter values. This newly introduced method to test the Cosmological Principle (CP) could potentially prove very effective due to the very homogeneous sky coverage of many galaxy cluster samples (in contrast to SNIa samples), the plethora of available data as well as large upcoming surveys such as *eROSITA* (Predehl et al., 2016) which will allows us to measure thousands of cluster temperatures homogeneously (Borm et al., 2014). For studying the isotropy of the Universe with the future surveys, it is of crucial importance that any existing systematic biases that could potentially affect the L_X and T measurements of galaxy clusters would have been identified and taken into account by then.

In this paper, we construct and use a new galaxy cluster sample in order to identify regions that share a significantly different $L_X - T$ relation compared to others. This could lead to pinpointing an anisotropy in the Hubble expansion or discover previously unknown factors which could potentially affect X-ray measurements of any kind. Except for the high quality observations and measurements, another advantage of our sample is the small overlap with the XCS-DR1 (Mehrtens et al., 2012) and ACC (Horner, 2001) samples used in M18. There are only three common clusters between our sample and XCS-DR1 ($< 1\%$) and only a 30% overlap with ACC. Since we reanalyze the XCS-DR1 and ACC sample in this paper as well, using the same methods we use for our sample in order to perform a consistent comparison, all the common clusters between the different catalogs are excluded from XCS-DR1 and ACC. Our cluster sample does not suffer from any strong archival biases in contrast to ACC. Throughout this paper we use a ΛCDM cosmology with $H_0 = 70$ km s^{-1}Mpc^{-1}, $\Omega_m = 0.3$ and $\Omega_\Lambda = 0.7$ unless stated otherwise.

The paper is organized as follows: In Sect. 3.2 we describe the construction of the sample and how we derive the properties of the clusters. In Sect. 3.3 we explain the steps we follow for the data reduction and the spectral analysis of the observations. In Sect. 3.4 we present the modeling of the $L_X - T$ relation together with the parameter fitting procedure. We also explain how we identify possible spatial anisotropies and assign their statistical significance. In Sect. 4.4 we present the first results, including the overall $L_X - T$ results and the 1-dimensional (1D) and 2-dimensional (2D) anisotropies of our sample. In Sect. 3.6 we investigate several X-ray and cluster-related causes that could possibly produce the observed anisotropic signal in our sample. In Sect. 3.7 we examine the case where the anisotropies in our sample have a cosmological origin instead, assuming there are no systematics associated with X-ray photons or cluster properties. In Sect. 3.8 we combine our results with those obtained from ACC and XCS-DR1. We express these joint-analysis anisotropies in cosmological terms. In Sects. 3.9 and 4.10 we discuss our findings and their implications, compare with other studies and summarize.

3.2 Sample selection and cluster measurements

The cluster sample used in this work is a homogeneously selected one based on the Meta-Catalogue of X-ray detected Clusters of galaxies (MCXC, Piffaretti et al., 2011). Initially it consisted of the 387 galaxy clusters above an unabsorbed flux cut of $f_{0.1-2.4\ \mathrm{keV}} \geq 5 \times 10^{-12}$ ergs/s/cm^2 excluding the Galactic plane ($|b| \leq 20^\circ$), the Magellanic clouds and the Virgo cluster area. The flux for every MCXC cluster is found based on the given X-ray luminosity and redshift, combined with a reversed K-correction (the necessary temperature input was found by the $L_X - T$ relation of Reichert et al. (2011). The MCXC luminosities (and therefore the calculated fluxes on which our sample is based) were corrected for absorption based

on HI measurements (see Sects. 3.2 and 3.2).

The parent catalogs of the clusters we use are The ROSAT extended Brightest Cluster Sample (**ebcs**), The Northern ROSAT All-Sky (NORAS) Galaxy Cluster Survey (Böhringer et al., 2000) and the ROSAT-ESO Flux-Limited X-Ray (REFLEX) Galaxy Cluster Survey Catalog (Böhringer et al., 2004). They are all based on the ROSAT All-Sky Survey (RASS, Voges et al., 1999).

Another selection criterion was for the clusters to have good quality *Chandra* (Weisskopf et al., 2000) or *XMM-Newton* (Jansen et al., 2001) public observations (as of July 2019). This criterion is satisfied for 331 clusters. The rest 56 clusters for which such observations were not available have a sparse sky distribution and similar average properties with the 331 clusters (as discussed later in the paper) and therefore their inclusion is not expected to alter the results.

We reduced these 331 available observations, analyzed them and extracted cluster properties as described below. This sample includes a large fraction ($\sim$ 85%) of the eeHIFLUGCS (extremely expanded HIghest X-ray FLUx Galaxy Cluster Sample Reiprich, 2017, Pacaud et al. in prep.) sample clusters. eeHIFLUGCS is a complete, purely X-ray flux-limited sample with similar selection criteria.

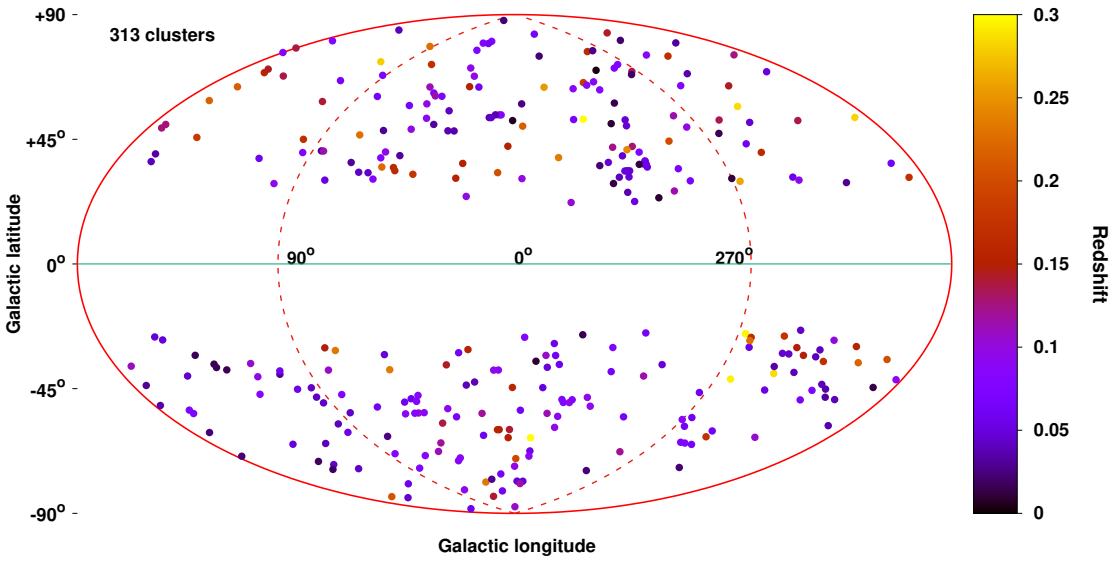

Figure 3.1: Sky distribution of the 313 clusters in Galactic coordinates, with the colorbar indicating their redshift. There are two clusters at $z > 0.3$ but the scale is set in such way so the color contrast is optimal.

The final sample we use for this paper consists of 313 galaxy clusters. The other 18 clusters are not used because of the following reasons. Firstly, we excluded 11 clusters from our analysis that we identified as apparent multiple systems (out of a total of 15). This is due to the fact that clusters in rich environments tend to be systematically fainter than single clusters (M18 and references therein), thus biasing the final results. Moreover, some of these seemingly multiple systems are located at different redshifts but projected in our line of sight as real double and triple systems (see Ramos-Ceja et al., 2019, hereafter R19). When these different components are accounted as one system in MCXC the flux of the "single cluster" is overestimated. As a result, some of these systems falsely overcome the selected flux limit while none of their true individual components has the necessary flux to be included in our catalog. On the other hand, there are cases where one of the individual extended components has enough flux to be kept in our sample and at the same time it is located at a different redshift than the other components of the system (it does not belong to the same rich environment). In this case, these extended sources were kept in the catalog and their L_X values were adjusted correspondingly (see Sect. 3.2) while the other

component(s) were excluded. Since we use *Chandra* and *XMM-Newton* observations while the MCXC $L_X - T$ values come from *ROSAT* observations, some minor inconsistencies between these values and our own measurements are expected. In order to account for this, we consider it as an extra source of uncertainty and adjust the confidence levels of the final cluster fluxes and luminosities accordingly as described later in the paper.

Furthermore, we identify nine clusters to be strongly contaminated by point sources, likely Active Galactic Nuclei (AGN). We confirm that by the absence of significant extended emission around the suspected point sources and by fitting a power-law (constraining the power index and the normalization) and an *apec* model to the spectra of the bright part of the point source using XSPEC (K. A. Arnaud, 1996). If the *pow* model returns a better fit than the *apec* model we mark the source as an AGN. Moreover, we search the literature for known stars and AGNs at these positions. For three of these nine clusters (A2055, A3574E, RXCJ1840.6-7709) the point sources are located close to the (bright) cores of the clusters and cannot be deblended. Thus, we chose to exclude these clusters since their MCXC L_X values would be overestimated and would add extra bias to our analysis. For another cluster (A1735) there is a strong AGN source and a galaxy cluster with extended emission with an angular separation of $\sim 7'$. This system has been identified as one cluster in the MCXC catalog centered at the AGN position, which has the higher contribution to the X-ray flux. Therefore, this system was also excluded since the single extended emission component does not surpass the necessary flux limit. For the rest five clusters, using the *Chandra* and *XMM-Newton* images the point sources are easily distinguishable from the cluster emission while the MCXC objects are centered close to the extended emission centers. For these five systems we calculate the flux of the point source using its spectra from one of the two aforementioned telescopes and a *pow* model, and subtract it from the MCXC flux in order to see if the extended emission alone overcomes the flux limit. This procedure results in the exclusion of three clusters (A0750, A0901, A2351), while the other two (A3392, S0112) stay above the desired flux limit and are considered in our analysis after appropriately decreasing their MCXC luminosity values (Sect. 3.2).

Since $\sim 50\%$ of the clusters included in our sample have been observed by both *Chandra* and *XMM-Newton*, we decide to analyze these common clusters with the former. This is due to the fact that *Chandra* data are generally less flared than *XMM-Newton* data. As a result, 237 clusters are analyzed using *Chandra* observations while 76 clusters are processed using *XMM-Newton* observations. For both telescopes, we extract and fit the spectra within the energy range of 0.7 to 7 keV. The cross calibration of the two satellites is discussed in Sect. 3.2. Using *Chandra* data for $\sim 75\%$ of our sample offers another advantage as well. As mentioned before, in M18 two samples are used: ACC which consists only of ASCA observations, and XCS-DR1 which consists only of *XMM-Newton* observations. Subsequently, mostly using a third independent telescope to built our sample and study the anisotropy of the $L_X - T$ eliminates any systematics that might occur in the results because of telescope-specific reasons.

Consequently, the sample with which this analysis is performed consists of 313 single galaxy clusters. For these clusters we have self-consistently measured their gas temperatures T and their uncertainties, as well as their metallicities Z and their X-ray redshifts z. Furthermore, we know their optical spectroscopic z, their fluxes f_X and their luminosities L_X within the 0.1-2.4 keV energy range together with their uncertainties, their Galactic (l, b) and Equatorial $(RA,\ Dec)$ coordinates and the atomic and molecular hydrogen column density $N_{\rm Htot}$ in their direction. The exact information for every parameter and where it comes from is described in the following subsections. Their spatial distribution together with the redshift value used for each cluster can be seen in Fig. 3.1. The vast majority of these 313 galaxy clusters are included in the eeHIFLUGCS sample.

Redshift

For 264 out of the 313 clusters the given MCXC redshifts are used. We have checked that all these clusters have at least seven galaxies with optical spectroscopic redshifts in the NASA/IPAC Extragalactic Database (NED) and that agree with the assigned MCXC redshift. The median number of galaxies per cluster is 52 for these cases. For seven other clusters we reassigned a redshift based on the already-existing optical spectroscopic data when the offset between the apparently correct redshift value and the MCXC redshift is $\Delta z \geq 0.007$, corresponding to $\sim$ 2000 km/s.

The remaining 42 clusters either do not have enough optical spectroscopic data in order to trust the given redshift or the distribution of the galaxy redshifts of the cluster is inconclusive. In that case, the redshift of the cluster was determined from the available X-ray data. For that, we extracted and fit the spectra within the $0 - 0.2\ R_{500}$[2] circle and within the $0.2 - 0.5\ R_{500}$. Using two *apec* models (one for each cluster region) with the temperature and metallicity parameters free to vary for both, the redshift is also fit simultaneously but linked for the two regions (same z for both regions). In Sect. 3.3 the technical details of the spectral fitting process are discussed.

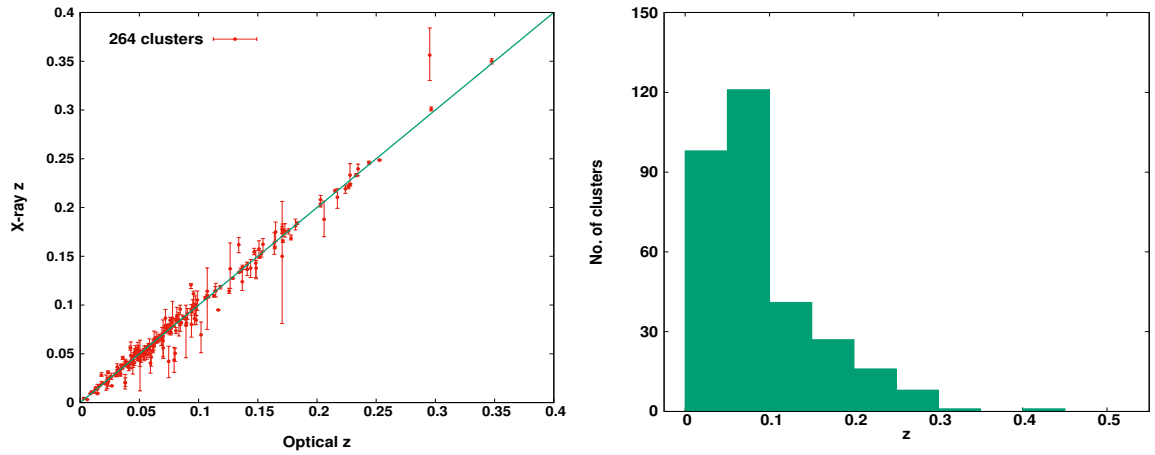

Figure 3.2: *Top*: Comparison between the safe optical redshifts and the X-ray redshifts obtained from this analysis. *Bottom*: Redshift distribution of the final sample.

In order to make sure that the obtained X-ray redshifts are trustworthy, we also determined them for the 264 clusters with safe optical redshifts. The comparison of the optical and X-ray redshifts is displayed in the top panel of Fig. 3.2. By comparing the well-known optical redshifts with the X-ray ones, we see that there is only a very small intrinsic scatter of $\Delta z = 0.0014$ ($\sim$ 420 km/s) with the agreement being remarkable. It is noteworthy that only 10% of the clusters have a deviation of more than $\Delta z/(1 + z_{\rm opt}) \geq 0.01$ between the X-ray and the good quality optical redshift, whilst only 3% deviate by more than $\Delta z/(1 + z_{\rm opt}) \geq 0.02$. Therefore, using the X-ray determined redshifts for the 42 clusters without optically spectroscopic redshifts seems to introduce no bias. The final redshift distribution is shown in the bottom panel of Fig. 3.2. Moreover, in the Appendix is further shown that using or not the clusters with X-ray redshifts one derives very similar results. The redshift distribution of our sample covers the $z = (0.003 - 0.45)$ range while the median redshift of the sample is $z = 0.075$ ($z = 0.072$ for the excluded clusters). All the aforementioned redshifts are heliocentric. The clusters for which we changed their z values compared to the ones from MCXC are displayed in Table 3.4 with a star (*) next to their names.

[2] R_{500}=the radius within which the mean density of the cluster is 500 times greater than the critical density of the Universe

Hydrogen column density

The value of $N_{\rm H}$ enters in both the determination of the $L_{\rm X}$ (as done in the parent catalogs) and in the T determination that is performed in this analysis. Hence, an inaccurate treatment of the input $N_{\rm H}$ values could potentially bias both parameters mostly in the opposite direction and eventually affect our results.

In the calculation of the $L_{\rm X}$ of every cluster, the REFLEX and NORAS catalogs used the neutral hydrogen $N_{\rm HI}$ values coming from Dickey et al. (1990) (thereafter DL90), while the (e)BCS catalog used again $N_{\rm HI}$ values but as given in Stark et al. (1992). As shown in Baumgartner et al. (2006) and Schellenberger et al. (2015) (S15 hereafter) the total hydrogen column density $N_{\rm Htot}$ (neutral+molecular hydrogen) starts to get significantly larger than $N_{\rm HI}$ for $N_{\rm HI} \geq 6 \times 10^{20}/{\rm cm}^2$. If this is not taken into account it would result in a misinterpretation of the total X-ray absorption due to Galactic material and hence to underestimating $L_{\rm X}$ while generally overestimating T. In order to account for this effect, we used the $N_{\rm Htot}$ values as given by Willingale et al. (2013) (hereafter W13) in all the spectra fittings we performed and for correcting the MCXC $L_{\rm X}$ values as described in the following subsections. The comparison between the $N_{\rm HI}$ used in the parent catalogs and the $N_{\rm Htot}$ values we use is displayed in Fig. 3.3.

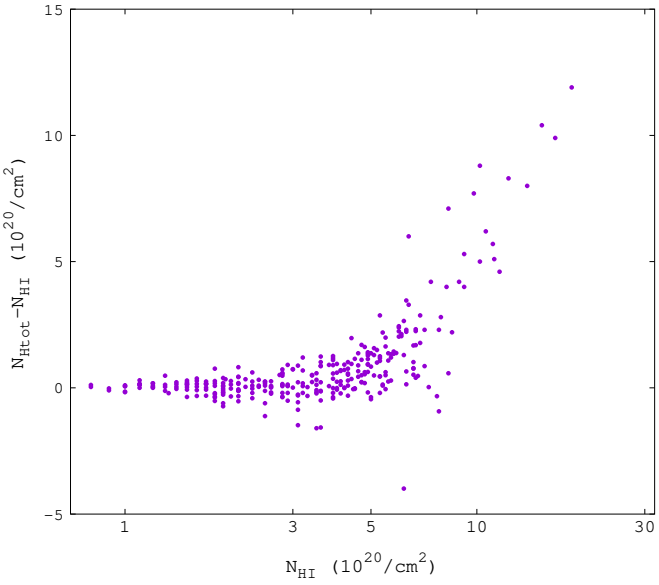

Figure 3.3: Comparison between the atomic hydrogen column density $N_{\rm HI}$ as given in DL90 and the total one $N_{\rm Htot}$ as given in W13 for the 313 clusters.

One can see that for certain clusters $N_{\rm Htot} < N_{\rm HI}$, something that seems counter-intuitive. This happens because in the calculation of $N_{\rm Htot}$, W13 use the $N_{\rm HI}$ from the LAB survey (Kalberla et al., 2005) and not from DL90. The LAB survey has a better resolution and tends to give slightly lower $N_{\rm HI}$ values than DL90 for the same sky positions, something that can create these small inconsistencies for clusters where the molecular hydrogen is not yet high enough. As stated above, we corrected these inconsistencies for all the 313 clusters. The LAB survey covers the velocity range of (−450 km/s, +400 km/s), within which all neutral hydrogen is supposed to be detected. This velocity range naturally propagates to the $N_{\rm Htot}$ values we use and any amount of hydrogen outside of this velocity range is not accounted for. The median $N_{\rm Htot}$ for the 313 clusters is $3.81 \times 10^{20}/{\rm cm}^2$ ($4.35 \times 10^{20}/{\rm cm}^2$ for the excluded clusters).

Luminosity

We chose to use *ROSAT* luminosity measurements for the simple reason that the entire R_{500} area of the clusters is observed in the RASS. On the contrary, the field of view (FOV) of *XMM-Newton* and (especially) *Chandra* does not cover the full R_{500} for most of our clusters[3]. It has been shown though that the *ROSAT* $L_{\rm X}$ values are fully consistent with the ones from XMM-Newton within the *ROSAT* $L_{\rm X}$ uncertainties (Böhringer et al., 2007; Y. .-.-Y. Zhang et al., 2011) (see Sect. 3.11 in Appendix for further tests)

Our estimates for the cluster X-ray luminosities used the reported X-ray luminosities in the MCXC catalog as a baseline. These luminosities were homogenized for systematics between the different parent catalogs, and were aperture-corrected to reflect the flux within R_{500} (for more details see Piffaretti et al. (2011), Chapter 3.4.1). For the relative luminosity uncertainty $\sigma_{L_{\rm X}}$ we assumed $\sigma_{L_{\rm X}} \sim \frac{1}{\sqrt{C_N}}$, where C_N is the RASS counts from the parent catalogs. We applied further corrections to the MCXC cluster luminosities.

Firstly, we calculated K-correction factors to account for the redshifted source spectrum when observed in the observer reference frame. We derived these factors in two iterative steps in XSPEC using the scaling relations by Reichert et al. (2011) for the input temperatures, and the 49 updated redshifts. The changes that occurred are much smaller than $\sigma_{L_{\rm X}}$. Secondly, the $L_{\rm X}$ values were adjusted accordingly for the 49 clusters for which we used new redshifts. The uncertainties of the fitted X-ray z (both statistical and intrinsic) were propagated to the $L_{\rm X}$ uncertainties and added in quadrature to the already existing ones. Next, we corrected the MCXC $L_{\rm X}$ for changes in the soft-band X-ray absorption by using the combined molecular and neutral hydrogen column density values as described in Sect. 3.2. We first derived an absorbed $L_{\rm X}$ by reversing the absorption correction from Piffaretti et al. (2011), and then derived updated unabsorbed $L_{\rm X}$ values in XSPEC employing the cluster temperatures and metallicities derived in this work. Finally, the redshift-derived distances of nearby clusters might be biased by peculiar velocities. For the five most nearby clusters ($50h^{-1}$ Mpc, $z \leq 0.0116$) we used redshift independent distance measurements from NED (published within the last 20 years) to derive the $L_{\rm X}$ from the unabsorbed, k-corrected flux. The standard deviation of these distance measurements was propagated to the uncertainty of the luminosity. The average change in the distance compared to the redshift distances is $\sim 7\%$. For one cluster (S0851), no redshift independent distance was available and thus we adopted the redshift-derived distance but added an uncertainty of 250 km/s[4] due to possible peculiar motions, which propagated in the $\sigma_{L_{\rm X}}$ as well.

The comparison between the MCXC $L_{\rm X}$ values and the values used in this analysis is shown in Fig. 3.4. As seen there, for 301 clusters (96% of the sample) the change in $L_{\rm X}$ is $\leq 25\%$. Since the intention of this paper is to look for spatial anisotropies of the $L_{\rm X} - T$ relation in the sky we need to ensure that we do not introduce any directional bias through all of our $L_{\rm X}$ corrections. To this end, we compare the fraction $L_{\rm X,ours}/L_{\rm X,MCXC}$ (the latter is the value given by MCXC) throughout the sky and we find it to be consistent within $\pm 4\%$. Similar results are obtained if one considers the fraction $L_{\rm X,MCXC}/L_{\rm X,parent}$, where $L_{\rm X,parent}$ is the value given in the parent catalogs (more details in Sect. 3.11 of the Appendix).

The final $L_{\rm X}$ range of the clusters we use is $L_{\rm X} = (1.15 \times 10^{42} - 3.51 \times 10^{45})$ erg/s while the median value is 1.45×10^{44} erg/s (1.10×10^{44} erg/s for the excluded objects). The median $\sigma_{L_{\rm X}}$ is 10.6%.

[3] For this particular study, another advantage of using *ROSAT* measurements is that we excluded the possibility of a *XMM-Newton*-related anisotropic bias, since such anisotropies have already been detected for XCS-DR1, a sample constructed purely by *XMM-Newton* observations (see M18).

[4] Average difference between recession velocity as obtained by redshift-independent distances and measured heliocentric velocities for the other four clusters.

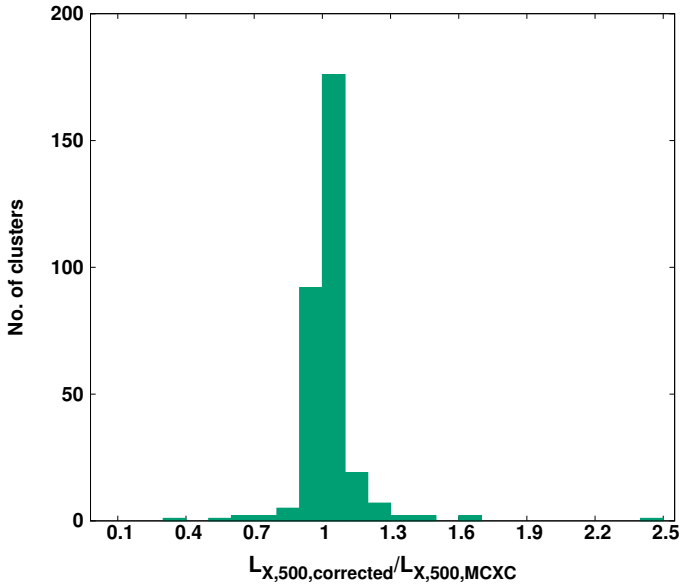

Figure 3.4: Comparison between the L_X values after all the corrections we applied and the MCXC values for the 313 clusters.

Cluster radius

The radii of the clusters were used for selecting the region within which the temperature and metallicity were measured. The R_{500} values of the clusters as given in MCXC were determined using the MCXC L_X value and the X-ray luminosity-mass scaling relation $L_X - M$ as given in M. Arnaud et al. (2010), which results in $L_X \sim R_{500}^{4.92}$. Since we applied certain changes to the MCXC L_X values it is expected that also the respective R_{500} should (slightly) change. Therefore, we used the same scaling relation to calculate the new R_{500} in Mpc units. After that, the appropriate conversion to arcmin units was required, using the angular diameter distance (D_A). Since there is only a weak R_{500} dependency on L_X when the latter changes only because of alternations in the N_H absorption, the new R_{500} value does not significantly differ from the MCXC one (all changes $\leq 5\%$, since D_A remains fixed). However, when L_X changes because of a modification in the used z value then also D_A changes, as well as the normalized Hubble parameter $E(z) = [\Omega_m(1+z)^3 + \Omega_\Lambda]^{1/2}$ and the critical density of the Universe $\rho_c(z)$,which are also included in the $L_X - R_{500}$ relation. This has a stronger impact on the final R_{500}^{arcmin} (R_{500} in arcmin units) than the absorption case alone. Nonetheless, the new R_{500}^{arcmin} eventually changes by more than 10% only for 5 out of 313 clusters. At the same time, 294 clusters (> 94% of the sample) show a $\leq 4\%$ relative change in R_{500}^{arcmin}. Therefore, the direct use of the MCXC R_{500}^{arcmin} values is practically equivalent to our new values.

Temperature

We determined the temperature of each cluster within the $0.2 - 0.5$ R_{500} annulus of every cluster in order to have self-consistent temperature measurements that reflect the other cluster properties (e.g., L_X) in a similar way. The cores of the clusters are excluded due to the presence of cool-cores, which significantly bias the temperature measurement and potentially increase the scatter of the $L_X - T$ relation (e.g., D. S. Hudson et al., 2010). As previously stated, here we used the N_{Htot} values in order to fit the spectra and obtain T. Since the new R_{500} values do not considerably vary compared to the MCXC

ones, we used the latter for the spectra extraction with one exception: when the difference between the two values was > 10% (only five clusters as stated above) then we used the redetermined R_{500} value. Generally, the temperature shows only a weak dependance to such small changes in R_{500} since the vast majority of the spectral extraction regions remains unchanged. The relative difference in the obtained temperature for these five clusters when we use both ours and the MCXC R_{500} is by average $\sim 8\%$.

It has been shown that the Chandra and *XMM-Newton* telescopes have systematic differences in the constrained temperature values for the same clusters (S15). Thus, one has to take into account these biases when using temperature measurements from both telescopes. To this end, for the 76 clusters in our sample for which we use *XMM-Newton* data since we do not have *Chandra* data, we converted their measured temperatures to *Chandra* temperatures adopting the conversion relation found in S15. To further check the consistency of this conversion, we applied this test ourselves choosing 15 clusters in an *XMM-Newton* temperature range of $1.2-8.5$ keV (same range as for the 76 *XMM-Newton* clusters) which have been observed by both telescopes. We constrained their temperatures with both instruments and we find that the best-fit relation provided by S15 still returns satisfactory results (Fig. 3.32 in Appendix). The final temperature range of these 313 clusters is $T = (0.83 - 19.24)$ keV with the median value being $T = 4.5$ keV, while the median uncertainty is $\sigma_T = 4.9\%$. Clearly the temperature range is considerably wide which significantly helps the purposes of our study. The suspiciously high temperature of 19.23 keV occurs for the galaxy cluster Abell 2163 (A2163) when the Asplund et al. (2009) abundance table is used. A2163 also lies in a high absorption region with $N_{\rm Htot} = 2 \times 10^{21}/{\rm cm}^2$. For other abundance tables, A2163 returns a temperature of $\sim 13 - 16$ keV. This large difference is mainly driven by the *phabs* absorption model and the change of the Helium and Oxygen abundances. Generally, the average difference between the obtained temperature values between different abundance tables do not vary by more than $\sim 3-5\%$ and thus, this cluster is a special case. For consistency reasons we use the 19.23 keV value. Excluding this cluster from the sample does not affect our results significantly since it is not an outlier in the $L_{\rm X} - T$ plane.

Metallicity

The metallicity of each cluster was determined simultaneously with the temperature. The two different telescopes are not shown to give systematically different metallicity values for the same clusters (although the intrinsic scatter of the comparison is relatively large), and thus no conversion between the *XMM-Newton* and *Chandra* values was needed. The metallicity range of the used sample is $Z = (0.04-0.87)\, Z_\odot$ except for two clusters with $Z = 1.53^{+1.50}_{-1.07}\, Z_\odot$ and $Z = 3.86^{+0.61}_{-0.71}\, Z_\odot$, where the metallicity determination of the latter is clearly inaccurate while the former is consistent with typical metallicity values within the 1σ uncertainties. Excluding these two clusters from our analysis has no significant effects on the derived results. Finally, the median value is $Z = 0.37\, Z_\odot$ with the median uncertainty being $\sigma_Z = 23.1\%$

3.3 Data reduction and spectral fitting

Data reduction

The exact data reduction process slightly differs for the two instruments. For the *Chandra* analysis, we followed the standard data reduction tasks using the CIAO software package (version 4.8, CALDB 4.7.6). A more detailed description is given in Schellenberger et al. (2017) (S17). For the *XMM-Newton* analysis, we followed the exact same procedure as described in detail by R19 (and more analytically in Chapter 2). In a nutshell, every observation was treated for solar flares, anomalous state of CCDs (Kuntz et al., 2008), instrumental background and exposure correction. For both instruments, the X-ray emission peak was

determined and used as the centroid for the spectral analysis[5], while bright point sources (AGNs and stars), extended structures unrelated to the cluster of interest (e.g., background clusters) and extended substructure sources were masked automatically and later by hand in a visual inspection. For this analysis, the HEASOFT 6.20, XMMSAS v16.0.0 and XSPEC v12.9.1 software packages were used.

Background modeling

For the *Chandra* clusters, complementary to the S17 process, the ROSAT All-Sky survey maps in seven bands (Snowden et al., 1997) were used to better constrain the X-ray background components. The background value in each of the seven bands was determined within $1^\circ - 2^\circ$ around the cluster.

For the *XMM-Newton* clusters, the only difference with the process described in R19 is the background spectra extraction region. The X-ray sky background was obtained when possible, from all the available sky region in the FOV outside of 1.6 R_{500} from the cluster's center. In this case, no cluster emission residuals were added in the background modeling. This was done mostly for the clusters located at $z \gtrsim 0.1$ which have a small apparent angular size in the sky. For most clusters, a partial overlap of the background extraction area with the 1.6 R_{500} circle is inevitable and thus, an extra *apec* component to account for the cluster emission residuals was added during the spectral fitting, with its temperature and metallicity free to vary. The normalizations of the background model components were also left free to vary during the cluster spectra fitting as described in detail in R19.

Spectral fitting

For the spectral fitting, the same methods were used as in R19 (*apec*×*phabs*+emission and fluorescence lines) with only some small differences which are described here. Firstly, the $0.7 - 7$ keV energy range was used for all spectral fittings for both instruments. This way we managed to exclude the emission lines close to 0.6 keV which originate from the Solar Wind Charge Exchange and cosmic X-ray background (S15, R19 and references therein). Moreover, we avoid the events produced by the fluorescent lines at 7.5, 8 and 8.6 keV which appear in the spectra of the pn detector of *XMM-Newton*. Furthermore, *Chandra* has a small effective area for energies higher than 7 keV. For all the spectral fits the Asplund et al. (2009) abundance table was used. Finally, for the 237 *Chandra* clusters the best-fit parameters of the spectral model were determined from an MCMC chain within XSPEC, while for the 76 *XMM-Newton* clusters the χ^2-statistic was used.

3.4 The $L_X - T$ scaling relation

For obtaining the best-fit values of the $L_X - T$ relation parameters and comparing them for clusters located in different directions in the sky, we use a similar approach to M18. Here the strong dependance of the L_X on the cosmological parameters should be stressed again, combined with the fact that T can be measured without any cosmological assumptions (see Appendix for the exact R_{500} and T dependance on the chosen cosmology).

3.4.1 Form of the $L_X - T$ scaling relation

We adopt a standard power-law form of the $L_X - T$ scaling relation as shown below:

[5] Good agreement with MCXC for the vast majority of clusters.

$$\frac{L_{\rm X}}{10^{44}\ {\rm erg/s}}\ E(z)^{-1} = A \times \left(\frac{T}{4\ {\rm keV}}\right)^{B}, \tag{3.1}$$

where the term $E(z) = [\Omega_{\rm m}(1+z)^3 + \Omega_\Lambda]^{1/2}$ scales $L_{\rm X}$ accordingly to account for the redshift evolution of the $L_{\rm X} - T$ scaling relation. The scaling of the temperature term was chosen to be close to the median $T = 4.5$ keV. The exact constant scaling of the $L_{\rm X}$ values (10^{44} erg/s) is not important since it is only a multiplication factor of the normalization. The exact scaling correction for the redshift evolution of the $L_{\rm X} - T$ relation [$E(z)$] is also not particularly significant for consistent redshift distributions and low-z samples like our own, as discussed later in the paper. In order to constrain the best-fit parameters the χ^2-minimization method is used and applied to the logarithmic form of the $L_{\rm X} - T$ relation,

$$\log L'_X = \log A + B \log T'. \tag{3.2}$$

Here, $L'_{\rm X}$ and T' are defined as

$$L'_{\rm X} = \frac{L_{\rm X}}{10^{44}\ {\rm erg/s}}\ E(z)^{-1} \quad \text{and} \quad T' = \frac{T}{4\ {\rm keV}}. \tag{3.3}$$

3.4.2 Linear regression

The exact form of the χ^2-statistic used to find the best-fit A, B, $\sigma_{\rm int}$ and H_0 values is given by

$$\chi^2_L = \sum_{i=1}^{N} \frac{\left(\log\left[L'_{\rm X,obs}\right] - \log\left[L'_{\rm X,th}(T', \mathbf{p})\right]\right)^2}{{\sigma_{\log L,i}}^2 + B^2 \times {\sigma_{\log T,i}}^2 + {\sigma_{\rm int}}^2}, \tag{3.4}$$

where N is the number of clusters used for the fit, $L'_{\rm X,obs}$ and T' are the measured luminosity and temperature values respectively (scaled as explained above), $L'_{X,\rm th}$ is the theoretically expected value for the luminosity based on the measured temperature in addition to the fitted parameters $\mathbf{p}$ (A and B, or H_0). Furthermore, $\sigma_{\log L,T,i}$ are the Gaussian logarithmic uncertainties which are derived in the same way as in M18 [6], while $\sigma_{\rm int}$ (which was not included in M18) accounts for the intrinsic scatter of the relation.

The latter is fitted iteratively, starting from 0 and increasing step-by-step until there is a combination of $\mathbf{p}$ that gives $\chi^2_{\rm red} \sim 1$, as in Maughan (2007), Maughan et al. (2012) and and Zou et al. (2016) etc. Under certain conditions, this procedure might return slightly underestimated $\sigma_{\rm int}$ values. However, this should not be a concern since the exact values of $\sigma_{\rm int}$ are not of particular importance for this analysis and they are only used to derive trustworthy parameter uncertainties from our χ^2 model.

Additionally, the 1σ uncertainties of the fitted parameters are based on the standard $\Delta\chi^2 = \chi^2 - \chi^2_{\rm min}$ limits ($\Delta\chi^2 \leq 1$ or 2.3 for one or two fitted parameters respectively). In the case of the slope being free to vary, the projection of the x-axis uncertainties to the y-axis also varies. This fitting method is comparable to the BCES Y|X fitting method described by Akritas et al. (1996).

Finally, we should stress that H_0 and A cannot be simultaneously constrained since they are degenerate. One can put absolute constraints only on the product $A \times H_0^2$. Therefore, one needs to fix one of the parameters to investigate the behavior of the other. In Sect. 4.4 we use a fixed $H_0 = 70$ km s^{-1}Mpc^{-1} to investigate the behavior of A. In Sect. 3.7 we fix A to its best-fit value and study the directional behavior of H_0 through the χ^2-minimization procedure described above[7].

[6] $\sigma_{\log x} = \log(e) \times \frac{x^+ - x^-}{2x}$, where x^+ and x^- are the upper and lower limits of the main value x of a quantity, considering its 68.3% uncertainty.

[7] This is equivalent to directly converting A values to H_0 values, since the product $A \times H_0^2$ remains unchanged.

3.4.3 Pinpointing anisotropies via sky scanning

With the purpose of studying the consistency of the fitted parameters throughout the sky and identifying specific sky patches that seem to show a significantly different behavior than the rest, we follow the method described below. We consider a cone of a given radius θ (we use $\theta = 45^\circ, 60^\circ, 75^\circ$ and 90°) and we only consider the clusters that lie within this cone. For instance, if we choose a $\theta = 60^\circ$ cone centered at $(l, b) = (150^\circ, 30^\circ)$ then the subsample of clusters consists of all the clusters with an angular separation of $\leq 60^\circ$ from these specific coordinates. By fitting the $L_X - T$ scaling relation to these clusters, we obtain the normalization (or H_0), slope and intrinsic and total scatter for these clusters. The extracted best-fit value for the fitted parameter is assigned at these coordinates.

Shifting this cone throughout the full sky in steps of $\Delta l = 1^\circ$ and $\Delta b = 1^\circ$ in Galactic coordinates[8], we can obtain the desired parameter values for every region of the sky. We additionally apply a statistical weighting on the clusters based on their angular separation from the center of the cone. This is given by simply dividing their uncertainties by $\cos\left(\frac{\theta_1}{\theta} \times 90^\circ\right)$, where θ_1 is the above-mentioned angular separation. Hence, the weighting cos term is calibrated in such way that it shifts from 1 to 0 as we move from the center of the cone to its boundaries, independently of the angular size of the cone. This enlargement of the uncertainties results in an artificial decrease of the $\sigma_{\rm int}$ which is not of relevance here since, as explained before, $\sigma_{\rm int}$ mostly acts as a nuisance parameter. Nevertheless, we perform tests to ensure this does not bias our results, as explained in 3.9.2.

All the A maps are plotted based on the A/A_{all} value, where A_{all} is the best-fit A when all the clusters are used independently of the direction. Finally, the maps have the same color scale for easier comparison, except for the $\theta = 45^\circ$ cone maps for which the color scale is enlarged for better visualization.

3.4.4 Statistical significance and sigma maps

With the desired best-fit values and their uncertainties for every sky region at hand, it is easy to identify the direction that shows the most extreme behavior and assess the statistical significance of their deviation. For quantifying the latter in terms of number of sigma for two different subsamples we use:

$$\text{No. of } \sigma = \frac{\mathbf{p_1} - \mathbf{p_2}}{\sqrt{\sigma^2_{\mathbf{p_1}} + \sigma^2_{\mathbf{p_2}}}}, \tag{3.5}$$

where $\mathbf{p_{1,2}}$ are the best-fit values for the two different subsamples and $\sigma^2_{\mathbf{p_{1,2}}}$ are their uncertainties[9].

Each time we constrain the anisotropic amplitude of the most extreme dipole in the sky, while we also compare the two most extreme regions in terms of the fitted parameter, regardless of their angular separation. This is done by calculating the statistical deviation (in terms of σ) between all the different cone subsamples. The two sky regions for which the largest deviation (highest no. of σ) is found between them, are the ones reported in the following sections as "the most extreme regions". In addition, a percentage value (%) is displayed next to each σ deviation. This value comes from the difference of these two extreme regions over the best-fit value for the full sample.

In order to create the significance maps, we use Eq. 4.7 to compare the best-fit result $\mathbf{p_1}$ of every cone with the best-fit result $\mathbf{p_2}$ of the rest of the sky. The obtained sigma value is assigned to the direction at

[8] $360 \times 181 = 65160$ different cones

[9] This formulation assumes that $\mathbf{p_1}$ and $\mathbf{p_2}$ are independent, which is true when the two subsamples do not share any common clusters. This is mostly the case for our results with few exceptions of $\lesssim 10\%$ common clusters between some compared subsamples. However, this does not significantly affect the significance especially when one considers that the weighting of these clusters is different for each subsamples based on their distance from the center of the cone.

the center of the cone. All the significance maps have the same color scale for easier comparison. For the majority of cases, the two most extreme regions as defined above match the highest σ regions in the significance maps.

Finally, as an extra test we also create 10^5 realizations using the bootstrap resampling method in order to check the probability of the extreme results to randomly occur independently of the sky direction. The followed procedure is described in detail in Sect. 3.9.2. Using all these estimates, one can determine the consistency with what one would expect in an isotropic universe.

3.5 Results

3.5.1 The $L_X - T$ scaling relation for the full sky

Before we search for apparent anisotropies in the sky we constrain the behavior of the $L_X - T$ scaling relation for the full sample. We do not account for any selection biases in our analysis since we believe that their effects are not important for this work. This is because we wish to study the *relative* $L_X - T$ differences between different sky regions (or from the overall best-fit line). If we indeed corrected for selection effects we would constrain the "true" underlying $L_X - T$ relation which would not represent our data (but the true distribution). This might cause wrong estimates for the relative $L_X - T$ differences. Therefore, we need to constrain the relation that describes our 313 clusters best. Nevertheless, in Sect. 3.6.4 we discuss the possible effects of selection systematics and find that there is no indication that they compromise our results.

We use the aforementioned 313 clusters and fit Eq. (3.1) obtaining the best-fit normalization and slope of the $L_X - T$ relation as well as its intrinsic scatter. The results are:

$$A_{\rm all} = 1.114^{+0.044}_{-0.040},\ B_{\rm all} = 2.102 \pm 0.064,\ \text{and}\ \sigma_{\rm int} = 0.242\ \text{dex}. \tag{3.6}$$

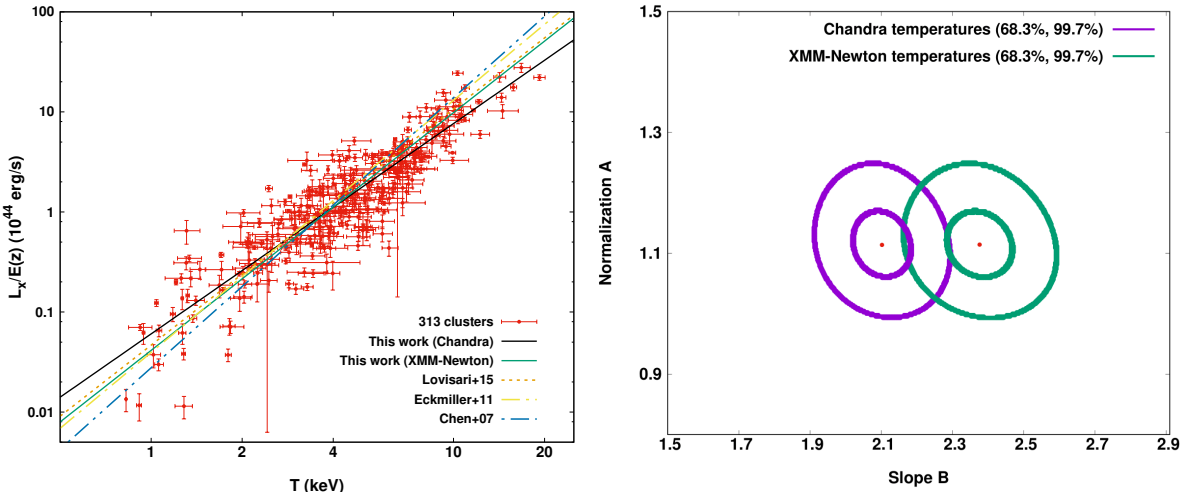

Figure 3.5: *Top*: $L_X - T$ relation for the 313 clusters (red) with their best-fit model (black). L_X is measured within the 0.1 − 2.4 keV energy range. The best-fit models of other studies are displayed as well (dashed lines). The best-fit solution when *XMM-Newton* temperatures are used is shown as well (solid green). *Bottom*: 1σ (68.3%) and 3σ (99.7%) confidence levels of the normalization and slope of the $L_X - T$ relation as derived using *Chandra*- or *XMM-Newton*-converted temperatures for all 313 clusters (purple and green respectively). As shown the best-fit values for the same data can shift by $\sim 3\sigma$ depending on the instrument used.

The statistical uncertainties for A and B are limited to $\sim 3-4\%$ which highlights the precision of our results based on the number and the quality of the data, combined with the large covered temperature range of the clusters. Moreover, the total scatter (statistical+intrinsic) of the $L_X - T$ is $\sigma_{\rm total} = 0.262$ dex, which means that the statistical uncertainties of the clusters contribute to only 7% of the total scatter. The $L_X - T$ fit of our sample is displayed in Fig. 3.5 (top panel).

The best-fit slope is slightly steeper than the expected value from the self-similar model. Naively, the slope best-fit value (~ 2.1) might seem surprising since most studies find a $L_X - T$ slope of $B \sim 2.3-3.6$ (see references in Sect. 3.1). However, the exact value depends on multiple aspects such as the energy range for which L_X was measured, the instrument used, the sample selection (when no bias correction is applied), the temperature distribution of the used sample, the cluster radius within which parameters were measured etc. Generally, it is expected that bolometric L_X values return a steeper slope than soft band L_X values, such as the $0.1-2.4$ keV band we use. This happens due to the fact that the bolometric emissivity ϵ of the ICM for thermal bremsstrahlung (which is the dominant emission process for $T \gtrsim 3$ keV) is $\epsilon \propto n_e^2 T^{0.5}$ (where n_e is the electron density), while ϵ in the soft band (0.1-2.4 keV as used here) is rather independent of T for $T \gtrsim 3$ keV ($\epsilon \propto n_e^2$). Therefore, one very roughly expects the slope of the $L_X - T$ relation to be smaller by ~ 0.5 in the 0.1-2.4 keV band; that is $L_X \sim T^{1.5}$ in the self-similar case. In general, the best-fit $L_X - T$ relation tends to change slightly when one corrects for selection biases (see references in Sect. 3.1 about the $L_X - T$ relation).

If we now convert all the measured temperatures to *XMM-Newton* temperatures[10] using the relation given in S15, we obtain a slope of $B \sim 2.38$, shifting by 2.8σ compared to our main result, while the normalization remains the same. This result is consistent with the previously reported values that used the 0.1-2.4 keV luminosities (e.g., Chen et al., 2007; Eckmiller et al., 2011; Lovisari et al., 2015)[11]. In the bottom panel of Fig. 3.5 the 68.3% and 99.7% confidence levels (1 and 3σ respectively) of the fitted parameters are shown for *Chandra*-converted temperatures and *XMM-Newton*-converted temperatures. It should be clear that this is done just for the sake of comparison and that the *Chandra* temperatures are used for the rest of the paper.

A comparison between our results and the derived $L_X - T$ scaling relation from other works is also shown in the top panel of Fig. 3.5. We note that L_X corresponds to the $0.1-2.4$ keV energy band for all the compared studies, while the results from the BCES (Y|X) fitting method were used when available. Additionally, the $L_X - T$ results for the full samples were used without any bias corrections. From this comparison, it is clear that all the derived results agree in the $L_X - T$ normalization value. In terms of the slope, our *Chandra* fit is more consistent with the high-T part of the distribution, while our *XMM-Newton* fit is quite similar to the results of Eckmiller et al. (2011) and Lovisari et al. (2015).

3.5.2 1-dimensional anisotropies

As a first test for the potentially anisotropic behavior of our galaxy cluster sample, we recreate the normalization against the Galactic longitude plot as presented in M18 (Fig. 3 in that paper). For this test, we consider regions centered at l with a width of $\Delta l = 90^o$. At the same time, the whole Galactic latitude range $b \in (-90^\circ, +90^\circ)$ is covered by every region.

Firstly, we allow both A and B to vary simultaneously. The behavior of these two parameters as functions of the Galactic longitude are displayed in Fig. 3.6. One sees that the slope remains relatively

[10] The measurements of the 76 *XMM-Newton* clusters are kept as they are while the measurements of the 237 *Chandra* clusters are converted to *XMM-Newton* temperatures based on S15.

[11] For Lovisari+15 we display the bias-uncorrected result when all the clusters and the Y|X fitting procedure are used. For Eckmiller+11 the shown result is for all the available clusters as well. The result from Chen+07 uses all the clusters and the hot temperature component as the T value.

constant throughout the sky, varying only by 18% from its lowest to highest value, and with a relatively low dispersion. Also, the largest deviation between any two independent sky regions is limited to 1.8σ. No obvious systematic trend in the slope as a function of the galactic longitude can be seen since all the regions return slope values consistent with the full sample at $\leq 1.2\sigma$. At the same time, this variation for the normalization reaches 31% with a higher dispersion and a clear trend with galactic longitude, while the strongest tension between two independent sky regions appears to be 3.2σ.

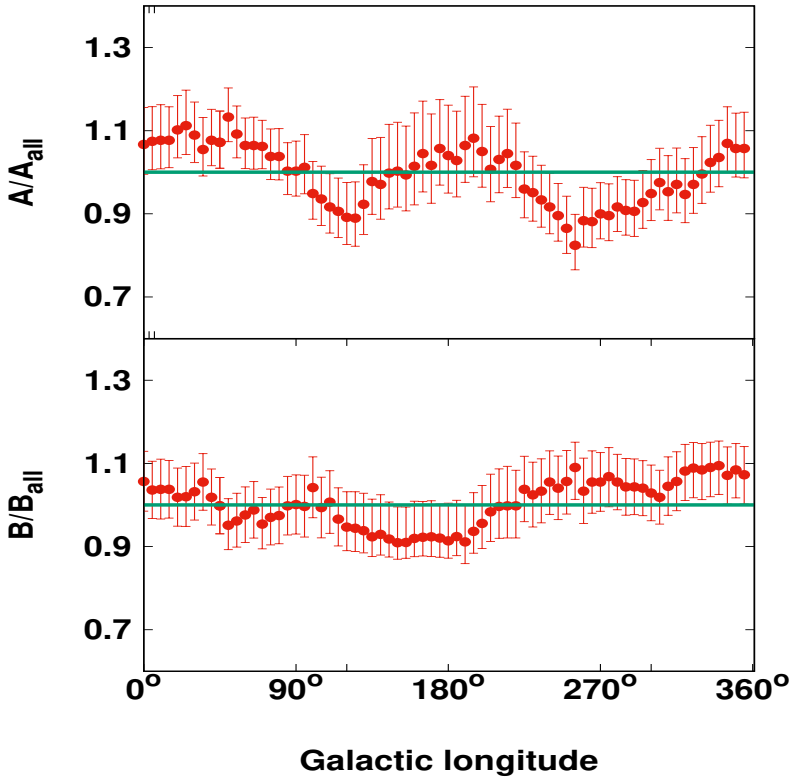

Figure 3.6: Best-fit normalization A (top) and slope B (bottom) of the $L_X - T$ relation for every sky region over the best-fit results for the full sample (A_{all} and B_{all}) as functions of the Galactic longitude. The 1σ (68.3%) uncertainties are also shown. Every region covers a sky area of $\Delta l = 90^\circ$ and $\Delta b = 180^\circ$. The x-axis values represent the central l value for every bin.

Based on these results, the slope is kept fixed at the best-fit value for the whole sample and only the normalization of the $L_X - T$ relation is free to vary. In the top left panel of Fig. 3.7 the best-fit normalization value A for every region is displayed with respect to the best-fit A_{all} for the full sky (all 313 clusters). The same is also done for ACC and XCS-DR1 with the results displayed in the top and bottom left panels of Fig. 3.7 respectively. The only difference with the M18 results for these two samples is that here the intrinsic scatter term is taken into account as well during the fitting as shown in Eq. 4.5.

Surprisingly enough, the pattern in the behavior of the $L_X - T$ normalization for our sample strongly resembles the results of both ACC and XCS-DR1, despite being almost independent with XCS-DR1, sharing only $\sim 30\%$ of the clusters with ACC and following different analysis strategies. Specifically, the region with the most anisotropic behavior compared to the rest of the sky (2.9σ significance) is the one with the lowest A lying within $l \in [210^\circ, 300^\circ]$. This region exactly matches the findings of M18 for XCS-DR1, while the lowest A region for ACC is separated by 40°. Here we should remind the reader that

the 313 clusters we use share only three common clusters with XCS-DR1 and 104 with ACC as these samples were used in M18. The opposite most extreme behavior (highest A) is detected in $l \in [-20^\circ, 70^\circ]$ (same brightest region in ACC as well, 25° away from XCS-DR1's brightest region) with a deviation of 2.5σ compared to the rest of the sky and 3.4σ compared to the lowest-A region, which is similar to the two other samples.

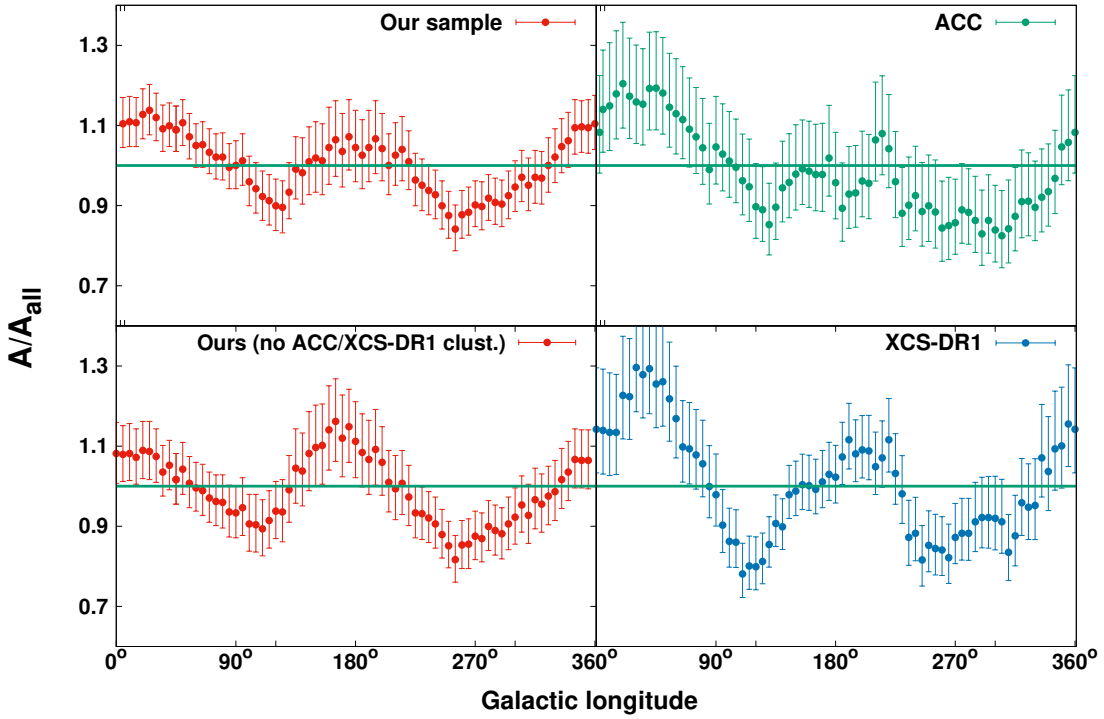

Figure 3.7: Best-fit normalization A of the $L_X - T$ relation for every sky region over $A_{\rm all}$ as a function of the Galactic longitude. The 1σ (68.3%) uncertainties are also shown. The results correspond to this work's sample (top left), ACC (top right), this work's sample excluding all the common clusters with ACC and XCS-DR1 (bottom left) and XCS-DR1 (bottom right).

In order to verify that the observed behavior is not caused by the few common clusters between our sample and ACC or XCS-DR1, we exclude all 104 of them from our sample and repeat the analysis. The result is shown in the bottom left panel of Fig. 3.7. One can see that this systematic trend persists and does not significantly depend on the common clusters between the two samples. The region with the largest deviation from the rest of the sky remains the same as for the full sample with an even higher significance of 3.1σ. This striking similarity between the three different samples in the 1D search for anisotropies should be investigated in more depth in order for its exact reason to be identified.

3.5.3 2-dimensional anisotropies

In order to identify the exact regions with the highest degree of anisotropy, we should consider every possible direction in the sky. Different size regions should be considered as well, thus systematic behaviors can be detected. To this end, we use scanning cones (solid angles), as described in Sects. 3.4.3 and 3.4.4. The slope is fixed to the best-fit value since the variations of the normalization are much

stronger. This choice does not bias our results, as shown in Sect. 3.6.5.

$\theta = 90^\circ$ cone

To begin with, we choose a scanning cone with $\theta = 90^\circ$, meaning we divide the sky in all the possible hemisphere[12] combinations. The lowest number of clusters in any hemisphere is 109 toward the $(l, b) = (150^\circ, -2^\circ)$ direction, with 204 clusters located in the opposite hemisphere. Constraining A for every hemisphere, one obtains the A and significance color maps displayed in the top left panels of Fig. 3.8 and Fig. 3.9 respectively.

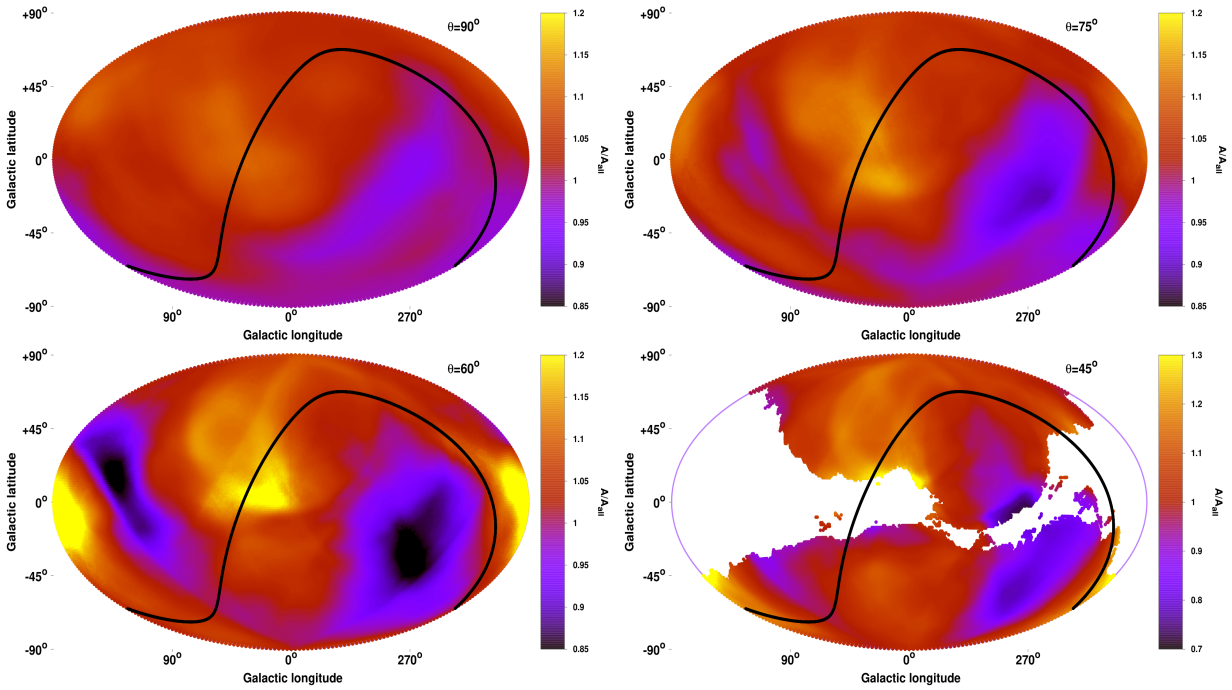

Figure 3.8: Best-fit normalization A of the $L_X - T$ relation for every sky region over A_{all} as a function of the position in the extragalactic sky. The maps are created with cones of $\theta = 90^\circ$ (top left), $\theta = 75^\circ$ (top right), $\theta = 60^\circ$ (bottom left) and $\theta = 45^\circ$ (bottom right, only region with ≥ 35 clusters are shown). The first three maps have the same color scale (85% − 120%), while the $\theta = 45^\circ$ map has a wider color scale (70% − 130%).

As shown in the plots, there is mainly one low A region within $\sim 20^\circ$ from $(l, b) \sim (270^\circ, -5^\circ)$ with a rather strong behavior. There is also one high A peak. It is noteworthy that the two most extreme regions in the map (deep purple and bright yellow) are located close to the Galactic plane (within $\sim 20^\circ$), where there are no observed clusters. The clusters toward the Galactic center in particular seem to be overluminous compared to other sky regions. Of course the color differences are not visually strong here since the color scale was chosen based on the largest deviations, appearing in later maps.

In detail, the most extreme hemispheres are found at $(l, b) = (272^\circ, -8^\circ)$ with $A = 1.062 \pm 0.048$ and at $(l, b) = (47^\circ, +22^\circ)$ with $A = 1.236 \pm 0.047$. The angular separation between them is 135° while they deviate by 2.59σ $(16 \pm 6\%)$ from each other. Although they are not completely independent, the contribution of the common clusters is not the same to both subsamples due to the applied statistical weighting based on the distance of every cluster from the center of the cone. The most extreme dipole (2 independent subsamples separated by 180° in the sky) appears at $(l, b) = (230^\circ, -20^\circ)$ with a significance

[12]Where by "hemisphere" we mean any half of the sky and not "Northern", "Southern" etc.

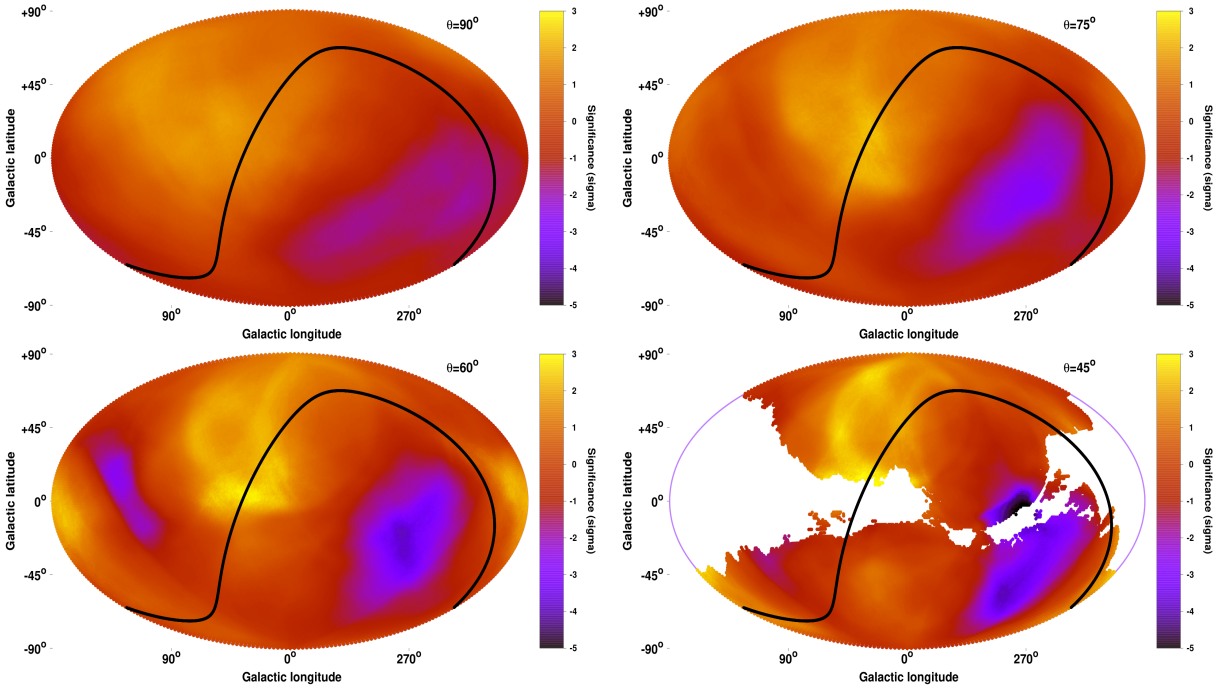

Figure 3.9: Statistical significance of the deviation of every sky region compared to the rest of the sky as a function of the position in the extragalactic sky. The maps are created with cones of $\theta = 90^\circ$ (top left), $\theta = 75^\circ$ (top right), $\theta = 60^\circ$ (bottom left) and $\theta = 45^\circ$ (bottom right, only regions with ≥ 35 clusters are shown). The value of every point is extracted by using all the clusters in the same cone. All maps have the same color scale $(-5\sigma, 3\sigma)$. The minus ("-") sign indicates that the corresponding sky region has a lower A than the rest of the sky.

of 1.90σ. This dipole is separated by 75° from the CMB dipole, although a dipole interpretation is obviously not reflecting the maximum apparent anisotropies in that case.

$\theta = 75^\circ$ cone

If an anisotropy toward one direction exists, the clusters lying close to that direction would be the most affected ones and as we move further away from that direction, the anisotropic effect on clusters would fade. Therefore, such anisotropic behaviors are better studied if one uses smaller solid angles in the sky. To this end, we decrease the radius of the scanning cone first to $\theta = 75^\circ$. Indeed, the fluctuations of A as well as the significance of the anisotropies increase, while the general behavior of the directional anisotropies in the $\theta = 75^\circ$ map however remains relatively unchanged compared to the previous map with a larger cone. The results are displayed in the top right panels of Fig. 3.8 and Fig. 3.9.

For the $\theta = 75^\circ$ cones, A varies from $A = 0.999 \pm 0.050$ at $(l, b) = (274^\circ, -22^\circ)$ to $A = 1.288 \pm 0.061$ toward $(l, b) = (17^\circ, -9^\circ)$. These two regions are separated by 99° and deviate from each other by 3.64σ $(26 \pm 7\%)$. Furthermore, the most significant dipole that appears is the one centered at $(l, b) = (263^\circ, -21^\circ)$ at 3.22σ, 68° away from the CMB dipole.

$\theta = 60^\circ$ cone

Further decreasing the size of the solid angles, we use $\theta = 60^\circ$ cones. We see that the behavior of the sky regions suffers some changes whilst staying generally consistent with the previous results. The most prominent change is the existence of a low A region close to $(l, b) \sim (120^\circ, +20^\circ)$, although its

statistical significance (as displayed in Fig. 3.9) is lower than the other, main low A region since it only contains ~ 45 clusters. Another change in the 60° map is that the brightest part of the sky is shifted toward $(l, b) \sim (170^\circ, -10^\circ)$. However, as one can clearly see in Fig. 3.9, the most statistically significant region with a high normalization remains in the same area as in the previous cases, namely toward $(l, b) = (34^\circ, +4^\circ)$ with 78 clusters and $A = 1.346 \pm 0.069$.

At the same time, the lowest normalization value $A = 0.940 \pm 0.051$ is located at $(l, b) = (281^\circ, -16^\circ)$ (84 clusters). The most extreme regions deviate from each other by 4.73σ ($36 \pm 8\%$), which constitutes a considerably strong tension. The most extreme dipole in this case is found toward $(l, b) = (260^\circ, -36^\circ)$ with a statistical significance of 3.77σ.

If we now exclude these two most extreme low and high A regions and their 159 individual clusters from the rest of the sky, we are left with 154 clusters. Performing the fit on these clusters, we obtain $A = 1.138 \pm 0.048$. We see that the rest of the sky is at a 2.49σ tension with the bright region toward $(l, b) = (34^\circ, +4^\circ)$, and at a 2.85σ tension with the faint region toward $(l, b) = (281^\circ, -16^\circ)$. Thus, the anisotropic behavior of the faint region is somewhat more statistically significant than the behavior of the bright region.

$\theta = 45^\circ$ cone

The last cone we use has $\theta = 45^\circ$. Since there are many regions mostly close to the Galactic plane, with fewer clusters than needed in order to obtain a trustworthy result, we enforce an extra criterion. We only consider regions with ≥ 35 clusters[13]. The A and σ maps are shown in the bottom right panels of Fig. 3.8 and Fig. 3.9 respectively. The white regions show the regions without enough clusters for a reliable fit. The most extreme regions are found toward $(l, b) = (280^\circ, +1^\circ)$ (42 clusters) and $(l, b) = (32^\circ, +14^\circ)$ (40 clusters) with $A = 0.822 \pm 0.067$ and $A = 1.413 \pm 0.095$. The statistical discrepancy between the rises to 5.08σ ($53 \pm 10\%$) being the most statistically significant result up to now.

Additionally, the most extreme dipole is centered at $(l, b) = (255^\circ, -53^\circ)$ with a significance of 4.22σ. However, it should be beared in mind that many regions that appeared to have the maximum dipoles for other cones are excluded now due to low number of clusters. This could lead the maximum dipole to shift toward lower Galactic latitudes on the low normalization side. Moreover, due to the low number of clusters in these regions the results are more sensitive to outliers, especially when these outliers are located close to the center of the regions where they have more statistical weight than other clusters. Nevertheless, the large statistical tension cannot be neglected.

Excluding once again the two extreme regions from the rest of the sample we are left with 234 clusters which have a best-fit of $A = 1.107 \pm 0.041$. Thus, they are in a 2.96σ tension with the brightest region and in a 3.63σ with the faintest region. Once again, the region toward $(l, b) = (280^\circ, +1^\circ)$ seems to be more anisotropic than the one toward $(l, b) = (24^\circ, +16^\circ)$.

3.5.4 Overview of results

As a summary of the above, we identify the clear existence of a region with galaxy clusters appearing systematically fainter than expected based on their temperature measurements. This region is roughly located at $(l, b) \sim (277^\circ \pm 5^\circ, -11^\circ \pm 12^\circ)$. On the contrary, the systematically brightest region is found toward $(l, b) \sim (32^\circ \pm 15^\circ, +8^\circ \pm 17^\circ)$. Their angular separation in the sky is $\sim 115^\circ$. The statistical tension between these two regions rises significantly while narrower cones are considered, reaching $\sim 5\sigma$ for the smaller cones. The same is true for the dipole anisotropies, going up to $\sim 4\sigma$. Interestingly

[13] Arbitrary low limit number that provides a satisfactory balance between number of regions available and sufficient insensitivity to outliers

enough, the same behavior for this sky patch is also detected for ACC and XCS-DR1 (see Sect. 3.8). Another interesting trend is the systematically bright region at $(l, b) \sim (175^\circ \pm 15^\circ, +5^\circ \pm 20^\circ$, which appears to have the same behavior in all three maps with the larger scanning cones. Unfortunately, not enough available clusters lie there for the 45° map to return reliable results.

The most statistically significant dipole anisotropy is consistently found toward $(l, b) \sim (253^\circ \pm 13^\circ, -32^\circ \pm 15^\circ)$, lying $\sim 30^\circ \pm 25^\circ$ away from the systematically fainter sky region. Finally, the correlation of these results with the CMB dipole is not strong since the faintest regions of our analysis are found $\sim 55^\circ - 75^\circ$ away from the CMB's corresponding dipole end, while the strongest anisotropic dipoles of the $L_X - T$ relation are located $\sim 70^\circ - 85^\circ$ away from the CMB one.

3.6 Possible X-ray and cluster-related causes and consistency of anisotropies

Galaxy clusters are complex systems where many aspects of physics come into play when one wishes to analyze them. Thus, we have to investigate if the apparent anisotropies are caused by any systematic effects. With a purpose of trying to identify the reason behind these strong $L_X - T$ anisotropies, we perform an in-depth analysis using different subsamples of the 313 clusters which are chosen based on their physical properties. If the best-fit $L_X - T$ relation of galaxy clusters significantly differs for clusters with different physical parameters (e.g., low and high T or Z clusters, different N_{Htot} values etc.), a nonuniform sky distribution of such clusters could create artificial anisotropies.

3.6.1 Excluding galaxy groups and low-z clusters

It has been shown that the low-T clusters (mainly galaxy groups) can sometimes exhibit a slightly different $L_X - T$ behavior compared to the most massive and hotter systems (e.g., Lovisari et al., 2015, and references therein). We wish to test if this possibly different behavior has any effects on the apparent anisotropies.

Hence, we first excluded all the systems below $T \leq 2.5$ keV. Moreover, all the clusters within ~ 130 Mpc ($z \leq 0.03$) were excluded in order to avoid the peculiar velocity effects on the measured redshift (the vast majority of these clusters are already excluded based on the $T \leq 2.5$ keV limit). This resulted in the exclusion of 67 objects.

We applied the necessary correction to convert our heliocentric redshifts to "CMB frame" redshifts. This conversion is not expected to cause any significant changes in our results for two reasons. Firstly, the spatial distribution of our sample is rather uniform, therefore only $\sim 25\%$ of this subsample's clusters are located within 30° from the CMB dipole for which this correction might have a notable impact. Secondly, due to the low-z cut we apply here, the CMB frame redshift correction is much smaller than the cosmological recession velocity ($\lesssim 4\%$). Hence, the final propagated correction to the L_X values is far less than the observed anisotropies. Nevertheless, we transformed the redshifts for the sake of completeness.

When we fit the $L_X - T$ relation to all the 246 clusters with $T > 2.5$ keV and $z > 0.03$, we obtain the following best-fit values:

$$A = 1.114^{+0.047}_{-0.041},\ B = 2.096 \pm 0.078,\ \text{and}\ \sigma_{\text{int}} = 0.218\ \text{dex}. \tag{3.7}$$

It is noteworthy that A and B remain unchanged compared to the case where all the 313 clusters are considered. This indicates that a single power law model can be an efficient option for fitting our sample.

The most clear difference of this subsample fitting is the decrease of the intrinsic scatter by 10%. The total scatter also goes down by the same factor ($\sigma_{\rm tot}$=0.236 dex). The 3σ solution spaces for the entire sample and for these 246 clusters are displayed in Fig. 3.30, being entirely consistent.

Performing the 2D scanning of the full sky using $\theta = 75^\circ$, the A map shown in the bottom panel of Fig. 3.10 is produced. A similar pattern with the previous maps persist, although there are some changes. The main differences are that the –statistically insignificant– bright region toward $(l, b) \sim (170^\circ, -10^\circ)$ vanishes whilst the behavior of the faint region toward $(l, b) \sim (120^\circ, +10^\circ)$ seems to be amplified. Despite of that, the most statistically significant low-A regions approximately remains in the sky patch that was found before, toward $(l, b) = (288^\circ, -35^\circ)$ with $A = 1.016 \pm 0.045$ (110 clusters). The most extreme high-A sky region is again consistent with our previous findings, lying at $(l, b) = (10^\circ, +16^\circ)$ with $A = 1.371 \pm 0.061$ (113 clusters). The statistical discrepancy between these two results is 4.68σ ($32 \pm 7\%$), not being alleviated by the exclusion of these groups and local clusters. Their angular separation in the sky is 93°. The most extreme dipole for this map is found toward $(l, b) = (196^\circ, -34^\circ)$ with 3.27σ, shifted compared to the previously found most extreme dipole regions by $\sim 45^\circ \pm 28^\circ$.

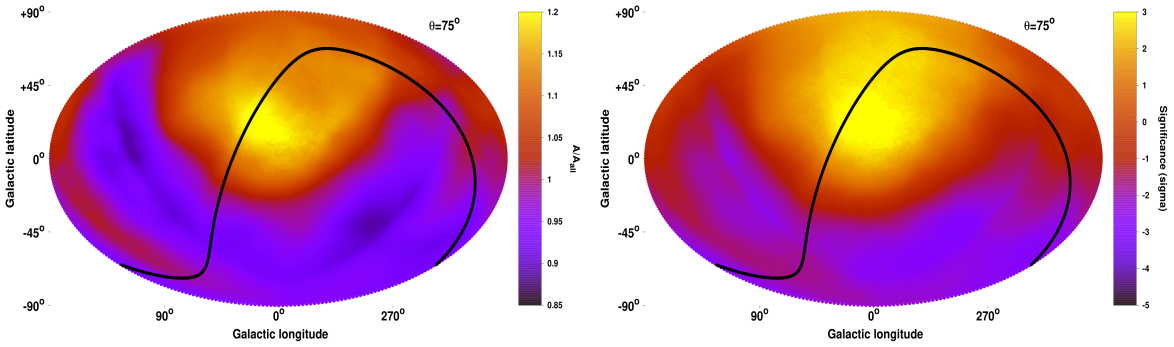

Figure 3.10: Normalization A of the $L_{\rm X} - T$ relation (left) and statistical significance of the deviation of every sky region compared to the rest of the sky (right) as functions of the position in the extragalactic sky for $\theta = 75^\circ$ when only the 246 clusters with $T > 2.5$ keV and $z > 0.03$ are used, as well as CMB frame redshifts.

To further scrutinize the effects of low-T systems on our results, as well as the effects of local clusters and their peculiar velocities, we wish to restrict our sample even more by expanding the lower limits of T and z. To this end, we excluded all the 115 objects with $T < 3$ keV or $z < 0.05$ (~ 210 Mpc). This left us with 198 clusters. The best-fit results are:

$$A = 1.172^{+0.053}_{-0.046},\ B = 2.049 \pm 0.077,\ \text{and}\ \sigma_{\rm int} = 0.205\ \text{dex}. \tag{3.8}$$

The best-fit $L_{\rm X} - T$ relation slightly changes compared to the full sample results, but remains consistent within 1.1σ. At the same time, $\sigma_{\rm int}$ further decreases, being 15% lower than the full sample's $\sigma_{\rm int}$. In Fig. 3.30, the comparison between the 3σ solution spaces for the full sample and for these 198 clusters is displayed. In the panel of Fig. 3.11 the A map is displayed for this subsample of clusters, with a $\theta = 75^\circ$ cone. The significance map is shown in the bottom panel of the same figure.

The behavior of A throughout the sky remains consistent with the previous results, even after excluding more low-T clusters and using only clusters with $z > 0.05$ with CMB-frame z values. The lowest $A = 1.081 \pm 0.054$ is found toward $(l, b) = (286^\circ, -36^\circ)$ (85 clusters) while the highest $A = 1.445 \pm 0.070$ is located toward $(l, b) = (9^\circ, +15^\circ)$ (91 clusters). The statistical tension between these two results is 4.12σ ($31 \pm 8\%$). The most extreme dipole on the other hand is centered toward $(l, b) = (223^\circ, -47^\circ)$ with a relatively low significance of 2.27σ. This highlights the fact that the most extreme behavior in the sky is not found in a dipole form, and this becomes more obvious as we go to higher redshifts. Consequently,

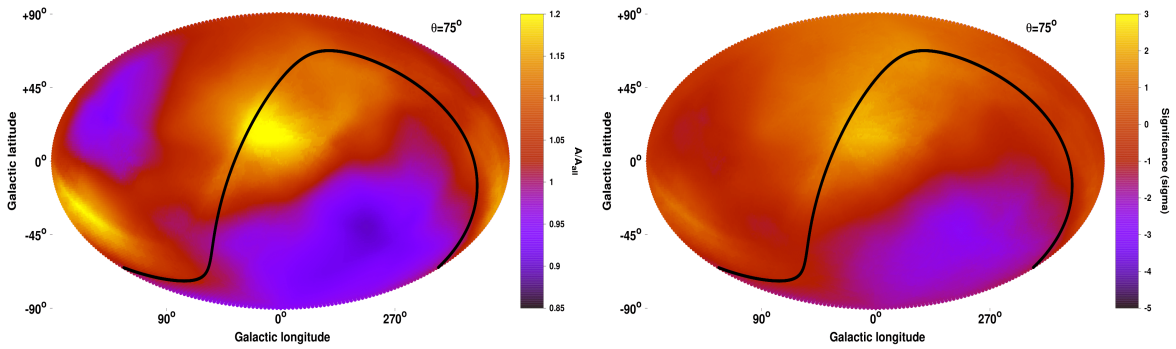

Figure 3.11: Same as in Fig. 3.10 for the 198 clusters with with $T > 3$ keV and $z > 0.05$.

it is quite safe to conclude that this anisotropic behavior is caused neither by the galaxy groups or the local clusters nor by the use of heliocentric redshifts.

3.6.2 Different cluster metallicities

A slightly nonsimilar behavior of the $L_X - T$ relation for varying metallicities of clusters can be expected mainly due to two factors. Firstly, in the parent catalogs from which our cluster sample has been constructed, the conversion of the count-rate to flux was done by using a fixed metal abundance of 0.3 $Z_\odot$. When the true metallicity of a cluster deviates from this fixed value, small biases can propagate in the flux and luminosity determination. In general, the measured luminosity of clusters with $Z > 0.3\ Z_\odot$ might be eventually slightly underestimated. However, this overestimation is only minimal. For instance, for $\Delta Z \sim 0.4\ Z_\odot$ between fixed and true Z, the final flux changes by $\sim 0 - 2\%$, where the exact change depends on the other cluster parameters, such as the temperature.

The second and most important factor is that clusters with higher Z values tend to be intrinsically brighter when the rest of the physical parameters are kept constant. This can be shown through an *apec* model simulation in XSPEC. Even for a small deviation of $\Delta Z \sim 0.1\ Z_\odot$ the flux of a cluster can fluctuate by $\gtrsim 17\%$ for a cluster with $T \lesssim 1$ keV, while this fluctuation becomes only $\lesssim 1\%$ for a cluster with $T \gtrsim 8$ keV. Therefore, a randomly different metallicity distribution between different sky regions could in principle cause small anisotropies. However, in order for the observed anisotropies to be purely caused by that, strong inhomogeneities in the metallicity distribution should exist, which, if detected, would be a riddle of its own.

Core metallicities within $0 - 0.2 \times R_{500}$

Galaxy clusters do not show a single metallicity component. Since we wish to focus first on the effects that a varying metallicity could have on the luminosity, we consider the metallicity of the core of the cluster ($Z_{\rm core}$, where by "core" we mean $0 - 0.2 \times R_{500}$) from where the bulk of the X-ray luminosity comes from. It is also expected that the clusters with the higher $Z_{\rm core}$ values would have a higher fraction of cool-core members, which are generally more luminous than non cool-core clusters for the same T (e.g., Mittal et al., 2011).

In order to investigate the behavior of the $L_X - T$ relation as a function of the metallicity of the galaxy clusters, we divided our sample into three subsamples based on their $Z_{\rm core}$ value. Our only criterion for this division was the equal number of clusters in each subsample. These subsamples are 105 clusters with $Z_{\rm core} \leq 0.452\ Z_\odot$, 104 clusters with $0.452\ Z_\odot < Z_{\rm core} \leq 0.590\ Z_\odot$ and 104 clusters with $Z_{\rm core} > 0.590\ Z_\odot$.

For each subsample, we perform the fitting letting A and B to vary. The following results are not particularly sensitive to the exact $Z_{\rm core}$ limits.

The 1σ solution spaces for each subsample are shown in Fig. 3.12. One can see that all the three subsamples share a very similar $L_{\rm X} - T$ solution. The maximum statistical deviation of $\sim 1.12\sigma$ is found between the two subsamples with the lowest and highest $Z_{\rm core}$, with the latter being slightly more luminous on average. Furthermore, the intrinsic scatter for the two subsamples with the lower $Z_{\rm core}$ is $\sigma_{\rm int} \sim 0.260$ dex while for the high-$Z_{\rm core}$ subsample is $\sigma_{\rm int} \sim 0.197$ dex.

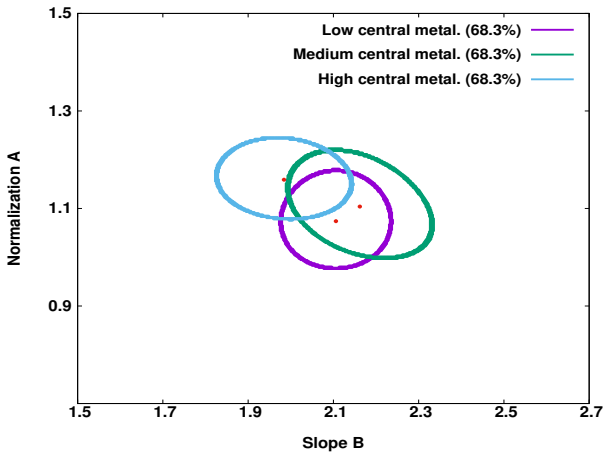

Figure 3.12: 1σ (68.3%) confidence levels of the normalization and slope of the $L_{\rm X} - T$ relation as derived for the 105 clusters with $Z_{\rm core} \leq 0.452\ Z_{\odot}$ (purple), the 104 clusters with $0.452\ Z_{\odot} < Z_{\rm core} \leq 0.590\ Z_{\odot}$ (green) and the 104 clusters with $Z_{\rm core} > 0.590\ Z_{\odot}$ (cyan).

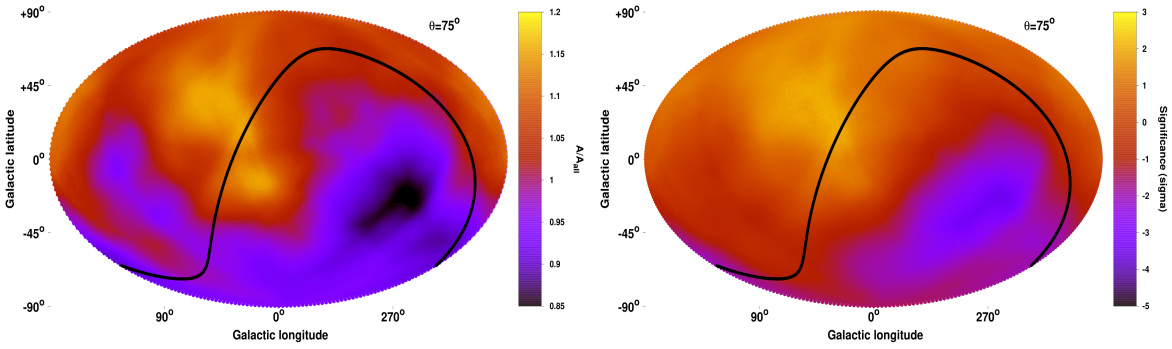

Figure 3.13: Same as in Fig. 3.10 for the 209 clusters with $Z_{\rm core} < 0.590\ Z_{\odot}$.

Although it is not expected that the high $Z_{\rm core}$ subsample would cause any apparent A anisotropies with a possibly nonhomogeneous spatial sky coverage, for the sake of completeness we excluded all the 104 clusters with $Z_{\rm core} > 0.590\ Z_{\odot}$ and scanned the sky again with a 75° radius cone. The produced A and significance maps are illustrated Fig. 3.13. The obtained directional behavior of A completely matches the results of the full sample. The lowest $A = 0.927 \pm 0.064$ and highest $A = 1.274 \pm 0.071$ are found toward $(l, b) = (264^{\circ}, -18^{\circ})$ (83 clusters) and $(l, b) = (30^{\circ}, +23^{\circ})$ (88 clusters) respectively. Their deviation is 3.63σ ($32 \pm 9\%$), staying unchanged despite the smaller number of available clusters. The most extreme dipole is found toward $(l, b) = (261^{\circ}, -20^{\circ})$ with 3.41σ significance.

Outer metallicities within $0.2 - 0.5 \times R_{500}$

The metallicity $Z_{\rm out}$ of the $0.2 - 0.5 \times R_{500}$ annulus might not affect the final $L_{\rm X}$ as strongly as the core metallicity. However, it could in principle correlate with the measured temperature of a galaxy cluster since these two quantities were fitted simultaneously. To check if there is an inconsistent $L_{\rm X} - T$ behavior based on $Z_{\rm out}$ we follow the same procedure as for $Z_{\rm core}$, dividing the full sample into three subsamples similarly with before. These subsamples are 105 clusters with $Z_{\rm out} \leq 0.320\ Z_\odot$, 104 clusters with $0.320\ Z_\odot < Z_{\rm out} \leq 0.426\ Z_\odot$ and 104 clusters with $Z_{\rm out} > 0.426\ Z_\odot$.

In the top panel of Fig. 3.14 the 99.7% (3σ) solution spaces for the three subsamples are shown. It is obvious that the 104 clusters with the highest $Z_{\rm out}$ share a significantly different $L_{\rm X} - T$ solution than the 105 clusters with the lowest $Z_{\rm out}$. The statistical deviation between these two subsamples is $\sim 4.3\sigma$. However, as shown in the bottom panel of Fig. 3.14, the main source of deviation are the local, low temperature groups. Excluding objects with $T < 2$ keV and $z < 0.02$, the deviation between low and high Z clusters drops to 2.5σ, which is still a nonnegligible tension. At the same time, the medium $Z_{\rm out}$ subsample seems to be consistent with the low Z subsamples while also being in tension with the high Z clusters. Furthermore, the intrinsic scatter remains similar for all three $Z_{\rm out}$ subsamples ($\sim 0.230 - 0.245$ dex).

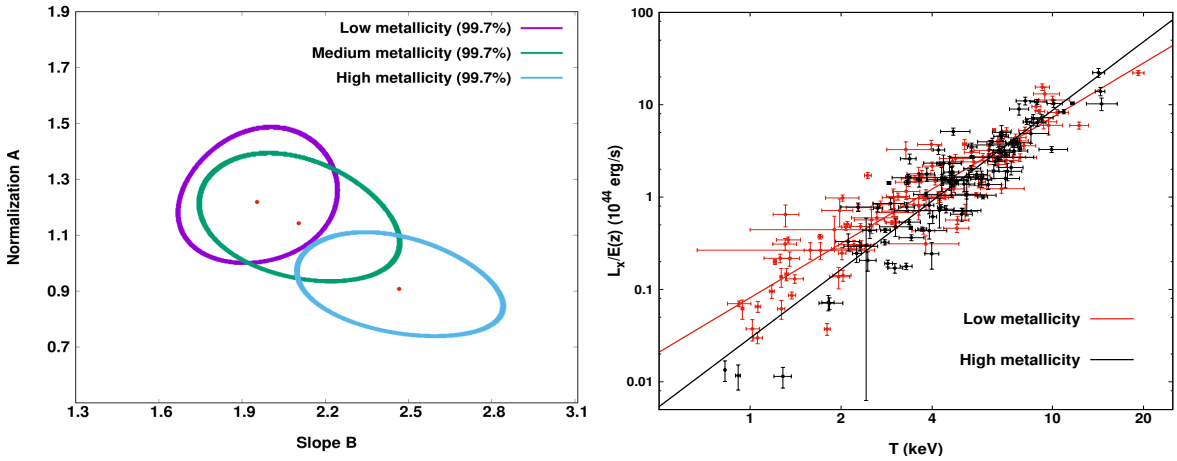

Figure 3.14: *Top*: 3σ (99.7%) confidence levels of the normalization and slope of the $L_{\rm X} - T$ relation as derived for the 105 clusters with $Z_{\rm out} \leq 0.320\ Z_\odot$ (purple), the 104 clusters with $0.320\ Z_\odot < Z_{\rm out} \leq 0.426\ Z_\odot$ (green) and the 104 clusters with $Z_{\rm out} > 0.420\ Z_\odot$ (cyan). *Bottom*: $L_{\rm X} - T$ relation for the 105 clusters with $Z_{\rm out} \leq 0.320\ Z_\odot$ (red) and for the 104 clusters with $Z_{\rm out} > 0.420\ Z_\odot$ (black) with their best-fit models.

With the purpose of examining whether the strong A anisotropies are affected in any way by these Z-dependent different $L_{\rm X} - T$ behaviors, we once again excluded all the 104 clusters with $Z_{\rm out} > 0.426\ Z_\odot$ and performed the usual sky scanning with a 75° radius cone. In Fig. 3.15 the results are displayed.

The similarity with the full sample $\theta = 75^\circ$ result is striking. The lowest and highest A directions are $(l, b) = (270^\circ, -14^\circ)$ (80 clusters) and $(l, b) = (24^\circ, +15^\circ)$ (93 clusters). The direction $(l, b) = (174^\circ, -12^\circ)$ (58 clusters) is actually brighter by $\sim 3\%$ but its statistical significance is lower, which is similar to the results of previous maps. The A values of the most extreme regions are $A = 1.035 \pm 0.069$ and $A = 1.390 \pm 0.066$ respectively with a tension of 3.72σ ($30 \pm 8\%$), not relieved despite the exclusion of the $Z_{\rm out}$ subsample with the significantly different $L_{\rm X} - T$ behavior. The most extreme dipole is located toward $(l, b) = (265^\circ, -16^\circ)$ but with a lower statistical significance of 2.26σ. Consequently, the derived anisotropies persist when the high Z clusters are excluded, while the significance of the dipolar anisotropy drops by $\sim 1\sigma$ compared to the full sample results.

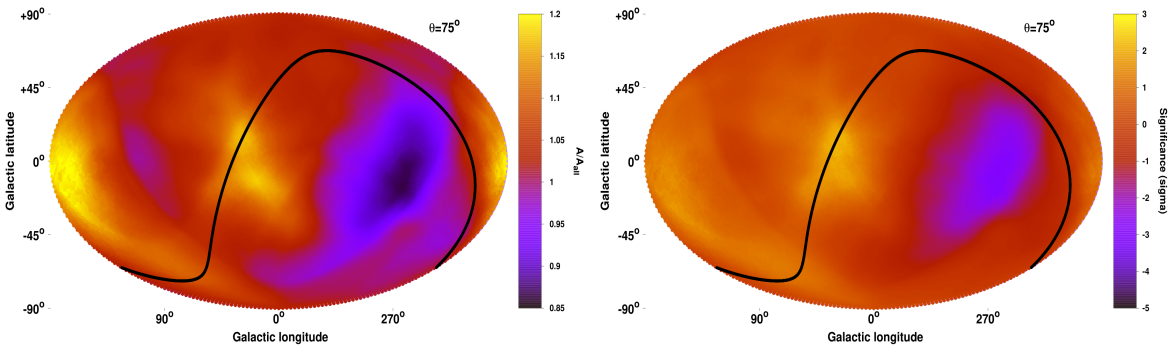

Figure 3.15: Same as in Fig. 3.10 for the 209 clusters with $Z_{\rm out} < 0.426\ Z_{\odot}$.

3.6.3 X-ray absorption correction

Another possible systematic effect resulting in the observed anisotropies could be the inaccurate treatment of the $N_{\rm Htot}$ column density correction in our *apec* model. This could lead to systematic differences in the $L_{\rm X} - T$ values of clusters in directions with different $N_{\rm H}$. Since also the most extreme regions always lie within 35° from the Galactic plane, we have to ensure that the apparent anisotropies are not caused by such effects. There are two main cases for which a systematic bias could be introduced through the absorption correction and they are described in the following subsections.

Consistency throughout $N_{\rm Htot}$ range

The first case is that the $N_{\rm Htot}$ value does not trace the true absorption consistently throughout the full $N_{\rm Htot}$ range. Thus, clusters in regions with different amounts of hydrogen get a systematically different boost in their $L_{\rm X} - T$ values after the applied correction.

This can be easily checked by comparing the $L_{\rm X} - T$ scaling relation for the clusters with low and high $N_{\rm Htot}$. To this end, we divided our sample into three subsamples of equal size based on their $N_{\rm Htot}$ values. These samples are the 105 clusters with $N_{\rm Htot} \leq 2.53 \times 10^{20}/{\rm cm}^2$, the next 104 clusters with $N_{\rm Htot} \leq 5.16 \times 10^{20}/{\rm cm}^2$ and finally the 104 clusters with $N_{\rm Htot} > 5.16 \times 10^{20}/{\rm cm}^2$.

We fit the full $L_{\rm X} - T$ relation for these three independent subsamples. As shown in the top panel of Fig. 3.16, clusters in high and low $N_{\rm H}$ regions show completely consistent $L_{\rm X} - T$ behaviors with each other. The only noticeable difference between the three subsamples is their intrinsic scatter. Going from the low to the high $N_{\rm Htot}$ subsamples, the intrinsic scatter is $\sigma_{\rm intr} = 0.214, 0.242$ and 0.258 dex respectively. This is not surprising since the high $N_{\rm Htot}$ clusters undergo stronger corrections based on the molecular hydrogen column densities of W13. However, one should not forget that these molecular hydrogen values are approximations and thus some random scatter around the true values is expected, which then propagates to the $L_{\rm X}$ values. In any case, this does not constitute any source of $N_{\rm Htot}$-related bias since the overall A and B behavior is similar for different $N_{\rm Htot}$ values (see also Sects. 3.6.4 and 3.6.4).

As an extra test, we excluded the 104 clusters with the highest absorption ($N_{\rm Htot} > 5.16 \times 10^{20}/{\rm cm}^2$) and repeated the 2D sky scanning with $\theta = 75^{\circ}$ in order to see if we observe the same anisotropies. The results are shown in Fig. 3.17. The previously detected anisotropic behavior persists, with the lower $A = 0.879 \pm 0.059$ (65 clusters) found toward $(l, b) = (242^{\circ}, -27^{\circ})$, which is consistent within $\sim 30^{\circ}$ from the previous findings. The brightest part of the sky remains unchanged compared with the full sample case, namely toward $(l, b) = (35^{\circ}, -15^{\circ})$ (93 clusters) with $A = 1.368 \pm 0.069$. These two regions share a statistical tension of 5.39σ (45 ± 8%), the most statistically significant result we found up to now. The

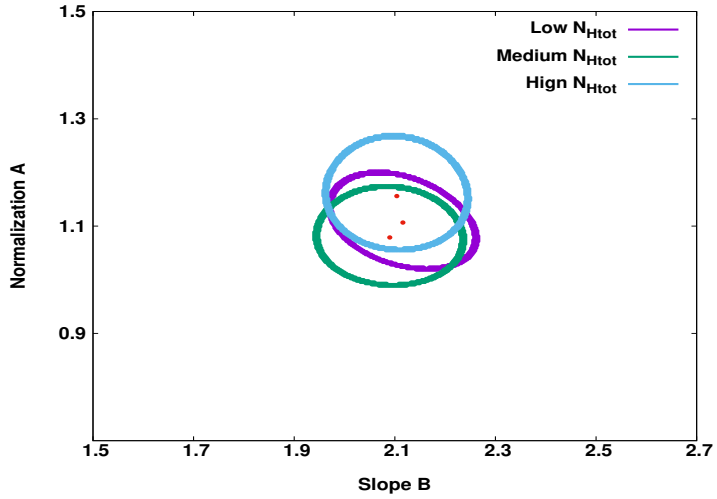

Figure 3.16: 1σ confidence levels (68.3%) of the normalization and slope of the $L_X - T$ relation for $N_{\rm Htot} \leq 2.53 \times 10^{20}/{\rm cm}^2$ (purple), $2.53 \times 10^{20}/{\rm cm}^2 < N_{\rm Htot} \leq 5.16 \times 10^{20}/{\rm cm}^2$ (green) and $N_{\rm Htot} > 5.16 \times 10^{20}/{\rm cm}^2$ (cyan).

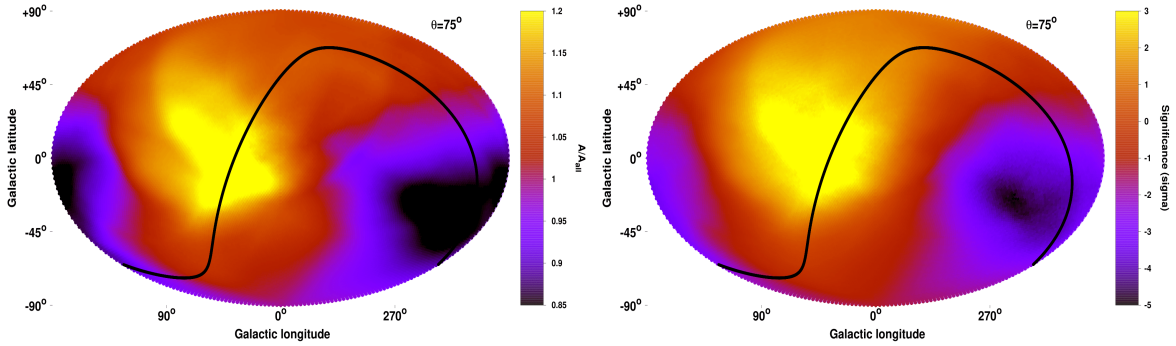

Figure 3.17: Same as in Fig. 3.10 for the 209 clusters with $N_{\rm Htot} < 5.16 \times 10^{20}/{\rm cm}^2$.

most extreme dipole anisotropy on the other hand is found toward $(l, b) = (221^\circ, -33^\circ)$ with 3.55σ.

Subsequently, the detected $> 3.5 - 4\sigma$ apparent anisotropies not only do not result due to the different amounts of absorbing material throughout the sky and its effects on X-ray photons, but they significantly increase to a $> 5\sigma$ level when the 104 clusters with the highest absorption are excluded. This is mostly due to the decrease of the intrinsic scatter of the clusters left, which leads to a decrease in the final A uncertainties.

Extra absorption from undetected material or varying metallicity of the Galactic material

The second case is that the exact amount of X-ray absorbing material is not accurately known and a higher or lower absorption correction is needed than the one applied. Such problems could occur for example if not all the absorbing material in the line of sight of a galaxy cluster has been detected by the radio surveys such as LAB, either because it is outside of the velocity range of the radio survey or for other unknown reasons (e.g., more than expected hydrogen in ionized or molecular form).

Another possible reason could be the varying metal abundance of the ISM throughout the Galaxy. The applied X-ray absorption correction is mostly applied as this: the amount of hydrogen detected is used as a proxy for the total amount of absorbing material that exists toward a given direction. The elements

of this material that contribute the most in the absorption of the X-ray photons are helium[14] and metals such as oxygen, neon, silicon etc. Based on the detected $N_{\rm Htot}$ value, a Solar metal abundance is assumed for the Galactic interstellar medium (ISM) in every direction in order to quantify the number of metals absorbing X-ray radiation. However, throughout the Galaxy the true metal abundance might diverge from this approximation since there are metal-rich and metal-poor regions. Consequently, the same amount of detected hydrogen could correspond to different amounts of X-ray absorption from metals, which is not taken into account by our current absorption correction models. It needs to be checked if the apparent anisotropies could in principle be caused by such effects.

In order to test this, one can estimate the needed absorption using two ways. Firstly, one can calculate the necessary "true" $N_{\rm Htot}$ in order to fully explain the observed anisotropies. Secondly, one can fit the extracted X-ray cluster spectra and leave $N_{\rm Htot}$ to vary. Then, the obtained best-fit $N_{\rm Htot}$ can be compared with the ones we use, which come from W13.

Necessary $N_{\rm Htot}$ to fully explain $L_{\rm X} - T$ anisotropies Any existence of X-ray absorbing "dark clouds" in certain parts of the sky could potentially explain the observed anisotropies. Approximately quantifying how much extra (or less) hydrogen column density would cause such an effect, one could see if this value can realistically be missed by radio surveys. Since any such clouds is unlikely to cover significantly large portions of the sky (more than 90° width) it is more appropriate to first look for them in the smallest radius cones.

To this end, we consider the region with the lowest normalization A for the $\theta = 45^\circ$ cone at $(l, b) = (280^\circ, +1^\circ)$ which includes 42 clusters. Its A value is $29 \pm 7\%$ lower than the rest of the sky (the fitting for the rest of the sky is performed without any distance weight) and therefore its clusters would need to be more luminous by the same degree in order to be consistent with an isotropic behavior. To quantify how much extra $N_{\rm Htot}$ is required to make these clusters more luminous by $\sim 29\%$ and explain the apparent anisotropy, we performed the following:

We selected 25 clusters from the region of interest with varying temperatures and metallicities. For each cluster we used an *apec* model in XSPEC, reproducing the current absorbed $L_{\rm X}$ value. For several $N_{\rm Htot}$ values we found the new unabsorbed $L_{\rm X}$. For the same clusters, we refit their X-ray spectra and constrained the new T for the same $N_{\rm Htot}$ values as above. For every cluster and for every $N_{\rm Htot}$ change compared to the W13 values, we thus knew the relative change of $L_{\rm X}$ and T compared to the standard values. Next, we were able to find the average relative change of $L_{\rm X}$ and T for every tested $N_{\rm Htot}$. Of course this change is not identical for every cluster since it depends on the exact T and Z. However, the actual average value of this change ($\sim 20\%$) is much larger than its variation between clusters with different properties ($\pm 4\%$). Assuming the slope to be $B = 2.102$, we could obtain the relative change of A for every sky region based on the tested $N_{\rm Htot}$ values. Consequently, we found how much extra or less $N_{\rm Htot}$ one would actually need toward the apparently anisotropic sky regions in order to explain their behavior.

We find that an extra $N_{\rm Htot} = 3.3 \pm 0.9 \times 10^{20}/{\rm cm}^2$ is required in order to make the above-mentioned low A region consistent with the rest of the sky. For its 37 clusters, the average $N_{\rm Htot}$ is $\sim 7 \times 10^{20}/{\rm cm}^2$. Thus, the final $N_{\rm Htot}$ which would explain the low A value of this region is $\sim 48\%$ larger than its current value. If we express this difference in terms of metal abundance of the existing Galactic ISM (and not just larger amounts of ISM material), the absorbing elements toward that direction should have a metallicity of $Z \sim 1.5\, Z_\odot$ to create such apparent anisotropies due to extra absorption.

The same analysis for the bright region toward $(l, b) = (24^\circ, +16^\circ)$ (which deviates by $31 \pm 10\%$ from the rest of the sky) yields that $3.5 \pm 1.1 \times 10^{20}/{\rm cm}^2$ less hydrogen would be needed toward that direction.

[14] When we refer to metals from now on, helium is also included for convenience.

This would mean that we falsely applied a higher absorption correction, systematically increasing the unabsorbed luminosities of the clusters lying in that part of the sky. For these 42 clusters included in that cone, the average total hydrogen column density is $\sim 6 \times 10^{20}/\mathrm{cm}^2$ (the actual individual values vary significantly within $0.9 - 20.6 \times 10^{20}/\mathrm{cm}^2$). Therefore, $\sim 60\%$ less absorbing material should exist toward this direction, in order for the A value to match the rest of the sky. This seems considerably unlikely. In terms of varying metallicity, the hydrogen cloud that was detected there should be metal-poor ($Z \sim 0.4\ Z_\odot$) to explain the obtained discrepancy.

This seems rather unlikely since it has been shown that toward the central bulges of spiral galaxies, and the Milky Way specifically, the metallicity of the ISM is expected to be higher (Boissier et al., 1999; Schönrich et al., 2017; Spina et al., 2017) than the metallicity in regions further away from the Galactic center. While these studies focus more on the Galactic plane and we do not use any clusters within 20° from the latter, they indicate that the high-A regions are expected to be more metal-rich than the low-A regions, instead of $\sim 3 - 4$ times more metal-poor (which could potentially explain the anisotropies). Since X-ray absorption models do not account for these effects that could potentially bias the extracted cluster properties, further testing will be needed in the future. Following the same reasoning for the $\theta = 60^\circ$ cones results in quantitatively very similar results[15].

Another possible explanation for the behavior of the low-A regions would be the existence of nearby dwarf galaxies (e.g., McConnachie, 2012a), that contain sufficient amounts of X-ray absorbing material to cause such dimming to the clusters, for which we do not account for. However, these systems would need to fulfill some conditions such as having a large apparent size in the sky and containing absorbing material not detected by LAB. For the latter to happen, the absorbing material would need to either have a line-of-sight velocity outside of the LAB range or its hydrogen content to be limited compared to the existing metals (as explained before). Even though this "hidden" absorption by nearby galactic systems would still not explain the behavior of the bright, high-A regions, the statistical significance of the latter would drop since clusters from other parts of the sky would see an increase in their L_X.

As an overview of this analysis, we see that such large differences between the detected and the true amount of N_Htot (if this is the only reason behind the apparent anisotropies), are relatively difficult to occur, but definitely worth further checking. The necessary metallicities of the ISM to explain the behavior of the anisotropic regions seem quite unlikely as well, since one would expect oversolar metallicities close to the Galactic center, and not undersolar ones.

Free to vary N_H results from literature A direct way to check if any of the above cases seems possible to explain our results is to try to estimate the absorption using only the X-ray spectra independently of the N_Htot measurements that were used above. This can be done by leaving the N_Htot parameter free to vary when fitting the cluster spectra. Comparing these estimations to the W13 N_Htot values, one can see if there is a systematic difference for sky regions that show extreme A behavior, indicating lower or higher absorption than the one previously adopted. These potential differences can reflect either differences in the actual amount of the ISM material as calculated before or differences of the true metallicity of that material, compared to the universally-assumed Solar one. Of course if different instruments are used for this estimation (e.g., *Chandra* and *XMM-Newton*), calibration issues must be taken into account.

In our case, the spectral fitting was performed only with a fixed N_Htot as described in previous sections. The results for a varying N_Htot will be presented in future work. For now, we use the N_Htot measurements as obtained by Lovisari et al. (2019) who fit the X-ray spectra of 207 nearby galaxy groups and clusters,

[15] We should note here that if the N_Htot of the extreme e.g., low$-A$ region, was indeed changed, then the needed offset of the opposite bright region would decrease, since the overall $L_\mathrm{X} - T$ best-fit would shift closer to the bright region $L_\mathrm{X} - T$. However, this effect would not change the overall conclusion since it is rather weak.

determining their metallicity radial profiles using only *XMM-Newton* observations. We assume that the determination of $N_{\rm Htot}$ does not strongly depend on the physical properties of the fitted cluster spectra, and thus only the sky coordinates of each object is of interest for our test. There are 142 overlapping clusters between these 207 clusters and our 313 clusters.

We plot the difference $D = N_{\rm H,free} - N_{\rm Htot}$ as a function of $N_{\rm Htot}$ for two regions: a cone with 45° radius centered at $(l, b) \sim (273^\circ, -19^\circ)$ and the same cone centered at $(l, b) \sim (26^\circ, +9^\circ$. The selected coordinates are the average values of all the results from the analysis up to now. The results are illustrated in Fig. 3.18.

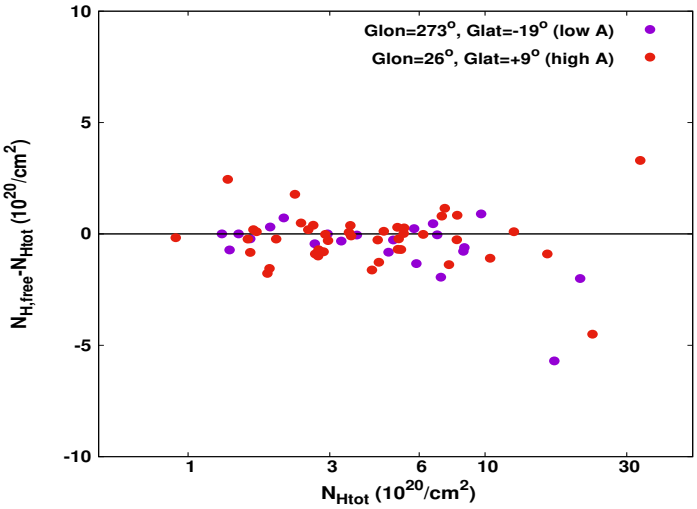

Figure 3.18: Difference between $N_{\rm Htot}$ as obtained from the X-ray spectra fit in Lovisari et al. (2019) and in W13. The difference is displayed as a function of the W13 $N_{\rm Htot}$ value for two sky regions. Within 45°from $(l, b) \sim (273^\circ, -19^\circ$ and from $(l, b) \sim (26^\circ, +9^\circ)$.

As one can see, there are no significant differences of D between the two extreme regions[16]. Moreover, the existing deviations between the free absorption and the previously assumed one are not large enough to explain the apparent anisotropies. For the low-A region, the median value of D is $D_{\rm med} = -0.28 \times 10^{20}/{\rm cm}^2$, while it would need to be $D \gtrsim +3 \times 10^{20}/{\rm cm}^2$ to alleviate the existing statistical tension. For the high-A region, the result is $D_{\rm med} = -0.22 \times 10^{20}/{\rm cm}^2$, while the anisotropies could be explained if $D \lesssim -4 \times 10^{20}/\ {\rm cm}^2$.

All in all, using the X-ray cluster spectra of Lovisari et al. (2019) as a first indication we see that the true, total absorption, does not seem to significantly deviate from the adopted absorption from W13. If a significant deviation between true and "currently-measured" absorption is detected in the future, it could potentially explain the observed anisotropies of the $L_{\rm X} - T$ relation in the sky. For now though, such an explanation seems unlikely.

Absorption from the Magellanic system

The Magellanic system is comprised of the Large Magellanic Cloud (LMC) galaxy, the Small Magellanic Cloud (SMC) galaxy, the Magellanic Stream (MS), the Magellanic Bridge (MB) and finally the Leading

[16]Systematics such as the specific abundance table used or calibration issues are expected to affect both regions in the same way (since the physical properties of the clusters are similar). Thus, even if the absolute value of D changes after all possible corrections, it would still be similar for both regions while one would need very different values to explain the apparent anisotropies.

Arm (LA). All these objects are known to contain sufficient amounts of neutral hydrogen which could potentially interfere with our measurements if not taken into account. However, the very vast majority of the hydrogen of the Magellanic system is well within the velocity range for which the $N_{\rm Htot}$ values are extracted (velocity range of LAB). Thus, it should already be included in the results of the Sect. 3.6.3 and taken into account during the correction of the $L_{\rm X} - T$ values for the absorption.

In addition, it has been shown (e.g., D'Onghia et al., 2016; Choudhury et al., 2016, and references therein) that the Magellanic system is metal-poorer ($\sim 10\% - 50\%$) than the Solar metallicity assumed in the absorption correction models. As a result, the latter will overestimate the absorption effects caused by the Magellanic system[17], eventually overestimating the unabsorbed $L_{\rm X}$ values of the clusters in these regions. Combining with the fact that the Magellanic system mostly covers sky regions in which clusters appear to be fainter than expected (low A anisotropies), one sees that is unlikely that the Magellanic system has any effects on our anisotropic results. Nevertheless, we examine all the above-mentioned components to see where they lie in the sky and if they correlate with the anisotropic behavior we observe.

The LMC is located at $(l, b) \sim (281^\circ, -33^\circ)$, within the low normalization regions, and moving away from us with +262 km/s (McConnachie, 2012b). This velocity implies that the LAB survey would have not detected only the neutral hydrogen with a peculiar velocity of $\geq +140$ km/s compared to the LMC center, and toward our line of sight. Moreover, its $N_{\rm HI}$ distribution is peaked close to the stellar population, covering a "circle" with a $\sim 3^\circ - 4^\circ$ radius in the sky, centered at the above coordinates D'Onghia et al. (2016) (thereafter D16). From the 313 galaxy clusters we use, only two are within 15° from LMC, but only one is dimmer than expected based on its temperature (however within the intrinsic scatter limits). The $N_{\rm Htot}$ value toward the LMC as given by W13 is $3 \times 10^{21}/{\rm cm}^2$. Therefore, based on all the above, it is safe to conclude that the LMC system does not bias our analysis since we would need multiple systems to be affected by that and appear underluminous.

The SMC is located at $(l, b) \sim (303^\circ, -44^\circ)$ (where $N_{\rm Htot} = 3 \times 10^{21}/{\rm cm}^2$), further away than LMC but still moderately close the low normalization regions. Its line of sight velocity compared to us is 145.6 km/s, therefore the greatest parts of its hydrogen components are expected to have been accounted for from the LAB survey. Its angular size is $\sim 50\%$ of LMC and the $N_{\rm HI}$ distribution still seems to be mostly concentrated within its optical counterpart (D16). From our sample, only two clusters are within 10° of SMC and five are within 15°. From these five clusters, three have minimal random residuals from the best-fit $L_{\rm X} - T$ relation for the whole sample, one is up-scattered and the last one is low-scattered. Thus, once again we can safely assume (mainly because of its low relative velocity and the normal $L_{\rm X} - T$ behavior of the few clusters) that SMC does not cause any significant bias to our results.

The MS extends over 100° on the sky, starting from LMC and spreading toward the south Galactic pole. Then it moves up to Galactic latitudes of $b \sim -40^\circ$, for $l \sim 100^\circ$ (Fig. 1 in D16) covering 2700 deg^2 in total. However, its $N_{\rm HI}$ density linearly decreases more than 20°away from LMC. Generally, MS is not expected to affect our results for two reasons. Firstly, the fraction of the sky it covers does not seem to correlate with low $L_{\rm X} - T$ normalization regions, since it lies at fairly low Galactic latitudes and to positions where high normalization regions are also located. Secondly, according to D16, its velocity range varies within -450 km/s to +180 km/s, so practically all of its hydrogen component is expected to be accounted for in the LAB survey.

The MB connects the LMC and SMC systems and unlike MS, it contains a stellar component as well. Its central coordinates are $(l, b) \sim (294^\circ, -37^\circ)$ and there are only three clusters within 15° of these coordinates. However, all these three clusters are already included in the 10° circles of LMC and SMC we considered before. The main velocity of MB with respect to us is ~ 225 km/s, therefore it should be included in the LAB results.

[17]For the detected hydrogen only, since the undetected is not taken into account

Finally, the LA extends in the opposite direction compared to the MS, starting from LMC and extending up to the northern Galactic hemisphere (for $l \sim 250^\circ - 280^\circ$). Its angular size is $\sim 60^\circ$ (D16). It is the least massive component of the Magellanic System while its velocity range is relatively constant, $\sim 180 - 270$ km/s. The fact that a large part of the LA lies within 20° of the Galactic plane, where no galaxy clusters exist in our sample, combined with its velocity range, indicates that no bias can occur for our results.

3.6.4 Systematics, selection effects, and correlation of results with cluster properties

Some cluster properties are usually associated with potential systematic effects. For instance, one might expect that clusters with a lower RASS exposure time might be generally up-scattered and vice versa. This is due to the fact that brighter clusters are more likely to be detected than fainter ones for the same exposure time. On the other hand, when the RASS exposure time is large enough, fainter clusters should also meet the detection thresholds set by the parent catalogs. If such a systematic indeed exists it might translate to higher and lower A values for the two cases respectively, creating artificial anisotropies. As shown in the next sections, this has no impact on our results.

Similar systematics might occur near the X-ray flux limit of our sample. For a similar temperature, intrinsically brighter clusters are more likely than other clusters to overpass the flux limit and be included in the final sample (Malmquist bias). Thus, if this applies to our sample and an excess of such clusters exist within a sky region, this will possibly result to higher A. As again shown in the following sections, our sample and analysis do not suffer of such effects.

A third possible systematic is the detection of clusters in high $N_{\rm Htot}$ regions since the difference between $N_{\rm Htot}$ and $N_{\rm HI}$ can have an impact on the selection of every X-ray flux-limited sample (including the parent catalogs). These selections are based on the unabsorbed flux, corrected only for $N_{\rm HI}$. This flux will be underestimated for clusters lying in high $N_{\rm Htot}$ and therefore they might not overcome the flux threshold set by each sample. A $\gtrsim 10\%$ underestimation is expected for regions with $N_{\rm Htot} - N_{\rm HI} > 4 \times 10^{20}/{\rm cm}^2$. The Galactic plane is usually excluded from such cluster selection processes. Nevertheless, there are still many sky regions with high $N_{\rm Htot}$ within which clusters could be missed. This could cause unaccounted selection biases and affect the completeness of the samples (which is not important to our study as explained before).

On the other hand, the high $N_{\rm Htot}$ clusters that overcome the flux limit of a sample might be intrinsically brighter in average (in order to be detected even though their estimated flux is biased low). This is "revealed" only when we correct their $L_{\rm X}$ for the molecular absorption. As a result, these clusters might be upscattered in the $L_{\rm X} - T$ plane and potentially jeopardize our results. In Sect. 3.6.3 we showed however that there is no such bias in our analysis. In the next sections we provide further evidence for this.

Correlations between A and subsample average parameters

As a generalization of the above, the apparent anisotropies in the behavior of the $L_{\rm X} - T$ relation could be in principle caused by different cluster subpopulations in the different regions. In practice, this would mean that these subpopulations might have different (average) physical properties, leading to the derived directional behavior of A. To investigate this, we perform a bootstrap resampling analysis. We drew 10^5 random subsamples of 65 clusters (typical number for the $\theta = 60^\circ$ cones) independently of the direction. For every subsample, we find the best-fit A and the weighted mean of the temperature, redshift, core and outer metallicity, flux, luminosity, $N_{\rm Htot}$, intrinsic scatter and RASS exposure time. Thus, we

can study if any correlation between the average values and A exists. Such a correlation, combined with a different parameter distribution in the most extreme regions could (at least partially) explain the observed anisotropies. Additionally, we created another 10^5 subsamples with a random number of clusters (between 35 and 170) in order to test if a correlation between the number of data and A exists.

In order to check for any possible correlations, we plot the A value against all these parameters parameters for every one of the 10^5 subsamples. The most characteristic of these plots are displayed in Fig. 3.19, while the rest can be found in the Appendix (Fig. 3.25). We also calculate the Pearson's correlation coefficient $r_{\rm corr}$ given by Eq. 3.9.

$$r_{\rm corr} = \frac{n\sum x_i y_i - \sum x_i \sum y_i}{\sqrt{n\sum x_i^2 - (\sum x_i)^2}\sqrt{n\sum y_i^2 - (\sum y_i)^2}}, \tag{3.9}$$

where x and y are the two quantities for which we wish to study their correlation, and $n = 10^5$ is the number of subsamples used. Depending on the obtained value of $r_{\rm corr}$ one can assess if there is indeed some correlation between the value of A and some average property of the different cluster subsamples.

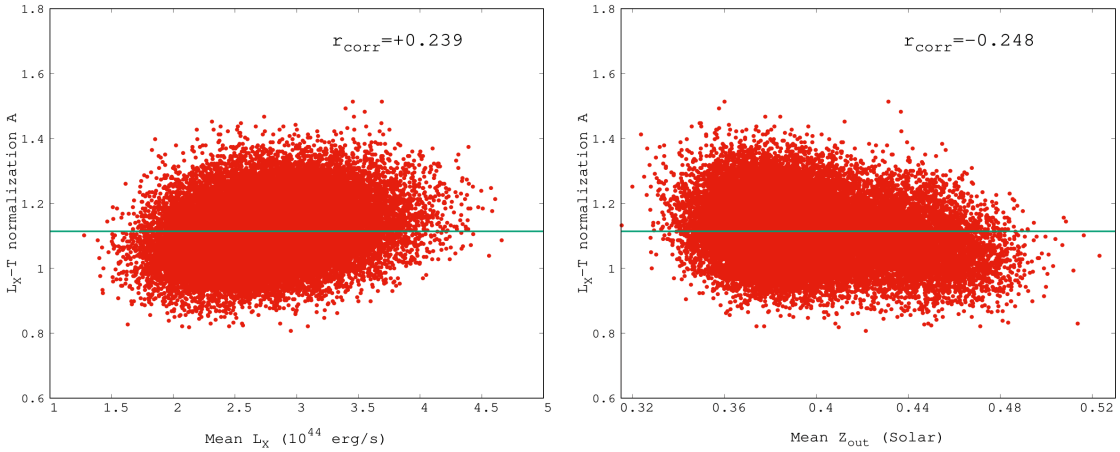

Figure 3.19: Correlation between the best-fit A value and the average $L_{\rm X}$ (left) and $Z_{\rm out}$ (ICM metallicity as measured within $0.2 - 0.5\ R_{500}$, right) as obtained for every one of the random 10^5 subsamples of 65 clusters. The Pearson's correlation coefficient is also displayed.

The only physical parameters that seem to mildly correlate with the behavior of the $L_{\rm X}-T$ normalization A are the average subsample luminosity ($r_{xy} = +0.239 \pm 0.006$) and the average $0.2-0.5\times R_{500}$ metallicity ($Z_{\rm out}$, ($r_{\rm corr} = -0.248 \pm 0.005$). As shown, the best-fit A tends to slightly increase for clusters with a higher average $L_{\rm X}$, which is expected. Subsamples with randomly more up-scattered clusters in the $L_{\rm X} - T$ plane will naturally return a higher A. Hence, pure randomness can produce similar small anisotropies, which are highly unlikely to explain the observed spatial $L_{\rm X} - T$ anisotropies (see additionally Sect. 3.9.2).

If randomly up- and down-scattered $L_{\rm X}$ values were not the reason behind the weak $A - L_{\rm X}$ correlation, then a similar (positive) correlation would exist between A and average T. However, there is no correlation between these parameters as shown in Fig. 3.25 ($r_{\rm corr} = +0.005 \pm 0.006$). Here we should also note that the weighted T average of the highest and lowest A regions is similar, shifting between ~ 5.1 keV and ~ 5.7 keV for both of them, depending on the cone radius. Hence, we can safely conclude that the observed anisotropies do not arise due to any different T distribution.

On the other hand, a slight decrease in A can be seen with an increasing average $Z_{\rm out}$. One can clearly conclude though that the obtained anisotropies of A cannot be attributed to this mild correlation since the

highest and lowest A regions have similar average $Z_{\rm out}$ values ($Z_{\rm out} \sim 0.40\ Z_{\odot}$).

A rather weak correlation is observed between A and average redshift ($r_{xy} = +0.198 \pm 0.007$), although the brightest and faintest regions have again a very similar average z ($\sim 0.09-0.1$ for both). This indicates that the exact choice of the redshift evolution parametrization in the $L_{\rm X} - T$ relation (e.g., $E(z)^{-1}$) is not particularly important, since any parametrization would approximately have the same effect in the two most anisotropic regions. Indeed, if one tries different x priors for the $E(z)^{x}$ term, the significance of the final anisotropies fluctuates only by $\pm 0.1\sigma$ compared to the used self-similar case (Appendix, Sect. 3.11).

Another weak correlation of A is observed with $\sigma_{\rm int}$ (($r_{\rm corr} = -0.194 \pm 0.006$). However, this trend cannot explain the apparent anisotropies since $\sigma_{\rm int}$ does not strongly differ for the highest and lowest A regions (0.10 dex and 0.13 dex[18] respectively for the $\theta = 60^{\circ}$ cones). No correlation is observed between the A value and $N_{\rm Htot}$, no. of clusters, RASS exposure time, $Z_{\rm core}$ and flux.

As an overview, no correlation of A with an average parameter (including systematics) can explain the apparent anisotropies. In the future, the correlation of A with combinations of these average parameters will be explored as a possible explanation behind the discrepancies, even if this seems unlikely based on the results up to now.

$L_{\rm X} - T$ fitting residuals as functions of cluster properties

As a further, secondary check, we tested the correlation between the cluster properties and their $\log L_{\rm X}$ residuals compared to the overall best-fit $L_{\rm X} - T$ model[19]. As expected, similar results with the bootstrap analysis were obtained. Thus, to avoid repetition we do not go into a detailed presentation of all the results, but instead focus on the ones usually related to systematic biases. The full discussion is found in Sect. 3.11.

In a nutshell, no strong systematic behavior of the $\log L_{\rm X}$ residuals is observed for varying RASS exp. time, $N_{\rm Htot}$ and z (Fig. 3.26). A mild systematic behavior of the residuals exists in terms of the flux and the statistical uncertainties ($\sigma_{\rm stat}$) of the clusters. However, this has no effect in the derived anisotropies since the strongly anisotropic sky regions have similar flux and $\sigma_{\rm stat}$ distributions. Finally, the residuals versus the outer cluster metallicity are also displayed in the same figure since there is a mild systematic behavior between these quantities. We already showed that this does not significantly affect our results in previous sections.

3.6.5 Fixed slope vs free slope

In our analysis until now we fixed the slope to its best-fit value for every subcategory of clusters, before we study the spatial anisotropies of A. This choice is motivated by the fact that B does not significantly fluctuate throughout the sky for the 1D analysis (Fig. 3.6, similar results obtained for a 2D scanning). Moreover, a significant correlation between A and B is not expected, due to the pivot point of the $L_{\rm X} - T$ relation being close to the median T. To investigate the possible biases that a fixed B introduces to our analysis, we perform the following:

- **Case 1**: we scan the sky using $\theta = 75^{\circ}$ while we treat B as a nuisance parameter. We allow B to vary simultaneously with A, within its 2σ limits from its overall best-fit value. We then marginalize over B to study the spatial behavior of A. The 1σ uncertainties of A are again extracted based on the $\Delta\chi^2 \leq 1$ limits since there is only one parameter of interest.

[18] Here we remind the reader that $\sigma_{\rm int}$ is this case is reduced because of the increase of the statistical uncertainties, due to the random weighting of the clusters as explained earlier in the paper.

[19] This test is equivalent to the bootstrap analysis correlation test in the previous section, but we include it for the sake of completeness

- **Case 2**: We repeat the procedure but this time we allow B to vary freely. We again study the A anisotropies and quantify the statistical significance using the $\Delta\chi^2 \leq 2.3$ limits (2 parameters of interest) for the 1σ parameter uncertainties.

For Case 1, the maximum anisotropy is found between the regions $(l, b) \sim (272^\circ, -21^\circ)$ ($A = 0.977 \pm 0.050$) and $(l, b) \sim (26^\circ, -13^\circ)$ ($A = 1.274 \pm 0.062$). The statistical significance of the tension is 3.74σ ($27 \pm 7\%$), slightly larger than before despite the marginalization over B. One sees that the results are entirely equivalent to the case where B is kept fixed, in terms of both statistical significance and direction. This strongly demonstrates the robustness of our method and the independence of the A constraints from B.

For Case 2, the A map is portrayed in Fig. 3.20 (top panel). The spatial fluctuations of A slightly intensify ($\sim 34\%$ between the most extreme values) and its directional pattern remains the same as when B is kept fixed. This once more illustrates that the derived A sky pattern does not depend on the true B values of the different sky regions.

As already shown for the 1D analysis, the fluctuations of B are smaller ($\sim 19\%$) than the ones of A. Every sky region is consistent within $< 2\sigma$ with the rest of the sky, making the behavior of B fairly consistent throughout the sky. The largest A anisotropy is found toward the same regions as for Case 1 (drifting by $< 6^\circ$) and now slightly drops to 2.78σ ($30 \pm 11\%$). This is due to the enlarged uncertainties obtained from the 2-parameter $\Delta\chi^2 \leq 2.3$ limits. These two regions return very similar slope values ($B = 2.256 \pm 0.110$ and $B = 2.109 \pm 0.119$ for lowest and highest A respectively). Their $L_X - T$ plot is displayed in the bottom panel of Fig. 3.20.

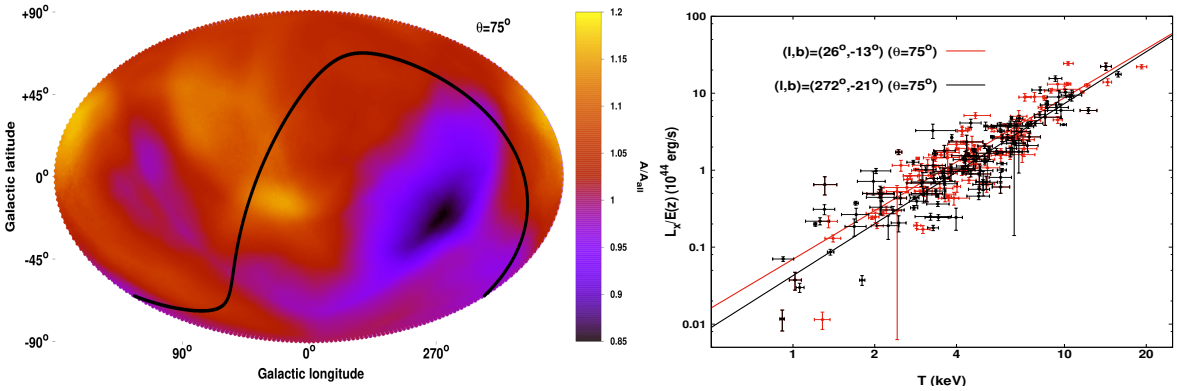

Figure 3.20: *Left:* Best-fit normalization A of the $L_X - T$ relation for every sky region over A_{all} as a function of the position in the extragalactic sky when the slope B is left completely free to vary. The cone size used is $\theta = 75^\circ$. *Right:* $L_X - T$ relation for the 136 clusters within 75° from $(l, b) \sim (26^\circ, -13^\circ)$ (red) and for the 124 clusters within 75° from $(l, b) \sim (272^\circ, -21^\circ)$ (black). Their best-fit models are displayed as solid lines.

These results confirm that the choice of keeping the slope fixed for the bulk of our analysis does not introduce any biases in the directional behavior of A or the statistical significance of the observed anisotropies.

3.7 Cosmological constraints

Many reasons that could potentially lead to a biased anisotropic behavior of the $L_X - T$ relation were tested until now. These tests explored the possibility that the apparent anisotropies could appear due to systematic differences of the subsamples in different patches of the sky or that unknown effects could

influence the observed X-ray photons coming from specific extragalactic regions. Furthermore, we tested if possible systematics, such as RASS exposure time, Malmquist bias close to the flux limit etc., could bias our results. The observed anisotropies seem to be consistent and are not significantly alleviated by such tests.

During our analysis up to now, we assumed fixed cosmological parameters toward all the directions in the sky when deriving the normalization and slope of the $L_X - T$ relation. On the contrary, one can reasonably assume that the physics within the ICM of galaxy clusters that determine the correlation between L_X and T should be the same regardless of the direction. As a result, the true normalization and slope of the $L_X - T$ relation should not depend on the coordinates and should be fixed to their best-fit values.

Consequently, the last thing to be checked is if any apparent anisotropies could occur because of an anisotropic Hubble expansion. In practice, this would mean that the luminosity distance would differ toward varying directions for a fixed z. These differences can be expressed in terms of the cosmological parameter H_0 which enters in the luminosity distance through the conversion of the X-ray flux to luminosity.

To explain the behavior of faint $L_X - T$ regions we would need a higher D_L for the same z (thus higher L_X). For $z \lesssim 0.3$ it is known that $D_L \approx \frac{1}{H_0}[z + \frac{z^2}{2}(1 - q_0) + O(z^3)]$, where q_0 is the deceleration parameter. Hence, a lower H_0, implying a lower current expansion rate, would return a higher D_L for a fixed z. The same would be true for a more negative q_0, implying a higher acceleration rate[20].

One could also study the directional behavior of Ω_m, but for low redshift objects (like the clusters we use), D_L is not very sensitive to this parameter. Therefore, large deviations from region to region would be needed in order to explain the anisotropies (see results of M18). Moreover, Ω_m variations would have a different effect to higher and lower redshift (and thus temperature) clusters, changing both the normalization and the slope of the $L_X - T$ relation. Other effects that have to be taken into consideration in such a case is the higher (lower) matter density of the Universe toward different directions, leading to more (less) structures. Structured environment can alter the behavior of the $L_X - T$ relation as we have shown in M18. Based on that, a robust directional study of Ω_m is not ideal for our sample and method. On the other hand, the effect of H_0 on D_L does not depend on z and hence variations of smaller amplitude than Ω_m could result in the observed anisotropies. Also, since H_0 variations will have the same effect on the L_X of every cluster independently of its z (and thus T), the slope of the $L_X - T$ will remain unchanged.

Therefore, we fix $A = 1.114$ and $B = 2.102$ and fit H_0 as the only free parameter (together with σ_{intr}) as described in Sect. 3.4.2. It should be noted that here we investigate the relative change of H_0 due to spatial anisotropies of the cosmic expansion, and absolute values of H_0 are arbitrary.

The H_0 map as produced using $\theta = 75^\circ$ is portrayed in Fig. 3.21. As one can see the H_0 and A maps show exactly the same behavior for the reasons explained above. We do not plot the significance map in this case since it is identical to the significance map of A using $\theta = 75^\circ$, as shown in Fig. 3.9.

The apparently maximum acceleration direction is found toward $(l, b) = (274^\circ, -22^\circ)$ with $H_0 = 66.20 \pm 1.72$ km/s/Mpc while the most extreme opposite behavior is found at $(l, b) = (17^\circ, -9^\circ)$ with $H_0 = 75.17 \pm 1.81$ km/s/Mpc. Their deviation from each other is at 3.59σ ($13 \pm 4\%$). The most extreme dipole is centered at $(l, b) = (263^\circ, -21^\circ)$ with a 3.15σ significance. One sees that these three directions completely match the directions for the normalization analysis using the 75° radius cones, highlighting the ability of the normalization of the $L_X - T$ relation to trace possible cosmological anisotropies. Moreover, the sigma values also match the ones from the normalization map as expected.

[20] With this paragraph we aim to make clear to the reader that a lower expansion rate is equivalent with a higher acceleration rate, which might seem counter-intuitive.

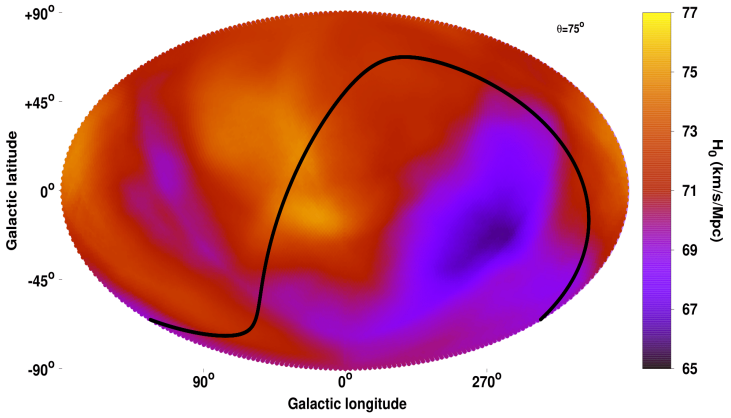

Figure 3.21: Best-fit H_0 value as obtained through the $L_X - T$ relation as a function of the position in the extragalactic sky for $\theta = 75^\circ$ cones using all the 313 clusters in our sample.

3.8 Combination with ACC and XCS-DR1

3.8.1 H_0 results for each sample

For the ACC and XCS-DR1 samples only the 1D analysis is presented in M18. In order to see if the behavior of the $L_X - T$ relation for these two samples is comparable to the one of our sample in the 2D space, we repeat the analysis described in this paper using these two samples. Prior to the analysis, the 104 common clusters between our sample and ACC are excluded from the latter. Since the focus of the paper is on the cluster sample we build and use, here we only present the results for $\theta = 75^\circ$. Nevertheless, we cannot use more narrow cones to either sample. This is due to the fact that ACC does not have enough clusters (168 in total, after the exclusion of the 104 common clusters) for such small cones, while the spatial distribution of the XCS-DR1 clusters is not entirely uniform. This results in the number of clusters falling below 30 for many regions when 60° cones are used. The results for both samples can be seen in Fig. 3.22.

For ACC the highest and lowest H_0 (brightest and faintest respectively in terms of A) regions are at $(l, b) = (77^\circ, +15^\circ)$ and $(l, b) = (317^\circ, -14^\circ)$ respectively. These two directions are relatively consistent with the general behavior of our sample, with a $\sim 40^\circ$ separation compared to the results of our sample. We remind the reader that the two samples are completely independent. The H_0 values of these extreme regions are $H_0 = 78.76 \pm 4.15$ km/s/Mpc and $H_0 = 58.12 \pm 2.68$ km/s/Mpc deviating by 4.18σ ($30 \pm 7\%$). Their angular separation is 122°, which is similar to the ones for the extreme regions of our sample. The most extreme dipole is found toward $(l, b) = (327^\circ, -21^\circ)$ with a 3.68σ. It is noteworthy that the low H_0 is much more statistically significant in this sample than the high H_0 region, indicating a monopole anisotropy. One obtains similar results for ACC when B is left free to vary within its 2σ limits as a nuisance parameter, but with a decreased statistical significance. In that case, the statistical significance of the anisotropy slightly drops to 3.12σ (from 4.18σ for a fixed B) toward similar sky directions.

For XCS-DR1 the most extreme regions are located at $(l, b) = (31^\circ, +25^\circ)$ (brightest) and $(l, b) = (281^\circ, +24^\circ)$ (faintest) separated by 117°. Their respective H_0 values are $H_0 = 77.91 \pm 2.20$ km/s/Mpc and $H_0 = 63.56 \pm 2.32$ km/s/Mpc deviating by 4.52σ ($21 \pm 5\%$). One can see that this discrepancy is larger than the one in our sample or the one obtained from ACC. However, XCS-DR1 has some properties that might lead to overestimating the anisotropies between different sky region. For instance, overluminous clusters tend to have smaller statistical uncertainties (M18), and when these clusters are in the center of the cones (higher statistical weight), this can lead to artificially high H_0 (or A). Thus,

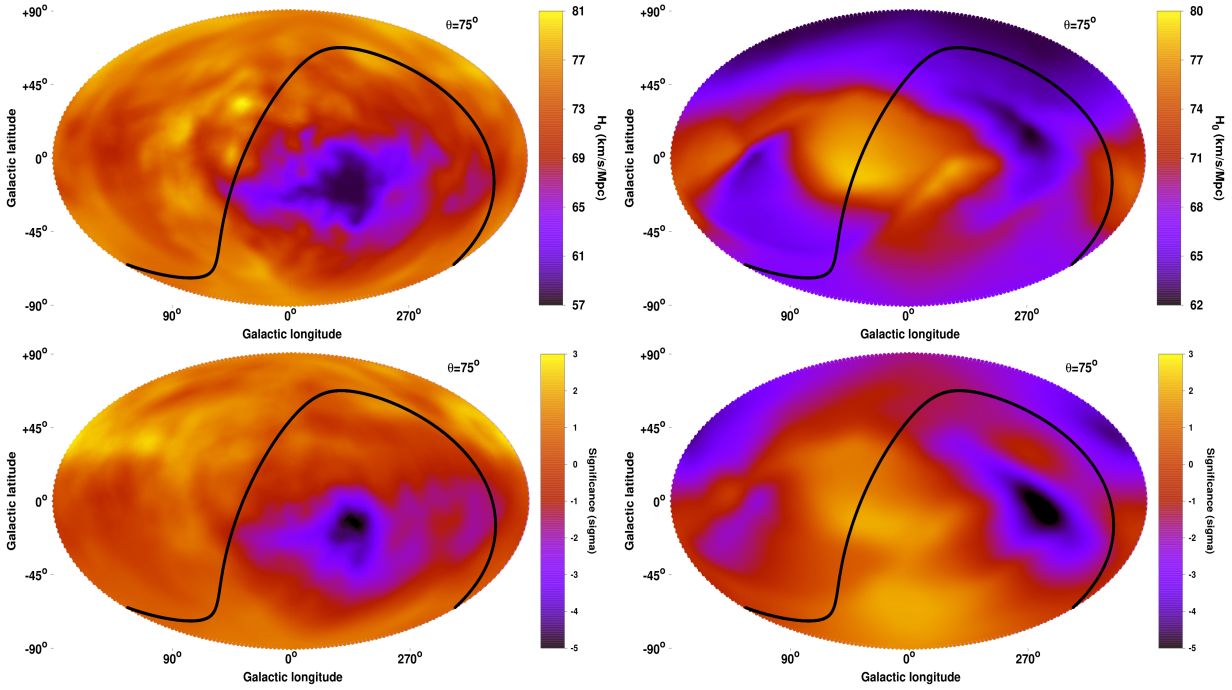

Figure 3.22: *Top:* Best-fit H_0 value as a function of the position in the extragalactic sky for $\theta = 75^\circ$ cones for ACC (left) and XCS-DR1 (right). *Bottom:* Significance map of the anisotropy between every sky region and the rest of the sky for ACC (left) and XCS-DR1 (right).

one has to be conservative when interprenting the statistical significance of the anisotropies found in the XCS-DR1 sample.

Interestingly, the direction for the lowest H_0 (which corresponds to the maximum cosmic expansion rate) is separated only by 28° from the CMB dipole. Since XCS-DR1 is a high redshift sample (median $z \sim 0.35$), naively one would not expect any effects on the XCS-DR1 results due to the peculiar velocity of the Solar System compared to the CMB frame and therefore there is no obvious reason why these two directions should be close. The most extreme dipole for XCS-DR1 is located toward $(l, b) = (211^\circ, +14^\circ)$ with a 2.75σ significance.

Now we allow B to vary within its best-fit 2σ limits. Some changes are observed, although the general directional behavior of H_0 remains relatively consistent. The statistical significance of the maximum anisotropies significantly decreases from 4.52σ to 2.82σ. This is due to the fact that the median $T = 2.7$ keV of the XCS-DR1 sample is smaller than the pivot point (4 keV) of the $L_X - T$ relation, and thus A and B values are more correlated than for our sample (or ACC). These small differences between the results of the two cases can be avoided if one chooses the pivot point to be ~ 2.7 keV for the XCS-DR1 modeling. Despite of these small alternations, the most extreme region is still found toward $(l, b) \sim (292^\circ, +23^\circ)$, only $\sim 10^\circ$ away from the previously found direction, and still with a $\sim 3\sigma$ significance.

3.8.2 Combining the H_0 results for the three samples

Remarkably, ACC and XCS-DR1 roughly agree with our sample on their $L_X - T$ anisotropic behavior despite the fact that they do not share any common clusters. While at first sight it might seem that the H_0 maps of ACC and XCS-DR1 look different, the location of their most extreme regions is still consistent within $\sim 40^\circ - 55^\circ$.

In total, they contain 842 different galaxy clusters. Consequently, any constraints on the fitted parameters would be much stronger if we combined them. While, the normalization values of the three samples are quite different (cluster populations, used energy range for L_X, T constrain method etc. vary significantly), H_0 is a global parameter that should not depend on specific samples or even cosmological probes. The normalization and slope values of the three different samples can be set in such way so the best-fit H_0 value considering the entire sample is $H_0 = 70$ km/s/Mpc. Nevertheless, we see that the three samples return a different H_0 range. As shown before ACC and XCS-DR1 show a larger variation of H_0 ($\pm \sim 20\%$) than our sample ($\pm \sim 9\%$). This correlates with the larger scatter of the other two samples and it can be attributed to randomness (since the H_0 uncertainties of ACC and XCS-DR1 are $\sim 2-3$ times larger than the ones of our sample), reasons that we have not yet identified or a combination of the above (the significance however remains similar for the three samples).

By performing the H_0 scanning analysis, one obtains three different and independent estimations of the likelihood of the H_0 parameter for every region. Multiplying these three likelihoods gives us the combined most likely H_0 value for every region in the sky. In order to consistently use the three samples, we use the smallest possible cone radius (75°) for which we have enough data for all three catalogs in any cone, and we use the same parameter fitting range ($H_0 \in [50, 90]$ km/s/Mpc) as well. Therefore, the H_0 map displayed in the left panel of Fig. 3.23 is obtained, while the significance map is shown in the bottom panel of the same figure (we also overplot the results of other studies, as discussed in Sect. 3.9.1 and Table 3.3).

From the combined H_0 results, the lowest value $H_0 = 65.20 \pm 1.48$ km/s/Mpc occurs toward $(l, b) = (303^\circ, -27^\circ)$ (237 clusters) while the highest value $H_0 = 76.64 \pm 1.41$ km/s/Mpc is found at $(l, b) = (34^\circ, +26^\circ)$ (302 clusters). Therefore, the null isotropy hypothesis between these two regions is rejected with a remarkable significance of 5.59σ ($16 \pm 3\%$). The angular separation of these two regions is 103°. On the other hand, the strongest dipole occurs toward $(l, b) = (265^\circ, -20^\circ)$ (57° away from the CMB dipole) with a significance of 4.06σ.

We repeat the joint analysis considering the obtained H_0 results from every sample when B was left free to vary as a nuisance parameter. As expected, the overall behavior of H_0 persists with some limited changes. The statistical significance of the maximum anisotropy drops to 4.55σ (from 5.59σ), and is found between $(l, b) \sim (312^\circ, -21^\circ)$ and $(l, b) \sim (45^\circ, +21^\circ)$. Consequently, the choice of keeping B fixed slightly overestimates the exact statistical significance of our findings but does not affect the general conclusion.

All these results demonstrate clearly that the similar anisotropies in all three independent samples are extremely unlikely to be random and that there is an underlying reason causing the $L_X - T$ relation to show a strong directionally depended behavior.

3.9 Discussion

The significance of cosmic isotropy for the standard cosmological paradigm is undisputed. Designing scrutinizing methods to test this hypothesis is vital since much new information about the Universe can be revealed through such tests.

One can assume that the isotropic expansion of the Universe holds, but a cosmological probe could still consistently show a significantly anisotropic behavior. This could result in the identification of yet unknown factors with a surprisingly strong impact on the data collection, analysis, or both. Since these factors are not accounted for in previous studies using similar wavelengths (e.g., X-rays) or the same astrophysical objects, these biases could in principle extrapolate to many aspects of relative research fields.

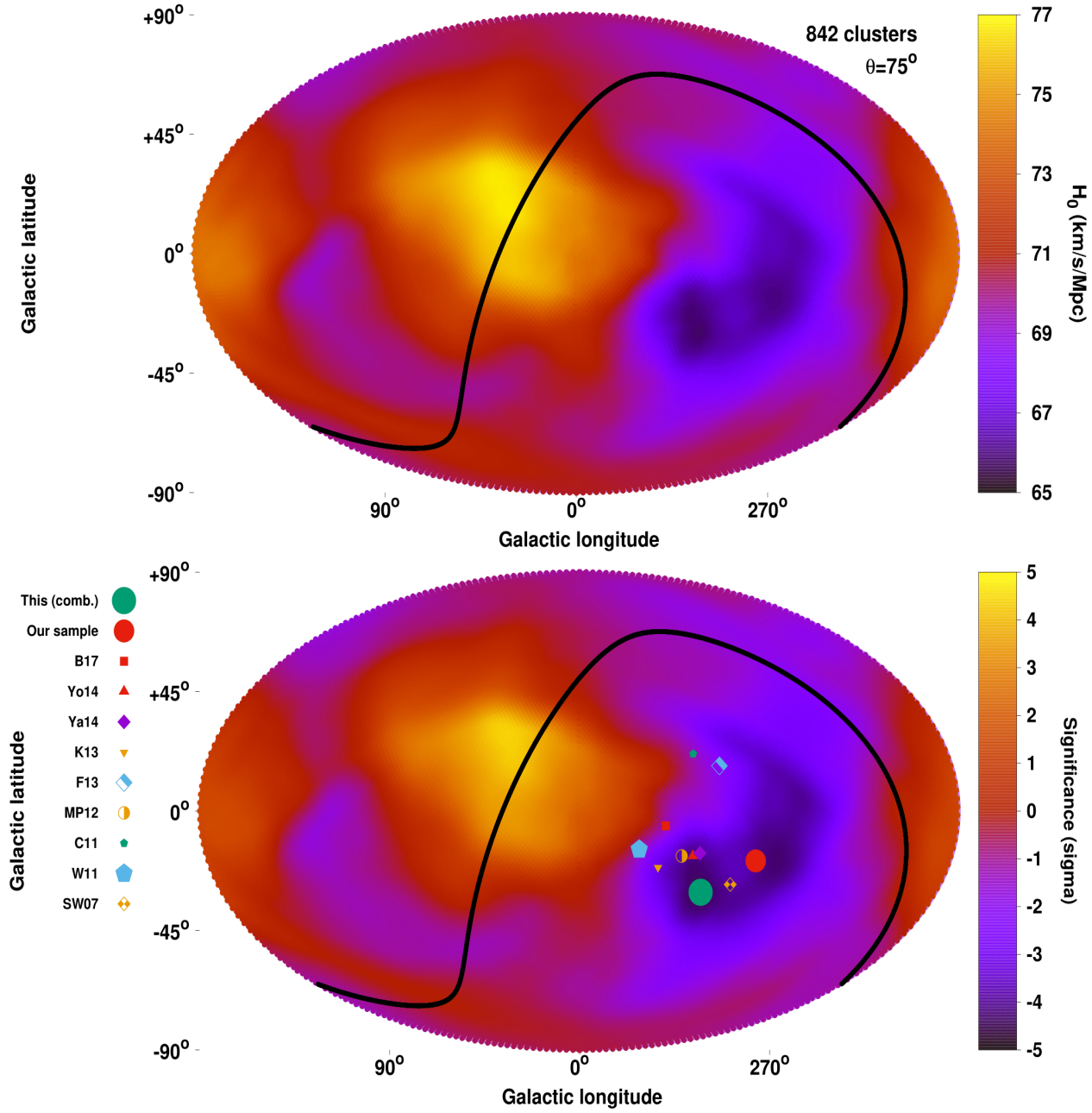

Figure 3.23: Combined results of H_0 as obtained through the $L_X - T$ relation using all three independent samples (this work's sample, ACC and XCS-DR1), as a function of the position in the extragalactic sky for $\theta = 75^\circ$ cones. *Top*: Most likely H_0 value for every sky region. *Bottom:* Combined significance map of the anisotropy between every sky region and the rest of the sky. We note that the color scale ($-5\sigma, +5\sigma$) is wider than the other significance maps since the amplitude of anisotropies is larger in this case. The most anisotropic directions as found in our analysis and other studies are overplotted. Larger symbols correspond to higher statistical significance. The order of the symbols (studies) follow the same order as in Table 3.3.

For instance, the anisotropy of the $L_X - T$ scaling relation found in this paper could have multiple implications for other studies using X-ray galaxy clusters or other X-ray objects. Since the strong anisotropies do not strongly depend on the specific sample, X-ray satellite etc. the vastly more probable scenario is that the underlying reason is not a sample-specific systematic.

Moreover, the amplitude and direction of the anisotropies are preserved even after excluding several cluster subcategories, such as low-T systems, local clusters, clusters with high absorption, metal-rich clusters, high flux ones etc. Thus, different subpopulations of clusters toward different directions is not a likely explanation as well. Additionally, possible biases due to selection effects do not explain the findings. Therefore, if this is eventually proven to be caused by an unknown (extra)Galactic effect acting on X-ray photons, previously published results would need modifications correcting for this effect.

Such an example would be the galaxy cluster masses obtained through the X-ray luminosity-mass scaling relation $L_X - M$. If we assume a typical scaling relation slope of $L_X \sim M^{1.5}$, then the masses of the clusters toward the faint regions of our analysis would be underestimated by $\sim 10 - 20\%$ while the clusters in the bright regions would end up with masses overestimated by the same amount. As a result, the cosmological parameters obtained via the halo mass function could be biased if the sky coverage of the clusters is not uniform. Even in the latter case, the scatter of the final results would increase. It is characteristic that without applying any statistical weighting in the clusters and performing the sky scanning using $\theta = 60^{\circ}$, $\sim 72\%$ of the subsamples in the different directions show a lower $\sigma_{\rm int}$ than the full sample results. This indicates the potential increase of the scatter in X-ray scaling relations when the full sky is used as if galaxy clusters were showing the same behavior everywhere. Possibly biased results when the used samples do not cover the full sky homogeneously can clearly occur to any other studies as well, if these use measured X-ray luminosities (or temperatures) of galaxy clusters.

Another useful test would be to study the dependance of these anisotropies on the exact energy range. This will be particularly helpful in order to check if the observed anisotropies could be the result of absorption effects, such as strong variations in the galactic ISM metallicity, metal-rich nearby dwarf galaxies etc. However, in Sect. 3.6.3 we showed that this is unlikely, but further testing is needed. Nevertheless, checking if these $L_X - T$ anisotropies also appear in the hard X-ray band alone, where the absorbing effects are minimal, would provide us with valuable information about their exact nature. This will be feasible with the upcoming eROSITA all-sky survey. Here we should remind the reader that while we only use the $0.1 - 2.4$ keV energy range for L_X, the ACC and XCS-DR1 samples (which also show similar anisotropies), use the bolometric energy range.

In the L_X measurements used for this study the cluster cores are not excluded, since this is very difficult to do with *ROSAT* data due to its large PSF. It has been shown however that core-excised luminosities scatter less in their scaling with temperature (e.g., Markevitch, 1998; G. W. Pratt et al., 2009; Maughan et al., 2012, etc.). Such values would be optimal for our analysis since a lower scatter in the $L_X - T$ relation would decrease the uncertainties of the derived A values. This could eventually allow the detection of spatial anisotropies with an even higher statistical significance and strengthen our results. This will be possible with *eROSITA* data and with possible future *XMM-Newton* and *Chandra*-based samples that provide core-excised luminosity values.

The summary of the best-fit A, B and $\sigma_{\rm int}$ values is shown in Table 3.1. The directions of the most extreme regions for every subsample, together with the statistical significance of the anisotropic signal between these two regions and the direction and significance of the most anisotropic dipole are shown in Table 3.2.

The consistent value of the slope throughout the different subsamples is noteworthy. The largest difference ($\sim 1\sigma$) is found between the $Z_{\rm out} \leq 0.426\, Z_{\odot}$ and the $N_{\rm Htot} \leq 7.37 \times 10^{20}/{\rm cm}^2$ subsamples. On the other hand, A deviates by $\sim 2\sigma$ between the $T > 3$ keV, $z > 0.05$ and the $N_{\rm Htot} \leq 7.37 \times 10^{20}/{\rm cm}^2$ subsamples, while it is quite consistent between the rest. As expected, the lowest scatter is found for the

Table 3.1: Best-fit normalization A and slope B values of the $L_X - T$ relation with their 1σ (68.3%) uncertainties. The results for different examined subsamples are displayed as well as for the full sample. Also, the XCS-DR1 and ACC results are displayed, where for the latter the $T - L_X$ fitting is performed (denoted by *) as described in M18. The intrinsic and total scatter are also shown for comparison.

Clusters (No.)	A	B	$\sigma_{\rm int}$ (dex)	$\sigma_{\rm tot}$ (dex)
		Our sample		
All (313)	$1.114^{+0.044}_{-0.040}$	2.102 ± 0.064	0.239	0.262
$T > 2.5$ keV, $z > 0.03$ (246)	$1.114^{+0.047}_{-0.041}$	2.096 ± 0.078	0.218	0.236
$T > 3$ keV, $z > 0.05$ (198)	$1.172^{+0.053}_{-0.046}$	2.049 ± 0.077	0.205	0.228
$Z_{\rm core} \leq 0.590\ Z_\odot$ (209)	$1.135^{+0.060}_{-0.051}$	2.034 ± 0.082	0.252	0.270
$Z_{\rm out} \leq 0.426\ Z_\odot$ (209)	$1.197^{+0.058}_{-0.051}$	2.006 ± 0.073	0.231	0.254
$N_{\rm Htot} \leq 5.16 \times 10^{20}/{\rm cm}^2$ (209)	$1.084^{+0.052}_{-0.046}$	2.082 ± 0.072	0.226	0.249
		Other samples		
XCS-DR1 (364)	$1.315^{+0.088}_{-0.079}$	2.462 ± 0.086	0.206	0.379
ACC* (168)	$2.660^{+0.243}_{-0.190}$	3.635 ± 0.135	0.101 ($\sigma_{T\|L_X}$)	0.119 ($\sigma_{T\|L_X}$)

subsamples with the highest T and z. On the contrary, the subsample where the high $Z_{\rm core}$ clusters were excluded returns the largest scatter, still consistent though with the other subsamples. We should also note here the significantly lower total scatter of our sample against XCS-DR1 and ACC (after converted to $L_X - T$ scatter).

Generally, as θ decreases, the statistical significance of the results increases, as we are able to pinpoint the anisotropies more effectively. However, the amount of available data is not yet enough to use even narrower angles. This will change with future surveys such as the upcoming all-sky *eROSITA* survey which will provide us with a larger number of observed clusters with temperature measurements (Borm et al., 2014). Nevertheless, the existence and consistency of these apparent $L_X - T$ anisotropies are already on solid ground granting these results, especially when one combines all three independent samples with a $> 5\sigma$ anisotropy emerging from this. This holds even when the slope is left free to vary (within a limited range) from region to region, and then marginalized over. It is also quite interesting that the maximum anisotropic directions in almost every tested case seem to prefer an angular separation of $\sim 80^\circ - 120^\circ$ instead of a dipole form. The most extreme observed dipole anisotropies have a statistical significance of $\sim 4\sigma$, with an angular distance of $\sim 50^\circ - 100^\circ$ from the CMB dipole direction. At the same time, the faintest parts of the maps are slightly closer ($\sim 35^\circ - 90^\circ$) to the corresponding end of the CMB dipole.

Here we should discuss some possible reasons for caution when one interprets the large statistical significance of the observed anisotropies. Firstly, while we have tested a large number of potential X-ray and cluster-related reasons and systematics that might cause such a spatially inconsistent behavior, we only tested them one by one. If one takes into account two or more such reasons simultaneously the statistical tension might decrease. Although it seems improbable that the observed anisotropies can be attributed purely to such effects (since three independent samples show similar behavior), one cannot discard the possibility of an overestimation of the anisotropies due to the (unchecked) combination of systematics. Secondly, the derived statistical significance of the results is based on the $\Delta\chi^2$ limits of the fit. While the applied bootstrap method returns similar results (see Sect. 3.9.2), one still has to consider

Table 3.2: Directions of the most statistically significant lowest and highest A and H_0 sky regions are displayed together with their statistical deviation from one another. Additionally, the direction and statistical significance of the most anisotropic dipole is displayed. The results are shown for the same subsamples as in Table 3.1. For the results labeled as "Case 1" and "Case 2" see Sect. 3.6.5.

Clusters (θ)	Lowest A/H_0 (l, b)	Highest A/H_0 (l, b)	Anisotropy significance	Max. dipole (l, b)	Dipole significance
			Our sample		
All (90°)	(272°, −8°)	(47°, +22°)	2.59σ	(230°, −20°)	1.90σ
All (75°)	(274°, −22°)	(17°, −9°)	3.64σ	(263°, −21°)	3.21σ
All (60°)	(281°, −16°)	(34°, +4°)	4.73σ	(260°, −36°)	3.77σ
All (45°)	(280°, +1°)	(32°, +14°)	5.09σ	(255°, −53°)	4.22σ
All (75°, varying B - Case 1)	(272°, −21°)	(26°, −13°)	3.74σ	(262°, −21°)	3.29σ
All (75°, varying B - Case 2)	(269°, −17°)	(23°, −10°)	2.78σ	(262°, −22°)	2.36σ
$T > 2.5$ keV, $z > 0.03$ (75^o)	(288°, −35°)	(10°, +16°)	4.68σ	(194°, −34°)	3.27σ
$T > 3$ keV, $z > 0.05$ (75^o)	(286°, −36°)	(9°, +15°)	4.12σ	(223°, −47°)	2.27σ
$Z_{\rm core} \leq 0.59\, Z_\odot$ (75^o)	(264°, −18°)	(30°, +23°)	3.63σ	(261°, −20°)	3.41σ
$Z_{\rm out} \leq 0.426\, Z_\odot$ (75^o)	(270°, −14°)	(24°, +15°)	3.72σ	(265°, −16°)	2.26σ
$N_{\rm Htot} \leq 5.16 \times 10^{20}/{\rm cm}^2$ (75^o)	(242°, −27°)	(35°, −15°)	5.39σ	(221°, −33°)	3.55σ
			Other samples		
ACC (75°)	(314°, −17°)	(77°, +15°)	4.18σ	(327°, −21°)	3.68σ
XCS-DR1 (75°)	(281°, +24°)	(31°, +25°)	4.52σ	(211°, +14°)	2.75σ
Our sample+ACC+XCS (75°)	(303°, −27°)	(34°, +26°)	5.59σ	(265°, −20°)	4.06σ
Same (varying B - Case 1)	(312°, −21°)	(45°, +21°)	4.55σ	(271°, −15°)	3.32σ

the so-called cosmic variance. To do so, one can use Monte Carlo simulations to draw similar samples from an inputted isotropic universe and, following the same method as in this paper, check how often such large anisotropies appear. This will be done in future work.

3.9.1 Comparison with other studies

Except for identifying previously unknown factors that can significantly affect the determination of physical parameters of astrophysical objects as discussed above, testing the isotropy of the Universe has of course another aspect as well. If many independent cosmological probes agree on a similar anisotropic direction and amplitude, while all known biases have been accounted and corrected for, then the hypothesis of cosmic isotropy should be reconsidered. This could eventually lead to a major shift in the standard cosmological model.

The direction we identify as the one with the maximum acceleration (or minimum expansion rate as explained before) if the anisotropies were indeed only of cosmological origin, agrees well with many other studies that used SNIa and other probes to look for possible anisotropies in the Hubble expansion. Several examples of such studies are shown in Table 3.3, together with their the most anisotropic directions and their significance.

Generally, it is usual that the anisotropies found in SNIa come mostly from $z \lesssim 0.1$ and they are attributed to local bulk flows, arising due to the Shapley supercluster at $(l, b) \sim (306^\circ, +30^\circ)$ with $z \sim 0.04 - 0.05$. We should note however that the anisotropic results of SNIa strongly depend on the used sample since studies that have been performed with the latest SNIa compilations tend to find consistency with isotropy as discussed in Sect. 3.1. Moreover, the rather inhomogeneous SNIa coverage of the sky

Table 3.3: Several examples of different probes and methods indicating similar anisotropic results to ours.

Reference	Used method	Maximum anisotropy (l, b)	Significance	Angular distance from our combined results	Comments
This work	Clusters $L_X - T$ (75°)	(303°, −27°)	5.59σ	–	Combination of all samples
This work	Clusters $L_X - T$ (60°)	(281°, −16°)	4.73σ	23°	Our sample
J. Bengaly C. A. P. et al. (2017)	Infrared galaxies	(323°, −5°)	$p = 0.064$	22°	
Yoon et al. (2014)	Infrared galaxies	(310°, −15°)	$\sim 2.5\sigma$	13°	
Yang et al. (2014)	SNIa	(307°, −14°)	$p = 0.046$	13°	
Kalus et al. (2013)	SNIa	(325°, −19°)	95%	22°	$z < 0.2$ SNIa
Feindt et al. (2013)	SNIa	(298°, +15°)	$p = 0.010$	41°	$z < 0.035$, probably bulk flow
Mariano et al. (2012)	SNIa+Quasars	(315°, −15°)	$\sim 99\%$	16°	
Colin et al. (2011)	SNIa	(309°, +19°)	$p = 0.054$	45°	$z < 0.06$, probably bulk flow
Webb et al. (2011)	Quasars	(334°, −13°)	4.2σ	33°	$0.22 < z < 4.18$,
Schwarz et al. (2007)	SNIa	(290°, −24°)	$> 95\%$	11°	$z < 0.2$ SNIa

can create problems in the search of a preferred cosmological axis.

Within an isotropic FLRW background the directions of peculiar velocities are expected to be randomly distributed. However, a coherent bulk flow toward a massive structure due to gravitational attraction, it would affect the redshifts of local objects in a systematic way. If not taken into account, the luminosity distance (calculated through z) of clusters would be over or underestimated depending on their position in the sky. This could inevitably lead to apparent anisotropies arising from local probes.

Although these local flow motions are not expected to extent beyond $\sim 200h^{-1}$ Mpc, the studies shown in Table 3.3 (among others) detect bulk flows (or anisotropies) further away than this scale and with amplitudes which are hard to explain within ΛCDM. This detection is performed by different independent probes. The statistical significance however decreases compared to local probes due to the limited number of data in certain sky patches. An example of studying the scale of bulk flows is given in Carrick et al. (2015) who find a 5σ bulk flow of ~ 160 km/s extending over $200h^{-1}$ Mpc toward $(l, b) \sim (304°, +6°)$. The structures that could fully explain such a bulk flow motion have not been identified yet. Moreover, the direction of the anisotropies of more distant probes tends to converge with the one from the CMB dipole, but often with a slightly larger amplitude.

The consistency of the apparent anisotropies beyond $\sim 210h^{-1}$ Mpc ($z > 0.05$) can be also seen in our results, where the tension with the null hypothesis of isotropy does not decrease. Another effective test could be to perform our $L_X - T$ anisotropy analysis with clusters at $z > 0.2$, beyond the effects of the recent large-scale bulk flow detections. Currently there are not enough data for such a test though, but this is expected to change with the upcoming all-sky eROSITA survey. Finally, if the only reason behind the anisotropies we observe in the $L_X - T$ behavior was local or cosmic coherent flow motions, one would expect to retrieve mostly dipole anisotropies, whether we have shown that anisotropies separated by $\sim 90° - 120°$ are more significant in our analysis. However, a more in-depth testing is needed to draw safe conclusions about this scenario.

3.9.2 Statistical significance validation by bootstrapping

In order to further investigate the statistical significance of our results and if they could be attributed to pure chance we perform a bootstrap resampling analysis. We consider two cases:

In the first case, we used all the 313 clusters covering the whole sky. We drew 10^5 random subsamples of the same size as the region we want to test its significance. We assigned random statistical weights

in the drawn clusters[21] to simulate the method we use during the sky scanning analysis. There, the weights were assigned based on the distance of every cluster from the center of the scanning cone. This test demonstrates how often our cluster sample can reproduce such low or high A values randomly and independently of the direction, when having the same number of clusters as in the extreme regions.

In the second case, we excluded the subsample of interest and performed the 10^5 resamplings based on the rest of the clusters. This way, we can estimate how many times the extreme result of the excluded subsample can occur randomly from data in other directions. The random statistical weighting is used here as well.

Both cases also offer a direct comparison with the deviations occurring from the $\Delta\chi^2$ limits, from which the reported statistical significance for every result comes from. In order to have minimal overlapping between the 10^5 realizations, we choose to perform this analysis for the results occurring for $\theta = 60^\circ$. The number of clusters in the extreme regions is small enough so there is no significant overlapping, while it is large enough to be relatively insensitive to strong outliers.

Drawing and analyzing 10^5 subsamples of 84 clusters from the full sample, we find that only 0.68% of the results have a lower A than the one found for the $(l, b) = (281^\circ, -16^\circ)$ direction ($A = 0.940 \pm 0.051$). This corresponds to a $p-$value of $p = 0.007$ for the null hypothesis, or in a Gaussian significance of 2.71σ. Now we repeat the analysis with a subsample size of 78 clusters, same as the brightest region for a $\theta = 60^\circ$ cone toward $(l, b) = (34^\circ, +4^\circ)$. We find that 10% ($p = 0.010, 1.65\sigma$) of the results have a higher $A \leq 1.346$ compared to the aforementioned bright region. Therefore, the statistical significance of the fainter region toward $(l, b) = (281^\circ, -16^\circ)$ is much higher in that case. The statistical deviation of these two extreme regions based on the based on the $\Delta\chi^2$ limits as shown in Eq. 4.7 is 4.73σ (Table 3.2). As found from the bootstrap resampling method however is $\sim 3.9\sigma$, slightly decreased but still significant. Finally, the most probable value for these 10^5 realizations is $A \sim 1.118 \pm 0.115$, which is consistent with the results of the full sample fitting.

For the second case, we first excluded the 84 clusters within 60° from $(l, b) = (281^\circ, -16^\circ)$ and we only considered the rest 229 clusters. Following the same procedure as before, we find that only 0.32% of the subsamples have $A \leq 0.940$ ($p = 0.003,\ 2.95\sigma$), the same result as the one we obtained from $\Delta\chi^2$ limits in Sect. 3.6.3. Doing the same for the 78 clusters (full sample except these 78) toward $(l, b) = (34^\circ, +4^\circ)$ we see that an $A \geq 1.346$ value is reproduced only for 0.45% of the 100000 subsamples ($p = 0.005,\ 2.85\sigma$), again consistent with our previous findings. In this case where only clusters from the rest of the sky are considered, the probability of the high A result to occur randomly drops significantly compared to the case where the full sample is used. This indicates that these 78 clusters strongly affect the bootstrap results when all 313 clusters are used.

Repeating the analysis for the results when $\theta = 45^\circ$, first we used the full sample with all the 313 clusters. For the results described in Sect. 3.5.3, we obtain a probability of 0.45% for the lowest A value to occur randomly from the whole sample, and a probability of 8.71% for the highest A value. The deviation between these two results is $\sim 3.9\sigma$. This is displayed in the left panel of Fig. 3.24.

Excluding these two extreme subsamples one at a time as we did in the second case before, the probability decreases to 0.09% ($p = 9 \times 10^{-4},\ 3.33\sigma$) for the faintest region and to 0.67% for the brightest region. The results are once again consistent with the deviations obtained from the $\Delta\chi^2$ in Sect. 3.6.3.

If one excludes both subsamples simultaneously and only considers the 234 left, it results in a probability of 0.21% and 0.69% of the null hypothesis to reproduce the A results of the faintest and brightest regions respectively. The result can be seen in the right panel of Fig. 3.24. The deviation of the two extreme results is at $\sim 5.4\sigma$, slightly higher from the 5.08σ value predicted from the $\Delta\chi^2$ limits.

[21] These weights follow the average $1/\cos(...)$ distribution of weights applied throughout the sky scanning method.

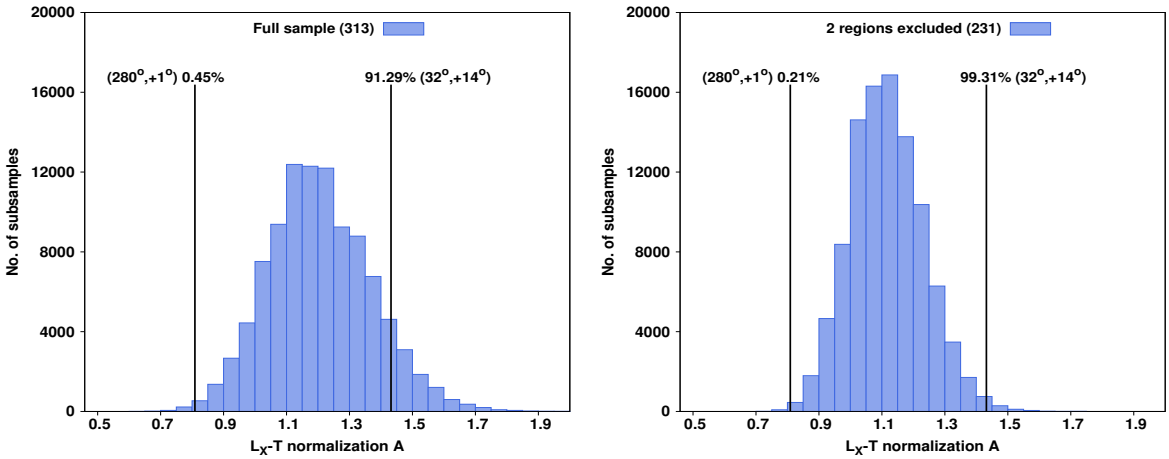

Figure 3.24: $L_X - T$ normalization results for 10^5 realizations of 40 clusters randomly drawn from the full sample (left panel) and from the 234 clusters left after the exclusion of the two extreme $\theta = 45^\circ$ regions at $(l, b) = (280^\circ, +1^\circ)$ and $(l, b) = (32^\circ, +14^\circ)$ (right panel). The statistical significance of these two regions is also displayed with the black vertical lines.

Finally, as discussed in Sect. 3.4.3, in order to ensure that the artificially low values of $\sigma_{\rm int}$ do not affect our results, we repeated the bootstrap analysis without including the $\sigma_{\rm int}$ term in our model (Eq. 4.5). For that we also found the A value of the extreme regions without accounting for $\sigma_{\rm int}$. The significance of the bootstrap results remains high, decreasing only by $\sim 5 - 12\%$ for every case (e.g., from $\sim 3.9\sigma$ to $\sim 3.7\sigma$ for the $\theta = 60^\theta$ case and from $\sim 5.4\sigma$ to $\sim 4.8\sigma$ for the $\theta = 45^\circ$) since outliers are now more likely to cause extreme A behaviors.

This analysis strongly demonstrates the high statistical significance of the results. Also, it is shown that the apparent anisotropies are very unlikely to be attributed to randomness, as well as that the statistical deviations obtained through $\Delta\chi^2$ limits match the ones from bootstrapping.

3.10 Conclusions

In this work, we constructed and analyzed a new, large homogeneously selected X-ray galaxy cluster sample of 313 objects, with the purpose of probing the anisotropic behavior of the $L_X - T$ scaling relation as first found in Migkas et al. (2018) (M18). Through the strong correlation between the X-ray luminosity and temperature and the null hypothesis that the $L_X - T$ behavior must be similar throughout the sky, one can probe the existence of up-to-now unknown factors affecting the behavior of X-ray photons, galaxy clusters or both, for different sky directions. Furthermore, one can estimate how isotropic the Hubble expansion seems to be by constraining the cosmological parameters for different sky patches. This can be done due to the inclusion of the cosmological parameters in the X-ray flux-luminosity conversion, where we take advantage of the fact that the determination of the temperature is cosmology-independent. A necessary requirement however is to verify that no underlying unknown systematics exist, affecting the X-ray observations and the galaxy cluster scaling relations in particular.

We tested the consistency of the $L_X - T$ relation for different directions by scanning the full sky using cones of different sizes, and quantify deviations in terms of the normalization parameter A, or the Hubble constant H_0. A consistent and strong directional behavior of these parameters emerged. Dividing the sky into hemispheres, we first found that the hemisphere with its pole located at $(l, b) = (272^\circ, -8^\circ)$ seems to be fainter (lower A or lower H_0) compared to the opposite hemisphere at a 2.58σ level. With

our cluster sample having a quite uniform spatial distribution we could pinpoint apparent anisotropies more effectively with narrower cones. Using cones with 75° down to 45° radius we found that the sky region toward $(l, b) \sim (277^\circ, -11^\circ)$ systematically returns a lower A/H_0 compared to the sky region toward $(l, b) \sim (32^\circ, +15^\circ)$ with a significance of $\sim 3.6 - 5\sigma$ (99.97 – 99.9999%). The main bulk of the deviations though come from the faint region rather than being balanced between the two extreme regions.

Surprisingly, the maximum dipole form anisotropies are systematically weaker by $\sim 0.4 - 0.9\sigma$ compared to these $\sim 110^\circ$ anisotropies, although still significant. Moreover, the region close to $(l, b) \sim (170^\circ, +15^\circ)$ is also systematically brighter with values comparable to the $(l, b) \sim (25^\circ, +4^\circ)$ region but with lower significance due to fewer clusters.

We examined multiple reasons, mostly related to galaxy cluster physics, X-ray analysis and systematic biases, that could provide us with an explanation about the derived anisotropies. For instance, the $L_X - T$ behavior of different cluster population was studied. We found that clusters in low absorption regions show the same behavior with clusters in high absorption regions after the proper corrections have been applied. Excluding the latter subcategory, the anisotropies remain. Moreover, excluding galaxy groups and clusters with $T > 3$ keV and redshifts of $z > 0.05$ do not significantly affect our results, as can be seen in Table 3.2. Dividing our cluster sample according to the metallicity values of our clusters (both core and outer regions) and performing the sky scanning also does not seem to explain our findings. The same is true if one allows the slope to vary within limits during the sky scanning, and then marginalizes over the slope values. We also checked if our analysis is biased by selection effects related to the RASS exposure times of the clusters, the applied flux limit and high molecular hydrogen regions, not finding any indication for such effects. However, all these tests were done one at a time. One can argue that a combination of such effects may partially decrease the high statistical significance of the anisotropies. Of course this is still a presumption since the full magnitude of the anisotropies seems unaffected by the different tests, but it is worth checking in future work.

Furthermore, we discussed the possibility of extragalactic, metal-rich systems causing X-ray absorption that is not accounted for in the LAB survey. The case where the true metal abundance in the Galaxy's ISM shows strong spatial variations, possibly biasing the applied absorption correction and causing these anisotropies, was also discussed. Even though we showed that the last two cases are unlikely to be the reason behind the apparent $L_X - T$ anisotropies, it is worth checking if this behavior persists also in the case where L_X is only measured in the hard X-ray band. In these photon energies the X-ray absorption is not significant and one would not expect any anisotropies caused by such effects. The eROSITA all-sky survey would be a great tool that will allow us to test that.

As a final test, we created 10^5 random bootstrap subsamples and investigated the correlation of the average properties of their clusters with the best-fit A value. No strong correlation was found, while the most extreme regions tended to have similar average properties. This bootstrapping method we used further verified the statistical significance of our results, while it hints to the faint sky region as the most statistically unique one. In future work, simulated isotropic samples similar to the one in this work will be used to test the frequency with which such strong anisotropies appear.

Some useful by-products of our analysis have to do with the general $L_X - T$ scaling relation behavior, such as the decrease in the scatter for higher T and z clusters, the slightly larger scatter of low core metallicity clusters compared to the rest, the $\sim 3\sigma$ discrepancy in the $L_X - T$ slope when *Chandra* or *XMM-Newton* were used, the excellent agreement between X-ray and optical redshifts, as well as the strong $L_X - T$ inconsistency between clusters with low and high metallicities within the $0.2 - 0.5 \times R_{500}$ annulus.

When our sample is combined with the ACC and XCS-DR1 samples as used in M18, we see that their sky behavior agree well with each other even without having even one common cluster among

them. Moreover, the fact that the observations of the three samples come mostly from three different telescopes and the sample have been compiled by different authors and sharing different properties (such as the z distribution) should be kept in mind. Creating a full-sky H_0 map using the 842 individual clusters included in these three catalogs, a $\sim 5.5\sigma$ anisotropy was obtained between the sky regions toward $(l, b) \sim (303^\circ, -27^\circ)$ ($H_0 \sim 65$ km/s/Mpc) and $(l, b) \sim (34^\circ, +26^\circ)$ ($H_0 \sim 77$ km/s/Mpc). These values were obtained keeping the slope fixed. When the slope is free to vary one obtains similar results at a $\sim 4.5\sigma$ level. This could either mean that indeed the explanation of the anisotropies might be of cosmological origin (including strong bulk flows) or that there is a hidden (extra)Galactic factor that affects X-ray cluster measurements independently of the used sample. The direction of the anisotropies strongly correlates with results from other independent probes as shown in Table 3.3.

The assumption of the isotropic nature of X-ray galaxy cluster scaling relation is common, even though this had not been observationally tested and confirmed before. The possible discovery of systematics which X-ray cluster studies do not account for until now, could considerably alter the way X-ray scaling relations are used and interpreted. If this anisotropic behavior persists in other X-ray wavelengths as well, it could indicate that also other X-ray astronomy studies might need readjustments.

On the other hand, the cosmic isotropy still remains an ambiguous topic since several independent cosmological probes have been found to have an anisotropic behavior recently. While there are results not reporting any significant anisotropies, others claim to detect $\sim 2-3\sigma$ anisotropies either in the local Universe ($z \lesssim 0.1$) or to larger distances. To assess this question, independent methods such as the $L_X - T$ test are needed to be applied and their results to be compared. If no biases are identified as the reason behind the anisotropies we observe and other probes seem to consistently agree, then the explanation might indeed be of cosmological origin. Such examples would be an anisotropic dark energy nature leading to different expansion rates for different directions in the late Universe, coherent bulk flow motions up to certain cosmic scales affecting the cosmological redshift measurements etc. Irrelevantly of the actual reason, studies dealing with X-ray cluster measurements are potentially affected from our findings.

3.11 Appendix A: Extra tests

Effect of redshift evolution parametrization

During this analysis, we choose a fixed prior of $E(z)^{-1}$ for the redshift scaling of the $L_X - T$ relation as shown in Eq. 3.2. If the true scaling is not self-similar and if two separate subsamples have a different redshift distribution, artificial normalization anisotropies might be induced. As already discussed in Sect. 3.6.4 though, the two most anisotropic sky regions (brightest and faintest) share a similar redshift distributions and are not expected to be affected by such possible biases. Also, the cluster redshifts are relatively low and thus $E(z)$ does not rise to high values in order to significantly affect our results.

Nevertheless, we wish to test the dependance of our results on the exact $E(z)$ prior selection. To this end, we repeat the $\theta = 75^\circ$ analysis for the full sample, for four different cases, $E(z)^{-2}$, $E(z)^{-1.5}$, $E(z)^{-0.5}$ and for no redshift evolution (keeping B fixed to the best-fit value obtained for every case separately). The location of the most extreme regions, both faintest and brightest, fluctuate only by $< 9^\circ$. The statistical significance for the anisotropy between these regions maximizes for the $E(z)^{-2}$ case (3.75σ) and decreases gradually to 3.57σ for the case without any redshift evolution. The A and the significance maps for all four $E(z)$ scenarios do not practically differ from the maps shown in the upper left panels of Fig. 3.8 and Fig. 3.9 respectively and thus we do not display them.

Correlations and systematics

As discussed in Sect. 3.6.4 we examine the possible correlations that might exist between A and the average physical parameters of every region subsample. In Fig. 3.25 the rest of the correlations are shown. None of the physical parameters seems to have a significantly enough correlation with A to explain the observed anisotropies.

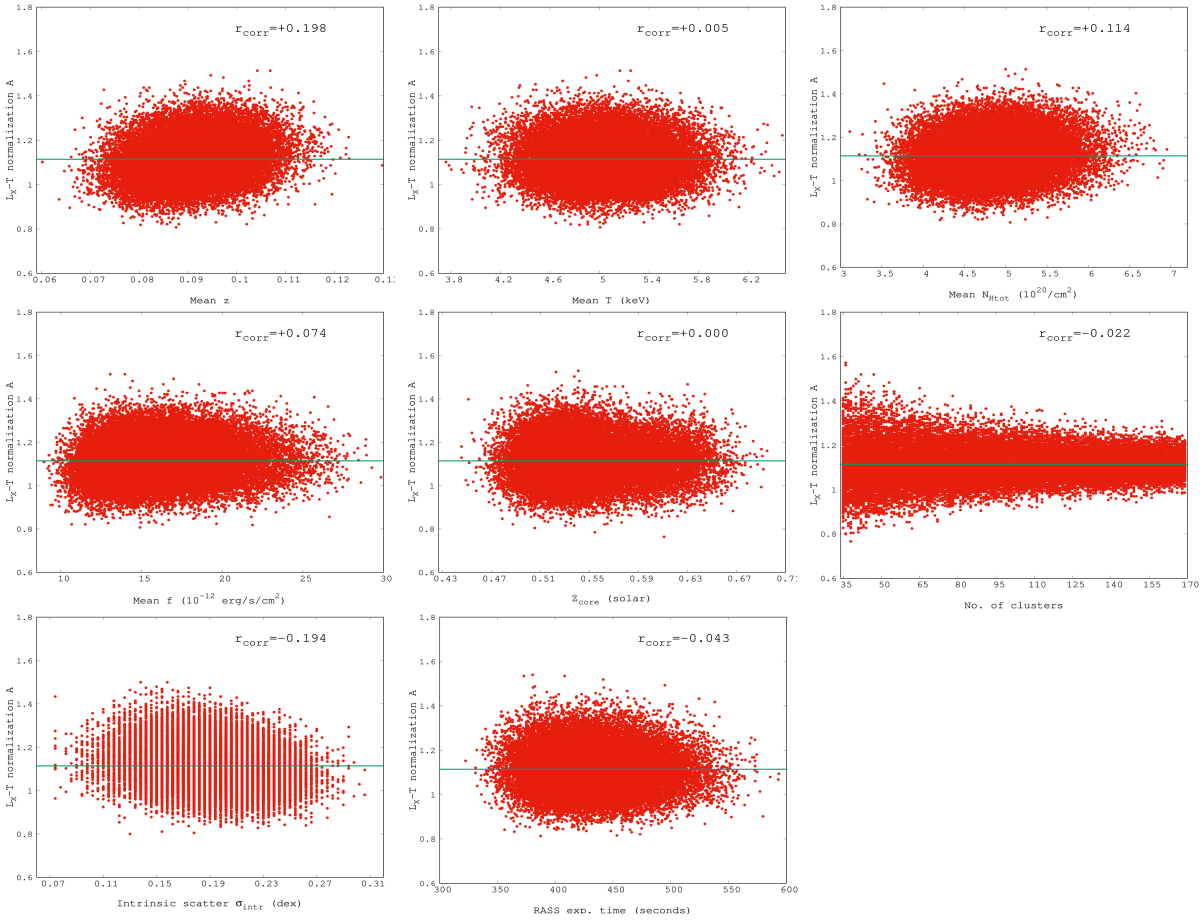

Figure 3.25: Correlation between the best-fit A value and the average parameters of the subsamples as obtained for every one of the 10^5 random subsamples. The correlation coefficient is also displayed in every plot. The parameters, moving from left to right and from top to bottom are: redshift, temperature, total hydrogen column density, flux, core metallicity, number of clusters, intrinsic scatter and RASS exposure time.

As also explained in Sect. 3.6.4, we look for any possible systematic behavior between the properties of our 313 clusters and their logarithmic luminosity ($\log L_{\rm X}$) residuals from the overall best-fit model. To this end, we fit the behavior of the residuals against every cluster property. Thus, we can quantify the significance of the possible deviation from the case of no systematic behavior. This method cannot be applied to the bootstrap realizations since the significance depends on the number of data points, and one creates as many realizations (data points) as one wishes.

The $\log L_{\rm X}$ residuals as a function of various cluster properties are displayed in Fig. 3.26.

No systematic behavior of the cluster $L_{\rm X} - T$ residuals arises for different RASS exposure times. This also holds true for the absorption correction measure $N_{\rm Htot}$. The only noticeable feature there is toward large $N_{\rm Htot}$ values where the clusters seem to be weakly upscattered compared to the overall $L_{\rm X} - T$ best

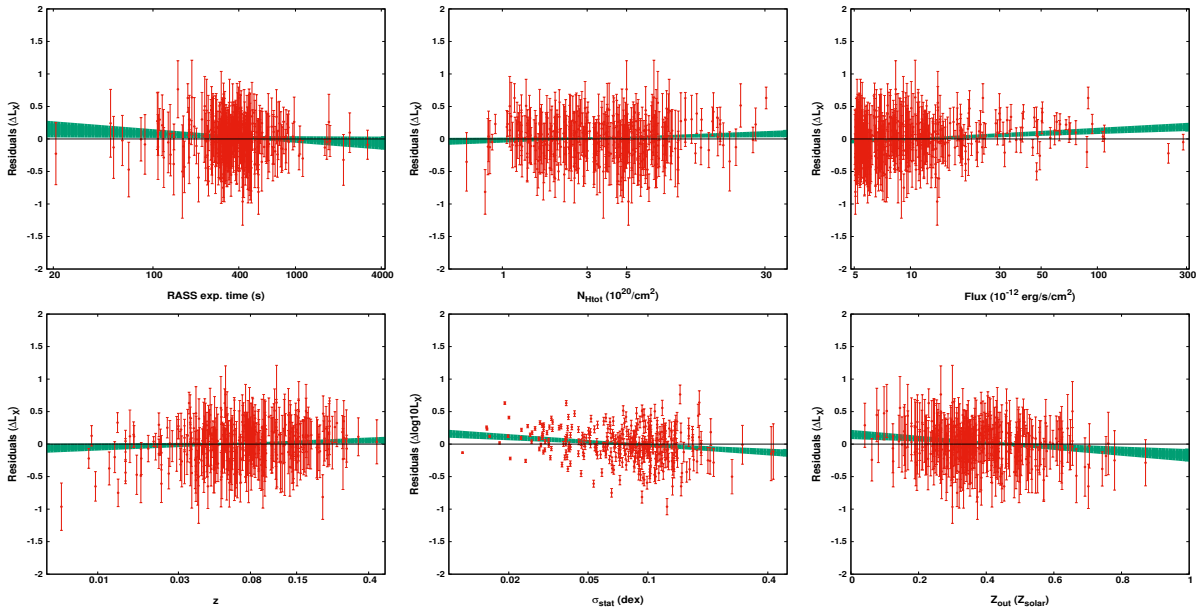

Figure 3.26: $\log L_{\rm X}$ residuals of the 313 clusters as a function of their RASS exposure time (upper left), total hydrogen column density (upper center), flux (upper right), redshift (bottom left), statistical uncertainty (bottom center) and outer metallicity (bottom right). The best-fit relation between the residuals and these quantities is also plotted with its 1σ uncertainty (green area). The black line represents the best-fit model for the full sample against which the residuals are calculated.

fit model. The effect of this in our observed anisotropies has been quantified in Sect. 3.6.3. There we found that if one excludes these clusters, the significance of the anisotropies actually increases, since these clusters lie in relatively low-A sky regions. The residuals seem to be consistent throughout the z range as well, with the exception of $z \lesssim 0.025$. In Sect. 3.6.1 we extensively show that excluding these clusters neither alleviate the statistical tension between the oppositely anisotropic regions nor changes their sky direction.

A mild systematic behavior can be seen for high flux clusters, being upscattered in average. This is the opposite behavior than the one expected due to selection biases. In low fluxes, one can see that the residuals are randomly distributed. This limited number of upscatered high flux clusters would only affect our anisotropy results if they were not randomly distributed in the sky (which they are). Despite of that, we excluded the 37 clusters with $f > 2.6 \times 10^{-11}$erg/s/cm^2 (after which this systematic behavior becomes clear) and repeated the sky scanning process with $\theta = 75^\circ$. The maximum anisotropy actually increased from 3.64σ to 3.91σ (for this cone size), and is found between the regions $(l, b) = (272^\circ, -26^\circ)$ and $(l, b) = (39^\circ, -7^\circ)$.

Another mild systematic behavior is observed for the clusters with low statistical uncertainties ($\sigma_{\rm stat} = \sqrt{\sigma^2_{\log L} + B^2 \times \sigma_{\log T}{}^2}$, with $B = 2.102$), as they tend to be intrinsically brighter than average. Based on the distance-weighing method we follow during the sky scanning process, when such a low $\sigma_{\rm stat}$ bright cluster is close to the center of a cone, the best-fit A value of that cone can be biased high to roughly match the behavior of this particular cluster. Consequently larger anisotropies might be obtained. However, this effect is limited in this work due to the inclusion of the intrinsic scatter term $\sigma_{\rm intr}$ in our model.

To test this, we excluded the 39 clusters with $\sigma_{\rm stat} < 0.035$ dex and repeated the analysis for $\theta = 75^\circ$. While the most anisotropic low-A region was found again toward $(l, b) = (272^\circ, -18^\circ)$, the brightest

region shifted toward $(l, b) = (75^\circ, +22^\circ)$. The statistical significance of their in-between anisotropy slightly decreased to 2.85σ (from 3.64σ). This small change is expected since for this test we discard from our sample the clusters with the best-quality measurements, marginally increasing the uncertainties of the derived A. Despite of that one sees that the significance of the anisotropies remains high. If we repeat the test for the $\theta = 60^\circ$ cones, the maximum anisotropy found is 3.76σ (from 4.73σ initially).

Finally, the clusters with high metallicities in the $0.2 - 0.5\ R_{500}$ annulus appear to be systematically fainter. This result and its effects on the apparent anisotropies have been extensively discussed in Sect. 3.6.2.

Chandra-only clusters

In order to make sure that the anisotropic behavior of the $L_X - T$ relation is not the result of a systematic bias coming between *Chandra* and *XMM-Newton* clusters (even if we calibrate the temperatures properly as described in the paper), we reproduce some of the A color maps using only the 237 *Chandra* clusters.

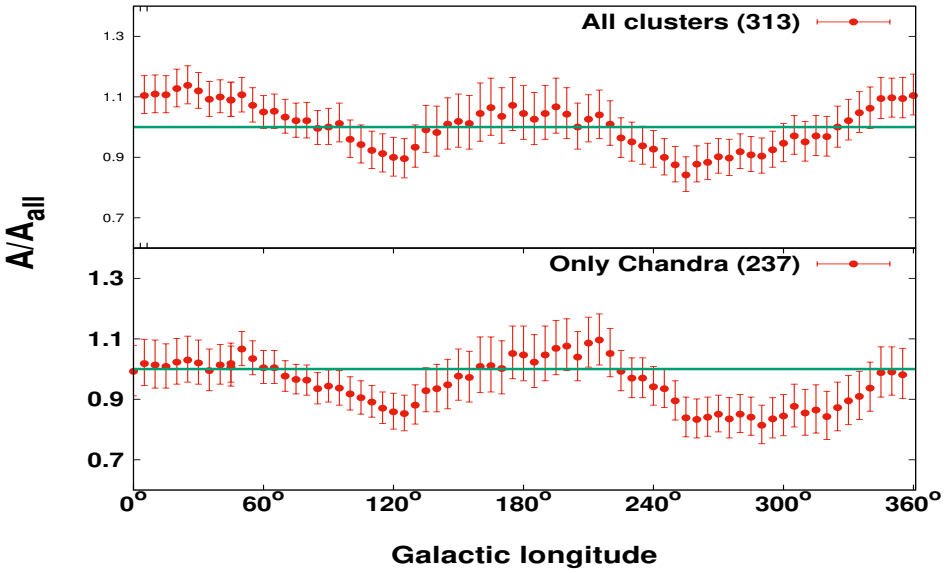

Figure 3.27: Normalization of the $L_X - T$ relation as a function of the Galactic longitude for all the 313 clusters (top) and for the 237 clusters with *Chandra* temperatures (bottom). The green lines represents the best-fit values for the full samples

In Fig. 3.27 and Fig. 3.28 is shown that both the 1D and the 2D analysis yield similar results to the full sample. In the 2D map the faint regions tend to shift to lower Galactic latitude. However, the lowest A is found toward $(l, b) = (294^\circ, -34^\circ)$ which is only 10° away from the combined lowest result found when all three independent samples were used. The location of the brightest regions is at $(l, b) = (25^\circ, -11^\circ)$. The statistically deviation between the two most extreme regions is 2.82σ, somewhat decreased compared to the full sample (3.64σ) but not relieved.

Optical redshifts only

Finally, we check if the use of X-ray redshifts affect our results somehow. This is not expected to happen since there is an excellent agreement between the two types of redshifts as discussed in Sect. 3.2.

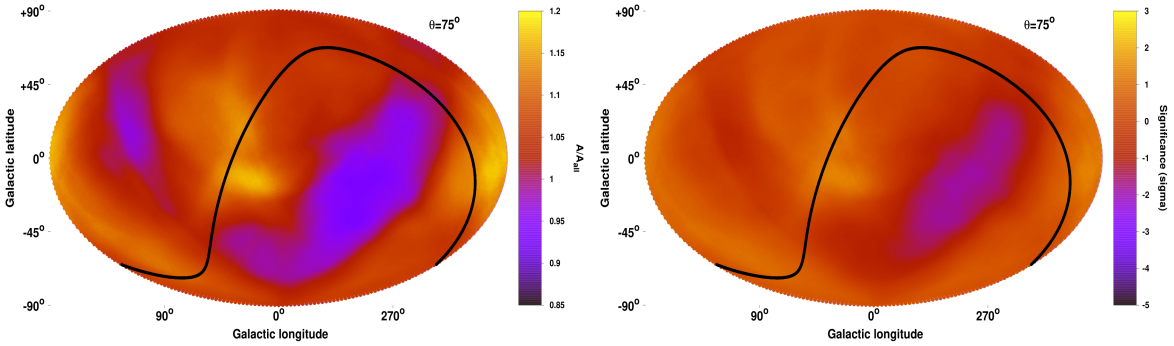

Figure 3.28: Same as in Fig. 3.10 for the 237 clusters with *Chandra* temperatures.

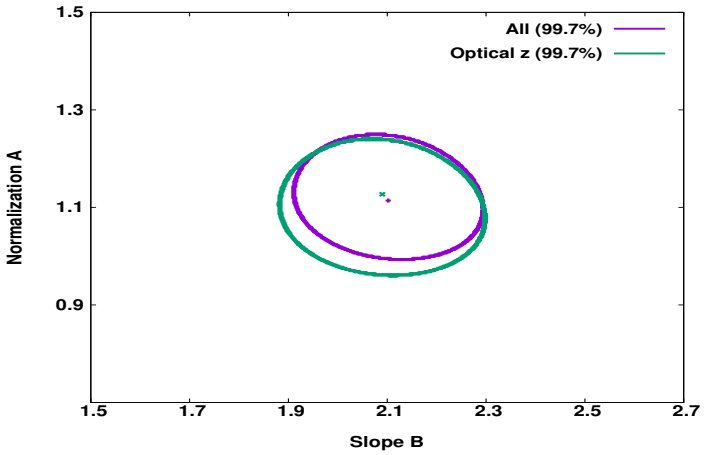

Figure 3.29: 3σ confidence levels (99.7%) of the normalization and slope of the $L_X - T$ relation for the full sample (purple) and for the 271 clusters with optical redshifts only (green).

As shown in Fig. 3.29, the A and B solution space remains identical when we considered all the 313 clusters or only the 271 clusters with optical z. Consequently, clusters with X-ray z do not bias the results and agree well with the rest.

Solution space excluding low T systems

If one excludes the low T and low z clusters, one can see that they do not strongly affect the overall $L_X - T$ solution of the sample. This is shown in Fig. 3.30 where the 3σ solution spaces are shown for the cases where we exclude all the clusters with $T < 2.5$ keV and $z < 0.03$ (left) and $T < 3$ keV and $z < 0.05$ (right), compared to the solution of the full sample.

While in the first case the two solutions are entirely consistent, in the second case they are consistent within $\sim 1\sigma$. Therefore, adding to all the tests done in the main sections of the paper, we can safely conclude that these systems do not affect our anisotropic findings.

REFLEX vs NORAS $L_X - T$ behavior

Our sample consists mainly of clusters from the REFLEX (185 clusters, 59%) and NORAS (105, 34%) clusters. A possible systematic difference between the two catalogs in their cluster population or in the flux measurements could artificially create apparent anisotropies and bias our findings. Here we should

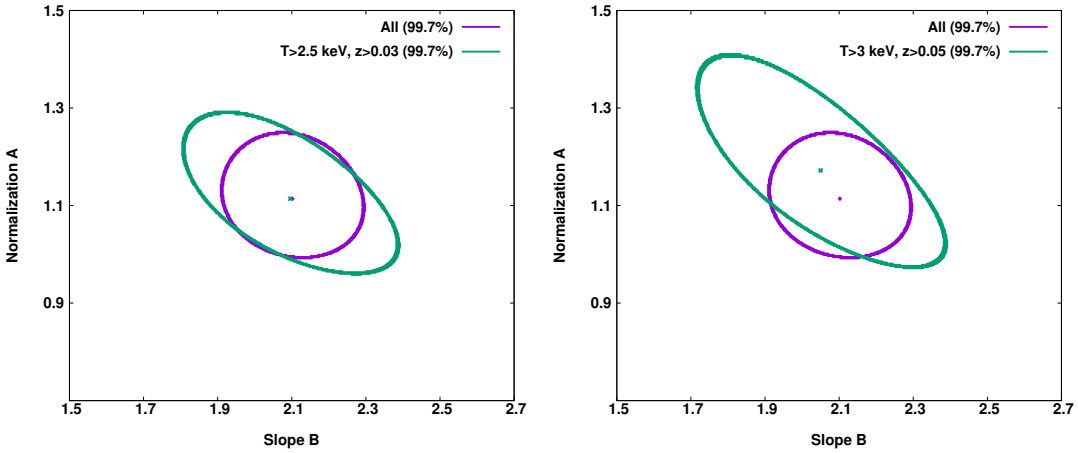

Figure 3.30: 3σ (99.7%) confidence levels of the normalization and slope of the $L_X - T$ relation as derived using the full sample (purple) and only clusters with $T > 2.5$ keV and $z > 0.03$ (green, left) and $T > 3$ keV and $z > 0.05$ (green,right).

note that the two catalogs were constructed by the same team and analyzed in a similar way, so naively significant discrepancies should not be expected.

In order to test the consistency of the $L_X - T$ behavior of the clusters coming from these two catalogs, we fit A and B for both subsamples, and compare the results. The 3σ contour plots for the two subsamples are shown in Fig. 3.31.

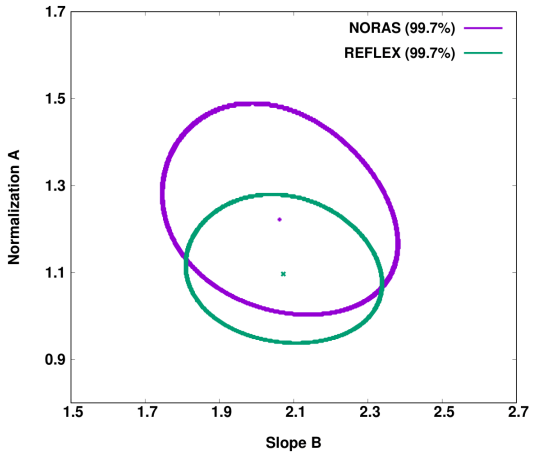

Figure 3.31: 3σ (99.7%) confidence levels of the normalization and slope of the $L_X - T$ relation as derived using the 105 clusters coming from NORAS (purple) and the 185 clusters coming from REFLEX (green).

The best-fit results are consistent for the two subsamples at a 1.4σ level. It is clear that this discrepancy is not the reason behind the observed anisotropies when the full sample is used. The NORAS clusters seem to be slightly more luminous than the REFLEX clusters, but this seems to be due to the existence of the strongest low-A anisotropic region in the REFLEX part of the sky (south ecliptic hemisphere). If one excludes the clusters within 25° from the lowest A sky direction as found for the $\theta = 75^\circ$ cones (Table 3.2), then the discrepancy between the two subsamples drops to 0.8σ, which is negligible.

Systematic temperature differences between *Chandra* and *XMM-Newton*

As explained in Sect. 3.2, the *Chandra* and *XMM-Newton* telescopes show systematic differences in the temperature determination. In order to consistently use the measurements from both telescopes, one has to take this into account. To this end, we converted all the temperatures measured with *XMM-Newton* into "Chandra" temperatures, using the relation found in S15. To verify that this relation sufficiently describes the needed conversion for our sample as well, we measured the temperature of 15 clusters with both instruments and compare the results, which are shown in Fig. 3.32.

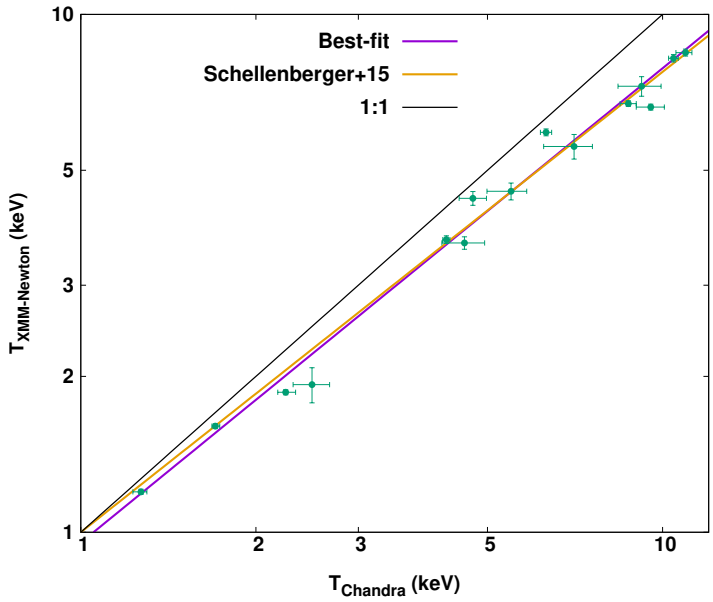

Figure 3.32: Comparison between the measured temperatures of 15 clusters using both *Chandra* and *XMM-Newton* data. The best-fit line for the relation between the two temperatures is shown (purple) together with the derived relation of S15 (orange) where more clusters were used. Also, the equality line is displayed (black).

As shown, the conversion relation found by S15 using 64 clusters is consistent with our results and thus used for the necessary temperature conversions. The statistical uncertainties of the S15 best-fit relation as well as the given scatter are taken into account in the final converted temperature values we use.

Isotropic L_X processing throughout catalogs

The L_X values have gone through several steps of processing (RASS to REFLEX/NORAS/eBCS to MCXC to our values). If the values suffered an anisotropically biased analysis during this multiprocessing, this would propagate to our results.

Firstly, we need to ensure that the L_X corrections we applied to the respective MCXC values did not introduce any artificial anisotropy. For this purpose, we check the directional behavior of the fraction between our luminosity estimated $L_{X,\,ours}$ and the MCXC $L_{X,\,MCXC}$. This is done with the same methodology as the A scanning of the sky, for $\theta = 75^\circ$ cones. Each cluster is assigned a statistical weight based on its distance from the center of each cone and the average $L_{X,\,ours}/L_{X,\,MCXC}$ is obtained. The produced map is displayed in the upper panel of Fig. 3.33. In order to directly compare with the observed anisotropies of the $L_X - T$, the same color scale is used.

One can see that the corrections we applied to the $L_{X,\,MCXC}$ values did not introduce any spatial anisotropies. The lowest fraction $L_{X,\,ours}/L_{X,\,MCXC} = 1.005$ is found toward $(l, b) \sim (320^\circ, -46^\circ)$ while

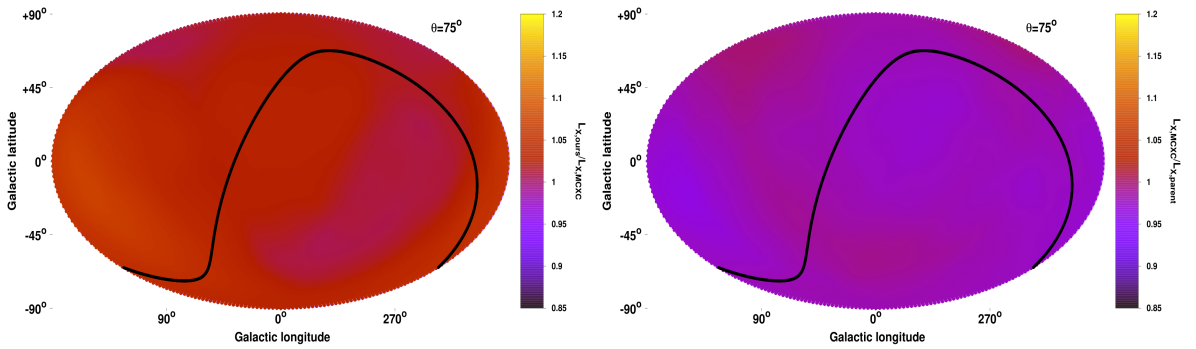

Figure 3.33: *Top panel:* Fraction of the luminosity values $L_{\rm X,ours}$ used in this analysis over the values coming from MCXC ($L_{\rm X,MCXC}$) over the full extragalactic sky. All the 313 clusters of our sample were used. The same distance-weighting was used as for the main A analysis. The color scale is the same as for the $A/A_{\rm all}$ maps throughout the paper. *Bottom panel:* Same as in top panel, for the fraction of $L_{\rm X,MCXC}$ over the luminosity values coming from the parent catalogs $L_{\rm X,parent}$.

the highest fraction $L_{\rm X,\,ours}/L_{\rm X,\,MCXC} = 1.071$ is found toward $(l, b) \sim (147^\circ, -15^\circ)$.

Next, we test the isotropy of the processing step from the parent catalogs to MCXC. We follow the same procedure as before, using the 313 clusters of our sample. As shown in the bottom panel of Fig. 3.33, the MCXC homogenization of the original $L_{\rm X,\,parent}$ is greatly isotropic. The lowest fraction $L_{\rm X,\,MCXC}/L_{\rm X,\,parent} = 0.964$ is found toward $(l, b) \sim (148^\circ, -17^\circ)$ while the largest $L_{\rm X,\,MCXC}/L_{\rm X,\,parent} = 0.999$ is found toward $(l, b) \sim (156^\circ, +54^\circ)$.

Thus, no anisotropic bias was introduced going from the original catalogs to our sample. The last step to be tested is the original $L_{\rm X}$ measurement from REFLEX, NORAS and eBCS using the RASS data. Such a procedure clearly cannot be checked unless we remeasure the cluster fluxes from the RASS data ourselves. However, there is no obvious reason why such a directional behavior would exist in the original analysis, especially since for the vast majority of clusters ($\sim 88\%$ of the sample) the analysis was conducted in a self-consistent way by the same authors (REFLEX/NORAS).

ROSAT vs *XMM-Newton* $L_{\rm X}$ measurements

It has already been discussed that *ROSAT* and *XMM-Newton* return consistent $L_{\rm X}$ values for the same clusters. As an additional test, we compare our $L_{\rm X,ours}$ values with the one derived by G. W. Pratt et al. (2009) ($L_{\rm X,\,Pratt09}$, *XMM-Newton* values) for the 19 common clusters between the two samples. For that, we calibrated our values using the same z as for $L_{\rm X,\,Pratt09}$. The comparison is portrayed in Fig. 3.34.

The weighted mean for the $L_{\rm X,ours}/L_{\rm X,\,Pratt09}$ fraction is 1.001 ± 0.150 and highlights that the luminosity measurements values based on the two different telescopes and studies agree with each other. There is no cluster more than 2σ away from the 1:1 line. Finally, the five clusters that are located in low-A regions in our analysis do not show a different behavior (weighted mean $L_{\rm X,ours}/L_{\rm X,\,Pratt09} = 0.954 \pm 0.116$) compared to the rest of the clusters.

R_{500} and temperature dependence on cosmology

The most useful feature of the X-ray galaxy cluster $L_{\rm X} - T$ scaling relation for cosmological isotropy studies is that the determination of the temperature is insensitive to cosmology. The only way that T can be affected by cosmological parameters is through the angular diameter distance D_A and the apparent size of R_{500}. The latter is used to select the area from which the spectrum is extracted and the X-ray

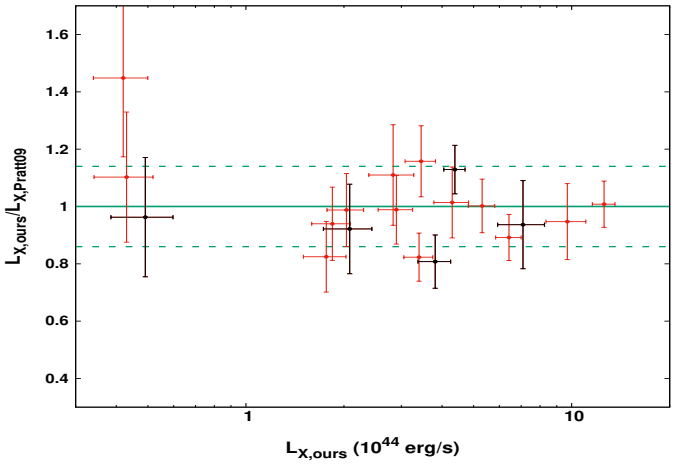

Figure 3.34: Fraction of the $L_{\rm X,ours}$ used in this analysis over the ones derived in G. W. Pratt et al. (2009) ($L_{\rm X,Pratt09}$) for the 19 common clusters between the two samples. The clusters lying in statistically significant low A regions are displayed with black. Also, the equality line is displayed (solid green) with its 1σ scatter (dashed green).

cluster parameters are constrained. Below we show that the way R_{500} is determined and used in our work is almost independent of changes in cosmological parameters (in particular H_0 which we fit), which propagates to the T determination.

The apparent size of R_{500} which we use, is in arcmin. Thus, it is equal to the physical size of R_{500} in Mpc over D_A. Moreover, the $R^{\rm Mpc}_{500}$ is derived based on the $L_{\rm X} \sim E(z)^{7/3} M^{1.64}_{500}$ relation of M. Arnaud et al. (2010) and the fact that $M_{500} \sim R^3_{500}\, H^2_0 E(z)^2$. With the measured redshift z of the clusters remaining unchanged and the cosmological parameters $\Omega_{\rm m}$ and Ω_Λ fixed to global values (as done in Sect. 3.7), this can be written as a function of H_0 as shown in Eq. 4.11.

$$R^{\rm arcmin}_{500} = \frac{R^{\rm Mpc}_{500}}{D_A} \sim \left(\frac{M_{500}}{H^2_0}\right)^{1/3} \frac{1}{D_A} \sim \frac{L^{0.203}_{\rm X}}{H^{0.667}_0} \frac{1}{D_A}. \tag{3.10}$$

The luminosity $L_{\rm X}$ depends on H_0 only through the luminosity distance $D_L \sim 1/H_0$. This dependance writes as $L_{\rm X} \sim D^2_L \sim 1/H^2_0$. Moreover, it also holds that $D_A \sim 1/H_0$. Plugging these two relation in Eq. 4.11 results in:

$$R^{\rm arcmin}_{500} \sim \frac{H^{-0.406}_0}{H^{0.667}_0} H_0 \implies R^{\rm arcmin}_{500} \sim H^{-0.073}_0. \tag{3.11}$$

Consequently, a 20% in H_0, which is similar to the H_0 deviations we obtain in Sect. 3.7, it would only cause a $\sim 1\%$ change in $R^{\rm arcmin}_{500}$ with a similar change in the measured T. At the same time, it would cause a $\sim 45\%$ change in $L_{\rm X}$. Additionally, due to the above, the angular radius within which $L_{\rm X,500}$ is measured does not significantly change as well. Thus, one can safely neglect the impact of H_0 anisotropies on the measured flux through the selection of the apparent radius.

All these strongly demonstrate the usefulness of the $L_{\rm X} - T$ relation for cosmic anisotropies studies.

3.12 Appendix B: Table of galaxy cluster data.

Table 3.4: Properties of the 313 clusters used in this work. Columns: (1) Cluster name. (2) Redshift (X-ray redshifts noted with "*", redetermined redshifts based on optical spectroscopic data noted with "**". (3) Galactic longitude ($^\circ$). (4) Galactic latitude ($^\circ$). (5) Temperature within $0.2 - 0.5\ R_{500}$ (keV). (6) X-ray luminosity within R_{500} for the 0.1-2.4 keV energy range (10^{44} erg/s). (7) Uncertainty of X-ray luminosity (%). (8) X-ray flux (10^{-12} erg/s/cm^2). (9) Neutral + molecular hydrogen column density (10^{20}/cm^2). (10) Metal abundance within $0.2 - 0.5\ R_{500}$ ($Z_\odot$). (11) Instrument used for analysis.

Cluster	z	l	b	T	L_X	σ_{L_X}	f	N_{Htot}	Z	Instrument
(1)	(2)	(3)	(4)	(5)	(6)	(7)	(8)	(9)	(10)	(11)
Coma	0.023	57.227	87.993	$7.410^{+0.049}_{-0.046}$	3.457	12.4	288.00	0.88	$0.417^{+0.021}_{-0.018}$	Chandra
A3526***	0.009	302.399	21.561	$3.401^{+0.041}_{-0.043}$	0.466	3.9	240.00	12.20	$0.436^{+0.022}_{-0.013}$	Chandra
A3571	0.039	316.320	28.561	$7.362^{+0.158}_{-0.171}$	3.932	10.0	109.00	5.08	$0.597^{+0.040}_{-0.042}$	Chandra
A1367	0.021	235.084	73.015	$3.812^{+0.011}_{-0.010}$	1.083	6.0	107.00	1.89	$0.333^{+0.022}_{-0.018}$	Chandra
A2199	0.030	62.931	43.694	$4.036^{+0.052}_{-0.045}$	1.908	2.6	93.90	0.91	$0.365^{+0.015}_{-0.011}$	Chandra
2A0335	0.035	176.261	-35.054	$3.219^{+0.052}_{-0.046}$	3.031	3.1	89.30	30.50	$0.385^{+0.027}_{-0.024}$	Chandra
A1060	0.013	269.596	26.488	$2.788^{+0.092}_{-0.079}$	0.326	6.5	87.90	6.18	$0.486^{+0.039}_{-0.045}$	Chandra
A0496	0.033	209.585	-36.485	$4.638^{+0.087}_{-0.085}$	1.869	3.7	76.70	5.99	$0.537^{+0.038}_{-0.046}$	Chandra
A0085	0.056	115.231	-72.029	$7.234^{+0.054}_{-0.076}$	5.006	3.2	71.50	3.10	$0.389^{+0.012}_{-0.014}$	Chandra
A0262	0.016	136.571	-25.090	$2.196^{+0.055}_{-0.038}$	0.444	4.0	70.60	7.14	$0.388^{+0.019}_{-0.013}$	Chandra
A3667	0.056	340.861	-33.391	$6.380^{+0.019}_{-0.018}$	4.870	5.3	68.00	5.26	$0.409^{+0.007}_{-0.012}$	Chandra
A2029	0.077	6.438	50.534	$8.446^{+0.126}_{-0.107}$	8.966	7.1	63.10	3.73	$0.401^{+0.034}_{-0.039}$	Chandra
NGC5044***	0.009	311.233	46.095	$1.267^{+0.010}_{-0.010}$	0.138	23.1	62.60	6.25	$0.282^{+0.021}_{-0.017}$	Chandra
A1795	0.062	33.822	77.184	$6.420^{+0.055}_{-0.083}$	5.486	2.8	60.60	1.23	$0.311^{+0.009}_{-0.011}$	Chandra
A3558	0.048	311.987	30.726	$5.831^{+0.164}_{-0.155}$	3.300	3.9	59.10	4.84	$0.334^{+0.072}_{-0.067}$	Chandra
A2142	0.089	44.222	48.685	$11.633^{+0.166}_{-0.158}$	10.803	3.0	56.00	4.36	$0.473^{+0.032}_{-0.033}$	Chandra
A2052	0.035	9.412	50.120	$2.879^{+0.040}_{-0.041}$	1.447	3.6	50.80	3.03	$0.430^{+0.021}_{-0.020}$	Chandra
A4038	0.030	25.139	-75.861	$2.843^{+0.060}_{-0.059}$	1.035	3.8	50.50	1.64	$0.398^{+0.031}_{-0.029}$	Chandra
A3266	0.059	272.127	-40.134	$9.919^{+0.248}_{-0.265}$	4.012	1.8	49.20	1.72	$0.340^{+0.055}_{-0.049}$	Chandra
A2147	0.035	28.970	44.535	$4.262^{+0.181}_{-0.137}$	1.369	7.0	47.90	3.38	$0.420^{+0.051}_{-0.058}$	Chandra
NGC4636***	0.004	297.745	65.470	$0.826^{+0.003}_{-0.002}$	0.014	25.1	47.30	2.07	$0.442^{+0.010}_{-0.011}$	Chandra
A0401	0.074	164.185	-38.870	$7.064^{+0.189}_{-0.182}$	6.866	6.5	47.20	15.2	$0.394^{+0.065}_{-0.062}$	Chandra
NGC1550	0.013	190.972	-31.847	$1.209^{+0.014}_{-0.016}$	0.200	6.1	46.00	16.2	$0.266^{+0.018}_{-0.022}$	Chandra
A2256	0.058	111.014	31.759	$8.234^{+0.076}_{-0.060}$	3.664	2.1	45.10	4.95	$0.365^{+0.018}_{-0.022}$	Chandra
A0780	0.054	242.925	25.096	$3.847^{+0.017}_{-0.027}$	2.720	9.1	40.20	5.53	$0.334^{+0.013}_{-0.013}$	Chandra
A2063	0.036	12.812	49.681	$3.337^{+0.098}_{-0.081}$	1.143	4.6	39.70	2.97	$0.381^{+0.043}_{-0.046}$	Chandra
A0478	0.088	182.433	-28.286	$10.895^{+0.052}_{-0.406}$	8.764	5.1	38.90	25.70	$0.437^{+0.001}_{-0.002}$	Chandra
A1644	0.047	304.878	45.450	$5.253^{+0.104}_{-0.089}$	1.886	10.0	36.80	5.10	$0.361^{+0.041}_{-0.042}$	Chandra
A1736	0.046	312.569	35.024	$3.336^{+0.065}_{-0.066}$	1.684	6.5	34.50	5.49	$0.513^{+0.049}_{-0.036}$	Chandra
A3158	0.059	265.052	-48.934	$5.417^{+0.089}_{-0.078}$	2.791	3.3	34.00	1.40	$0.517^{+0.039}_{-0.036}$	Chandra
MKW3s	0.044	11.394	49.458	$3.306^{+0.075}_{-0.069}$	1.469	5.1	32.90	3.00	$0.441^{+0.051}_{-0.046}$	Chandra
A0119	0.044	125.714	-64.062	$5.824^{+0.172}_{-0.126}$	1.487	5.3	31.90	3.98	$0.313^{+0.038}_{-0.035}$	Chandra
A4059	0.047	356.360	-76.081	$4.395^{+0.078}_{-0.072}$	1.640	5.5	31.30	1.26	$0.490^{+0.046}_{-0.043}$	Chandra
A3581	0.023	323.139	32.856	$1.703^{+0.036}_{-0.026}$	0.377	5.8	30.20	5.32	$0.313^{+0.034}_{-0.038}$	Chandra
RBS0540	0.040	203.300	-36.161	$2.774^{+0.135}_{-0.147}$	1.293	5.8	29.90	12.40	$0.412^{+0.082}_{-0.076}$	Chandra
A0399	0.072	164.315	-39.458	$6.686^{+0.138}_{-0.129}$	4.146	5.4	29.20	16.8	$0.249^{+0.047}_{-0.042}$	Chandra
A3112	0.075	252.934	-56.076	$5.486^{+0.133}_{-0.128}$	3.820	3.9	28.60	1.38	$0.387^{+0.066}_{-0.066}$	Chandra
A2589	0.042	94.620	-41.200	$3.560^{+0.059}_{-0.063}$	0.986	11.2	25.20	3.53	$0.390^{+0.027}_{-0.029}$	Chandra
A2657	0.040	96.720	-50.259	$3.755^{+0.113}_{-0.128}$	1.000	6.0	24.70	8.17	$0.319^{+0.055}_{-0.048}$	Chandra
S1101	0.056	348.329	-64.811	$2.447^{+0.070}_{-0.057}$	1.761	7.2	24.40	1.17	$0.230^{+0.028}_{-0.028}$	Chandra
A3562	0.049	313.328	30.357	$5.104^{+0.150}_{-0.150}$	1.378	6.6	24.20	4.47	$0.425^{+0.085}_{-0.088}$	Chandra
A2204	0.151	21.083	33.236	$10.241^{+0.240}_{-0.253}$	14.253	4.8	23.70	7.28	$0.378^{+0.066}_{-0.060}$	Chandra
RXJ0123.6+3315	0.016	130.646	-29.127	$1.320^{+0.018}_{-0.016}$	0.147	15.2	23.30	6.37	$0.307^{+0.022}_{-0.019}$	Chandra
A0576	0.038	161.364	26.247	$4.274^{+0.116}_{-0.107}$	0.792	7.0	22.80	7.03	$0.487^{+0.073}_{-0.077}$	Chandra
A1651	0.084	306.726	58.618	$7.471^{+0.373}_{-0.311}$	3.840	6.0	22.50	1.63	$0.655^{+0.149}_{-0.125}$	Chandra
A2065	0.072	42.837	56.617	$6.593^{+0.112}_{-0.118}$	2.687	5.5	21.20	3.39	$0.428^{+0.037}_{-0.039}$	Chandra
RXCJ1504.1-0248	0.215	355.076	46.198	$10.308^{+0.452}_{-0.384}$	27.156	5.3	20.70	8.39	$0.404^{+0.075}_{-0.061}$	Chandra

Table 3.4: Properties of the 313 clusters used in this work (continued).

Cluster	z	l	b	T	L_X	σ_{L_X}	f	N_{Htot}	Z	Used instrument
(1)	(2)	(3)	(4)	(5)	(6)	(7)	(8)	(9)	(10)	(11)
A2597	0.085	65.341	-64.854	$4.443^{+0.096}_{-0.113}$	3.593	5.8	20.50	2.75	$0.344^{+0.028}_{-0.027}$	Chandra
A2634	0.031	103.479	-33.086	$3.706^{+0.130}_{-0.117}$	0.457	5.1	20.40	6.20	$0.522^{+0.052}_{-0.051}$	Chandra
A1650	0.084	306.676	61.062	$5.724^{+0.085}_{-0.082}$	3.461	6.1	20.30	1.43	$0.323^{+0.023}_{-0.016}$	Chandra
A3376	0.047	246.519	-26.084	$5.891^{+0.212}_{-0.234}$	1.027	4.8	19.70	5.84	$0.743^{+0.118}_{-0.112}$	Chandra
Zw1215.1+0400	0.077	282.503	65.186	$7.600^{+0.383}_{-0.326}$	2.768	5.4	19.70	1.88	$0.423^{+0.113}_{-0.109}$	Chandra
A0133	0.057	149.524	-84.154	$4.251^{+0.061}_{-0.059}$	1.463	6.7	19.30	1.65	$0.364^{+0.032}_{-0.040}$	Chandra
A2255	0.081	93.931	34.924	$7.008^{+0.201}_{-0.181}$	2.976	4.2	18.90	2.74	$0.491^{+0.041}_{-0.047}$	Chandra
A3391	0.051	262.377	-25.149	$5.893^{+0.237}_{-0.257}$	1.246	3.8	18.90	7.59	$0.341^{+0.102}_{-0.091}$	Chandra
A2163	0.203	6.768	30.465	$19.236^{+0.850}_{-0.805}$	24.421	6.4	18.80	20.60	$0.313^{+0.095}_{-0.080}$	Chandra
MKW4	0.020	276.888	62.370	$1.727^{+0.041}_{-0.036}$	0.167	6.0	18.80	1.87	$0.393^{+0.057}_{-0.051}$	Chandra
A2244	0.095	56.789	36.312	$5.994^{+0.134}_{-0.140}$	4.037	3.8	18.60	2.01	$0.366^{+0.056}_{-0.053}$	Chandra
A3532	0.055	304.426	32.478	$4.627^{+0.254}_{-0.281}$	1.428	24.0	18.50	8.44	$0.705^{+0.131}_{-0.126}$	Chandra
UGC03957	0.034	162.219	28.934	$2.318^{+0.231}_{-0.182}$	0.488	7.5	18.50	5.04	$0.257^{+0.122}_{-0.096}$	Chandra
A3827	0.098	332.222	-46.379	$7.521^{+0.253}_{-0.244}$	4.223	6.3	18.20	2.95	$0.501^{+0.054}_{-0.078}$	Chandra
RXCJ1539.5-8335*	0.064	307.564	-22.294	$3.610^{+0.350}_{-0.310}$	1.842	17.5	17.80	10.70	$0.318^{+0.247}_{-0.169}$	Chandra
RXJ0341.3+1524	0.031	172.183	-30.786	$2.072^{+0.080}_{-0.063}$	0.480	7.5	17.80	26.60	$0.255^{+0.039}_{-0.037}$	Chandra
A0400	0.024	170.271	-44.954	$2.250^{+0.086}_{-0.067}$	0.249	20.5	17.30	13.10	$0.647^{+0.070}_{-0.059}$	Chandra
Zw1742.1+3306	0.076	57.910	27.645	$4.252^{+0.125}_{-0.114}$	2.384	4.6	17.00	4.47	$0.438^{+0.063}_{-0.058}$	Chandra
A2151a	0.037	31.478	44.658	$2.098^{+0.066}_{-0.053}$	0.519	7.0	16.30	3.91	$0.266^{+0.037}_{-0.036}$	Chandra
A2107	0.041	34.401	51.527	$4.017^{+0.120}_{-0.096}$	0.625	15.7	16.10	5.35	$0.503^{+0.071}_{-0.059}$	Chandra
A3528S	0.054	303.784	33.643	$4.316^{+0.384}_{-0.318}$	1.164	16.0	15.80	8.23	$0.391^{+0.159}_{-0.165}$	Chandra
A3695	0.089	6.702	-35.548	$6.693^{+0.473}_{-0.456}$	2.945	12.4	15.40	3.46	$0.162^{+0.153}_{-0.110}$	Chandra
S0540	0.036	246.416	-30.291	$2.799^{+0.113}_{-0.098}$	0.444	5.2	15.30	3.33	$0.626^{+0.086}_{-0.073}$	Chandra
A2420	0.085	46.485	-49.454	$6.399^{+0.376}_{-0.345}$	2.706	7.5	15.00	4.26	$0.364^{+0.136}_{-0.146}$	Chandra
A3822	0.076	335.589	-46.457	$5.081^{+0.347}_{-0.286}$	2.133	6.8	14.90	2.53	$0.335^{+0.134}_{-0.119}$	Chandra
A0193	0.049	136.915	-53.268	$3.908^{+0.144}_{-0.149}$	0.835	19.3	14.80	4.92	$0.466^{+0.090}_{-0.079}$	Chandra
NGC6338i	0.028	85.802	35.401	$2.012^{+0.063}_{-0.053}$	0.251	15.4	14.70	2.43	$0.241^{+0.038}_{-0.033}$	Chandra
A1689	0.183	313.361	61.129	$10.442^{+0.238}_{-0.265}$	12.583	8.0	14.50	1.98	$0.381^{+0.036}_{-0.039}$	Chandra
A3558B	0.049	312.396	30.565	$3.609^{+0.156}_{-0.142}$	0.828	30.0	14.40	4.62	$0.302^{+0.078}_{-0.082}$	Chandra
RXCJ2014.8-2430*	0.154	18.329	-28.512	$7.750^{+0.590}_{-0.540}$	9.674	14.0	14.40	11.60	$0.469^{+0.158}_{-0.166}$	Chandra
A2877	0.024	293.051	-70.847	$3.284^{+0.149}_{-0.150}$	0.180	8.0	14.20	1.98	$0.446^{+0.083}_{-0.080}$	Chandra
A2415	0.058	53.978	-45.108	$2.497^{+0.175}_{-0.177}$	1.187	16.2	14.00	6.40	$0.405^{+0.125}_{-0.105}$	Chandra
A3560	0.049	312.721	28.953	$3.594^{+0.180}_{-0.191}$	0.797	9.3	14.00	5.16	$0.328^{+0.108}_{-0.105}$	Chandra
RXCJ1252.5-3116	0.054	303.216	31.603	$2.022^{+0.268}_{-0.246}$	1.003	7.8	14.00	7.49	$0.145^{+0.127}_{-0.145}$	Chandra
RXCJ1558.3-1410*	0.097	356.517	28.672	$5.400^{+0.230}_{-0.170}$	3.665	9.8	14.00	16.80	$0.619^{+0.094}_{-0.091}$	Chandra
NGC5846***	0.006	0.427	48.794	$1.284^{+0.085}_{-0.085}$	0.012	25.3	13.90	5.12	$3.858^{+0.615}_{-0.700}$	Chandra
A2593	0.043	93.448	-43.178	$3.474^{+0.406}_{-0.333}$	0.594	14.5	13.70	4.77	$0.353^{+0.182}_{-0.150}$	Chandra
A0548E	0.042	230.259	-24.417	$3.357^{+0.300}_{-0.247}$	0.546	6.2	13.60	1.63	$0.433^{+0.164}_{-0.132}$	Chandra
S0405*	0.049	296.421	-32.488	$5.019^{+0.299}_{-0.291}$	0.732	35.3	13.60	7.37	$0.535^{+0.155}_{-0.139}$	Chandra
USGCS152	0.015	262.763	40.402	$0.920^{+0.086}_{-0.078}$	0.071	6.8	13.60	4.55	$0.081^{+0.052}_{-0.081}$	Chandra
A2069	0.115	46.901	56.489	$6.599^{+0.282}_{-0.235}$	4.251	14.2	13.30	2.04	$0.280^{+0.091}_{-0.083}$	Chandra
A2665	0.056	96.949	-53.626	$4.255^{+0.272}_{-0.273}$	1.017	11.7	13.20	7.50	$0.249^{+0.176}_{-0.139}$	Chandra
A3921	0.094	321.953	-47.965	$6.166^{+0.250}_{-0.247}$	2.809	8.5	13.20	2.60	$0.347^{+0.087}_{-0.086}$	Chandra
A2061	0.078	48.130	57.161	$4.668^{+0.141}_{-0.159}$	1.873	14.4	13.10	1.80	$0.368^{+0.073}_{-0.063}$	Chandra
IC1365	0.049	53.513	-29.830	$4.448^{+0.279}_{-0.256}$	0.757	8.9	13.00	7.38	$0.623^{+0.158}_{-0.130}$	Chandra
A0376	0.049	147.108	-20.546	$5.045^{+0.337}_{-0.354}$	0.725	6.6	12.90	7.27	$0.552^{+0.192}_{-0.181}$	Chandra
A2572a	0.042	93.858	-38.801	$3.038^{+0.220}_{-0.241}$	0.547	15.3	12.70	5.97	$0.124^{+0.093}_{-0.124}$	Chandra
RXCJ2344.2-0422*	0.080	84.840	-62.163	$4.660^{+0.240}_{-0.290}$	1.941	14.9	12.60	3.82	$0.546^{+0.141}_{-0.137}$	Chandra
RXJ0123.2+3327	0.015	130.500	-28.943	$0.943^{+0.010}_{-0.008}$	0.063	23.5	12.50	6.48	$0.266^{+0.015}_{-0.021}$	Chandra
A1914	0.171	67.204	67.456	$9.055^{+0.368}_{-0.287}$	9.214	5.2	12.30	1.10	$0.316^{+0.042}_{-0.039}$	Chandra

Table 3.4: Properties of the 313 clusters used in this work (continued).

Cluster	z	l	b	T	L_X	σ_{L_X}	f	N_{Htot}	Z	Used instrument
(1)	(2)	(3)	(4)	(5)	(6)	(7)	(8)	(9)	(10)	(11)
MKW8	0.026	355.494	54.791	$2.853^{+0.104}_{-0.066}$	0.194	8.7	12.30	2.68	$0.447^{+0.047}_{-0.043}$	Chandra
A1750	0.085	322.606	59.485	$4.565^{+0.362}_{-0.274}$	2.143	11.6	12.20	2.67	$0.339^{+0.229}_{-0.140}$	Chandra
CAN010*	0.045	151.856	-75.045	$2.520^{+0.260}_{-0.310}$	0.579	28.7	12.20	1.99	$0.247^{+0.175}_{-0.124}$	Chandra
A1307	0.083	243.664	67.753	$5.386^{+0.405}_{-0.297}$	2.109	8.2	12.10	3.26	$0.445^{+0.150}_{-0.135}$	Chandra
A2426	0.098	49.685	-49.489	$5.888^{+0.534}_{-0.498}$	2.862	8.7	12.00	4.80	$0.142^{+0.181}_{-0.100}$	Chandra
A2734	0.062	19.563	-80.985	$4.405^{+0.208}_{-0.177}$	1.076	9.0	12.00	1.45	$0.242^{+0.088}_{-0.086}$	Chandra
A3128	0.062	264.800	-51.123	$3.823^{+0.358}_{-0.351}$	1.101	5.5	12.00	1.53	$0.589^{+0.207}_{-0.191}$	Chandra
A1413	0.143	226.184	76.785	$8.730^{+0.291}_{-0.207}$	6.123	6.4	11.90	1.97	$0.363^{+0.055}_{-0.043}$	Chandra
A1775*	0.075	31.955	78.714	$3.621^{+0.061}_{-0.062}$	1.594	16.7	11.90	1.07	$0.615^{+0.041}_{-0.042}$	Chandra
A1767	0.070	112.443	57.001	$5.710^{+0.350}_{-0.416}$	1.373	5.4	11.80	1.96	$0.309^{+0.175}_{-0.144}$	Chandra
AWM4	0.033	39.940	46.490	$2.420^{+0.087}_{-0.085}$	0.303	97.9	11.80	6.42	$0.437^{+0.052}_{-0.055}$	Chandra
IC1262	0.031	69.523	32.072	$1.953^{+0.046}_{-0.054}$	0.244	5.1	11.70	1.89	$0.336^{+0.035}_{-0.031}$	Chandra
S0861	0.051	345.831	-34.282	$2.973^{+0.489}_{-0.347}$	0.697	9.6	11.70	4.93	$0.313^{+0.104}_{-0.078}$	XMM-Newton
A2249	0.080	57.591	34.944	$5.837^{+0.376}_{-0.353}$	1.772	6.1	11.60	2.38	$0.236^{+0.167}_{-0.146}$	Chandra
A2626	0.056	100.448	-38.435	$3.223^{+0.074}_{-0.074}$	0.878	7.5	11.60	4.59	$0.387^{+0.031}_{-0.028}$	Chandra
A1831*	0.078	40.068	74.948	$3.411^{+0.235}_{-0.204}$	1.682	28.9	11.50	1.42	$0.430^{+0.153}_{-0.117}$	Chandra
A1835	0.253	340.387	60.586	$10.909^{+0.372}_{-0.283}$	19.729	7.3	11.50	2.24	$0.411^{+0.063}_{-0.057}$	Chandra
A3911	0.097	336.589	-55.433	$6.467^{+0.492}_{-0.365}$	2.536	9.7	11.40	1.14	$0.557^{+0.166}_{-0.155}$	Chandra
A3341	0.038	235.171	-31.090	$3.415^{+0.344}_{-0.306}$	0.370	7.3	11.30	1.59	$0.546^{+0.230}_{-0.167}$	Chandra
A0970	0.059	253.046	36.859	$4.516^{+0.285}_{-0.298}$	0.922	8.8	11.20	5.59	$0.324^{+0.137}_{-0.114}$	Chandra
A2034	0.113	53.580	59.530	$7.793^{+0.097}_{-0.093}$	3.526	6.4	11.20	1.62	$0.430^{+0.036}_{-0.032}$	Chandra
A2495	0.077	81.204	-41.952	$4.639^{+0.576}_{-0.477}$	1.595	35.7	11.10	6.12	$0.761^{+0.273}_{-0.284}$	Chandra
A3888	0.151	3.938	-59.428	$12.242^{+0.919}_{-0.829}$	6.422	8.9	11.10	1.38	$0.296^{+0.168}_{-0.151}$	Chandra
ZwCl235	0.083	120.731	-38.437	$3.840^{+0.235}_{-0.208}$	1.848	16.4	11.10	4.22	$0.496^{+0.119}_{-0.104}$	Chandra
RXCJ1524.2-3154	0.103	337.056	20.659	$4.195^{+0.206}_{-0.165}$	3.418	15.4	11.00	15.40	$0.367^{+0.093}_{-0.083}$	Chandra
A4010	0.096	359.039	-70.604	$4.361^{+0.645}_{-0.612}$	2.440	22.1	11.00	1.62	$0.641^{+0.185}_{-0.162}$	XMM-Newton
A3880	0.058	18.003	-58.506	$2.701^{+0.174}_{-0.154}$	0.861	8.2	10.90	1.21	$0.296^{+0.118}_{-0.075}$	Chandra
A2457	0.059	68.629	-46.585	$3.726^{+0.301}_{-0.290}$	0.928	15.7	10.70	7.24	$0.345^{+0.161}_{-0.132}$	Chandra
IVZw038	0.017	126.849	-30.288	$1.815^{+0.081}_{-0.088}$	0.073	18.9	10.70	6.55	$0.501^{+0.072}_{-0.071}$	Chandra
A0665	0.182	149.767	34.700	$10.349^{+0.927}_{-0.734}$	9.000	7.5	10.60	5.06	$0.285^{+0.141}_{-0.156}$	Chandra
A2837	0.114	302.863	-36.862	$3.274^{+0.704}_{-0.444}$	3.454	21.2	10.60	7.12	$0.300^{+0.441}_{-0.100}$	Chandra
A3392*	0.043	243.456	-19.963	$2.095^{+0.308}_{-0.232}$	0.453	39.6	10.32	7.96	$0.306^{+0.206}_{-0.127}$	Chandra
A2390	0.233	73.949	-27.817	$14.419^{+0.484}_{-0.557}$	15.674	10.3	10.30	8.39	$0.558^{+0.072}_{-0.071}$	Chandra
RXJ1720.1+2638	0.164	49.222	30.859	$8.224^{+0.280}_{-0.226}$	7.067	6.4	10.30	3.89	$0.496^{+0.115}_{-0.108}$	Chandra
A2219	0.228	72.621	41.469	$12.119^{+0.291}_{-0.267}$	14.189	5.2	10.20	1.87	$0.357^{+0.050}_{-0.046}$	Chandra
PegasusII	0.042	84.146	-47.545	$3.743^{+0.335}_{-0.315}$	0.441	8.3	10.20	6.04	$0.284^{+0.033}_{-0.028}$	XMM-Newton
RXJ1205.1+3920	0.038	158.229	74.447	$1.337^{+0.130}_{-0.115}$	0.350	7.4	10.10	2.92	$0.098^{+0.079}_{-0.049}$	Chandra
A0168	0.045	135.647	-61.953	$2.779^{+0.122}_{-0.110}$	0.469	9.3	10.00	3.33	$0.416^{+0.054}_{-0.055}$	Chandra
A3530	0.054	303.991	32.533	$3.621^{+0.330}_{-0.316}$	0.729	10.4	9.96	8.03	$0.289^{+0.047}_{-0.044}$	XMM-Newton
ZwCl1665	0.029	219.738	22.364	$1.681^{+0.178}_{-0.127}$	0.188	25.4	9.85	2.53	$0.404^{+0.253}_{-0.144}$	Chandra
A0550	0.099	226.157	-21.948	$6.596^{+0.483}_{-0.479}$	2.369	6.8	9.81	4.87	$0.203^{+0.118}_{-0.125}$	Chandra
A2110	0.098	48.791	53.194	$4.003^{+0.321}_{-0.292}$	2.268	10.7	9.73	2.49	$0.305^{+0.205}_{-0.161}$	Chandra
A3404*	0.167	263.670	-22.546	$9.350^{+0.980}_{-0.820}$	7.092	16.2	9.73	7.62	$0.151^{+0.155}_{-0.151}$	Chandra
A3528N	0.054	303.709	33.845	$5.143^{+0.517}_{-0.431}$	0.715	20.0	9.71	8.15	$0.268^{+0.165}_{-0.141}$	Chandra
A1668	0.064	323.376	81.649	$3.089^{+0.244}_{-0.216}$	0.941	8.1	9.60	2.39	$0.342^{+0.153}_{-0.135}$	Chandra
A2670	0.076	81.335	-68.530	$4.449^{+0.179}_{-0.162}$	1.344	12.1	9.58	2.99	$0.390^{+0.098}_{-0.085}$	Chandra
A2811	0.108	357.977	-87.509	$5.891^{+0.490}_{-0.469}$	2.759	9.8	9.58	1.79	$0.364^{+0.036}_{-0.035}$	XMM-Newton
A1084	0.134	256.393	44.037	$4.518^{+0.413}_{-0.397}$	4.378	12.2	9.57	3.89	$0.331^{+0.045}_{-0.043}$	XMM-Newton
A1991	0.059	22.787	60.496	$2.641^{+0.105}_{-0.083}$	0.779	9.0	9.56	2.72	$0.500^{+0.082}_{-0.065}$	Chandra
A0194	0.018	142.065	-62.999	$1.830^{+0.196}_{-0.141}$	0.072	14.1	9.55	4.80	$0.667^{+0.088}_{-0.114}$	XMM-Newton

Table 3.4: Properties of the 313 clusters used in this work (continued).

Cluster	z	l	b	T	$L_{\rm X}$	$\sigma_{L_{\rm X}}$	f	$N_{\rm Htot}$	Z	Used instrument
(1)	(2)	(3)	(4)	(5)	(6)	(7)	(8)	(9)	(10)	(11)
A1800	0.075	40.626	77.139	$4.716^{+0.412}_{-0.393}$	1.270	8.2	9.54	1.20	$0.262^{+0.241}_{-0.147}$	Chandra
S0780*	0.235	340.910	35.074	$9.430^{+1.130}_{-0.780}$	14.755	18.2	9.44	10.10	$0.179^{+0.103}_{-0.179}$	Chandra
S0810	0.073	319.494	-27.513	$3.283^{+0.360}_{-0.327}$	1.192	18.1	9.42	7.10	$0.203^{+0.041}_{-0.041}$	XMM-Newton
A1285*	0.095	275.200	43.877	$6.400^{+0.260}_{-0.310}$	2.007	17.7	9.39	3.88	$0.487^{+0.126}_{-0.106}$	Chandra
S0753	0.013	319.611	26.536	$1.796^{+0.044}_{-0.037}$	0.038	14.4	9.21	6.68	$0.314^{+0.023}_{-0.025}$	Chandra
A0007	0.107	113.289	-29.710	$4.674^{+0.389}_{-0.321}$	2.565	9.1	9.17	5.45	$0.157^{+0.136}_{-0.157}$	Chandra
A3866	0.154	9.408	-56.946	$4.699^{+0.635}_{-0.435}$	5.530	8.8	9.16	1.10	$0.655^{+0.257}_{-0.268}$	Chandra
ZwCl8338	0.050	77.722	26.708	$2.947^{+0.105}_{-0.124}$	0.541	5.0	9.16	4.75	$0.317^{+0.061}_{-0.060}$	Chandra
RXCJ2104.9-5149	0.049	346.393	-41.376	$2.081^{+0.267}_{-0.277}$	0.511	12.3	9.11	2.80	$0.421^{+0.114}_{-0.098}$	XMM-Newton
A3809	0.062	356.057	-49.524	$3.297^{+0.203}_{-0.202}$	0.803	11.0	8.96	1.55	$0.561^{+0.215}_{-0.152}$	Chandra
A0076	0.040	117.861	-55.941	$3.809^{+1.096}_{-1.022}$	0.318	21.5	8.94	3.70	$0.300^{+0.159}_{-0.044}$	XMM-Newton
A2261	0.224	55.591	31.861	$8.913^{+0.644}_{-0.478}$	12.001	6.6	8.93	3.63	$0.623^{+0.146}_{-0.139}$	Chandra
A2009	0.153	28.894	60.141	$6.785^{+0.487}_{-0.456}$	5.405	18.5	8.90	3.89	$0.521^{+0.160}_{-0.149}$	Chandra
RXCJ1304.2-3030	0.012	306.203	32.275	$1.058^{+0.040}_{-0.031}$	0.030	13.6	8.86	8.85	$0.245^{+0.053}_{-0.039}$	Chandra
A2667*	0.233	34.017	-76.609	$10.010^{+1.382}_{-1.010}$	12.652	10.1	8.81	1.85	$0.253^{+0.194}_{-0.253}$	Chandra
A0957	0.045	242.902	42.839	$2.857^{+0.214}_{-0.175}$	0.403	12.8	8.79	3.87	$0.403^{+0.159}_{-0.120}$	Chandra
A2033	0.082	7.309	50.795	$5.099^{+0.434}_{-0.308}$	1.439	17.8	8.79	3.35	$0.469^{+0.195}_{-0.189}$	Chandra
A3378*	0.148	241.785	-24.012	$5.800^{+0.810}_{-0.420}$	4.092	9.8	8.75	4.82	$0.396^{+0.189}_{-0.163}$	Chandra
NGC1650	0.036	213.871	-34.941	$3.212^{+0.623}_{-0.397}$	0.254	10.3	8.58	5.34	$0.333^{+0.105}_{-0.087}$	XMM-Newton
A2428	0.083	51.381	-49.328	$3.345^{+0.331}_{-0.322}$	1.509	10.1	8.57	5.65	$0.245^{+0.033}_{-0.042}$	XMM-Newton
A3733	0.038	17.771	-39.604	$2.205^{+0.244}_{-0.246}$	0.311	11.5	8.49	9.77	$0.221^{+0.050}_{-0.048}$	XMM-Newton
1ES0657	0.296	266.025	-21.248	$15.771^{+0.398}_{-0.326}$	20.510	7.9	8.42	6.44	$0.378^{+0.053}_{-0.042}$	Chandra
A3694	0.094	8.793	-35.204	$3.697^{+0.397}_{-0.374}$	1.772	14.2	8.35	3.48	$0.246^{+0.062}_{-0.045}$	XMM-Newton
A3998	0.089	348.313	-66.442	$4.311^{+0.498}_{-0.472}$	1.609	13.3	8.34	1.66	$0.495^{+0.097}_{-0.088}$	XMM-Newton
RXCJ1926.9-5342	0.057	343.814	-26.671	$1.309^{+0.141}_{-0.117}$	0.667	26.6	8.33	5.00	$0.266^{+0.015}_{-0.017}$	XMM-Newton
A3541	0.129	306.515	38.535	$5.122^{+0.074}_{-0.075}$	3.989	12.5	8.32	13.2	$0.287^{+0.040}_{-0.042}$	Chandra
RBS1847	0.095	324.525	-44.980	$5.619^{+0.484}_{-0.427}$	1.836	8.9	8.27	2.45	$0.579^{+0.246}_{-0.223}$	Chandra
A3126	0.085	269.309	-49.884	$5.087^{+0.377}_{-0.364}$	1.352	7.6	8.25	1.62	$0.415^{+0.216}_{-0.172}$	Chandra
A0189	0.018	140.101	-59.993	$1.269^{+0.034}_{-0.036}$	0.062	23.1	8.21	3.32	$0.275^{+0.056}_{-0.039}$	Chandra
A1437	0.134	273.601	63.262	$7.923^{+0.531}_{-0.421}$	3.723	8.6	8.21	2.29	$0.346^{+0.130}_{-0.119}$	Chandra
A3104	0.072	255.328	-56.297	$3.556^{+0.344}_{-0.354}$	0.947	9.5	8.20	2.03	$0.414^{+0.061}_{-0.069}$	XMM-Newton
A2556	0.087	41.352	-66.966	$4.572^{+0.242}_{-0.286}$	1.508	18.0	8.18	1.97	$0.466^{+0.169}_{-0.126}$	Chandra
NGC7556	0.027	76.065	-56.279	$1.405^{+0.095}_{-0.094}$	0.132	10.6	8.12	4.19	$0.229^{+0.016}_{-0.017}$	XMM-Newton
A0514	0.072	219.486	-35.910	$3.086^{+0.279}_{-0.262}$	1.051	8.8	8.10	4.40	$0.295^{+0.121}_{-0.121}$	Chandra
NGC4325	0.026	279.578	72.198	$1.041^{+0.014}_{-0.013}$	0.125	7.8	8.08	2.54	$0.364^{+0.100}_{-0.079}$	Chandra
A0545	0.154	214.598	-22.706	$8.110^{+0.361}_{-0.377}$	5.684	8.7	7.99	16.3	$0.179^{+0.111}_{-0.179}$	Chandra
A2409	0.147	77.897	-26.625	$6.768^{+0.390}_{-0.373}$	4.882	12.0	7.96	9.02	$0.528^{+0.192}_{-0.206}$	Chandra
A2717	0.049	349.329	-76.489	$2.488^{+0.132}_{-0.130}$	0.444	17.8	7.94	1.22	$0.489^{+0.08}_{-0.077}$	Chandra
A3825	0.075	331.962	-45.782	$4.239^{+0.439}_{-0.405}$	1.069	10.3	7.82	3.28	$0.299^{+0.044}_{-0.038}$	XMM-Newton
RXCJ0340.6-0239	0.035	189.216	-42.735	$1.258^{+0.107}_{-0.146}$	0.221	10.6	7.82	7.33	$0.211^{+0.054}_{-0.014}$	XMM-Newton
A1068	0.137	179.119	60.121	$4.720^{+0.280}_{-0.287}$	3.725	8.3	7.79	1.78	$0.347^{+0.102}_{-0.107}$	Chandra
HCG62	0.015	303.620	53.669	$1.281^{+0.017}_{-0.019}$	0.039	13.2	7.78	3.81	$0.335^{+0.044}_{-0.032}$	Chandra
A2566	0.082	44.835	-67.242	$3.134^{+0.413}_{-0.377}$	1.205	18.2	7.67	1.98	$0.409^{+0.092}_{-0.090}$	XMM-Newton
A1033	0.126	189.303	59.229	$6.333^{+0.252}_{-0.250}$	2.892	11.1	7.65	1.73	$0.296^{+0.077}_{-0.080}$	Chandra
A2384	0.094	33.541	-48.431	$5.830^{+0.270}_{-0.260}$	1.661	20.0	7.56	3.01	$0.754^{+0.356}_{-0.291}$	Chandra
RXJ0352.9+1941*	0.111	171.034	-25.776	$3.370^{+0.170}_{-0.230}$	2.747	12.3	7.54	21.90	$0.460^{+0.188}_{-0.150}$	Chandra
A1205	0.078	255.066	56.002	$5.197^{+1.313}_{-1.039}$	1.088	9.2	7.51	4.40	$0.497^{+0.148}_{-0.135}$	XMM-Newton
A0586	0.171	187.537	21.946	$7.045^{+0.275}_{-0.230}$	5.620	9.1	7.50	5.84	$0.279^{+0.072}_{-0.055}$	Chandra
A3651	0.060	342.826	-30.498	$5.815^{+0.465}_{-0.397}$	0.622	17.0	7.43	4.72	$0.417^{+0.208}_{-0.206}$	Chandra
A3364	0.148	236.934	-26.646	$7.799^{+0.526}_{-0.517}$	4.363	7.5	7.36	2.27	$0.212^{+0.158}_{-0.117}$	Chandra

Table 3.4: Properties of the 313 clusters used in this work (continued).

Cluster	z	l	b	T	L_X	σ_{L_X}	f	N_{Htot}	Z	Used instrument
(1)	(2)	(3)	(4)	(5)	(6)	(7)	(8)	(9)	(10)	(11)
A3301	0.054	242.414	-37.413	$4.832^{+0.462}_{-0.465}$	0.471	10.0	7.29	2.23	$0.301^{+0.078}_{-0.047}$	XMM-Newton
Zw1021.0+0426	0.285	239.399	47.957	$9.254^{+0.524}_{-0.480}$	17.966	8.2	7.26	2.70	$0.239^{+0.074}_{-0.104}$	Chandra
A0990	0.144	165.071	54.123	$8.044^{+0.761}_{-0.700}$	3.858	8.2	7.22	0.85	$0.189^{+0.152}_{-0.123}$	Chandra
S0805	0.015	332.248	-23.600	$1.017^{+0.057}_{-0.047}$	0.038	26.1	7.22	8.24	$0.062^{+0.025}_{-0.019}$	Chandra
NGC1132	0.023	176.442	-51.078	$1.179^{+0.023}_{-0.022}$	0.097	16.2	7.19	6.70	$0.266^{+0.029}_{-0.033}$	Chandra
A0907*	0.164	249.368	33.268	$6.820^{+0.210}_{-0.150}$	5.121	9.3	7.12	6.67	$0.471^{+0.070}_{-0.073}$	Chandra
CID36	0.039	230.415	-26.019	$3.432^{+0.299}_{-0.366}$	0.247	8.9	7.12	1.70	$0.386^{+0.023}_{-0.034}$	XMM-Newton
A0520	0.203	195.810	-24.327	$8.603^{+0.126}_{-0.121}$	8.049	10.6	7.10	6.87	$0.349^{+0.023}_{-0.024}$	Chandra
A1132	0.137	149.227	54.182	$9.937^{+1.282}_{-0.912}$	3.504	7.3	7.08	0.63	$0.692^{+0.273}_{-0.213}$	Chandra
S1063	0.347	349.483	-59.933	$14.200^{+0.676}_{-0.617}$	26.677	10.9	7.04	1.28	$0.433^{+0.088}_{-0.102}$	Chandra
A2175	0.097	49.323	44.378	$5.818^{+0.476}_{-0.453}$	1.634	8.4	7.03	2.87	$0.493^{+0.199}_{-0.212}$	Chandra
AWM5	0.034	49.017	35.928	$2.040^{+0.110}_{-0.099}$	0.192	8.2	7.00	6.37	$0.351^{+0.067}_{-0.070}$	Chandra
S0301	0.023	229.003	-63.960	$1.373^{+0.042}_{-0.034}$	0.087	8.6	6.99	2.56	$0.276^{+0.048}_{-0.041}$	Chandra
A0655	0.127	172.661	35.155	$4.776^{+0.666}_{-0.548}$	2.779	10.9	6.95	4.39	$0.218^{+0.232}_{-0.150}$	Chandra
A2377	0.081	45.090	-43.191	$5.207^{+0.568}_{-0.439}$	1.114	41.6	6.95	4.60	$0.779^{+0.172}_{-0.172}$	XMM-Newton
A0646*	0.127	172.652	34.585	$6.165^{+2.505}_{-1.595}$	2.871	9.1	6.94	4.71	$1.531^{+1.496}_{-1.072}$	Chandra
A1190	0.079	172.773	65.321	$4.061^{+0.344}_{-0.336}$	1.048	10.3	6.90	1.39	$0.330^{+0.217}_{-0.167}$	Chandra
S0555	0.044	243.544	-26.290	$2.334^{+0.235}_{-0.237}$	0.310	10.9	6.88	3.93	$0.304^{+0.073}_{-0.063}$	XMM-Newton
UGC09480*	0.097	28.192	64.419	$4.092^{+0.753}_{-0.746}$	1.556	9.0	6.83	2.59	$0.254^{+0.084}_{-0.075}$	XMM-Newton
S0112	0.066	301.951	-50.303	$3.614^{+0.411}_{-0.392}$	0.687	36.0	6.81	2.37	$0.351^{+0.071}_{-0.063}$	XMM-Newton
S0592	0.227	263.134	-23.433	$10.457^{+0.386}_{-0.319}$	10.106	8.1	6.79	8.28	$0.408^{+0.080}_{-0.096}$	Chandra
A0795	0.136	217.084	40.152	$5.396^{+0.343}_{-0.283}$	3.254	9.6	6.77	3.62	$0.256^{+0.129}_{-0.117}$	Chandra
A2124	0.065	57.691	52.300	$5.165^{+0.361}_{-0.294}$	0.688	22.6	6.74	1.85	$0.352^{+0.153}_{-0.129}$	Chandra
A2104	0.153	2.818	39.212	$9.443^{+0.371}_{-0.359}$	4.862	10.1	6.72	14.50	$0.401^{+0.115}_{-0.109}$	Chandra
A0021	0.094	114.819	-33.711	$6.134^{+0.648}_{-0.434}$	1.428	11.6	6.68	4.46	$0.624^{+0.243}_{-0.251}$	Chandra
RXJ1740.5+3539	0.043	60.603	29.071	$2.149^{+0.249}_{-0.290}$	0.280	6.8	6.58	2.64	$0.160^{+0.035}_{-0.044}$	XMM-Newton
Zw1420.2+4952	0.072	91.322	61.677	$2.283^{+0.231}_{-0.203}$	0.797	8.0	6.57	2.09	$0.197^{+0.052}_{-0.028}$	XMM-Newton
A3856	0.141	2.744	-56.171	$6.931^{+0.547}_{-0.552}$	3.395	10.2	6.55	1.18	$0.432^{+0.147}_{-0.185}$	Chandra
A3490	0.070	287.732	26.484	$5.817^{+0.561}_{-0.537}$	0.833	15.6	6.51	9.69	$0.372^{+0.065}_{-0.063}$	XMM-Newton
A0602	0.062	191.462	25.516	$3.872^{+0.454}_{-0.375}$	0.585	21.0	6.50	3.99	$0.331^{+0.065}_{-0.058}$	XMM-Newton
A3806	0.076	336.952	-45.734	$4.854^{+0.491}_{-0.517}$	0.926	34.6	6.49	2.86	$0.324^{+0.062}_{-0.062}$	XMM-Newton
A3638*	0.080	355.356	-24.025	$2.980^{+0.281}_{-0.247}$	1.025	24.1	6.44	7.36	$0.260^{+0.048}_{-0.053}$	XMM-Newton
A1631	0.046	303.574	47.489	$1.306^{+0.119}_{-0.118}$	0.317	14.9	6.42	3.99	$0.076^{+0.016}_{-0.076}$	XMM-Newton
A3444	0.260	266.827	25.078	$8.130^{+0.610}_{-0.550}$	12.548	9.7	6.41	6.97	$0.576^{+0.144}_{-0.122}$	Chandra
RXJ2129.6+0005	0.235	53.670	-34.474	$7.139^{+0.388}_{-0.350}$	10.004	11.2	6.37	4.21	$0.390^{+0.173}_{-0.144}$	Chandra
A3497	0.068	290.256	30.199	$3.006^{+0.335}_{-0.279}$	0.727	32.4	6.23	6.90	$0.168^{+0.037}_{-0.028}$	XMM-Newton
A1185	0.031	202.971	67.749	$1.963^{+0.171}_{-0.133}$	0.139	26.1	6.15	1.95	$0.125^{+0.042}_{-0.035}$	Chandra
RXJ1347.5-1145*	0.447	324.035	48.812	$16.753^{+1.183}_{-0.894}$	35.140	10.4	6.14	5.82	$0.354^{+0.094}_{-0.085}$	Chandra
A0500	0.067	220.577	-38.484	$5.010^{+0.425}_{-0.413}$	0.673	16.1	6.12	3.53	$0.483^{+0.056}_{-0.054}$	XMM-Newton
A2941*	0.121	285.500	-62.262	$7.301^{+0.692}_{-0.661}$	2.214	16.9	6.09	2.91	$0.488^{+0.046}_{-0.048}$	XMM-Newton
A1451	0.199	288.265	39.973	$9.704^{+1.105}_{-1.041}$	6.605	21.4	6.06	4.48	$0.269^{+0.081}_{-0.078}$	XMM-Newton
A2622	0.061	102.790	-32.498	$2.416^{+0.246}_{-0.207}$	0.543	20.0	6.04	5.75	$0.366^{+0.029}_{-0.019}$	XMM-Newton
A3122	0.064	247.581	-56.069	$4.854^{+0.442}_{-0.425}$	0.582	9.7	6.03	1.57	$0.282^{+0.048}_{-0.047}$	XMM-Newton
Zw1703.8*	0.097	18.813	22.409	$6.989^{+0.793}_{-0.735}$	1.666	21.0	5.97	19.00	$0.428^{+0.042}_{-0.071}$	XMM-Newton
A2443	0.107	80.387	-33.224	$6.305^{+0.127}_{-0.161}$	1.813	20.0	5.94	6.31	$0.425^{+0.059}_{-0.056}$	Chandra
A1757*	0.123	315.371	38.565	$6.526^{+0.642}_{-0.656}$	2.344	93.6	5.91	9.40	$0.381^{+0.083}_{-0.087}$	XMM-Newton
A1927*	0.095	34.784	67.662	$6.783^{+1.279}_{-1.005}$	1.288	10.5	5.90	2.54	$0.320^{+0.512}_{-0.227}$	Chandra
A3814	0.118	16.602	-50.212	$4.399^{+0.431}_{-0.415}$	2.035	12.9	5.90	2.10	$0.425^{+0.057}_{-0.056}$	XMM-Newton
A2064*	0.065	79.876	54.049	$3.700^{+0.410}_{-0.399}$	0.590	23.4	5.86	1.71	$0.326^{+0.267}_{-0.225}$	Chandra
A2218	0.171	97.744	38.127	$6.750^{+0.362}_{-0.323}$	4.623	4.4	5.85	2.83	$0.333^{+0.117}_{-0.108}$	Chandra

Table 3.4: Properties of the 313 clusters used in this work (continued).

Cluster	z	l	b	T	$L_{\rm X}$	$\sigma_{L_{\rm X}}$	f	$N_{\rm Htot}$	Z	Used instrument
(1)	(2)	(3)	(4)	(5)	(6)	(7)	(8)	(9)	(10)	(11)
A3854	0.149	8.457	-56.330	$6.156^{+0.758}_{-0.656}$	3.449	10.7	5.84	1.25	$0.210^{+0.150}_{-0.113}$	Chandra
A1553	0.165	285.589	72.733	$7.650^{+0.817}_{-0.631}$	4.189	10.9	5.83	2.29	$0.558^{+0.237}_{-0.236}$	Chandra
A0013	0.094	72.276	-78.455	$4.719^{+0.196}_{-0.194}$	1.246	11.3	5.82	2.13	$0.332^{+0.061}_{-0.071}$	Chandra
MKW11	0.022	335.015	72.244	$1.061^{+0.023}_{-0.022}$	0.066	13.4	5.82	2.27	$0.285^{+0.076}_{-0.053}$	Chandra
S0868*	0.061	22.879	-29.105	$3.630^{+0.347}_{-0.390}$	0.502	20.6	5.81	5.85	$0.384^{+0.091}_{-0.075}$	XMM-Newton
RXCJ0510.7-0801	0.220	208.598	-26.006	$8.638^{+0.626}_{-0.492}$	7.876	10.7	5.80	8.88	$0.607^{+0.135}_{-0.158}$	Chandra
APMCC772*	0.089	336.029	-51.363	$3.817^{+0.601}_{-0.519}$	1.007	24.4	5.77	1.90	$0.265^{+0.160}_{-0.039}$	XMM-Newton
S0384*	0.061	246.009	-51.760	$3.025^{+0.358}_{-0.345}$	0.491	21.6	5.74	1.29	$0.499^{+0.036}_{-0.065}$	XMM-Newton
CID28*	0.039	217.445	-33.625	$2.450^{+0.160}_{-0.150}$	0.210	23.7	5.72	4.91	$0.871^{+0.175}_{-0.148}$	Chandra
A3836*	0.113	342.543	-50.959	$5.285^{+0.644}_{-0.552}$	1.753	17.5	5.70	1.77	$0.534^{+0.054}_{-0.101}$	XMM-Newton
A2399	0.058	49.815	-44.541	$3.915^{+0.554}_{-0.387}$	0.446	19.0	5.68	3.41	$0.570^{+0.093}_{-0.090}$	XMM-Newton
RXCJ1314.4-2515	0.244	309.482	37.317	$10.628^{+0.947}_{-0.907}$	10.676	16.5	5.68	8.95	$0.358^{+0.049}_{-0.048}$	XMM-Newton
S0851	0.010	350.900	-32.639	$0.913^{+0.016}_{-0.018}$	0.012	30.4	5.67	4.63	$0.453^{+0.096}_{-0.072}$	Chandra
RXJ0228.2+2811*	0.043	147.571	-30.009	$1.449^{+0.067}_{-0.104}$	0.272	20.4	5.66	10.70	$0.041^{+0.024}_{-0.019}$	Chandra
A0407	0.046	150.614	-19.933	$2.504^{+0.151}_{-0.139}$	0.343	26.1	5.61	17.50	$0.338^{+0.102}_{-0.079}$	Chandra
A3570	0.038	314.850	23.711	$2.242^{+0.215}_{-0.215}$	0.194	33.8	5.61	6.37	$0.345^{+0.057}_{-0.052}$	XMM-Newton
A0022	0.141	42.851	-82.977	$7.414^{+0.743}_{-0.708}$	2.897	12.1	5.59	2.55	$0.265^{+0.060}_{-0.059}$	XMM-Newton
A0773	0.217	166.093	43.368	$8.917^{+0.599}_{-0.532}$	7.121	9.0	5.55	1.34	$0.610^{+0.128}_{-0.135}$	Chandra
A2254	0.178	41.438	29.107	$7.548^{+0.631}_{-0.609}$	4.810	9.3	5.53	5.53	$0.295^{+0.041}_{-0.040}$	XMM-Newton
A1918	0.139	106.401	50.819	$5.489^{+0.497}_{-0.498}$	2.573	11.2	5.52	1.42	$0.277^{+0.230}_{-0.180}$	Chandra
A1035	0.079	179.316	58.472	$2.277^{+0.396}_{-0.282}$	0.811	10.4	5.52	1.12	$0.433^{+0.135}_{-0.118}$	XMM-Newton
A2402*	0.081	47.528	-45.776	$2.916^{+0.321}_{-0.365}$	0.886	14.4	5.52	4.24	$0.460^{+0.075}_{-0.092}$	XMM-Newton
ZwCl4905	0.075	276.859	66.152	$3.932^{+0.377}_{-0.366}$	0.743	10.4	5.50	1.54	$0.415^{+0.044}_{-0.043}$	XMM-Newton
A1763	0.228	92.660	73.452	$9.198^{+0.852}_{-0.662}$	8.111	8.1	5.47	0.84	$0.574^{+0.203}_{-0.194}$	Chandra
A1837	0.070	329.236	48.130	$3.872^{+0.296}_{-0.289}$	0.638	13.4	5.47	5.20	$0.354^{+0.030}_{-0.029}$	XMM-Newton
S0987	0.069	30.308	-51.402	$2.627^{+0.448}_{-0.462}$	0.616	15.0	5.45	2.42	$0.197^{+0.081}_{-0.072}$	XMM-Newton
A2721	0.115	352.146	-77.668	$6.323^{+0.670}_{-0.633}$	1.822	13.6	5.45	1.38	$0.323^{+0.073}_{-0.071}$	XMM-Newton
A3653	0.107	346.336	-30.319	$4.732^{+0.499}_{-0.412}$	1.581	14.3	5.42	4.99	$0.529^{+0.209}_{-0.167}$	Chandra
A0697	0.282	186.363	37.261	$14.527^{+1.851}_{-1.579}$	11.803	15.6	5.41	3.28	$0.518^{+0.268}_{-0.239}$	Chandra
A1204	0.171	230.650	65.454	$3.974^{+0.325}_{-0.397}$	4.034	10.8	5.40	1.36	$0.106^{+0.111}_{-0.080}$	Chandra
A0458	0.106	218.840	-50.783	$4.295^{+0.424}_{-0.405}$	1.443	10.0	5.40	1.28	$0.359^{+0.058}_{-0.055}$	XMM-Newton
RXCJ2124.3-7446*	0.062	317.663	-35.777	$3.112^{+0.436}_{-0.385}$	0.511	22.0	5.40	7.15	$0.351^{+0.046}_{-0.066}$	XMM-Newton
A2496*	0.121	47.720	-60.153	$7.098^{+0.815}_{-0.776}$	2.015	21.0	5.37	3.27	$0.525^{+0.102}_{-0.094}$	XMM-Newton
HerA	0.154	23.057	28.942	$4.199^{+0.203}_{-0.172}$	3.490	10.8	5.36	8.60	$0.510^{+0.100}_{-0.080}$	Chandra
RBS0653*	0.286	244.366	-32.130	$10.090^{+0.690}_{-0.480}$	11.926	9.2	5.36	2.26	$0.459^{+0.094}_{-0.098}$	Chandra
A2312	0.093	98.978	24.852	$5.596^{+0.459}_{-0.474}$	1.110	5.4	5.35	5.76	$0.195^{+0.189}_{-0.124}$	Chandra
A3140	0.173	245.471	-53.610	$6.675^{+0.694}_{-0.615}$	4.126	15.4	5.35	1.44	$0.275^{+0.180}_{-0.164}$	Chandra
A3984*	0.197	358.974	-67.268	$8.489^{+1.229}_{-0.724}$	5.382	21.6	5.34	1.67	$0.430^{+0.132}_{-0.064}$	XMM-Newton
A0543	0.171	225.559	-27.266	$6.210^{+1.487}_{-0.946}$	3.991	11.2	5.32	2.61	$0.491^{+0.566}_{-0.336}$	Chandra
A3396	0.176	249.893	-21.649	$6.312^{+0.695}_{-0.659}$	4.330	9.2	5.30	6.95	$0.507^{+0.130}_{-0.108}$	XMM-Newton
S1136	0.064	13.116	-73.048	$2.123^{+0.237}_{-0.253}$	0.505	20.5	5.29	1.28	$0.370^{+0.080}_{-0.073}$	XMM-Newton
A0980	0.158	163.712	53.546	$7.456^{+0.828}_{-0.694}$	3.408	9.2	5.28	0.83	$0.460^{+0.225}_{-0.207}$	Chandra
RXCJ1215.4-3900*	0.114	295.335	23.326	$6.790^{+0.550}_{-0.350}$	1.837	47.3	5.24	9.76	$0.359^{+0.142}_{-0.141}$	Chandra
A2328*	0.143	28.730	-33.561	$7.036^{+0.704}_{-0.683}$	2.675	15.8	5.23	5.42	$0.301^{+0.065}_{-0.054}$	XMM-Newton
Zw1717.9+5636	0.114	84.866	35.068	$3.509^{+0.346}_{-0.348}$	1.668	8.5	5.22	2.39	$0.189^{+0.194}_{-0.125}$	Chandra
A3558C	0.045	312.796	30.287	$3.986^{+0.221}_{-0.203}$	0.249	32.0	5.21	4.46	$0.702^{+0.197}_{-0.156}$	Chandra
S0520	0.295	262.246	-35.377	$9.522^{+1.071}_{-0.891}$	10.385	21.5	5.21	2.21	$0.334^{+0.172}_{-0.168}$	Chandra
RXCJ1353.4-2753	0.047	319.304	33.003	$1.709^{+0.192}_{-0.200}$	0.271	20.8	5.21	5.81	$0.159^{+0.045}_{-0.039}$	XMM-Newton
RBS1842*	0.138	39.954	-53.125	$4.563^{+0.425}_{-0.409}$	2.472	19.6	5.21	2.27	$0.446^{+0.074}_{-0.062}$	XMM-Newton
A3739*	0.159	0.409	-41.860	$6.760^{+0.750}_{-0.410}$	3.291	17.0	5.20	3.48	$0.624^{+0.237}_{-0.219}$	Chandra

Table 3.4: Properties of the 313 clusters used in this work (continued).

Cluster	z	l	b	T	L_X	σ_{L_X}	f	N_{Htot}	Z	Used instrument
(1)	(2)	(3)	(4)	(5)	(6)	(7)	(8)	(9)	(10)	(11)
A0761*	0.091	240.373	24.548	$4.905^{+0.544}_{-0.509}$	1.030	14.9	5.20	5.49	$0.366^{+0.082}_{-0.092}$	XMM-Newton
A1348*	0.113	277.351	47.091	$4.631^{+0.446}_{-0.119}$	1.601	15.0	5.19	2.98	$0.428^{+0.050}_{-0.044}$	XMM-Newton
A1648*	0.075	304.978	36.175	$1.978^{+0.208}_{-0.251}$	0.741	33.6	5.18	8.68	$0.168^{+0.056}_{-0.023}$	XMM-Newton
RXCJ1742.8+3900*	0.042	64.471	29.408	$1.352^{+0.106}_{-0.102}$	0.221	17.6	5.17	3.74	$0.191^{+0.025}_{-0.012}$	XMM-Newton
ZwCl3179	0.143	228.640	53.054	$7.817^{+1.035}_{-0.902}$	2.881	9.4	5.14	4.08	$0.228^{+0.268}_{-0.157}$	Chandra
Zw0959.6+3257	0.050	193.759	53.241	$2.311^{+0.331}_{-0.269}$	0.300	11.1	5.13	1.76	$0.617^{+0.291}_{-0.270}$	Chandra
A2533*	0.110	53.801	-63.036	$3.712^{+0.383}_{-0.362}$	1.539	26.7	5.13	2.91	$0.322^{+0.106}_{-0.031}$	XMM-Newton
RXCJ1337.4-4120*	0.051	312.148	20.713	$2.111^{+0.189}_{-0.193}$	0.338	21.0	5.11	8.52	$0.457^{+0.061}_{-0.067}$	XMM-Newton
A0209	0.206	159.877	-73.507	$9.250^{+0.936}_{-0.712}$	5.681	10.4	5.10	1.51	$0.370^{+0.187}_{-0.181}$	Chandra
A1758a	0.280	107.128	65.292	$8.830^{+0.330}_{-0.279}$	11.024	9.5	5.08	1.06	$0.263^{+0.065}_{-0.058}$	Chandra
A3744	0.038	21.436	-40.136	$3.010^{+0.188}_{-0.157}$	0.173	11.8	5.08	6.00	$0.570^{+0.107}_{-0.108}$	Chandra
A2442	0.090	56.917	-49.823	$4.177^{+0.511}_{-0.468}$	1.040	14.3	5.08	6.40	$0.297^{+0.084}_{-0.077}$	XMM-Newton
ZwCl2701	0.214	163.870	48.543	$6.116^{+0.439}_{-0.315}$	6.074	17.4	5.07	0.80	$0.374^{+0.109}_{-0.116}$	Chandra
A1142	0.035	240.076	59.151	$2.029^{+0.128}_{-0.153}$	0.144	13.7	5.06	2.44	$0.192^{+0.057}_{-0.059}$	Chandra
A2259	0.164	50.386	31.163	$6.655^{+0.580}_{-0.488}$	3.508	8.6	5.05	3.82	$0.649^{+0.265}_{-0.269}$	Chandra
MS1306.7*	0.084	312.143	60.939	$3.484^{+0.442}_{-0.337}$	0.858	15.1	5.05	1.88	$0.223^{+0.113}_{-0.087}$	XMM-Newton

CHAPTER 4

Cosmological implications of the anisotropy of ten multiwavelength galaxy cluster scaling relations

This Chapter presents the second project of my thesis. Here I extend the work of the first project by utilizing various new cluster measurements and probing the isotropy of nine more cluster scaling relations, covering several different parts of the electromagnetic spectrum. Significantly more information on the observed cluster anisotropies is extracted. This offers valuable insights into the cosmological phenomena from which the anisotropies probably originate. The integrated Compton parameter measurements, the half-light radii, and the BCG magnitudes were provided by Dr. Jens Erler, Dr. Florian Pacaud, and Nhan Nguyen, respectively. This Chapter has been submitted for publication to the Astronomy & Astrophysics journal, to which was published (after the submission of this dissertation) as Migkas, K., Pacaud, F., Schellenberger, G., Erler, J., Nguyen, N., Reiprich, T. H., Ramos-Ceja, M.E., and Lovisari, L., 2021, A&A, 649, A151 (link: https://doi.org/10.1051/0004-6361/202140296, Bibcode: 2021A&A...649A.151M).

Abstract

Most cosmological studies, including galaxy cluster ones, adopt the assumption that the Universe is isotropic and homogeneous. Bulk flows are also often presumed to be negligible compared to the Hubble expansion, even at local scales. Their effects on the redshift-distance conversion are hence usually ignored. Any deviation from this consensus can strongly bias the results of such studies, and thus the importance of testing these assumptions cannot be understated. Scaling relations of galaxy clusters can be effectively used for that. In previous works, we observed strong anisotropies in cluster scaling relations, whose origins remain ambiguous. By measuring many different cluster properties, several scaling relations with different sensitivities can be built, and nearly independent tests of cosmic isotropy and large bulk flows are then feasible. In this work, we make use of up to 570 clusters with measured properties at X-ray, microwave and infrared wavelengths, to construct 10 different cluster scaling relations (five of them presented for the first time to our knowledge), and test the isotropy of the local Universe. Through rigorous and robust tests, we ensure that our analysis is not prone to generally known systematic biases, X-ray absorption issues, etc. By combining all available information, we detect an apparent 9% anisotropy in the local H_0 toward $(l, b) \sim (280^{\circ}{}^{+35^{\circ}}_{-35^{\circ}}, -15^{\circ}{}^{+20^{\circ}}_{-20^{\circ}})$. Using isotropic Monte Carlo simulations,

we assess the statistical significance of the anisotropy to be $> 5\sigma$. This result could also be attributed to a $\sim$ 900 km/s bulk flow which seems to extend out to at least $\sim$ 500 Mpc. These two effects are indistinguishable until more high$-z$ clusters are observed by future all-sky surveys, such as eROSITA.

4.1 Introduction

The isotropy of the late Universe has been a question of great debate during the last decades, and a conclusive answer is yet to be given. As precision cosmology enters a new era with numerous experiments covering the full electromagnetic spectrum, the underlying assumption of isotropy for widely adopted cosmological models has to be scrutinized as well. The importance of new, independent tests of high precision cannot be understated. A possible departure of isotropy in the local Universe could have major implications for nearly all aspects of extragalactic astronomy.

Galaxy clusters, the largest gravitationally bound objects in the Universe, can be of great service for this purpose. Due to the multiple physical processes taking place within them, different components of clusters can be observed almost throughout the full electromagnetic spectrum (e.g., S. W. Allen et al., 2011). This provides us with several possible cosmological applications for these objects.

Such a possible application for instance comes from the so-called scaling relations of galaxy clusters (e.g., Kaiser, 1986). These are simply the correlations between the many cluster properties, and can be usually described by simple power-law forms. Some of their measured properties depend on the assumed values of the cosmological parameters (e.g. X-ray luminosity), while others do not (e.g. temperature). Utilizing scaling relations between properties of these two categories can provide us with valuable insights about different aspects of cosmology.

More specifically, the cosmic isotropy can be investigated using such methods. In Migkas et al. (2018) and in Migkas et al. (2020) (hereafter M18 and M20 respectively) we performed such a test with very intriguing results. We studied the isotropy of the X-ray luminosity-temperature ($L_{\rm X} - T$) relation, which we used as a potential tracer for the isotropy of the expansion of the local Universe. In M20 we combined the extremely expanded HIghest X-ray FLUx Galaxy Cluster Sample (eeHIFLUGCS, Reiprich, 2017, Pacaud et al. in prep.) with other independent samples, and detected a $\sim 4.5\sigma$ anisotropy toward the Galactic coordinates $(l, b) \sim (305^{\circ}, -20^{\circ})$. The fact that several other studies using different cosmological probes and independent methods find similar anisotropies toward the same sky patch makes these findings even more interesting.

Multiple possible systematics were tested separately as potential explanations for the apparent anisotropies, but the tension could not be sufficiently explained by any such test. Therefore, the anisotropy of the $L_{\rm X} - T$ relation should be attributed to an underlying, physical reason. There are three predominant phenomena that could create this: unaccounted X-ray absorption, bulk flows, and Hubble expansion anisotropies. Firstly, the existence of yet undiscovered excess X-ray absorption effects could bias our estimates. The performed tests in M20 however showed that this is quite unlikely to explain the apparent anisotropies. Further investigation is needed nonetheless to acquire a better understanding of these possibilities.

Secondly, coherent motions of galaxies and galaxy clusters over large scales, the so-called bulk flows (BFs), could also be the cause of the observed cluster anisotropies. The objects within a BF have a peculiar velocity component toward a similar direction, due to the gravitational attraction of a larger mass concentration such as a supercluster. These nonrandom peculiar velocities are imprinted in the observed redshifts. If not taken into account, they can result in a biased estimation of the clusters' redshift-based distances, and eventually their other properties (e.g., $L_{\rm X}$). The necessary BF amplitude and scale to wash away the observed cluster anisotropies by far surpasses ΛCDM expectations, which predicts that

such motions should not be present at comoving scales of $\gtrsim 200$ Mpc (see references below). If such a motion is confirmed, a major revision of the large scale structure formation models might be needed. BFs have been extensively studied in the past with various methods (e.g., Lauer et al., 1994; M. J. Hudson et al., 2004; Kashlinsky et al., 2008; Kashlinsky et al., 2010; Colin et al., 2011; Osborne et al., 2011; Feindt et al., 2013; Appleby et al., 2015; Carrick et al., 2015; Hoffman et al., 2015; Scrimgeour et al., 2016; Watkins et al., 2015; Peery et al., 2018; Qin et al., 2019). However, most of them used galaxy samples which suffer from the limited scale out to which they can be constructed. No past study has used cluster scaling relations to investigate possible BF signals to our knowledge. A more in-depth analysis to determine if such effects are the origin of the observed cluster anisotropies is thus necessary.

The vast majority of cluster studies ignores the effects of BFs in the observed redshifts assuming the peculiar velocities to be randomly distributed. The frequent use of heliocentric redshifts in local cluster studies (instead of CMB-frame redshifts) might also amplify the introduced bias from BFs. Hence, such discovered motions could strongly distort the results for most cluster studies, and their cosmological applications.

The third possible explanation for our results is an anisotropy in the Hubble expansion, and the redshift-distance conversion. To explain the observed anisotropies obtained in M20 solely by a spatial variation of H_0, one would need a $\sim$ 10% variation between $(l, b) \sim (305^\circ, -20^\circ)$ and the rest of the sky. This scenario would contradict the assumption of the cosmological principle and the isotropy of the Universe, which has a prominent role in the standard cosmological model. This result was derived in M20 based on relatively low$-z$ data, with the median redshift of all the 842 used clusters being $z \sim 0.17$. Hence, for now it is not possible to distinguish between a possibly primordial anisotropy or a relatively local one purely from galaxy clusters. New physics that interfere with the directionality of the expansion rate would be needed in that case, assuming of course that no other underlying issues cause the cluster anisotropies. Many recent studies have tackled this question, with contradicting results (e.g., Bolejko et al., 2016; C. A. P. Bengaly et al., 2018; Colin et al., 2019; Soltis et al., 2019; Andrade et al., 2019; Hu et al., 2020; Fosalba et al., 2020; Salehi et al., 2020; Secrest et al., 2020, see Sect. 4.9 for an extended discussion).

The interplay of the different possible phenomena and the effects they may have on cluster measurements can make it hard to identify the exact origin of the anisotropies. Additionally, maybe a combination of more than one phenomena affects the cluster measurements, since, for instance, the existence of a dark gas cloud does not exclude the simultaneous existence of a large BF. In order to provide a conclusive answer to the problem, other tests with the same cluster samples must be utilized. These new tests should have somewhat different sensitivities than the $L_X - T$ relation. This way, we can cross check if the anisotropies also appear in tests sensitive to X-ray effects only, BFs or cosmological anisotropies only, etc.

In this work, alongside L_X and T, we also measure and use the total integrated Compton parameter Y_{SZ}, the half-light radii of the clusters R and the infrared luminosity L_{BCG} of the brightest galaxy of each cluster (BCGs). This allows us to study 10 different scaling relations between these properties and test their directional dependance. Based on these results, we try to fully investigate the nature of the observed anisotropies and provide conclusive results. Throughout this paper we use a ΛCDM cosmology with $H_0 = 70$ km s^{-1}Mpc^{-1}, $\Omega_m = 0.3$ and $\Omega_\Lambda = 0.7$ in order to constrain the scaling relation parameters, unless stated otherwise.

The paper is organized as follows: in Sect. 4.2 we describe the measurements of the used samples. In Sect. 4.3 we describe the modelling of the scaling relations and the statistical methods and procedures used to constrain their directional behavior. In Sect. 4.4, the full sky best-fit parameters for the 10 scaling relations are presented. In Sect. 4.5, we study the anisotropic behavior of scaling relations which are sensitive only to X-ray absorption effects, and not cosmological factors. In Sect. 4.6, the focal point of

this work is presented, namely the anisotropy of scaling relations which are sensitive to cosmological anisotropies and BFs. In Sects. 4.7 and 4.8, the possible systematic biases are discussed, and the comparison of our results to the ones from isotropic Monte Carlo simulations is presented. Finally, in Sects. 4.9 and 4.10 the discussion and conclusions of this work are given.

4.2 Sample and measurements

As a general basis, we use the eeHIFLUGCS sample. The only exception is the use of the full Meta-Catalog of X-ray detected Clusters of galaxies (MCXC, Piffaretti et al., 2011) for the $L_X - Y_{SZ}$ relation. This is done in order to maximize the available clusters (since both L_X and Y_{SZ} are available beyond eeHIFLUGCS). From eeHIFLUGCS, a slightly different cluster subsample is used for different scaling relations (the vast majority of the subsamples naturally overlap), where all available measurements for both quantities that enter the scaling relation are considered. For the four scaling relations that include T, we use the same sample as in M20. In a nutshell, the sample includes 313 galaxy clusters, the vast majority of which are part of the eeHIFLUGCS sample. It is a relatively low redshift sample with median $z = 0.075$ ($z \in [0.004, 0.45]$), which includes objects with an X-ray flux of $f_{X,0.1-2.4\ keV} \geq 5 \times 10^{-12}$ erg/s/cm^2[1]. The Galactic plane region ($b \leq |20^\circ|$) and the regions around the Virgo cluster and the Magellanic clouds were masked, and no clusters are considered from there. The spatial distribution of the sample in the rest of the sky is quite homogeneous. The X-ray luminosity L_X, the temperature T, the redshift z, the R_{500}, the metallicities of the core Z_{core} and of the $0.2 - 0.5\ R_{500}$ annulus Z_{out} are obtained as described in M20. The only change we make in the sample is the spectral fit of NGC 5846. When Z_{out} is left free to vary it results to unrealistically large values, affecting also the measured T and making NGC 5846 a strong outlier in the $L_X - T$ plane. Thus we repeat the spectral fitting with a fixed value of $Z_{out} = 0.400\ Z_\odot$ (sample's median), which returns $T = 0.927 \pm 0.013$ keV.

For the rest of the scaling relations, the number of clusters used depends on the availability of each measurement, which is described below and summarized in Table 4.2.

4.2.1 Total integrated Compton parameter Y_{5R500}

Galaxy clusters can be observed in the submillimeter regime through the thermal Sunyaev-Zeldovich effect (tSZ). The tSZ is a spectral distortion of the CMB toward the sky positions of galaxy clusters caused by inverse Compton scattering of CMB photons by the hot electrons of the intracluster plasma. This causes a decrement (increment) in the observed temperature of the CMB at frequencies below (above) $\sim$ 217 GHz. The amplitude of this spectral distortion is proportional to the Comptonization parameter y defined as

$$y(r) = \frac{\sigma_T}{m_e c^2} \int_{l.o.s.} k_B\, n_e(r)\, T_e(r)\, dl, \tag{4.1}$$

where σ_T is the Thompson cross section, m_e is the electron rest mass, c is the speed of light, k_B is the Boltzmann constant, n_e the electron number density, T_e their temperature and l.o.s. denotes the line of sight toward the cluster. The product of $k_B n_e(r) T_e(r)$ represents the electron pressure profile $P_e(r)$. We adopted the form of the latter from the widely used Generalized Navarro-Frenk-White (GNFW) pressure profile (Nagai et al., 2007). The necessary values of R_{500} and M_{500} are taken from MCXC.

A common technique for the extraction of the tSZ signal from multifrequency datasets are matched multifilters (MMFs). MMFs allow us to construct a series of optimal spatial filters that are build from the

[1] Measured by (ROSAT).

SED of the tSZ together with a spatial template computed from the expected pressure profile of clusters. MMFs have been widely used in blind cluster searches by the ACT, SPT, and *Planck* collaborations (Hasselfield et al., 2013; Bleem et al., 2015; Planck Collaboration et al., 2016, respectively) and allow for the estimation of the integrated Comptonization parameter Y_{5R500}, where $Y_{5R500} = \int y \, \mathrm{d}\Omega$, with Ω being the chosen solid angle. We measure the Y_{5R500} values with MMFs that are build by using the relativistic tSZ spectrum (e.g., Wright, 1979; Itoh et al., 1998; Chluba et al., 2012), and have zero response to the kinematic SZ (kSZ) spectrum. Values of Y_{5R500} obtained using standard MMFs derived from the nonrelativistic tSZ spectrum without additional kSZ removal were also tested, with completely negligible changes in the results. The exact details of the processes used to extract the Y_{5R500} values are presented in detail in Erler et al. (2019, E19 hereafter) and in Appendix 4.11.

We measure Y_{5R500} for all the 1743 entries in MCXC. We derive a signal-to-noise (S/N) of > 1 for 1472 clusters , S/N> 2 for 1094 clusters, S/N> 3 for 746 clusters, and S/N> 4.5 for 460 clusters. The latter matches the threshold set by the *Planck* 2nd Sunyaev-Zeldovich Source Catalog Planck Collaboration et al. (PSZ2, 2016, hereafter A16). We compare our derived Y_{5R500} values with the ones from PSZ2 in Sect. 4.11. For our work, we only kept clusters with S/N> 2 to avoid using most measurements dominated by random noise, but without losing too many clusters[2]. We always check if increasing the S/N threshold alters our results.

Finally, the cluster quantity that enters the cluster scaling relations is the total integrated Comptonization parameter Y_{SZ}, which is given by

$$Y_{\mathrm{SZ}}[\mathrm{kpc}^2] = Y_{5R500}[\mathrm{arcmin}^2] \times \left(\frac{\pi}{60 \times 180}\right)^2 \times D_A^2, \tag{4.2}$$

where D_A is the angular diameter distance of the cluster in kpc. The dependance of Y_{SZ} on the cosmological parameters therefore enters through D_A.

4.2.2 Half-light radius *R*

The apparent angular size within which half of a cluster's X-ray emission is encompassed, is a direct observable. By using a cosmological model, this observable can be converted to a physical size of a cluster, the half-light radius R. The size of a cluster correlates with many other cluster properties and can be used to construct scaling relations. We measured R for all eeHIFLUGCS clusters, and additionally for all MCXC clusters with $f_{\mathrm{X,0.1-2.4\ keV}} \geq 4.5 \times 10^{-12}$ erg/s/cm^2. This led to 438 measurements.

To measure R, the ROSAT All-Sky Survey (RASS) maps were used. The count-rate growth curves were extracted for all eeHIFLUGCS clusters, and additionally for all MCXC clusters with $f_{\mathrm{X,0.1-2.4\ keV}} \geq 4.5 \times 10^{-12}$ erg/s/cm^2. By a combination of applied iterative algorithms and visual validation by six different astronomers, the plateau of the count-rate growth curves (i.e., the boundaries of cluster X-ray emission) were determined. The radii R within which half of the total emission is enclosed were then found. The exact details of this process will be presented in Pacaud et al. (in prep.).

The point spread function (PSF) of the XRT/PSPC imager of ROSAT varies with the off-axis angle and the photon energies. In general, it is $\leq 1.5'$. To avoid strong biases due to PSF smearing, we excluded all the clusters with $R \leq 2'$. This left us with 418 cluster measurements with a median $R = 3.76'$. Residual PSF smearing effects are still expected to affect the measurements. Since the scaling relations including R are anyway currently inconclusive (see Sect. 4.12), we neglect these effects for now. In future work, any PSF effects will be fully taken into account. eROSITA will also be able to provide R values rather

[2] This S/N threshold is a safe choice since we already know galaxy clusters exist at these sky positions, through their X-ray detection.

insensitive to PSF effects, due to its better spatial resolution.

4.2.3 Near infrared BCG luminosity L_{BCG}

The BCGs were found for the 387 clusters of the eeHIFLUGCS sample. To determine the BCG for all clusters, we used the optical/near infrared (NIR) data from the SDSS (York et al., 2000), Pan-STARRS (Kaiser et al., 2002; Kaiser et al., 2010), VST ATLAS (Shanks et al., 2015), DES (Abbott et al., 2018), 2MASS (Skrutskie et al., 2006) and WISE (Wright et al., 2010) catalogs. The redshifts of the galaxies were either taken from the SDSS catalogue or the NASA/IPAC Extragalactic Database (NED)[3]. All the galaxy magnitudes were corrected for Galactic extinction and the proper k-correction was applied. The exact details on the BCG selection are described in Appendix 4.11.

For this work, we use the magnitudes coming from the 2MASS catalog for two reasons. First and foremost, 2MASS returns the largest number of available BCGs for our sample. Out of the 387 clusters of eeHIFLUGCS, we detected the BCG in 2MASS for 331 of them. Secondly, the infrared BCG luminosities are not strongly sensitive to extinction effects, minimizing the potential risk of unaccounted absorption biases. We exclude all BCGs with $z < 0.03$, as they appear to be systematically overluminous based on all L_{BCG} scaling relations, indicating a flattening of the L_{BCG} relations as low cluster masses. This flattening was also observed by Bharadwaj et al. (2014).

Additionally, the redshift evolution of the BCG luminosity versus the other quantities is unknown. Due to the large scatter of the L_{BCG} scaling relation as shown later in the paper, the applied evolution cannot be left free to vary simultaneously with the other scaling relation parameters, since no reliable constraints are obtained. Subsequently, we opt to also exclude all clusters with $z \geq 0.15$. This allows us to ignore any evolution during the model fitting. Even if this added a small bias in our estimates, it would not be expected to affect the anisotropy analysis, since the cluster redshift distributions of different sky regions are similar (see M20). As such, any potential bias would cancel out when comparing cluster subsamples from different sky regions. These criteria eventually leave us with 244 clusters with 2MASS L_{BCG} measurements with a median redshift of 0.069.

4.2.4 X-ray determined $N_{\mathrm{H,Xray}}$

We determined the total hydrogen column density $N_{\mathrm{H,Xray}}$ using the X-ray spectra of the 313 clusters from M20. The exact details of our methodology can be found in Appendix 4.11. Overall, we were able to obtain a safe estimation of $N_{\mathrm{H,Xray}}$ for 156 clusters. Several systematics might creep in during the whole process, hence we approach the analysis done with these measurements conservatively.

4.2.5 X-ray luminosity L_{X} and redshift z for clusters not included in M20

For the 1430 MCXC clusters not included in the M20 sample, we started from their L_{X} values given in MCXC which are corrected for the absorption traced by the neutral hydrogen column density only. We further corrected them in order to account for the total hydrogen absorption based on the Willingale et al. (2013, hereafter W13) N_{Htot} values. The procedure is exactly the same as the one followed in M20. The only difference here is the use of fixed $T = 5$ keV and $Z = 0.4\ Z_{\odot}$ values for all clusters in the XSPEC (K. A. Arnaud, 1996) apec·phabs model, since we do not have spectral measurements for these clusters. The redshift values were adopted from MCXC.

[3] https://ned.ipac.caltech.edu/

4.2.6 ACC sample

We measured Y_{SZ} for the ACC sample as well, after we excluded all the clusters already included in any of our different subsamples. We also excluded the 55 clusters with Y_{SZ} S/N< 2. This results in 168 clusters with X-ray luminosity and temperature values, with 113 of them having a Y_{SZ} measurement with S/N> 2. Cross-checking the results of a completely independent cluster sample with our sample's results is crucial in order to understand the origin of the observed anisotropies (e.g., to exclude that sample selection effects may bias our results). The properties of the ACC sample as we use it are already given in detail by M18 and M20. In a nutshell, it mainly consists of massive galaxy clusters, spanning across $z \in [0.009, 0.839]$, with a median redshift of 0.226 (for the 113 clusters with Y_{SZ} measurements). The temperatures are obtained by a single-thermal model for the whole cluster, while the X-ray luminosities L_{bol} are given in the bolometric band, within the R_{200} of the cluster (measured within 0.5-2 keV and within a "significance" radius, and then extrapolated). All measurements are performed by Horner (2001) and the ASCA telescope, while we corrected the L_{bol} for the total absorption similarly to our sample's L_X corrections. The necessary R_{500} values to measure Y_{SZ} were obtained using the mass-temperature scaling relation of Reichert et al. (2011). The latter mostly uses XMM-Newton-derived temperatures, which might differ from the ASCA temperatures in general. Thus, we compared the ACC temperatures with our temperatures for the common clusters between the two samples, and applied the necessary calibration factors before calculating R_{500}.

4.3 Scaling relations

We study 10 cluster scaling relations in total, namely the $L_X - Y_{SZ}$, the $L_X - T$, the $Y_{SZ} - T$, the $L_X - L_{BCG}$, the $L_{BCG} - T$, the $R - Y_{SZ}$, the $R - L_X$, the $R - L_{BCG}$, the $R - T$, and the $Y_{SZ} - L_{BCG}$ relations.

The first nine relations are sensitive to either additionally needed X-ray absorption corrections (1), BFs (2), or possible cosmological anisotropies (3). The $Y_{SZ} - L_{BCG}$ cannot trace any of the above effects (4), as explained in Sect. 4.12. An observed anisotropy then could point to systematics in the measurements or methodology, which may affect the other nine scaling relations of interest.

In principle, it's quite challenging to distinguish cases (2) and (3) since their effects on the observed scaling relations are similar. One way to distinguish between the two is to perform a tomography analysis, analyzing redshift shells individually and see if the anisotropies persist at all scales. Evidently, the power with which each scaling relation traces a possible effect varies, since it depends on the relation's scatter and the exact way each effect might intervene with each measurement. The information of what effect each scaling relation can detect is given in Table 4.1. The exact explanation on how a scaling relation detects (or not) an anisotropy origin is given in Sects. 4.5 and 4.6.

The form of the studied scaling relations between some measured cluster quantities Y and X is

$$\frac{Y}{C_Y} E(z)^{\gamma_{YX}} = A_{YX} \times \left(\frac{X}{C_X} \right)^{B_{YX}}, \tag{4.3}$$

where C_Y is the calibration term for the Y quantity, the term $E(z) = [\Omega_m (1+z)^3 + \Omega_\Lambda]^{1/2}$ accounts for the redshift evolution of the $Y - X$ relation, γ_{YX} is the power index of this term, A_{YX} is the normalization of the relation, C_X is the calibration term for the X quantity, and B_{YX} is the slope of the relation. The calibration terms C_Y and C_X are taken to be close to the median values of Y and X respectively. They are shown in Table 4.2, together with the assumed (self-similar) values of γ_{YX}.

Table 4.1: Possible anisotropy causes that can be traced by each cluster scaling relation. 1: Unaccounted X-ray absorption effects. 2: Bulk flows. 3: Cosmological anisotropies. 4: Expected to look isotropic if no systematics exist in the measurements or methodology. The star * means that the detection of an underlying effect is rather weak, and cannot be achieved by current samples.

Measurement	$L_{\rm X}$	$Y_{\rm SZ}$	R	$L_{\rm BCG}$	T
$L_{\rm X}$		1	2*,3*	1	1,2,3
$Y_{\rm SZ}$			2*,3*	4	1*,2,3
R				2*,3*	1*,2,3
$L_{\rm BCG}$					1*,2,3

4.3.1 Linear regression

Similar to M20, in order to constrain the scaling relation parameters we perform a linear regression in the logarithmic space using a χ^2 minimization procedure. We consider two separate cases.

The first case is when we assume to know the universal, isotropic cosmological parameters (or when they do not matter due to canceling out between the two parts of the scaling relation) and wish to constrain the normalization, slope and scatter of a scaling relation. We then constrain the desired parameters by minimizing the expression

$$\chi^2_Y = \sum_{i=1}^{N} \frac{\left(\log Y'_i - \log A_{YX} - B_{YX} \times \log X'_i\right)^2}{{\sigma_{\log Y,i}}^2 + B^2_{YX} \times {\sigma_{\log X,i}}^2 + {\sigma_{{\rm int},YX}}^2}, \tag{4.4}$$

where N is the number of clusters, $Y' = \dfrac{Y(z,H_0)}{C_Y} E(z)^\gamma$, $X' = \dfrac{X(z,H_0)}{C_X}$[4], $\sigma_{\log Y}$ and $\sigma_{\log X}$ are the Gaussian logarithmic uncertainties for Y and X respectively (derived as in M20), and $\sigma_{{\rm int},YX}$ is the intrinsic scatter of the $Y-X$ relation with respect to (wrt) Y, in orders of magnitude (dex). Following Maughan (2007), $\sigma_{{\rm int},YX}$ is iteratively increased and added in quadrature as an extra uncertainty term to every data point until the reduced $\chi^2_{\rm red} \sim 1$[5]. $\sigma_{{\rm tot},YX}$ is the total scatter, equal to the average value of the denominator of Eq. 4.5 for all considered clusters. Finally, we always choose Y to be the quantity with the largest measurement uncertainties.

The second case applies only when there is a strong cosmological dependency on the best-fit scaling relations (i.e., all the T scaling relations). Here we assume the normalization and slope of the scaling relation to be known and direction-independent. This is a reasonable assumption since these two quantities are associated with intrinsic properties of the clusters, and as such there is no obvious reason why they should spatially vary. In this case, the free parameters we wish to constrain are the Hubble constant H_0 or the BF amplitude and direction $u_{\mathbf{BF}}$. To do so, we minimize the following equation:

$$\chi^2_D = \sum_{i=1}^{N} \frac{\left(D_{i,{\rm obs}}(Y,X,A_{YX},B_{YX},\gamma) - D_{i,{\rm th}}(H_0,z,\mathbf{u_{BF}})^{\mathbf{2}}\right)}{\sigma^2_{D_{i,{\rm obs}}} + \sigma^2_{{\rm int},D}}, \tag{4.5}$$

[4] X does not depend on z and H_0 when X =temperature T.

[5] Our analysis and conclusions are rather insensitive to a (small) systematic over- or underestimation of $\sigma_{{\rm int},YX}$. This was tested by repeating our anisotropy analysis using 20% smaller or larger $\sigma_{{\rm int},YX}$. The exact values of $\sigma_{{\rm int},YX}$ are relevant only in Sect. 4.7.2 (Malmquist bias), but a systematic small bias on $\sigma_{{\rm int},YX}$ would again minimize the effects on this test as well.

where D is either the luminosity distance D_L (e.g., for $L_X - T$) or the angular diameter distance D_A (e.g., for $Y_{SZ} - T$), D_{obs} is the observed distance given the measurements Y and X and their exact scaling relation $Y - X$, D_{th} is the theoretically expected distance based on the cosmological parameters (e.g., H_0), the redshift z and the existing BF $u_{\mathbf{BF}}$, $\sigma_{D_{i,obs}}$ is the statistical uncertainty of the observed distance (which is a function of the measurement uncertainties of Y and X), and $\sigma_{int,D}$ is the intrinsic scatter of the relation in Mpc units. The observed distance D_{obs} enters every scaling relation differently. Generally, it is given by

$$D_{obs} = \left[\frac{A_{YX}X'^{B_{YX}}}{Y'}\right]^k \times D_{H_0=70}. \tag{4.6}$$

Here $D_{H_0=70}$ is the distance found for $H_0 = 70$ km/s/Mpc, which enters in the calculation of Y. Its use here cancels out this cosmological contribution to Y. For this, we need $k = \left(1/2, 1/2, 1, -\frac{1}{2B_{TL_{BCG}}}\right)$ for $L_X - T$, $Y_{SZ} - T$, $R - T$, and $L_{BCG} - T$ respectively. This leaves us with X-ray flux (in the cluster's rest frame), apparent size in arcmin, Y_{5R500}, and BCG flux respectively.

We should stress that when searching for cosmological anisotropies, the calculated H_0 variations express *relative* differences between regions. The absolute H_0 values cannot be constrained by cluster scaling relations only since a fiducial H_0 value was assumed to calibrate the relation initially. Hence, the H_0 anisotropy range always extends around the initial H_0 choice. Apparent H_0 fluctuations could also mirror other underlying cosmological effects we are not yet aware of.

4.3.2 Bulk flow detection

We follow two different methods to estimate the best-fit BF. Firstly, we fit the scaling relations to all the clusters, adding a BF component in our fit, as in Eq. 4.5. The free parameters are the direction and amplitude of the BF, and the intrinsic scatter. A_{YX} and B_{YX} are left free to vary within their 1σ uncertainties of the considered (sub)sample, when no BF is applied. Every cluster's redshift (and thus D_{th}) is affected by the BF depending on the angle between the direction of the cluster and the BF direction. Since the spatial distribution of clusters is nearly uniform, any applied BF does not significantly affect the best-fit A_{YX} and B_{YX}, but it does affect the scatter. This procedure essentially minimizes the average Y residuals around each scaling relation (i.e., we get $\chi^2_{red} \sim 1$ for a smaller $\sigma_{int,YX}$), and is thus labeled as "Minimum Residuals" (MR) method.

The second method we follow to detect the best-fit BF is that of the "Minimum Anisotropies" (MA) method. When we add a BF component directly toward the most anisotropic region, other regions start altering their behavior and might appear anisotropic. Absolute apparent isotropy cannot then be achieved. Therefore, the amplitude and direction of the BFs are found so that the final, overall anisotropy signal of the studied relation is minimized. For this, we repeat the anisotropy sky scanning (Sects. 4.3.4 and 4.3.5) every time for a different BF. This procedure is computationally expensive, and thus we reduce the number of bootstrap resamplings to 500 when estimating the uncertainties of the BF characteristics.

We consider both independent redshift shells (redshift tomography) and cumulative redshift bins to constrain the BF motions, with both the MR and MA methods. It is important to note that flux limited samples suffer from certain biases when determining BFs. Probably the most important one is the nonuniform radial distribution of objects. If this is not taken into account, the BFs found for spherical volumes with a large radius, will be strongly affected by low$-z$ objects and not clearly reflect the larger scale motions. This can be partially accounted for if the iterative redshift steps with which we increase the spherical volumes encompass similar numbers of clusters (e.g., Peery et al., 2018, and references therein). That way, the contribution of every scale to the overall BF signal is averaged out. Here, to

minimize the biased contribution of low$-z$ systems to the larger volumes, we consider redshift bins with similar cluster numbers. Finally, the size and redshift range of our sample did not allow us to use the kSZ signal of the clusters to detect any BFs (see Sect. 4.9).

4.3.3 Parameter uncertainties

To estimate the uncertainties of the best-fit parameters, we use a bootstrap resampling method with replacement. We randomly draw 5000 resamplings from the studied (sub)sample of clusters with the same size, constrain their best-fit parameters, and obtain the final distribution of the latter. The quoted parameter uncertainties refer to the 68.3% credible interval defined by the positive and negative $34.1_{\rm th}$ percentile of the distributions wrt to the best-fit value of the full (sub)sample. The best-fit parameters with their uncertainties are therefore marginalized over all the other fit parameters. This method provides more conservative and robust parameter uncertainties than the approach followed in M20, since it depends only on the true, random variation of the studied statistic and not on analytical expressions (e.g., $\Delta\chi^2$ limits).

4.3.4 Detection of anisotropies and parameter sky maps

The methodology followed here is described in detail in Sect. 4.3 of M20, and thus we direct the reader there. In a nutshell, we consider cones of various radii ($\theta = 60^\circ - 90^\circ$) and point them toward every possible direction in the sky (with a resolution of $\leq 1^\circ$). Each time, we consider only the clusters within each cone, and we obtain the best-fit parameters (usually A_{YX} or H_0) with their uncertainties, as described in the two previous sections. We then create a color-coded full sky map based on the best-fit parameters of every direction.

There are only two differences with the method followed in M20. Firstly, in this work we leave the slope B_{YX} free to vary, instead of fixing it to its best-fit value for the full sample. That way, the parameter of interest is marginalized over B_{YX}. In M20 we demonstrated that this choice does not significantly alter our results compared to the case where B_{YX} is kept fixed, but it constitutes a more conservative approach and thus we make it the default. Secondly, we slightly change the applied statistical weight of the fitted clusters which depends on their angular distance from the center of the cone. In M20 we divided the statistical uncertainties $\sigma_{\log Y}$ and $\sigma_{\log X}$ with a normalized cosine factor that shifted from 1 (center of cone) to 0 (edge of cone), despite the actual radius of the cone. Under certain conditions however[6], this method can slightly overestimate the final statistical significance of the observed anisotropies. Even if this does not have an effect on the conclusions of M20, here we choose to follow a more conservative approach, dividing the uncertainties with the $\cos\theta_1$ term, where θ_1 is the angular separation of a cluster from the center of the cone we consider. This results in the same weighting as in M20 for $\theta = 90^\circ$, and in a weaker weighting for $\theta < 90^\circ$.

In order to provide anisotropy direction uncertainties, we perform bootstrap resamplings similar to the ones described in Sect. 4.3.3. For every sample used to create a sky map, we create 1000 bootstrap resamplings and perform the sky scanning again for each one of them. The 68.3% limits of the posterior distribution of the maximum anisotropy direction are reported as the 1σ limits.

4.3.5 Statistical significance of anisotropies

We wish to assess the statistical significance of the observed differences of the scaling relations' behavior toward different directions. The procedure followed here is described in Sect. 4.4 of M20, with only

[6] Only when there are strongly up- or downscattered clusters close to the center of the cone, i.e. with high statistical significance, and the number of clusters is relatively small.

minor differences, such as the the way we calculate the parameter uncertainties (Sect. 4.3.3). Briefly, we obtain the best-fit values of the fitted parameters together with their uncertainties for every direction in the sky. We then identify the region that shares the most statistically significant anisotropy from the rest of the sky (similar to a dipole anisotropy). We assess the statistical significance of the deviation between them by

$$\text{No. of } \sigma = \frac{\mathbf{p_1} - \mathbf{p_2}}{\sqrt{\sigma^2_{\mathbf{p_1}} + \sigma^2_{\mathbf{p_2}}}}, \tag{4.7}$$

where $\mathbf{p_{1,2}}$ are the best-fit values for the two independent subsamples and $\sigma_{\mathbf{p_{1,2}}}$ are their uncertainties derived by bootstrapping[7]. Finally, the statistical significance (sigma) maps are color-coded based on the observed anisotropy level between every region and the rest of the sky.

4.3.6 Monte Carlo simulations

To further validate the effectiveness of our methodology and the statistical significance of the observed anisotropies, we perform Monte Carlo (MC) simulations. We create isotropic cluster samples to which we apply the same procedure as in the real data. That way we estimate the frequency with which artificial anisotropies would be detected in an isotropic Universe, and compare this to the real data. More details are described in Sect. 4.8.

4.3.7 Summary of statistical improvements compared to M20

Here we summarize the improvements in the statistical analysis of this work compared to M20: 1) The parameter uncertainties at every stage of this work are found by bootstrap resampling instead of $\Delta\chi^2$ limits. 2) During the sky scanning for identifying anisotropies, all the "nuisance" parameters (e.g., the slope B) are left free to vary and marginalized over at the end, instead of fixing them to their best fit values. 3) The statistical weighting of clusters during the anisotropy searching is relaxed, to avoid creating any artificial anisotropies. 4) Uncertainties of the anisotropy directions are provided. 5) Monte Carlo simulations are carried out to further assess the statistical significance of the anisotropies.

4.4 General behavior of the 10 scaling relations

As a first step we constrain the overall behavior of the *observed* scaling relations when one considers all the available data from across the sky. The effects of selection biases are discussed in Sect. 4.7.7. The overview of the best-fit results of all the scaling relations is given in Table 4.2, while the scaling relations themselves are plotted in Fig. 4.1.

The $L_X - T$ relation

The full analysis of the $L_X - T$ relation for our sample is presented in detail in M20. The only changes compared to the M20 results are the slightly changed T for NGC 5846 (see Sect. 4.2), and the use of bootstrap resampling for estimating the parameter uncertainties. Accounting for these changes, the best-fit values for the $L_X - T$ relation remain fully consistent with M20 and with previous studies. For a detailed discussion see Sect. 5.1 of M20, while a more recent work confirming our results can be found in Lovisari et al. (2020). The $L_X - T$ plot for the full sample can be found in the top left panel of Fig. 4.1.

[7] In M20 we identified the two regions with the most extreme, opposite behaviors. Naturally, the currently adopted method leads to slightly reduced anisotropy signals, and is part of the most conservative approach we follow here.

The $L_{\rm bol} - T$ results for ACC are shown in M18 and M20. The only difference here is that we perform the χ^2-minimization in the $L_{\rm bol}$ axis, using bootstrap for estimating the parameter uncertainties. Since the bolometric X-ray luminosity is used for ACC (within R_{200}), both A_{LT} and B_{LT} are larger than the results of our sample. Also, $\sigma_{\rm int}$ is $\sim 38\%$ larger for ACC.

The $L_{\rm X} - Y_{\rm SZ}$ relation

The $L_{\rm X} - Y_{\rm SZ}$ scaling relation has been studied in the past (e.g., Morandi et al., 2007; Planck Collaboration et al., 2011; Planck Collaboration et al., 2011; De Martino et al., 2016; Ettori et al., 2020; C. T. Pratt et al., 2020) mostly using $Y_{\rm SZ}$ from *Planck* and $L_{\rm X}$ from ROSAT data and the MCXC catalog. Both of these quantities are efficient proxies of the total cluster mass, they also scale with each other. Their scatter wrt to mass is mildly correlated (e.g., Nagarajan et al., 2019). This results in $L_{\rm X} - Y_{\rm SZ}$ having the lowest scatter among all the scaling relations used in this study.

As mentioned in Sect. 4.2.1, we measured $Y_{\rm SZ}$ for 1095 MCXC clusters with S/N> 2. Studying the $L_{\rm X} - Y_{\rm SZ}$ relation for these objects, we see that there are significant systematic differences between cluster subsamples based on their physical properties. For example, clusters with low $N_{\rm Htot}$ or high z tend to be significantly fainter on average than clusters with high $N_{\rm Htot}$ or low z respectively. Surprisingly, the same behavior persists even when the original MCXC $L_{\rm X}$ values and the $Y_{\rm SZ}$ values from PSZ2 are used. As we increase the S/N threshold, these inconsistencies slowly fade out. More details on these effects can be found in Appendix 4.13. Due to this, we choose to apply a low S/N$\geq$ 4.5 threshold to the $Y_{\rm SZ}$ values (same as in the PSZ2 sample), leaving us with 460 clusters with a median $z \sim 0.14$. The clear benefits of this choice are that clusters with different properties now show fully consistent $L_{\rm X} - Y_{\rm SZ}$ solutions and no systematic behaviors are observed. Additionally, the intrinsic scatter of the $L_{\rm X} - Y_{\rm SZ}$ relation decreases drastically compared to cases with lower S/N thresholds, allowing us to put precise constraints on the best-fit parameters and the possibly observed anisotropies of the relation. For these 460 clusters, the best-fit values are in full agreement with past studies within the uncertainties. The scatter we obtain however is lower than most past studies, most probably due to the use of the same R_{500} between $L_{\rm X}$ and $Y_{\rm SZ}$ in our analysis. The observed slope $B_{LY} \sim 0.93$ is slightly larger than the self-similar prediction of $B_{LY} = 0.8$.

For ACC, no trends for the $Y_{\rm SZ}$ residuals are observed for S/N> 2, with any of the cluster parameters. Therefore all 113 clusters can be used. The slope lies again close to unity, while the scatter is $\sim 32\%$ larger than when our sample is used. Nevertheless, the $L_{\rm X} - Y_{\rm SZ}$ scatter for ACC is sufficiently small to allow for precise constraints. We should note here that for S/N> 4.5, the scatter of ACC is similar to our sample, but this cut would leave us with only 67 clusters, which are not enough for our purposes. The best-fit parameter values and the $L_{\rm X} - Y_{\rm SZ}$ relation are displayed in Table 4.2 and Fig. 4.1 for both samples.

The $L_{\rm X} - L_{\rm BCG}$ relation

The $L_{\rm X} - L_{\rm BCG}$ scaling relation has not been extensively studied in the past. Mittal et al. (2009) and Bharadwaj et al. (2014) used 64 and 85 low-z clusters respectively, to compare the $L_{\rm X} - L_{\rm BCG}$ relation between cool- and noncool-core clusters, finding mild differences mostly for the slope. Furnell et al. (2018) also studied the correlation of the stellar mass of BCGs (which is proportional to its luminosity) with the cluster's $L_{\rm X}$. Here we use significantly more clusters to study the $L_{\rm X} - L_{\rm BCG}$ relation, namely 244. For these objects, the best-fit parameter values for the $L_{\rm X} - L_{\rm BCG}$ relation can be found in Table 4.2. The slope of our analysis is less steep than the one Bharadwaj et al. (2014) find, however they use the bolometric X-ray luminosity, contrary to us. The scatter we obtain is considerably smaller than theirs,

although still significantly large. In fact, this is the scaling relation with the largest scatter out of the 10 we examine. The L_X residuals do not show any systematic behavior as a function of cluster properties.

The $R - L_X$ relation

The relation between R and L_X for galaxy clusters has not been investigated before to our knowledge. Here we use the 418 clusters with both measurements available to constrain this relation. The redshift evolution of $R - L_X$ is unknown, thus we attempt to constrain it since the high number of clusters and the low scatter allow us to do so. We leave γ_{RL_X} free to vary, simultaneously with the rest of the parameters. This results in $\gamma_{RL_X} = -2.15 \pm 1.51$. The implied evolution is not statistically significant since the limited redshift range of the sample does not allow us to constrain it more efficiently. One should not expect the same evolution as in the $R_{500}-L_X$ relation (self-similar prediction of $\gamma \sim 1.3$), since a redshift evolution between the half-light radius R and R_{500} is also expected (e.g., due to the time-varying cool-core cluster fraction).

Since $\gamma_{RL_X} = -2.15$ describes our data best, we fix γ_{RL_X} to this value for the rest of our analysis. After performing the fit for all 418 clusters, we notice that clusters at $z < 0.01$ are systematically downscattered compared to the rest. To avoid any biases during our anisotropy analysis, we exclude them. The final used subsample consists of the remaining 413 clusters. The obtained best-fit parameters are shown in Table 4.2. The R residuals appear to be randomly scattered wrt z, RASS exposure time, $N_{\rm Htot}$, and R. However, a nonnegligible correlation is observed between the residuals and the apparent half-light radius $R_{\rm app}$. The clusters with the lowest $R_{\rm app}$ appear to be downscattered in the $R - L_X$ plane, and vice versa. A mild correlation of the R residuals is also observed with the offset between the X-ray peak and the BCG position. The latter can be used as a tracer of the dynamical state of the cluster, which correlates with the existence (or not) of a cool core in the center of the cluster (e.g., D. S. Hudson et al., 2010; Zitrin et al., 2012; Rossetti et al., 2016; Lopes et al., 2018). Cool-core clusters are expected to strongly bias the scaling relations involving R, since they emit most of their X-ray photons from near their centers. As a result, the half-light radius will be lower compared with noncool-core clusters at a fixed mass. More details on that can be found in Sect. 4.12.

The best-fit parameter values can be found in Table 4.2. The slope is lower than the self-similar prediction for the $R_{500}-L_X$ relation ($B \sim 0.33$), while there is a moderate scatter. Surprisingly, the latter is the largest one observed between all R scaling relations.

The $Y_{SZ} - T$ relation

The $Y_{SZ} - T$ relation has been previously studied by several authors, i.e., Morandi et al. (2007), Planck Collaboration et al. (2011), Bender et al. (2016) and and Ettori et al. (2020) among others. It has never been studied before with such a large number of clusters as the one used in this work. Since the T measurement is needed, we use the sample from M20. We retrieve 263 clusters with Y_{SZ} measurements with S/N> 2 from the M20 sample. No systematic differences in the $Y_{SZ} - T$ relation are observed for different cluster subsamples with different properties. The Y_{SZ} residuals remain consistent with zero with increasing T, z, $N_{\rm Htot}$, and other cluster parameters, while A_{YT}, B_{YT} and $\sigma_{\rm int,YT}$ also stay constant with an increasing S/N cut. These results clearly indicate that the applied S/N threshold does not introduce any strong biases to the $Y_{SZ} - T$ relation (see Appendix 4.13 for more details). The best-fit parameter values that we obtain for these clusters are in line with previous findings. The value of the slope agrees with the self-similar prediction ($B_{YT} = 2.5$), while the scatter is lower than the one for the $L_X - T$ relation. Finally, a single power law perfectly describes the relation since a change in $A_{YT,\rm all}$ and $B_{YT,\rm all}$ is not observed for a changing low T cut. The $Y_{SZ} - T$ relation is displayed in Fig. 4.1.

When using the ACC sample, we obtain a similar scatter with our sample, but with a slightly steeper slope and larger normalization. This is due to the fact that temperatures are measured for ACC considering the entire cluster, leading to generally lower T than our sample (where T is measured within $0.2-0.5\,R_{500}$).

The $Y_{SZ} - L_{BCG}$ relation

The $Y_{SZ} - L_{BCG}$ scaling relation has not been studied in the past, and it is constrained for the first time in this work. The two quantities are expected to scale with each other since they both scale with the cluster mass. We have both measurements for 214 clusters with S/N> 2 for the Y_{SZ} measurement, and the applied redshift limits for the BCGs. When we performed the fit, we did not detect any strong systematic behavior of the residuals as a function of cluster parameters, with the exception of Y_{SZ} S/N, with high Y_{SZ} S/N clusters tending to be upscattered. This behavior persists even with an increasing S/N threshold. Although the best-fit $B_{YL_{BCG}}$ stays unchanged for different S/N cuts, the $A_{YL_{BCG}}$, varies by $\sim 3.4\sigma$ for S/N> 4.5 (Fig. 4.20 in Appendix). Since the residuals are a function of S/N in any case, and since the $Y_{SZ} - L_{BCG}$ relation offers only limited insights in the anisotropy analysis, we adopt S/N> 2, but suggest caution because of the aforementioned dependance of $A_{YL_{BCG}}$. The $Y_{SZ} - L_{BCG}$ best-fit parameters are shown in Table 4.2. The slope lies close to linearity, while the scatter is $\sim 10\%$ smaller than the $L_X - L_{BCG}$ scaling relation.

Table 4.2: Best-fit parameters of the 10 scaling relations. Below we display the scaling relations, their number of used clusters N, their best-fit normalization A and slope B, their intrinsic and total scatter σ_{int} and σ_{tot} respectively, their calibration terms C_Y and C_X, and the power of their redshift evolution γ.

$Y-X$	N	A_{YX}	B_{YX}	$\sigma_{int,YX}$ (dex)	$\sigma_{tot,YX}$ (dex)	C_Y	C_X	γ_{YX}
				Our sample				
$L_X - T$	313	$1.132^{+0.042}_{-0.046}$	$2.086^{+0.073}_{-0.065}$	0.233 ± 0.016	0.258 ± 0.018	10^{44} erg/s	4 keV	-1
$L_X - Y_{SZ}$	460	$2.737^{+0.043}_{-0.049}$	$0.928^{+0.015}_{-0.018}$	0.108 ± 0.008	0.143 ± 0.009	10^{44} erg/s	60 kpc^2	-5/3
$L_X - L_{BCG}$	244	$1.236^{+0.101}_{-0.091}$	0.775 ± 0.152	0.372 ± 0.020	0.379 ± 0.020	10^{44} erg/s	$6 \times 10^{11}\ L_\odot$	-
$Y_{SZ} - T$	263	$1.110^{+0.029}_{-0.033}$	$2.546^{+0.071}_{-0.067}$	0.146 ± 0.013	0.192 ± 0.015	35 kpc^2	5 keV	1
$Y_{SZ} - L_{BCG}$	214	$0.745^{+0.104}_{-0.094}$	0.868 ± 0.138	0.328 ± 0.021	0.341 ± 0.022	35 kpc^2	$6 \times 10^{11}\ L_\odot$	-
$L_{BCG} - T$	196	$0.847^{+0.020}_{-0.025}$	$0.542^{+0.052}_{-0.110}$	0.170 ± 0.008	0.177 ± 0.009	4 keV	$6 \times 10^{11}\ L_\odot$	-
$R - L_X$	413	0.794 ± 0.016	$0.191^{+0.020}_{-0.017}$	0.142 ± 0.008	0.156 ± 0.009	10^{44} erg/s	350 kpc	-2.15
$R - Y_{SZ}$	347	0.895 ± 0.017	$0.141^{+0.015}_{-0.013}$	0.112 ± 0.008	0.128 ± 0.008	350 kpc	35 kpc^2	-2.72
$R - T$	308	0.829 ± 0.016	$0.568^{+0.036}_{-0.040}$	0.126 ± 0.008	0.144 ± 0.010	350 kpc	4 keV	-1.98
$R - L_{BCG}$	243	0.920 ± 0.019	0.232 ± 0.022	0.128 ± 0.009	0.140 ± 0.010	350 kpc	$6 \times 10^{11}\ L_\odot$	-
				ACC				
$L_{bol} - T$	168	$1.074^{+0.067}_{-0.063}$	3.208 ± 0.122	0.345 ± 0.028	0.394 ± 0.033	5×10^{44} erg/s	5 keV	-1
$L_{bol} - Y_{SZ}$	113	$1.591^{+0.063}_{-0.060}$	1.168 ± 0.036	0.149 ± 0.014	0.195 ± 0.019	5×10^{44} erg/s	60 kpc^2	-5/3
$Y_{SZ} - T$	113	1.774 ± 0.084	2.812 ± 0.150	0.159 ± 0.019	0.227 ± 0.026	35 kpc^2	5 keV	1

The $R - Y_{SZ}$ relation

A relation between Y_{SZ} and the X-ray isophotal radius R is expected to exist since both quantities scale with cluster mass. Such a relation has not been observationally constrained however until now. For this

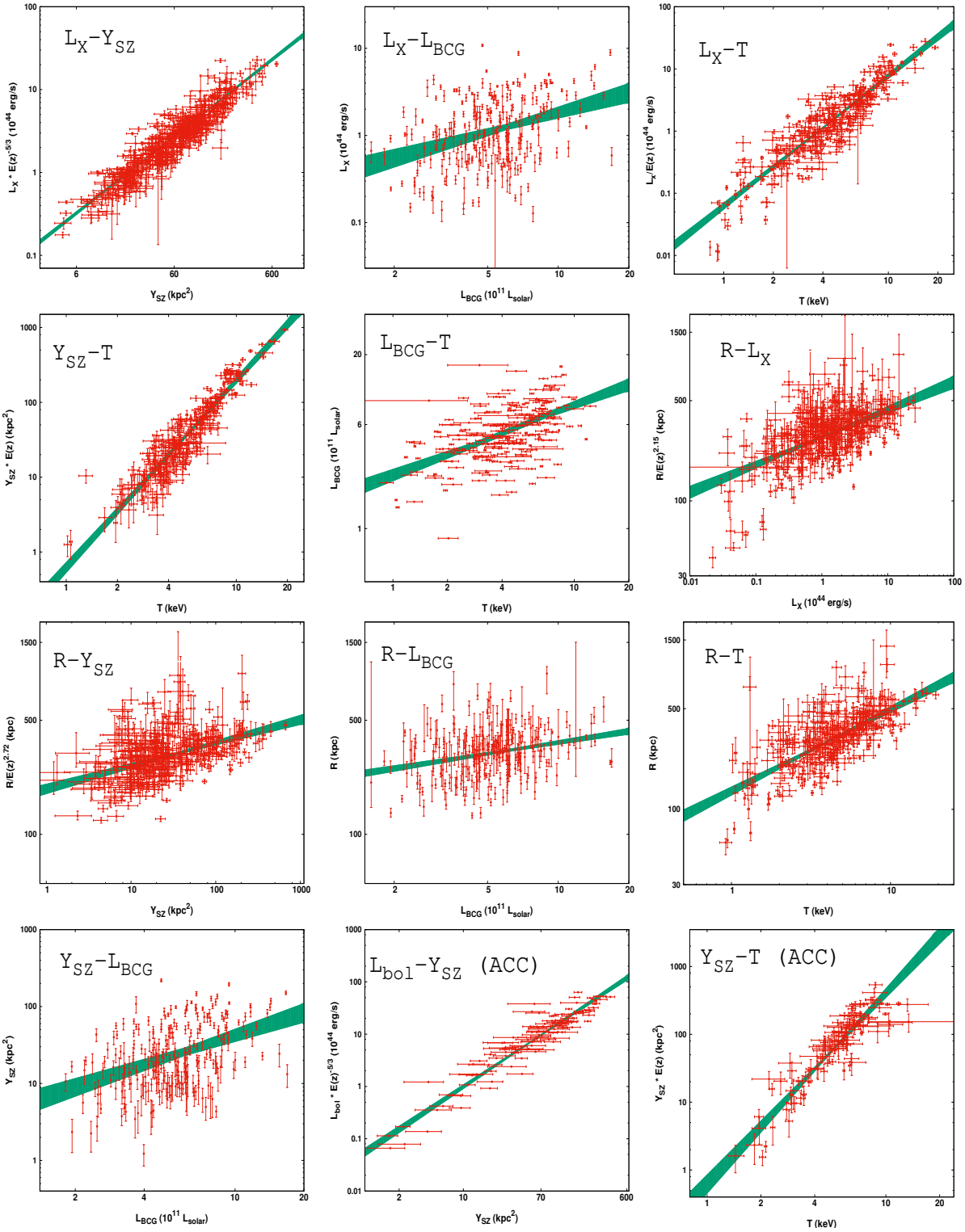

Figure 4.1: Best-fits of the 10 scaling relations studied in this work. The green area displays the 1σ limits of the best-fit area. From top left panel to the right: the $L_X - Y_{SZ}$, $L_X - L_{BCG}$, $L_X - T$, $Y_{SZ} - T$, $L_{BCG} - T$, $R - L_X$, $R - Y_{SZ}$, $R - L_{BCG}$, $R - T$, $Y_{SZ} - L_{BCG}$, $R - Y_{SZ}$, $L_{bol} - Y_{SZ}$ (ACC), and $Y_{SZ} - T$ (ACC) relations.

work, both quantities were measured for 347 clusters. The redshift evolution of the relation is not known, however due to the small scatter it can be obtained observationally, similarly to the $R - L_X$ relation. We find that the scatter is minimized for $\gamma_{RY_{SZ}} = -2.72 \pm 1.41$. Expectingly, the result is similar to γ_{RL_X}. It should be reminded that we look for the evolution describing our data best, and not necessarily for the true one. Fixing $\gamma_{RY_{SZ}}$ to its best-fit value, we repeat the fitting for the rest of the parameters. The results and the $R - Y_{SZ}$ plot are displayed in Table 4.2 and Fig. 4.1 respectively. The residuals of R behave in exactly the same way as for $R - L_X$. While no trend is seen wrt z, the systematic behaviors as functions of R_{app} and of the X-ray-BCG offset persist. The observed scatter is the smallest one between all R scaling relations, $\sim 20\%$ smaller than the $R - L_X$ scatter. Finally, the slope of $R - Y_{SZ}$ is also the flattest compared to the other scaling relations.

The $L_{BCG} - T$ relation

Similarly to the $L_X - L_{BCG}$ relation, the $L_{BCG} - T$ relation has not been the focus of many studies in the past. Bharadwaj et al. (2014) studies the scaling of L_{BCG} with the mass of clusters. The latter is however obtained through a cluster mass-temperature scaling relation. For the $L_{BCG} - T$ relation the exact redshift evolution is also not known, and constraining it from the existing data is not trivial due to the relation scatter and the other simultaneously fit parameters. Due to that, from the 259 clusters for which we have measured both T and L_{BCG}, here we again use only the 196 of them with $z < 0.15$ in order to safely ignore any existing redshift evolution of the relation. The scatter of the $L_{BCG} - T$ relation is considerably large, namely $\sim 70\%$ larger than the $L_X - T$ scatter when the latter is minimized wrt T. The scaling between the two quantities however is clear, although with a less steep slope than the reversed $L_X - T$ one (~ 2.8). The slope has also a larger relative uncertainty ($\sim 10\%$) than the normalization ($\sim 5\%$). The best-fit values are given in Table 4.2.

The $R - L_{BCG}$ relation

The $R - L_{BCG}$ is another scaling relation that is presented for the first time in this work. Both measurements are available for 243 clusters, after the previously described L_{BCG} redshift cuts. As shown in Table 4.2, the intrinsic scatter of the relation is similar to the other R relations, while the slope is slightly larger than the $R - L_X$ and $R - Y_{SZ}$ relations. The same behavior for the R residuals is observed as in the $R - L_X$ and $R - Y_{SZ}$ scaling relations.

The $R - T$ relation

The $R - T$ relation has not been studied extensively in the past, although some studies with both observations and simulations were performed two decades ago (Mohr et al., 1997; Mohr et al., 2000; Verde et al., 2001). The relation has been used as a cosmological probe as well by Mohr et al. (2000), to constrain Ω_m and Ω_Λ. These authors however used only a few tens of clusters to constrain the relation. In this work, we use 308 clusters for which both R and T have been measured. In Mohr et al. (2000) it is argued that there is no redshift evolution for the $R - T$ relation. However, this conclusion specifically depends on their methodology for measuring R, and cannot be adopted for our method. Therefore, we choose to constrain the redshift evolution from our data, leaving it free to vary. We obtain $\gamma_{RT} = -1.98 \pm 1.42$, similar to the other R relations. Fixing $\gamma_{RT} = -1.98$, we obtain the best-fit results shown in Table 4.2. The slope is the largest (~ 0.57) among all R scaling relations. The same R residual behavior as for the other R scaling relations is observed.

4.5 Anisotropies due to unaccounted X-ray absorption effects

In this section we study the scaling relations, whose observed anisotropies could be caused purely by previously unknown soft X-ray effects, such as extra absorption from "dark", metal-rich, gas and dust clouds. If the anisotropies observed in the $L_X - T$ relation by M20 were due to such effects, one should detect the same anisotropies in the scaling relations studied in this section. We report the most anisotropic directions and the statistical significance of the observed tension and quantify the amount X-ray absorbing material that should exist to fully explain the discrepancy.

4.5.1 $L_X - Y_{SZ}$ anisotropies

Our sample

The anisotropies of the $L_X - Y_{SZ}$ relation are the focal point of the search for hidden X-ray effects that we were not aware of in the past. This relation exhibits the lowest scatter and the largest number of clusters among all scaling relations studied in this work. This allows for precise pinpointing of its anisotropies. Even more importantly, $L_X - Y_{SZ}$ is almost completely insensitive to any spatial H_0 variations, since both quantities depend on cosmological parameters in the same way. They also scale almost linearly with each other. Thus, if one changed H_0, no significant change in the best-fit A_{LY} B_{LY} would be observed. Analytically, as $L_X \propto D_L^2 = D_A^2(1+z)^4$ and $Y_{SZ} \propto D_A^2$, their ratio (considering their best-fit $B_{LY} = 0.928$) would be

$$\frac{L_X}{(Y_{SZ})^{0.928}} \propto A_{LY} E(z)^{5/3} \implies A_{LY} \propto \frac{(1+z)^4 D_A^{0.144}}{E(z)^{5/3}}. \tag{4.8}$$

Thus, a $\sim 15\%$ spatial variation of H_0 would cause a nondetectable $\sim 2\%$ variation in A_{LY}. Moreover, the $L_X - Y_{SZ}$ relation is quite insensitive to BFs as well. Based on the above calculation, if a BF of ~ 1000 km/s existed at $z \sim 0.05$ toward a sky region, this would only lead to a $< 2\%$ increase in A_{LY} of this region.

Therefore, any statistically significant anisotropies in the $L_X - Y_{SZ}$ relation should mainly be caused by unaccounted X-ray absorption effects acting on L_X. To scan the sky, we adopt a $\theta = 60^\circ$ cone. This returns at least 72 clusters for each cone, which, considering the very low scatter of the relation, are sufficient to robustly constrain A_{LY}. The variation and significance maps are displayed in Fig. 4.2. We detect the most anisotropic sky region toward $(l, b) = (118^{\circ}{}^{+39^\circ}_{-31^\circ}, +7^{\circ}{}^{+41^\circ}_{-12^\circ})$ which shares a 3.5σ anisotropy with the rest of the sky. The 100 clusters within this region appear to be $12 \pm 3\%$ fainter in average than the rest of the sky. The extra N_{Htot} needed to explain this discrepancy is $\sim 3.9 \pm 1.1 \times 10^{20}/\mathrm{cm}^2$ (the uncertainties were symmetrized). If the assumed hydrogen quantity based on W13 was indeed the true one, then the metallicity of the absorbing material toward that direction would need to be $Z \sim 1.54 \pm 0.16\ Z_\odot$ (currently assumed to be $Z = Z_\odot$). Considering that the specific region lies close to the Galactic plane, this metallicity value does not seem unlikely. The A_{LY} and the anisotropy significance maps of $L_X - Y_{SZ}$ are displayed in Fig. 4.2. One can see that there are no anomalously bright regions. This indicates that there are no regions with significantly lower-than-solar metallicities of the Galactic material. Assuming availability of a much larger number of clusters with L_X and Y_{SZ} measurements, ideally extending to low Galactic latitudes, this scaling relation could potentially be used as a new probe of the ISM metallicity.

It should be stressed that in M20, the most anisotropic direction for the $L_X - T$ relation was found to be $(l, b) \sim (300^\circ, -20^\circ)$. Based on the above test, this region does not show any signs of extra, previously unaccounted absorption. Adding up to the numerous tests done in M20, this further supports the hypothesis that the observed $L_X - T$ anisotropies are not caused by unmodeled Galactic effects.

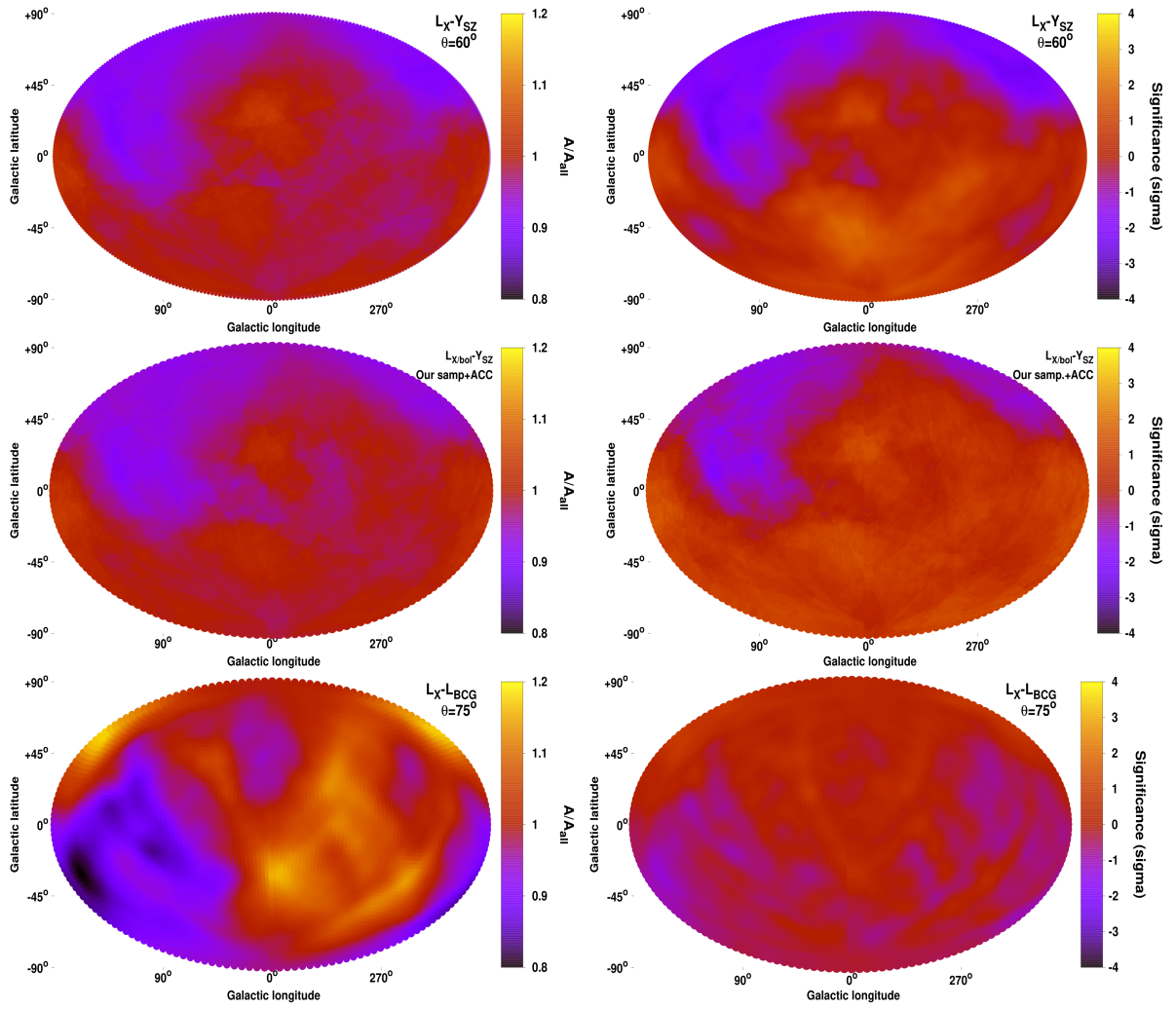

Figure 4.2: Normalization anisotropy maps (left) and the respective statistical significance maps of the anisotropies (right), for $L_X - Y_{SZ}$ (top), joint $L_X - Y_{SZ}$ (our sample + ACC, middle), and $L_{BCG} - T$ (bottom). All the maps in this work are shown in a Hammer projection.

Joint analysis of the $L_X - Y_{SZ}$ relation for our sample and ACC

If the $L_X - Y_{SZ}$ anisotropies seen in our sample indeed originate by the unaccounted absorption effects of a yet undiscovered mass (or a higher interstellar gas and dust metallicity), then we should obtain similar results for the ACC sample. Before extrapolated to L_{bol}, the flux of the ACC clusters was initially measured within the 0.5-2 keV energy range, and thus is sensitive to X-ray absorption effects. Therefore, jointly analyzing the two samples should provide us with better insights for any possible X-ray absorption issues.

To combine the results of the two independent cluster samples, we perform a joint likelihood analysis. The applied method is the one followed in M20 (Sect. 8.2) where we determined the overall apparent H_0 variation. Here, the joint parameter is the $L_X - Y_{SZ}$ normalization for every region over the normalization of the full sample ($A_{LY}/A_{LY,all}$), marginalized over the slope. We extract the posterior likelihood of $A_{LY}/A_{LY,all}$ for every sky region, for both samples. Then by multiplying the two posterior likelihoods, we obtain the combined, final one.

Performing the joint analysis, we find that the most anisotropic region lies toward $(l, b) = (122^{\circ}{}^{+33^{\circ}}_{-34^{\circ}}, +8^{\circ}{}^{+37^{\circ}}_{-12^{\circ}})$, where the clusters appear to be fainter in average by $11 \pm 5\%$ than the rest of the sky. Our sample dominates the joint fitting due to the much higher number of clusters and lower scatter. However, since ACC does not show a strongly deviating behavior toward that region, the statistical significance of the anisotropy drops to just 2.1σ. To fully explain the mild tension, an undetected $N_{Htot} \sim 3.5 \pm 1.7 \times 10^{20}/cm^2$ would be needed, or alternatively a $Z \sim 1.49 \pm 0.23\ Z_{\odot}$ for the already-detected Galactic gas and dust.

As such, the tension could be attributed to chance and not necessarily to an unaccounted X-ray absorption on top of the already applied one. This is also indicated by the MC simulations later on. The normalization and sigma maps of the $L_X - Y_{SZ}$ anisotropies can be found in Fig. 4.2.

4.5.2 $L_X - L_{BCG}$ anisotropies

Following the same reasoning as for $L_X - Y_{SZ}$, the $L_X - L_{BCG}$ scaling relation cannot detect cosmological anisotropies or BFs, since both quantities depend on D_L and the slope is close to unity. Assuming that L_{BCG} does not suffer from any unaccounted extinction in near-infrared, the only origin of any observed (statistically significant) anisotropies should be a stronger true X-ray absorption, affecting L_X. We adopt a $\theta = 75^{\circ}$ cone to scan the sky so each cone contains ≥ 70 objects. The results are displayed in the bottom panel of Fig. 4.2.

The most anisotropic region turns out to be again the one with the lowest $A_{L_X L_{BCG}}$, toward $(l, b) = (171^{\circ}{}^{+29^{\circ}}_{-61^{\circ}}, -22^{\circ}{}^{+23^{\circ}}_{-32^{\circ}})$. It appears to be $23 \pm 14\%$ dimmer than the rest of the sky. Its statistical significance however does not overcome 1.7σ, and therefore the relation is consistent with being statistically isotropic. This might be due to the large scatter and parameter uncertainties of the relation and not necessarily due to the lack of anisotropy-inducing effects. The reported direction is also 57° away from the faintest direction found by the joint $L_X - Y_{SZ}$ analysis, although within $\leq 1.5\sigma$. The necessary excess N_{Htot} to explain this mild discrepancy in the $L_X - L_{BCG}$ relation is $\sim 8.7 \pm 5.1 \times 10^{20}/cm^2$. Alternatively, a metal abundance of $Z \sim 2.4 \pm 0.8\ Z_{\odot}$ of the already-detected hydrogen cloud would also alleviate this small tension. Thus, the $L_X - L_{BCG}$ relation does not show any indications of previously unknown X-ray absorption, although the large scatter of the relation limits the confidence of our conclusions.

Finally, it is noteworthy that for once more, no apparent anisotropy exist toward $(l, b) \sim (300^{\circ}, -20^{\circ})$.

4.5.3 Comparison between $N_{\rm H,Xray}$ and $N_{\rm Htot}$

As a final test for detecting potential excess absorption effects, we compare the X-ray determined $N_{\rm H,Xray}$ with the $N_{\rm Htot}$ value given in W13, used in our default analysis. If a region shows a systematically larger $N_{\rm H,Xray}$, it could indicate an extra, previously unaccounted X-ray absorption taking place toward there. This comparison is performed for the 156 clusters left after the cuts we apply, described in Sect. 4.2.4. The best-fit relation is $N_{\rm H,Xray} = (7.14 \pm 0.34) \times \left(\frac{N_{\rm Htot}}{4 \times 10^{20} {\rm cm}^{-2}}\right)^{0.67 \pm 0.06} \times 10^{20} / {\rm cm}^2$. The X-ray based values are systematically higher than $N_{\rm Htot}$, except for the high $N_{\rm Htot}$ range where the two values converge. This behavior marginally agrees with the findings of Schellenberger et al. (2015), when they used Chandra T measurements and the same abundance table with us. However, this $N_{\rm Htot}$ discrepancy should not be taken at face value, since the overall comparison is biased by the exclusion of clusters with large $N_{\rm H,Xray}$ uncertainties. As discussed in Appendix 4.11, these are mostly low $N_{\rm H,Xray}$ clusters lying below the equality line since the $N_{\rm H,Xray}$ measurement for these clusters is very challenging, due to the lower spectral cut at 0.7 keV. This selection effect would, therefore, tend to flatten the slope. Thus, this systematic upscatter of the remaining $N_{\rm H,Xray}$ values, does not necessarily mean that the true X-ray absorption is higher than previously thought, but it is probably the result of unaccounted systematics. To avoid such issues as much as possible, we just compare the results of a region against the rest of the sky to evaluate if this region deviates more from the W13 values, compared to the rest of the sky. This assumes that any systematics should not be direction-dependent. It should be born in mind that this is an approximate, complementary test due to its limitations, and not a stand-alone check for excess X-ray absorption.

Firstly, we consider the region within 45° around $(l, b) = (281^\circ, -16^\circ)$. This is the most anisotropic and faintest region of the $L_{\rm X} - T$ relation as found in M20, when only our sample is considered. For the 16 clusters lying within this region We find that the best-fit relation is $N_{\rm H,Xray} = (7.64 \pm 1.22) \times \left(\frac{N_{\rm Htot}}{4 \times 10^{20} {\rm cm}^{-2}}\right)^{0.75 \pm 0.25} \times 10^{20} / {\rm cm}^2$. As also shown in the upper panel of Fig. 4.3, the behavior of this region is completely consistent with the rest of the sky. Assuming that the low $N_{\rm Htot}$ clusters indeed have a larger, true $N_{\rm H,Xray}$, then the clusters of the tested region would be less biased, since they have a larger median $N_{\rm Htot}$, compared to the rest of the sky. Consequently, there is no indication that an untraced, excess X-ray absorption is the cause behind the $L_{\rm X} - T$ anisotropies.

The second region we consider is within 45° around $(l, b) = (122^\circ, +8^\circ)$. This region shows mild indications of uncalibrated true X-ray absorption that differs from the W13 values. Using its 11 clusters, we find $N_{\rm H,Xray} = (7.56 \pm 1.04) \times \left(\frac{N_{\rm Htot}}{4 \times 10^{20} {\rm cm}^{-2}}\right)^{0.72 \pm 0.24} \times 10^{20} / {\rm cm}^2$. The results (Fig. 4.3) are again consistent with the rest of the sky, not revealing any signs of a biased applied X-ray absorption correction.

4.5.4 Overall conclusion on possible X-ray biasing effects on the anisotropy studies

The main purpose of this section's analysis was to address if the strong observed $L_{\rm X} - T$ anisotropy found in M20, is caused by unaccounted soft X-ray absorption, not traced by the $N_{\rm Htot}$ values of W13. For instance, a yet undiscovered gas and dust cloud, or some galactic dust with oversolar metallicities, could cause such an effect. Additionally, we also wished to discover if there is such a region elsewhere in the sky.

All the different tests we performed, mostly independent to each other, did not show any signs of possible absorption biases toward $(l, b) \sim (300^\circ, -20^\circ)$. Future tests, particularly with the eROSITA

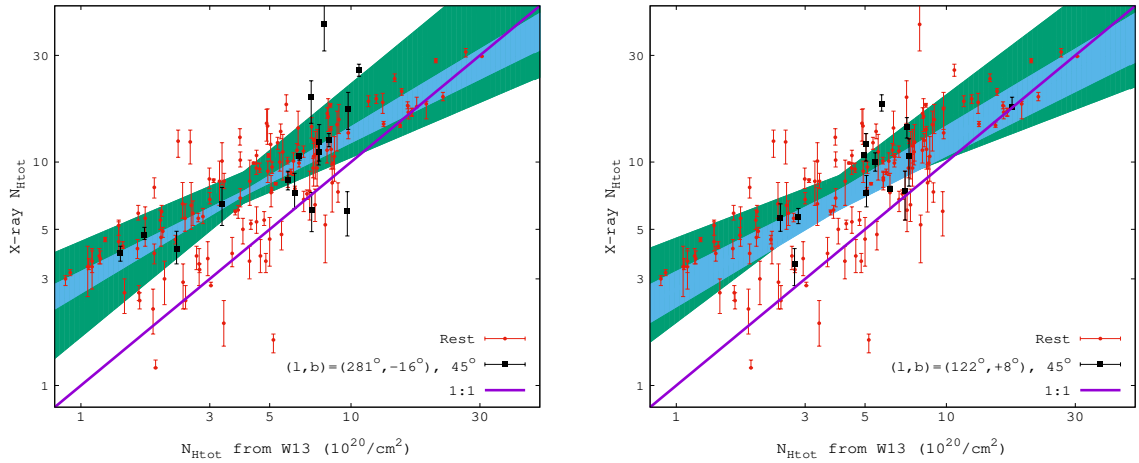

Figure 4.3: Comparison between the N_{Htot} from W13 and the N_{Htot} constrained by our X-ray spectral analysis. The equality line is displayed (purple), as well as the 1σ space of the best-fit function for the region of interest (green, black points) and for the rest of the sky (cyan, red points). The reason for the systematic difference is given in the main text. The region of interest is within 45° from $(l, b) = (281^\circ, -16^\circ)$ (top) and from $(l, b) = (122^\circ, +8^\circ)$ (bottom).

All-Sky Survey (eRASS), will reveal more information on that topic. For now though, we can safely conclude that the anisotropies found in M20 are *not* the result of any biases in the applied soft X-ray absorption correction.

If a mysterious *hard* X-ray absorbing material existed that did not affect soft X-rays, this would have an effect only on the measured T. However, this would lead to underestimated T values, which would cause the opposite anisotropic behavior compared to the M20 results. So this hypothetical scenario is also rejected.

Finally, using the $L_{\mathrm{X}} - Y_{\mathrm{SZ}}$ relation for our sample and ACC, we identified a region, $(l, b) \sim (122^\circ, +8^\circ)$, that might imply an extra needed soft X-ray absorption correction for the clusters there. However, the statistical significance of this result is only $\sim 2\sigma$, while the $L_{\mathrm{X}} - L_{\mathrm{BCG}}$ and the $N_{\mathrm{H,Xray}}$ tests did not reveal any deviations toward that region. Future work will again give a clearer answer, but for now we conclude that no extra correction is needed for the L_{X} values of the clusters lying within this region.

4.6 Anisotropies due to bulk flows or H_0 variations

We have established that strong biases in the X-ray measurements related to previously uncalibrated absorption do not seem to exist, particularly toward $(l, b) \sim (300^\circ, -20^\circ)$. The anisotropies observed in M20 thus cannot arise from such issues. Two more possible origins of such anisotropies are BF motions or spatial variations of cosmological parameters. The first adds a systematic, nonnegligible, local velocity component on the measured redshift of the objects toward a particular direction. If not accounted for, it leads to a systematic over- or underestimation of the clusters' distances, and hence of their cosmology-dependent quantities. The same is true if the real underlying values of the cosmological parameters, e.g., H_0, vary from region to region. This spatial H_0 variation in that case only has to extend up to the redshift range of our samples, as the result of a local, unknown effect, while a convergence to isotropy at larger scales would be perfectly consistent with our results. We proceed to search for anisotropies in scaling relations sensitive to these two phenomena, and attempt to quantify the BF, or the needed H_0 variation to explain the observations.

4.6.1 The $L_X - T$ relation

Our inference of L_X would be strongly affected by either BFs or a cosmological anisotropy through the assumed luminosity distance ($L_X \sim D_L^2$). At the same time, our T measurement would remain relatively unchanged. This allows us to predict the L_X values of the clusters across the sky based on their T and the globally calibrated $L_X - T$, and attribute any directionally systematic deviations to BFs or H_0 anisotropies.

Our sample

The anisotropies of the $L_X - T$ relation are extensively discussed in M20. Here we update our results based on the new statistical methods we follow, whose differences with M20 are described in Sect. 4.3.7. Based on the observed scatter and the number of available clusters, we consider $\theta = 75^\circ$ cones to scan the sky. The maximum anisotropy is detected toward $(l, b) = (274^\circ \pm 43^\circ, -9^\circ \pm 32^\circ)$ (120 clusters), deviating from the rest of the sky by $19 \pm 7\%$ at a 2.8σ level. The decreased statistical significance of the anisotropy compared to the M20 results (3.64σ there) is due to the more conservative parameter uncertainty evaluation which is now based on bootstrap resampling with marginalization over the slope, and the weaker statistical weighting of the clusters close to the center of the considered cones. Also, here we do not compare the two most extreme regions with opposite behavior, but only the most extreme one with the rest of the sky. The $A_{LT}/A_{LT,\mathrm{all}}$ and the sigma maps are given in Fig. 4.4. As expected, they are not significantly different than the ones obtained in M20. The most noticeable difference is the lack of the particularly bright region close to the Galactic center. Now the brightest region is located $\sim 150^\circ$ away from the faintest, indicating an almost dipolar anisotropy.

Cosmological anisotropies and bulk flows We assume that the cause of the observed tension is an anisotropic H_0 value. One would need $H_0 = 66.0 \pm 1.7$ km/s/Mpc toward $(l, b) \sim (274^\circ, -9^\circ)$, and $H_0 = 72.1 \pm 1.4$ km/s/Mpc for the rest of the sky. The respective Hubble diagrams are compared in the top panel of Fig. 4.5.

We now assume that a BF motion is the sole origin of the observed anisotropies, with H_0 being isotropic. Based on the MR method, we find a BF of $u_{\mathbf{BF}} = 1080 \pm 330$ km/s toward $(l, b) = (313^\circ \pm 34^\circ, -17^\circ \pm 20^\circ)$ for the full sample. This result is dominated however by lower z clusters, since there are only 26 clusters with $z > 0.2$. For the redshift range $z \in [0, 0.06]$, we obtain $u_{\mathbf{BF}} = 1160 \pm 420$ km/s toward $(l, b) = (318^\circ \pm 37^\circ, -5^\circ \pm 23^\circ)$. One retrieves a similar BF for clusters within 270 Mpc as for the full sample. Both the direction and amplitude of the BF, as well as its statistical significance, stay within the uncertainties as we consider iteratively larger volumes. The detailed results are given in Table 4.4. For the concentric redshift bins $z \in [0.06, 0.12]$ and $z \in [0.12, 0.3]$, one obtains $u_{\mathbf{BF}} = 1280 \pm 440$ km/s toward $(l, b) = (262^\circ \pm 52^\circ, +2^\circ \pm 26^\circ)$, and $u_{\mathbf{BF}} = 1210 \pm 670$ km/s toward $(l, b) = (253^\circ \pm 60^\circ, -18^\circ \pm 31^\circ)$ respectively. The BF direction is consistent within 1σ between all redshift shells, not showing any convergence even at $\gtrsim 600$ Mpc. The limited number of clusters beyond ~ 600 Mpc is a challenge however for the precise pinpointing of the BF at larger scales. The results are in tension with ΛCDM which predicts negligible BFs at scales of $\gtrsim 200$ Mpc (e.g., Li et al., 2012; Carrick et al., 2015; Qin et al., 2019).

Using the MA method, we find a BF of $u_{\mathbf{BF}} = 650 \pm 280$ km/s toward $(l, b) = (298^\circ \pm 25^\circ, -21^\circ \pm 18^\circ)$ for the full sample. When this BF is applied to our data, the $L_X - T$ relation is consistent with isotropy within 1.4σ based on the usual sky scanning. Unfortunately, for the MA method we need to consider broader redshift bins than with the MR method, in order to have enough data available per sky patch.

For the redshift bins $z \in [0, 0.09]$[8] we find $u_{\mathbf{BF}}$= 730 ± 320 km/s toward $(l, b) = (268^\circ \pm 31^\circ, -5^\circ \pm 23^\circ)$, while iteratively increasing the cosmic volume does not significantly affect this result. For $z > 0.09$, while the anisotropy toward $(l, b) \sim (270^\circ, -25^\circ)$ persists at a $\sim 2\sigma$ level, the search for a BF is inconclusive due to the limited number of clusters, which leads to large uncertainties. To get an idea of the possible BF signal in the MA method purely at larger scales, one can exclude local clusters ($\leq$ 300 Mpc, $z < 0.067$)[9], and only consider the 170 clusters at larger distances. For these, we obtain $u_{\mathbf{BF}}$= 690 ± 340 km/s toward $(l, b) = (293^\circ \pm 39^\circ, -12^\circ \pm 27^\circ)$. Although there is some overlap with the $z \in [0, 0.09]$ results, these findings serve as a hint for BFs extending to larger scales.

We see that both methods reveal large BFs, with no signs of fading when larger volumes or different redshift bins are considered. The direction appears to be relatively consistent between both methods, well within the 1σ uncertainties. The main difference is that the MA method returns a smaller amplitude for the BF, consistent within 1σ though with the MR method. Finally, one sees that the $L_{\rm X} - T$ anisotropies are not subject to a specific redshift bin but consistently extend throughout the z range.

Joint analysis of the $L_{\rm X} - T$ relation for our sample and ACC

As shown in M20 (and in Appendix 4.12), ACC shows a similar anisotropic behavior with our sample, even though it is completely independent of the latter. We perform a joint likelihood analysis of the two independent samples, with the 481 individual clusters they include. We express the apparent anisotropies in terms of H_0, similar to Fig. 23 of M20. The results are plotted in Fig. 4.4. H_0 seems to vary within $\sim 65 - 76$ km/s/Mpc. The most anisotropic region is found toward $(l, b) = (284^{\circ}{}^{+31^\circ}_{-12^\circ}, -4^{\circ}{}^{+7^\circ}_{-23^\circ})$. Its best-fit is $H_0 = 66.2 \pm 1.6$ km/s/Mpc , while for the rest of the sky one gets $H_0 = 72.7 \pm 1.5$ km/s/Mpc. While the posterior H_0 range is identical to the one found in M20, the significance of the anisotropies do not exceed 3σ, due to the more conservative methodology followed here (and due to the nonuse of XCS-DR1 here). The peak anisotropy is close to our sample's result since it dominates the joint fit, something that also shows from the fact that the σ level compared to our sample alone increases only slightly. There is a second, weaker peak on the maximum anisotropy position of ACC.

In terms of a BF motion, there is no meaningful way to combine the two independent datasets in an analytical way similar to the H_0 analysis, since any BF has meaning only within a certain z range. The redshift distribution of the two samples differ however, and in every given redshift shell, one data set will dominate over the other.

4.6.2 The $Y_{\rm SZ} - T$ relation

The anisotropies of the $Y_{\rm SZ} - T$ relation are presented in this work for the first time. $Y_{\rm SZ}$ strongly depends on the angular diameter distance ($Y_{\rm SZ} \sim D_A^2$), which is affected by BFs and possible spatial changes of the cosmological parameters. At the same time T is independent of these effects and thus the same reasoning as in the $L_{\rm X} - T$ relation applies. The advantages of the $Y_{\rm SZ} - T$ relation are three. Firstly, the scatter is clearly smaller than the $L_{\rm X} - T$ relation allowing for more precise constraints. Secondly, $Y_{\rm SZ}$ is unaffected by absorption issues, while T (determined using spectra with photon energies of > 0.7 keV) only has a weak dependence on uncalibrated absorption effects, with much less severe effects than $L_{\rm X}$. Thus, in practice no $Y_{\rm SZ} - T$ anisotropies can occur from unaccounted Galactic absorption issues. Finally, due to the applied redshift evolution of $Y_{\rm SZ} - T$, the latter is more sensitive to BFs than $L_{\rm X} - T$.

[8] Here we go beyond the median z, since low z clusters exhibit a larger scatter (due to galaxy groups), thus we need more than half our sample to obtain valuable constraints. For higher redshifts, the scatter reduces, so fewer clusters can also be used.

[9] This is the scale that many studies consider for studying BFs or local voids (e.g., Betoule et al., 2014; Carrick et al., 2015), see later discussion.

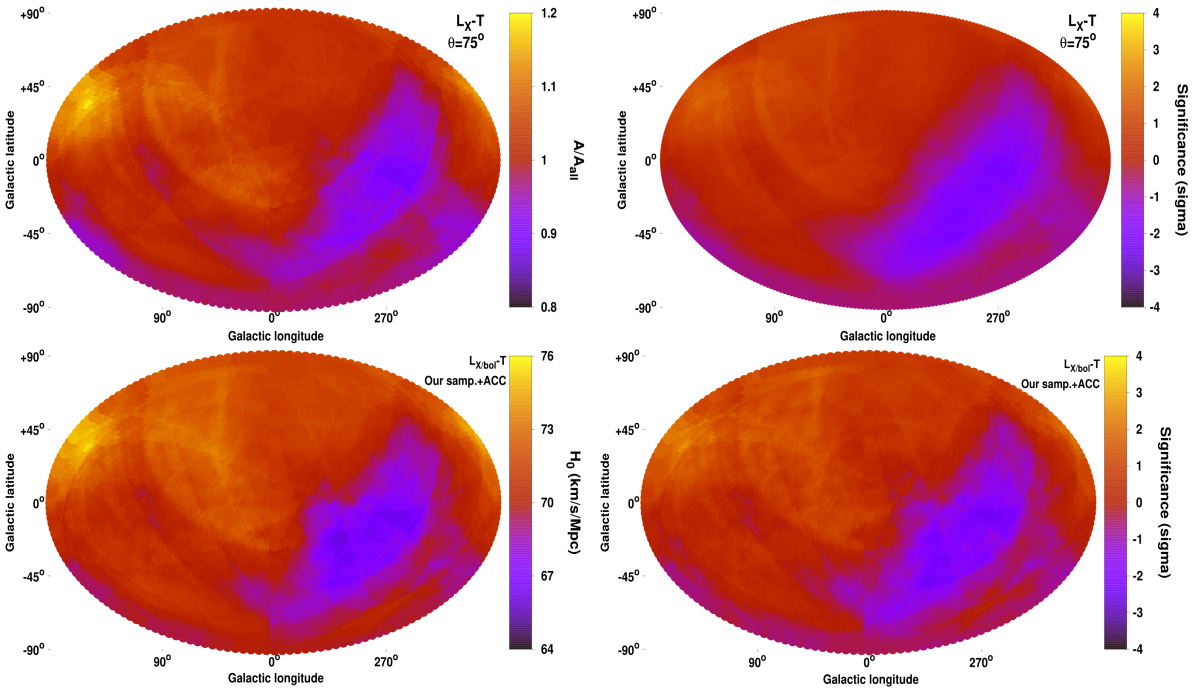

Figure 4.4: *Top*: Same as in Fig. 4.2, for $L_X - T$. *Bottom*: The H_0 anisotropy map derived from the joint $L_X - T$ (our sample+ACC).

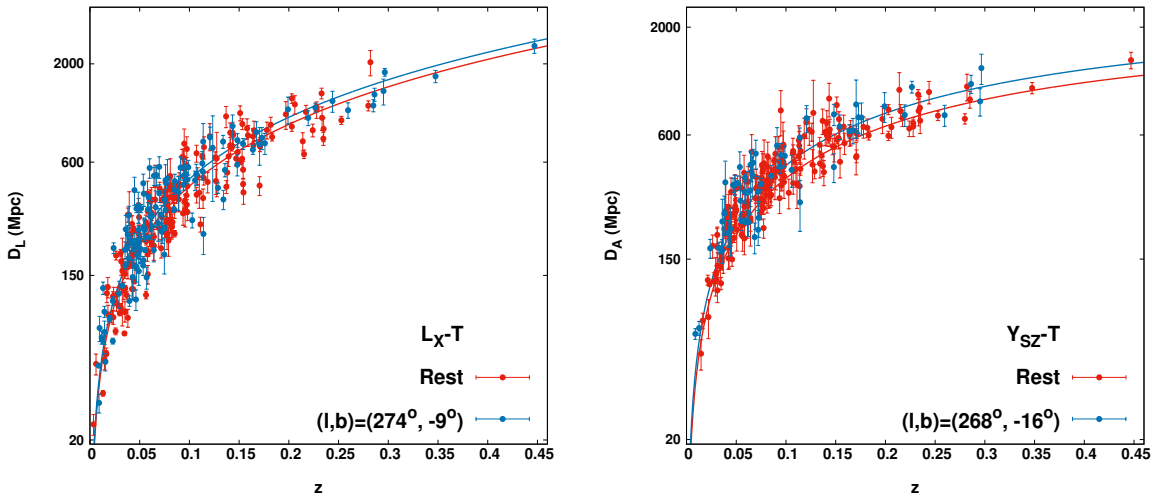

Figure 4.5: Hubble diagram of galaxy clusters as derived by the $L_X - T$ (top) and the $Y_{SZ} - T$ (bottom) relations. The clusters from the most anisotropic region of each scaling relation are displayed (blue), together with the clusters from the rest of the sky (red). The best-fit lines are displayed with the same color.

Our sample

Due to the low observed scatter and the 263 clusters with quality Y_{SZ} measurements, we consider $\theta = 60^\circ$ cones to scan the sky. The maximum anisotropy is detected toward $(l, b) = (268^\circ \pm 34^\circ, -16^\circ \pm 29^\circ)$ (57 clusters), deviating from the rest of the sky by $27 \pm 7\%$ at a 4.1σ level. The direction agrees remarkably with the results from the $L_X - T$ relation. The amplitude of the anisotropy is larger, due to the narrower cones, which limit the "contamination" of unaffected clusters in each cone. The statistical significance of the anisotropies is also considerably larger, as a result of the smaller $Y_{SZ} - T$ scatter and the narrower scanning cones.

This result strongly demonstrates that the observed $L_X - T$ anisotropies are not due to X-ray absorption issues. The $A_{YT}/A_{YT,all}$ and the sigma maps are shown in Fig. 4.6. Here we should note that there is a mild correlation between the L_X and Y_{SZ} scatter compared to T due to the physical state of galaxy clusters. If the origin of the anisotropies was sample-related (surprisingly strong archival bias, etc.), one would expect to indeed see similar anisotropies in $L_X - T$ and $Y_{SZ} - T$. However, this would still not explain the large statistical significance of the $Y_{SZ} - T$ anisotropies, or the fact that we see a similar effect in ACC. Nonetheless, we further explore this possibility later in the paper (Sects. 4.7.6 and 4.8), and confirm that this is not the reason for the agreement of the two relations. Finally, if one uses the Y_{SZ} values from PSZ2 instead, one obtains similar anisotropic results (Sect. 4.13).

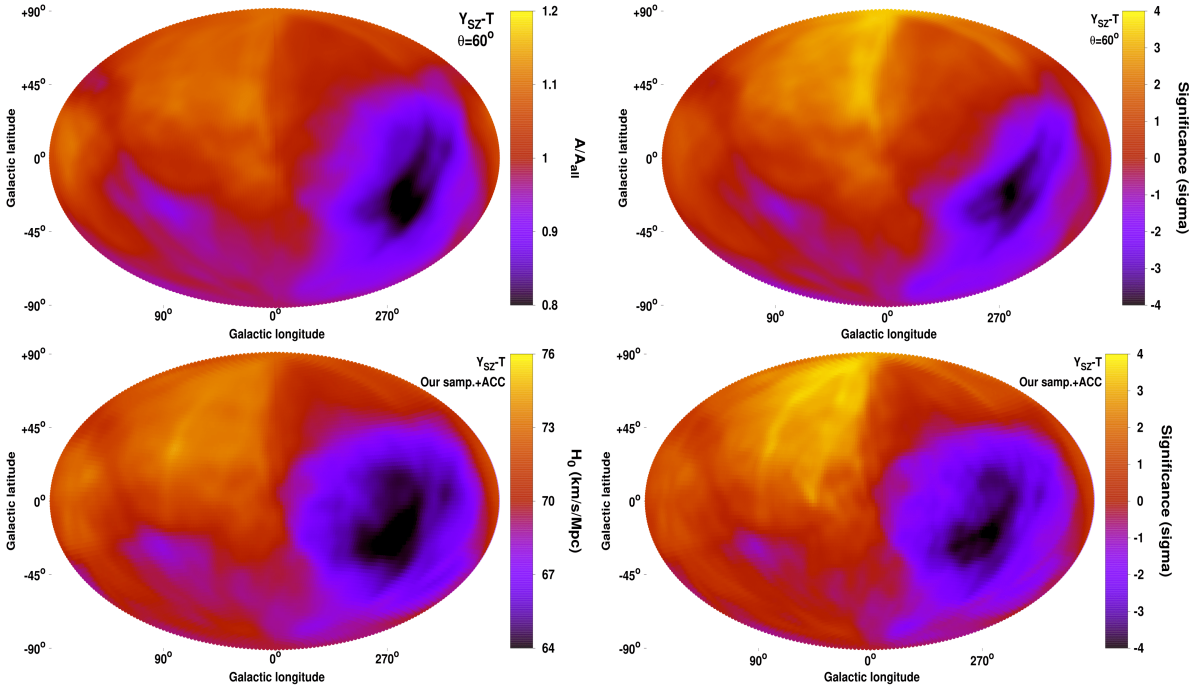

Figure 4.6: *Top*: Same as in Fig. 4.2 for $Y_{SZ} - T$. *Bottom*: The H_0 anisotropy map (left) and the respective significance map (right), derived from the joint $Y_{SZ} - T$ (our sample+ACC, bottom).

Cosmological anisotropies and bulk flows We now investigate the necessary H_0 variations to fully explain the observed anisotropies. One would need $H_0 = 62.3 \pm 2.2$ km/s/Mpc toward $(l, b) \sim (268^\circ, -16^\circ)$, and $H_0 = 72.1 \pm 0.9$ km/s/Mpc for the rest of the sky. The result is consistent within 1.4σ with the H_0 value obtained from the joint $L_X - T$ analysis. The corresponding Hubble diagram is shown in the bottom panel of Fig. 4.5.

The observed anisotropies cannot be caused by a local spatial variation of Ω_m. The $Y_{SZ} - T$ relation is rather insensitive to such changes due to the low z of the clusters and the opposite effect that an Ω_m change would have on the Y_{SZ} value, and in the redshift evolution of the relation. However, the anisotropies appear to be even stronger now compared to the $L_X - T$ relation.

Assuming the apparent anisotropies are due to a BF affecting the entire sample, using the MR method one finds $u_{\mathbf{BF}} = 1030 \pm 370$ km/s toward $(l, b) = (263^\circ \pm 39^\circ, -22^\circ \pm 20^\circ)$. For the redshift bin $z \in [0, 0.07]$ we obtain $u_{\mathbf{BF}} = 1110 \pm 420$ km/s toward $(l, b) = (254^\circ \pm 42^\circ, -17^\circ \pm 19^\circ)$, similar to the full sample's results. By gradually expanding the redshift range, the best-fit results remain within the uncertainties, without an amplitude decay. For the $z \in [0.07, 0.12]$ bin, we obtain $u_{\mathbf{BF}} = 920 \pm 540$ toward $(l, b) = (312^\circ \pm 61^\circ, -34^\circ \pm 31^\circ)$. The BF drifts by $\sim 50^\circ$, but remains within the (large) uncertainties and within the marginal anisotropic region. The amplitude is also slightly decreased, but still well above the ΛCDM prediction for such scales. For the $z > 0.12$ clusters we find $u_{\mathbf{BF}} = 1280 \pm 780$ km/s toward $(l, b) = (321^\circ \pm 103^\circ, -42^\circ \pm 45^\circ)$. There is some indication that the BF persists toward a similar direction up to scales larger than ~ 600 Mpc, however the poor constraining power of the $z > 0.12$ subsample does not allow for robust conclusions.

From the MA method, we obtain $u_{\mathbf{BF}} = 1040 \pm 310$ km/s toward $(l, b) = (267^\circ \pm 22^\circ, -28^\circ \pm 16^\circ)$, completely consistent with the MR method. Within $z \leq 0.09$, the constrained BF is $u_{\mathbf{BF}} = 1270 \pm 370$ km/s toward $(l, b) = (254^\circ \pm 22^\circ, -18^\circ \pm 16^\circ)$. For $z > 0.09$, the amplitude is reduced ($u_{\mathbf{BF}} = 820 \pm 430$ km/s), while its direction $(l, b) = (242^\circ \pm 87^\circ, -13^\circ \pm 22^\circ)$ is rather uncertain (pointing however toward a similar sky patch).

One sees that the $Y_{SZ} - T$ anisotropies reveal similar BFs than the $L_X - T$ case. In both cases, the MR and MA methods agree on the full sample and the low z regime, while the results are uncertain for higher redshifts. Both the scale out to which the apparent BF extends, and its amplitude, by far exceed the ΛCDM expectations.

Joint analysis of the $Y_{SZ} - T$ relation for our sample and ACC

The ACC sample shows a very similar anisotropic $Y_{SZ} - T$ behavior to our sample (Appendix 4.12). We combine the two independent samples and their 376 different clusters, to jointly constrain the apparent H_0 anisotropies with the $Y_{SZ} - T$ relation. The H_0 spatial variation with the sigma maps are given in the bottom panel of Fig. 4.6. The combined maximum anisotropy direction is found toward $(l, b) = (276^\circ \pm 26^\circ, -14^\circ \pm 20^\circ)$, with $H_0 = 63.4 \pm 2.5$ km/s/Mpc, at a 4.3σ tension with the rest of the sky ($13 \pm 3\%$). The statistical significance is slightly increased compared to our sample alone, while the direction is mostly determined by our sample. The obtained anisotropies remarkably agree with the joint $L_X - T$ results. Finally, a dipole form of the anisotropy is apparent in the sigma maps.

4.6.3 The $L_{BCG} - T$ relation

The final scaling relation that can potentially trace cosmological anisotropies and BFs is the $L_{BCG} - T$ relation. Absorption effects are rather irrelevant for this relation, since L_{BCG} is measured in infrared. Furthermore, the latter strongly depends on the luminosity distance ($L_{BCG} \sim D_L^2$). The large scatter of the relation and the fewer number of clusters compared to $L_X - T$ and $Y_{SZ} - T$ constitute the main disadvantages of $L_{BCG} - T$. Due to that, $\theta = 90^\circ$ scanning cones are considered.

Despite the aforementioned disadvantages, the $L_{BCG} - T$ relation can offer additional insights on the observed anisotropies. Indeed, a 1.9σ anisotropy is detected toward $(l, b) = (257^\circ \pm 55^\circ, -12^\circ \pm 38^\circ)$, where the BCGs appear to be $19 \pm 10\%$ fainter than the rest of the sky. The normalization anisotropy map is displayed in the bottom panel of Fig. 4.25. This mild tension does not provide sufficient statistical

evidence for a deviation of isotropy. However, the agreement of the direction with the $L_X - T$ and $Y_{SZ} - T$ results offers additional confirmation of the existence of the physical phenomenon causing this.

Cosmological anisotropies and bulk flows In terms of H_0, one obtains $H_0 = 66.2 \pm 2.5$ km/s/Mpc for that direction, and $H_0 = 72.6 \pm 2.3$ km/s/Mpc for the opposite hemisphere. The H_0 values are consistent with the other scaling relations, for similar directions.

To search for any BFs, we can only consider the full sample, due to the restricted $0.03 < z < 0.15$ range, and the few available clusters. For the MR method, we obtain $u_{\mathbf{BF}} = 620 \pm 400$ km/s toward $(l, b) = (293^\circ \pm 50^\circ, +2^\circ \pm 29^\circ)$. With the MA method, we find similar results as well, displayed in detail in Table 4.4. Even though the direction is rather uncertain, the BF results are consistent with the ones found in $L_X - T$ and $Y_{SZ} - T$.

4.6.4 Combined anisotropies of $L_X - T$, $Y_{SZ} - T$, and $L_{BCG} - T$

We now combine the information from the $L_X - T$, $Y_{SZ} - T$, and $L_{BCG} - T$ anisotropies, for both our sample and ACC into one single H_0 anisotropy map. The joint analysis procedure is the same as before, where the different H_0 posterior likelihoods for every region, from every scaling relation are combined. We should stress that this method makes three assumptions.

Firstly, it assumes that the underlying effect causing the anisotropies does not affect T, but only L_X, Y_{SZ}, and L_{BCG}, which is true for cosmological anisotropies and BFs. This also requires that there are no unaccounted X-ray absorption effects that bias the T measurement, which should be the case according to our Sect. 4.5 analysis. If a strong temperature outlier exists due to chance, it would not significantly affect the results by propagating to all scaling relations. The effect of the outlier would be "buried" under the average behavior of the rest of the clusters in its region, if no reason for an anisotropy exists. The posterior H_0 likelihood from the entire region will be then combined with the same results from the other scaling relations.

The second assumption is that the anisotropies are not biased by our methodology, since this would affect all three scaling relations, and the results from combining them would be biased. In Sects. 4.7 and 4.8 we show however that this seems very unlikely.

Thirdly, we assume that the scatter of L_X, Y_{SZ}, and L_{BCG} wrt T is not strongly correlated. Although we show this to be true between L_{BCG} and the other quantities, a moderately correlated scatter indeed exists between L_X and Y_{SZ} for our sample and for ACC. We discuss this in detail in Sect. 4.7.6 and account for this effect in the MC simulations later on (Sect. 4.8). Under the unlikely condition that the anisotropies are a result of a strongly inhomogeneous spatial distribution of the cluster population, this correlation will artificially boost the statistical significance of our results. Even so, this would not significantly alter the final conclusions, hence we ignore this for now.

When $L_X - T$, $Y_{SZ} - T$, and $L_{BCG} - T$ results for both our sample and ACC are combined, we obtain $H_0 = 66.5 \pm 1.0$ km/s/Mpc toward $(l, b) = (273^\circ \pm 40^\circ, -11^\circ \pm 27^\circ)$, and $H_0 = 72.8 \pm 0.6$ km/s/Mpc for the rest of the sky. There is a 5.4σ tension between the two values, demonstrating the high statistical significance of the detected anisotropies. The small H_0 uncertainties are not surprising if one considers that five nearly independent results have been combined into one map. Even if our assumptions were not true and we overestimated the statistical significance, we would not expect the anisotropy signal to drop below $\sim 4.5\sigma$[10].

[10] This is expected due to the results of the MC simulations in Sect. 4.8.

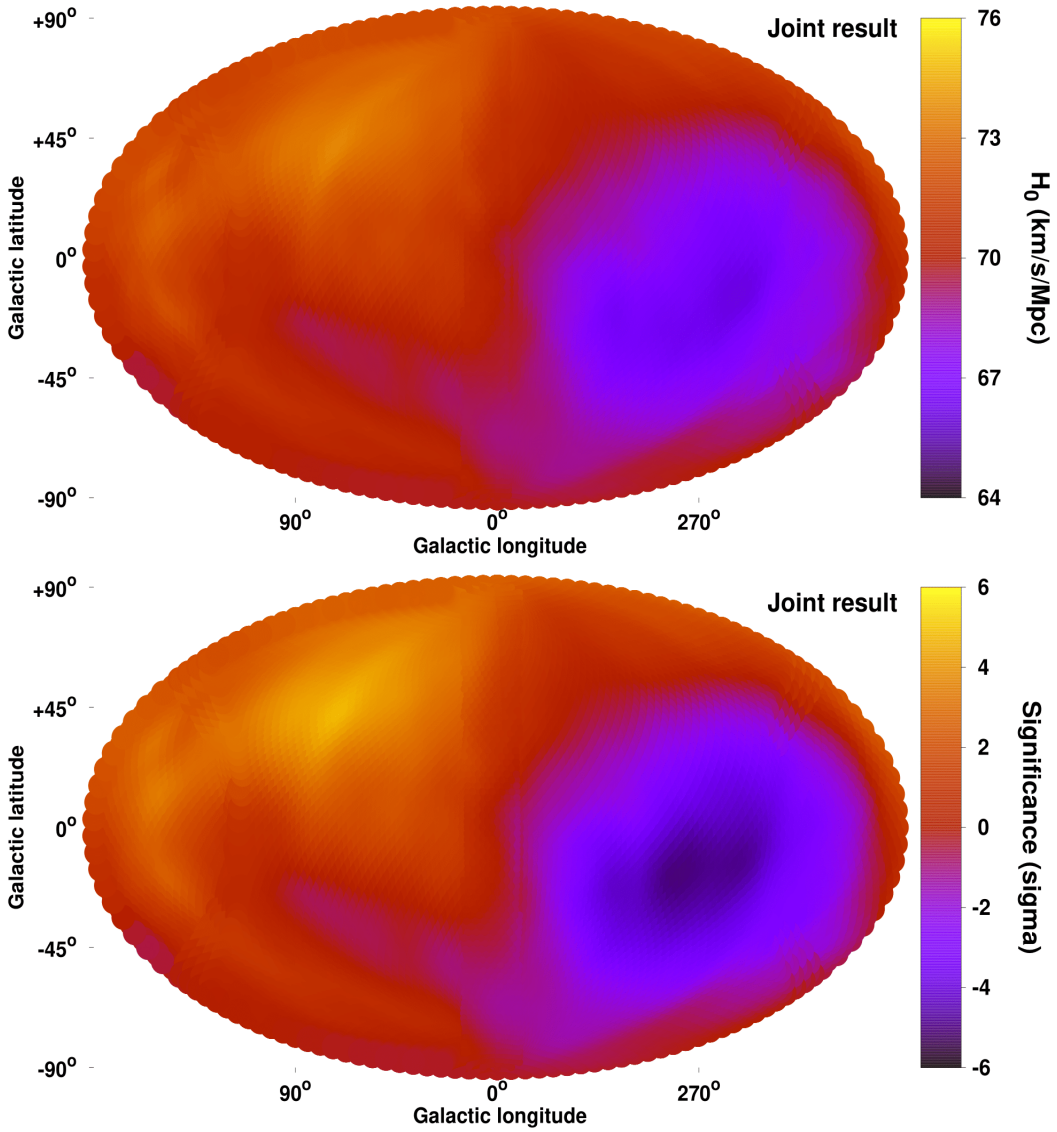

Figure 4.7: H_0 anisotropy map as derived from the joint analysis of $L_X - T$, $Y_{SZ} - T$, and $L_{BCG} - T$ relations for both samples.

4.7 Possible systematics

Several possible biases could jeopardize the interpretation of the observed cluster anisotropies. A large number of them, including numerous X-ray and sample-related issues were tested and discussed for the $L_X - T$ relation in M20. Here we explore some additional effects that might undermine the significance of our results.

4.7.1 Cool-core and morphologically relaxed clusters

Cool-core (CC) clusters have a strong central peak in their surface brightness profile, and they are known to be intrinsically brighter in X-rays than noncool-core (NCC) clusters (e.g. Mittal et al., 2011). This bias propagates to scaling relations when the two physical quantities are not similarly affected by the (N)CC nature of clusters. Previous studies have indeed found differences for such scaling relations between CC and NCC, or morphologically relaxed (i.e., regular) and disturbed clusters (e.g., Maughan, 2007; G. W. Pratt et al., 2009; Y.-Y. Zhang et al., 2017; Maughan et al., 2012; Bharadwaj et al., 2015; Lovisari et al., 2020). Environmental effects have been also found to mildly correlate with some cluster properties (M18, Manolopoulou et al., 2020).

For classifying clusters as CC or NCC, one needs a robust proxy of the dynamical state of the clusters, such as the central cooling time, the shape of the surface brightness profile, the concentration parameter, etc. Future work will soon provide such information for eeHIFLUGCS, which will allow for a more precise calibration of our scaling relations. For now, we use the offset between the X-ray peak and the BCG position (XBO) to categorize clusters as morphologically relaxed or disturbed. This categorization is not the same as CC and NCC, however there is a rather strong correlation between them. Specifically, the XBO has been shown to approximately correlate with the existence of a CC in the center of the cluster (e.g., D. S. Hudson et al., 2010; Zitrin et al., 2012; Rossetti et al., 2016; Lopes et al., 2018). We consider as morphologically relaxed, and possibly CC, the clusters with XBO$< 0.01\ R_{500}$. We also consider as disturbed, possibly NCC clusters, the ones with XBO$> 0.08\ R_{500}$. Each of these subsamples constitutes $\sim 30\%$ of our sample.

For any anisotropy study, this bias is only relevant if the spatial distribution of morphologically relaxed and disturbed clusters is not relatively uniform. Due to the homogeneous selection of our sample however, one sees only mild, random variations in the fraction of such clusters across the sky (Fig. 4.8). There is a small excess of relaxed clusters toward $(l, b) \sim (60^\circ, +30^\circ)$. This mild distribution imbalance strongly correlates with the directional behavior of the R scaling relations (see Appendix 4.12 for more details).

Finally, it is important to stress that the $(l, b) \sim (280^\circ, -15^\circ)$ region shows an average behavior in its cluster population, and hence no relevant bias is expected there (as is further shown later).

Lack of bias in $L_X - T$, $Y_{SZ} - T$, and $L_{BCG} - T$

Relaxed and disturbed clusters do not show any meaningful difference in their $Y_{SZ} - T$ and $L_{BCG} - T$ normalization, as displayed in Fig. 4.9. Therefore, the possible CC bias is irrelevant for these two scaling relations. For $L_X - T$, relaxed clusters appear $26 \pm 10\%$ brighter than the disturbed ones (right panel of Fig. 4.9), which is generally expected. Of course, all these clusters are not found in only one region, but they are distributed sparsely across the sky. Thus, their effects will be hardly detectable over the possible cosmological effects. Even more importantly, there is only an average number of relaxed and disturbed clusters toward the $L_X - T$ anisotropy region, hence no considerable bias is expected.

This was indeed shown in M18, where using core-excised L_X did not have any effect on the $L_X - T$ anisotropies of the HIFLUGCS sample (Reiprich et al., 2002). Excluding the possibly relaxed clusters

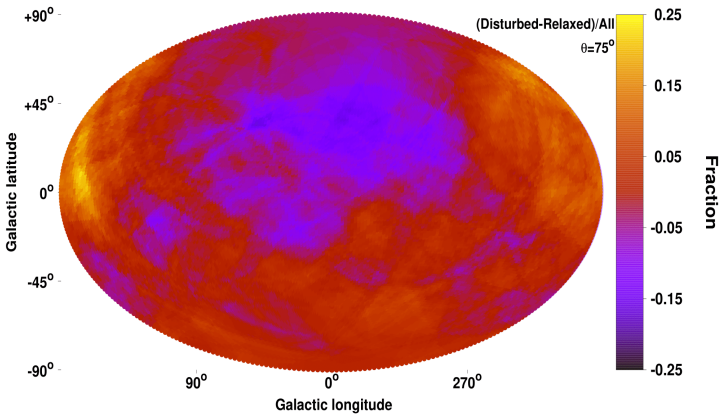

Figure 4.8: Fractional difference between disturbed and relaxed clusters over all the clusters for every sky patch of the extragalactic sky.

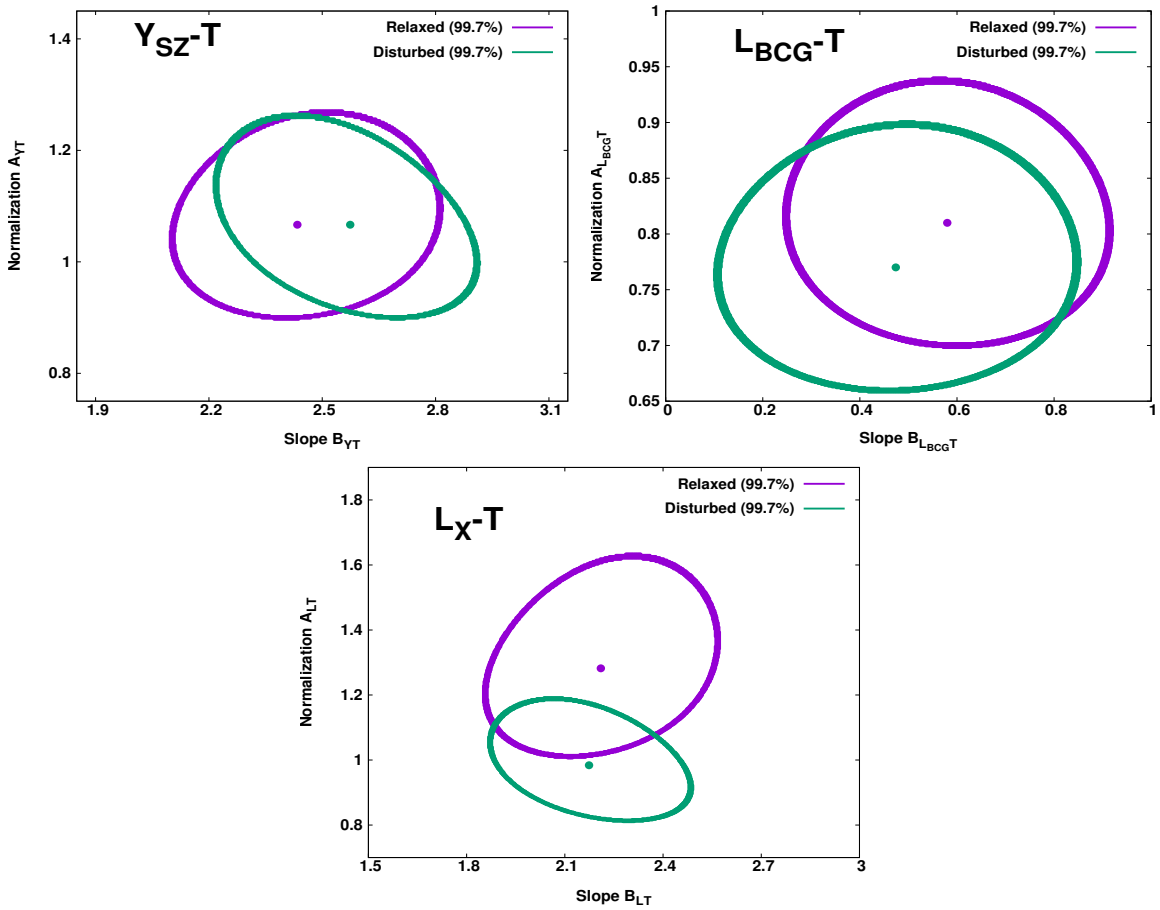

Figure 4.9: 3σ (99.7%) parameter space of the normalization and slope of the $Y_{\rm SZ} - T$ (left), $L_{\rm BCG} - T$ (middle), and $L_{\rm X} - T$ (right) relations, for relaxed (purple) and disturbed (green) clusters.

(through a supercluster member vs field cluster classification), did not affect the anisotropies either.

To provide further evidence that the dynamical state of clusters does not have an effect on the detected $L_X - T$ anisotropies, we create 10^5 randomly drawn bootstrap subsamples (same process as in M20), independent of direction. We investigate the correlation between the A_{LT} and the median XBO for every subsample. In Fig. 4.10, one sees that there is only a quite weak anticorrelation between the sample's median XBO and A_{LT} (Pearson's correlation coefficient $r = -0.11$). This simply shows that it is extremely improbable for enough relaxed clusters to be included in a subsample to make a noticeable difference in A_{LT}.

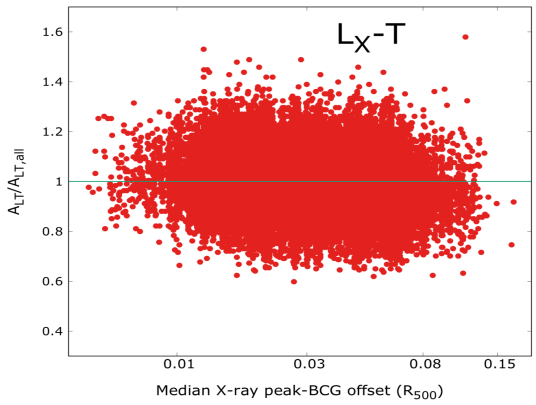

Figure 4.10: Correlation between the best-fit A_{LT} (over the full sample's best-fit value) and the median XBO for every of the 10^5 bootstrap subsamples.

From all the above, it is evident that an inhomogeneous distribution of morphologically relaxed and disturbed clusters is not the reason behind the observed anisotropies.

4.7.2 Malmquist and Eddington biases

Malmquist bias

Flux-limited samples like eeHIFLUGCS, suffer from the so-called Malmquist bias (MB). Clusters that are intrinsically brighter than the others, are overrepresented in the sample, especially close to the flux limit. If not taken into account, this results in a biased estimation of the scaling parameters of the true, underlying cluster population (e.g., D. S. Hudson et al., 2010; Mittal et al., 2011; Eckert et al., 2011). This bias is expected to be stronger for scaling relations including L_X, since the selection of the sample was conducted based on the clusters' X-ray flux. At the same time, the effects of the MB should be relatively weaker for the other scaling relations. We wish to assess if the MB could affect the statistical significance of the detected anisotropies. We focus on the $L_X - T$ relation since this is probably the most affected one, and the one we used in M20.

If the MB influences all regions equally, then there is no effect on the detected anisotropies. This is indeed the naive expectation, since the MB is directly linked to the scatter of the $L_X - T$ relation (for decreasing scatter, the effects of the MB are also weakened). The scatter of a relation is an intrinsic cluster property, since it mainly depends on the physical state of these objects. In an isotropic Universe, there is no obvious reason why such an intrinsic cluster property would spatially vary. A risk factor that would make the MB relevant is if the cluster population differs from region to region (e.g., due to archival bias). For large enough, homogeneously selected samples like our own, one does not expect significant differences, but nevertheless we try to quantify the possible bias in our anisotropy estimates.

For $L_X - T$, the faintest, maximum anisotropy region lies toward $(l, b) \sim (274^\circ, -9^\circ)$, containing 120 clusters with $\sigma_{int} = 58.9 \pm 4.6\%$. The rest of the 193 clusters are 19% brighter with a 2.8σ tension, and with $\sigma_{int} = 50.9 \pm 3.5\%$[11]. The scatter of the faint region is actually larger than the rest of the sky, at a 1.4σ level. According to Vikhlinin et al. (2009), the observed scatter estimate is also the true, underlying scatter for X-ray flux-limited samples.

The MB correction to be applied in L_X for low$-z$, flux-limited samples like our own is $MB_{corr} \approx \exp\left(-1.5\sigma_{int}^2\right)$ (Vikhlinin et al., 2009). Consequently, for the $(l, b) \sim (274^\circ, -9^\circ)$ region we have $MB_{corr} \approx 0.594 \pm 0.048$, and for the rest of the sky $MB_{corr} \approx 0.678 \pm 0.036$. Therefore, there is a 84% chance that after the proper MB correction, the faint region will become even more anisotropic compared to the rest of the sky. Based on the MB_{corr} uncertainties, there is only a 0.007% (4σ) probability that the full amplitude of the $L_X - T$ anisotropy is a result of the MB.

Similarly to the effects of the scatter, one might expect that larger L_X uncertainties could lead to larger normalizations, and vice versa. However, the faintest region has again a slightly larger average L_X uncertainty than the rest of the sky, while the median value is similar between the two subsamples.

This result strongly suggests that the MB is not the reason behind the $L_X - T$ anisotropies, even though there is a small chance ($< 16\%$) that it might lead to a slight overestimation of the statistical significance of the findings. However, considering the even larger relative anisotropy of the $Y_{SZ} - T$ relation and the weaker effects that MB has there, one concludes that the latter is probably irrelevant for our analysis.

Eddington bias

The Eddington bias refers to the fact that at large distances, only luminous, massive clusters will exceed the flux limit of a survey. Thus, they are overrepresented at large z. This leads to a different L_X, Y_{SZ}, and T (i.e., mass) distributions between low and high z. Low and high mass systems might share slightly different scaling laws. If the z distributions of the compared cluster subsamples were significantly different, this could lead to a biased comparison and artificial anisotropies. However, in M20 we showed that the z and T distributions of the $(l, b) \sim (280^\circ, -15^\circ)$ are very similar to the rest of the sky, as expected for a homogeneously selected sample. This is further confirmed by our physical properties test in Sect 4.7.4. Subsequently, the Eddington bias is rather irrelevant to our analysis.

4.7.3 Zone of Avoidance bias

The fact that the direction of the observed anisotropies mostly lies close to the Galactic plane gap, or the Zone of Avoidance (ZoA, $|b \leq 20^\circ|$) is another issue that might raise concerns about their underlying origin. In Sect. 4.5, we demonstrated that uncalibrated X-ray absorption issues are not the reason behind $L_X - T$ anisotropies, and definitely cannot explain the $Y_{SZ} - T$ anisotropies. Subsequently, the only possible bias that might lead to the artificial detection of anisotropies close to the ZoA is the applied methodology, or some unaccounted archival bias toward that region.

We use two independent tests to ensure that our applied methodology is not biased toward this region. Firstly, we repeat the sky scanning for the $L_X - T$, $Y_{SZ} - T$ and $L_{BCG} - T$ relations of our sample, this time *without* applying any weighting on the cluster uncertainties (these weights were based on each cluster's distance from the center of each cone). As a result, the scanning algorithm does not take into

[11] Here we display σ_{int} in terms of percentile and not dex, in order to make the following calculations clearer. σ_{int} mirrors the standard deviation of the distribution of clusters around the best-fit line. The relative difference of the two subsamples though corresponds to the standard error difference, which is the uncertainty of the mean of this distribution (i.e., the best-fit normalization). The statistical significance of this relative difference (i.e., anisotropy) accounts of course for σ_{int} through the normalization uncertainties.

account the spatial distribution of clusters, and does not "see" the ZoA gap. The only information it reads is the number of clusters in each cone. The cones close to the most anisotropic region happen to have average numbers of objects (Fig. 4.27 in Appendix). Even if fewer clusters were included in the cones, in M20 we showed that the best-fit normalization is completely independent of the number of clusters.

When repeating the analysis for $L_X - T$ we obtain an anisotropy of 2.7σ toward $(l, b) = (284^\circ \pm 44^\circ, -4^\circ \pm 33^\circ)$. The result is similar to the default analysis both in terms of the anisotropy direction and amplitude. In a similar manner, for the $Y_{SZ} - T$ relation we obtain a 3.9σ anisotropy toward $(l, b) = (262^\circ \pm 33^\circ, -22^\circ \pm 30^\circ)$, again similar to the default case. The anisotropies of the $L_{BCG} - T$ anisotropies are practically not affected. These results establish that the observed anisotropies in our data are not an artefact of the ZoA effect on our analysis.

The second test we utilize is twofold. Firstly, we consider the 10000 isotropic MC simulated samples used in Sect. 4.8, which are drawn from the same distribution as the real sample. There the positions of the clusters are kept fixed, and and thus the ZoA remains empty. For the same scaling relations as before, we measure how many times the maximum anisotropy is found within the ZoA. We then compare this to the random expectation based on the fraction of the full sky area the ZoA covers, namely $\sim 33\%$. We find that $\sim 43\%$ of the maximum anisotropy directions lie within the ZoA. This indicates that the applied statistical (distance) weighting of the clusters during the sky scanning can introduce a small bias in the direction of the detected anisotropies. However, this bias is quite small, and completely disappears if one repeats the procedure with uniform weighting. The real data anisotropies however do not drift in this case.

For the next part of this test, we randomly fill in the empty ZoA area of these 10000 MC samples with $\sim 130 - 150$ simulated clusters. These clusters have the same number density as the rest of the sky, and the same T and scatter distributions. We measure again the level of the anisotropies, and compare it with the case where the ZoA is excluded. That way we wish to see if excluding the clusters within the ZoA in the real data introduces a bias in our anisotropy estimates. We find that the amplitude of the anisotropies decreases by $14 \pm 8\%$, which is expected due to the larger number of isotropic data. Additionally, $\sim 36\%$ of the most deviate directions are located within ZoA, slightly decreased compared to the case when the ZoA clusters are excluded, and consistent with the random expectation. Hence, the gap of the ZoA can weakly affect the direction of the detected anisotropies, but not enough to compromise our results.

These tests combined strongly suggest that there is no significant bias in our methodology that favors and amplifies anisotropic signals close to the ZoA. The minor changes that can be indeed caused are much smaller than the measured direction uncertainties. Relative plots for these tests can be found in Appendix. 4.14. Future surveys will offer a more robust cluster detection toward that region, which will help us pinpoint the clusters anisotropies slightly more accurately.

4.7.4 Anomalous combination of cluster properties

In M20 we have investigated if a single average physical property of cluster subsamples can be associated with an anomalous behavior of A_{LT}. Here we wish to find out if such a behavior of A_{LT} (or A_{YT}) could also result from a certain combination of average cluster properties. To do so, we construct 10^6 random bootstrap cluster subsamples of random size ($10-60\%$ of the total sample's size), as done in M20. Except for the best-fit A_{LT}, B_{LT} and $\sigma_{\mathrm{int},LT}$, 12 more average properties of each subsample are also derived[12]. We express A_{LT} as a function of all the parameters p_i (normalized by their sample mean p_{mean}), and their

[12]These are the average redshift, temperature, $< 0.2\,R_{500}$ (core) temperature, flux, core metallicity, $0.2-0.5\,R_{500}$ metallicity, N_{Htot}, RASS time exposure, X-ray peak-BCG offset, number of clusters, original source catalog (REFLEX/BCS=1, NORAS=2), and instrument used for T measurement (XMM-Newton=1, Chandra=2).

power-law index v_i, as follows:

$$A_{LT} = 1.132 + \sum_{i=1}^{N=14} v_i \log\left(p_i / p_{\rm mean}\right). \quad (4.9)$$

The 1.132 term corresponds to the best-fit value for the full sample.

To understand which combination of properties could lead to a significantly altered A_{LT}, one needs to constrain v_i. Knowing these, one can predict the best-fit A_{LT} based just on the physical properties of the clusters. To do so, we perform a Markov-Chain Monte Carlo (MCMC) fitting to the 10^6 bootstrap subsamples. The exact details of the fitting process together with the relevant plots can be found in Appendix 4.14. A_{LT} shows a negligible dependence on 11 out of the 14 parameters. There is a weak anti-correlation with the best-fit B_{LT} ($v_B = -0.4 \pm 0.22$), a moderate anti-correlation with mean T ($v_T = -0.87 \pm 0.21$), and a moderate correlation with mean z ($v_z = +0.82 \pm 0.19$). In flux-limited samples and due to the Eddington bias, high$-z$ clusters are also high$-T$ clusters. As a result, the contribution of these two terms in the predicted A_{LT} balances out. In general, subsamples with local, hot clusters tend to appear fainter than average, and vice versa.

To determine if the observed $L_{\rm X} - T$ anisotropies are caused by the physical cluster properties of the $(l, b) \sim (274^\circ, -9^\circ)$, we predict its A_{LT} using Eq. 4.9 and its mean cluster properties. We obtain $A_{LT} \sim 1.12$, and $A_{LT} \sim 1.14$ for the rest of the sky. The two results are similar and so we confirm that the strong apparent anisotropies are not caused by a possible bias due to an inhomogeneous distribution of different cluster populations. This result was expected, since in M20 we showed that the average physical cluster properties are similar across the sky. Repeating the analysis for $Y_{\rm SZ} - T$ returns similar results.

4.7.5 Temperature calibration issues

If the measured cluster temperatures suffered from calibration issues and were biased toward higher values within the $(l, b) \sim (280^\circ, -10^\circ)$ region, this would create apparent anisotropies in all scaling relations that include T. This would eventually lead to an overestimation of the statistical significance of the anisotropies, when we combine all the T scaling relations.

However, this scenario is highly unlikely for several reasons. Firstly, if T was overestimated toward $(l, b) \sim (280^\circ, -10^\circ)$, the same anisotropies should appear in the $R - T$ scaling relation as well, but they do not (Sect. 4.12). Secondly, there is no obvious reason why the ACC sample would show similar anisotropies to our sample, when its temperatures were measured two decades ago with a different X-ray telescope and data analysis process. Thirdly, clusters in that region were not observed within a certain, narrow time interval, but throughout many years. As such, any calibration issues could not have affected only these clusters, but it should affect clusters from the entire sky. One would not observe strong anisotropies then, since one needs several clusters from one region to show a systematic behavior in order for a statistically significant signal to appear.

One possible effect that could bias the directionality of T scaling relations, is the fraction between clusters with measured T from Chandra (237 in total) or XMM-Newton (76). As shown in Schellenberger et al. (2015) and further confirmed in M20, T values measured with the two telescopes slightly (and systematically) differ. They follow a clear, low-scatter relation though, which we used to convert XMM-Newton temperatures to the equivalent Chandra ones. Therefore, one should not expect any dependance of the results on the fraction of Chandra and XMM-Newton clusters. This is confirmed by the analysis in Sect. 4.7.4, where this fraction does not strongly correlate with the best-fit A_{LT}. Nevertheless, we test if the spatial variation of this fraction correlates with the observed anisotropies in $L_{\rm X} - T$, $Y_{\rm SZ} - T$, and $L_{\rm BCG} - T$. We find that the $(l, b) \sim (280^\circ, -10^\circ)$ does not show any strong imbalance (Fig. 4.29).

There is an excess of Chandra clusters toward $(l, b) \sim (150^\circ, +40^\circ)$, while an excess of XMM-Newton clusters is found toward $(l, b) \sim (334^\circ, -50^\circ)$. Moreover, when only Chandra clusters were used in M20, the same $L_X - T$ anisotropies were observed.

Based on all the above, one can safely conclude that the observed anisotropies are not due to T measurement calibration issues. Finally, eRASS will provide cluster observations from a single instrument, analyzed within a strict time interval, and thus avoid such possible systematics.

4.7.6 Correlation of L_X and Y_{SZ} scatter with T

Past studies (i.e. Nagarajan et al., 2019, and references therein) have reported a positive correlation between the scatter of L_X and Y_{SZ} at fixed mass (or T equivalently). Here we test this correlation with much larger samples, as well as the correlation of the scatter between these two quantities and L_{BCG}. Considering the 263 clusters with both Y_{SZ} and L_X measurements, we confirm that their residuals wrt T are correlated, with a Pearson's correlation coefficient of $r_{corr} = 0.668 \pm 0.089$. This is shown in Fig. 4.11. The best-fit line has a slope of ~ 0.63, while the total scatter of the relation is ~ 0.16 dex.

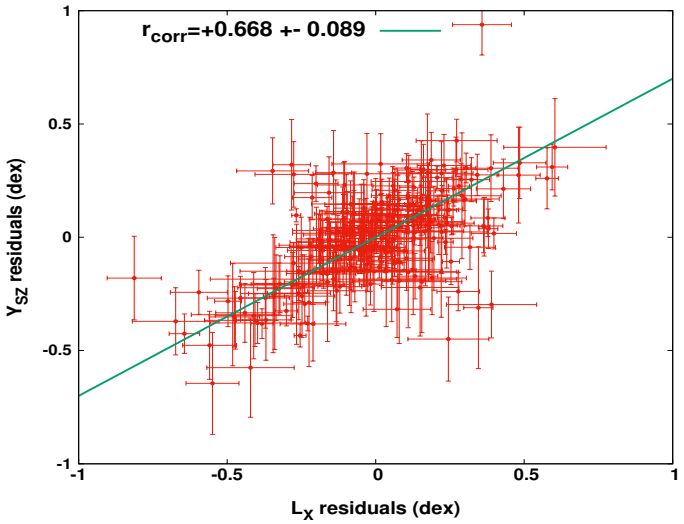

Figure 4.11: Correlation between the Y_{SZ} scatter from the $Y_{SZ} - T$ relation, and the L_X scatter from the $L_X - T$ relation.

We should note that this correlation has no effect on the statistical significance values extracted for every scaling relation individually, although it can affect the combined statistical significance of the anisotropies as obtained in Sect. 4.6.4. In practice, this means that both $Y_{SZ} - T$ and $L_X - T$ would exhibit similarly biased anisotropies in the case of an inhomogeneous distribution of CC clusters or mergers for instance. Their results then could not be considered independent and combined as in Sect. 4.6.4. Our previous analysis showed that such a CC (or merger) bias is quite unlikely to cause the observed anisotropies, since no correlation was found between the A_{LT} and A_{YT} and the average dynamical state of a subsample's clusters. We fully explore the effect that this correlation has in our results however in the next section where MC simulations are carried out.

Similar results are obtained for the ACC sample, for both the correlation coefficient and the slope of the relation. Finally, the scatter of L_{BCG} wrt T does not show any meaningful correlation with the scatter of L_X or Y_{SZ}.

4.7.7 Selection biases

As extensively argued in M20, selection biases are not expected to significantly affect our anisotropy results. We attempt to constrain the *relative* deviations between sky regions and thus we use the overall best-fit scaling relations as a frame of reference. The bias-corrected scaling relations are not a necessity for that, as long as the cluster properties across the sky do not vary significantly. This was shown to be true in both M20 and in this work. Our results however are still directly comparable with similar literature results since many studies focus on the observed scaling relations. Nonetheless, we performed several tests to evaluate how some selection biases can affect the statistical significance of the anisotropies. The results from Sects. 4.7.1 and 4.7.2 support the notion that the observed anisotropies are not overestimated by selection biases. More tests are performed in Appendix 4.13, yielding the same conclusion. The bias-corrected scaling relations will be presented in future work.

Overall, the results of Sect. 4.7 further suggest that the observed anisotropies do not emerge due to unaccounted biases.

4.8 Comparison with isotropic Monte Carlo simulations

The well-established statistical methods used up to now provide reliable parameter uncertainties and a robust estimation of the rareness of the observed anisotropies. Nonetheless, biases we are not aware of, can still be present in our analysis and lead to overestimated anisotropy signals. The same is true for cosmic variance. To further investigate this, we need to apply our analysis to simulated isotropic MC simulations. For the $L_{\rm X} - T$, $Y_{\rm SZ} - T$, and $L_{\rm BCG} - T$ scaling relations, we create 10000 simulated isotropic samples similar to the real ones. Analyzing these samples with the same procedures as in the main analysis, we test the frequency with which anisotropies equal or larger than the ones observed in the real data are retrieved. We also calculate the frequency with which the directions of the anisotropies for different scaling relations are randomly found to be as close as in the real data.

4.8.1 Constructing the isotropic simulated samples

To build every isotropic MC realization, we create the same number of clusters as in the real sample (for both our sample and ACC). We start from the $L_{\rm X} - T$ relation. We keep the coordinates, redshifts, and T (together with $\sigma_{\log T}$) of the simulated clusters fixed to the real values. This is done to incorporate all the possible effects that could create anisotropies, including the spatial distribution of the real clusters. Based on the best-fit scaling relation for the full, real sample, we calculate the predicted $L_{\rm X}$ value. We then add a random offset to the latter, drawn from a log-normal distribution with a standard deviation of $\sqrt{\sigma^2_{{\rm int},LT} + \sigma^2_{\log L_{\rm X}} + B^2_{LT} \times \sigma^2_{\log T}}$. Since low mass systems might exhibit a larger intrinsic scatter, we consider three different values of $\sqrt{\sigma_{{\rm int},LT}}$. We divide the sample in three equally sized subsamples according to their T value, and for every subsample we constrain $\sigma_{{\rm int},LT}$[13] given the best-fit A_{LT} and B_{LT} for the entire sample. Based on the T value of each simulated cluster, we then use the respective $\sigma_{{\rm int},LT}$ to draw the random offset of the $L_{\rm X}$ value. We ensure that the posterior distribution of the best-fit values of the simulated samples follow the input values for every parameter.

After that, we need to simulate $Y_{\rm SZ}$ for every cluster with S/N> 2 by taking into account the correlated scatter of $Y_{\rm SZ}$ and $L_{\rm X}$ with T. We first predict $Y_{\rm SZ}$ for every cluster, based on the best-fit $Y_{\rm SZ} - T$ relation and T. Then, we further add the expected scatter of $Y_{\rm SZ}$ based on the observed best-fit correlation in Sect. 4.7.6 and the random, simulated $L_{\rm X}$ scatter from before. On top of that, further noise is added on the

[13] One finds $\sigma_{{\rm int},LT}$=(0.29,0.23,0.16) for the $T < 3.5$ keV, 3.5 keV< $T <$ 5.8 keV, and $T > 5.8$ keV clusters respectively.

Y_{SZ} value, based on the scatter of this correlation (drawn from a log-normal distribution combining the statistical uncertainties of the observed L_X and Y_{SZ} residuals and the intrinsic scatter). We constrain the best-fit A_{YT}, B_{YT}, and $\sigma_{intr,YT}$ for all 10000 samples and confirm their distribution follow the values from the real samples.

A simulated, isotropic L_{BCG} value is also drawn for the 196 clusters with $0.03 < z < 0.15$, in the same way as for $L_X - T$. The infrared BCG luminosity does not show any correlation in its scatter with L_X and Y_{SZ}, and therefore no extra procedures are needed. We finally repeat the $L_{bol} - T$ and $Y_{SZ} - T$ simulations for ACC as well.

4.8.2 Results

We firstly explore our sample and ACC separately, for the available scaling relations. At the end, we combine the results to estimate the overall probability that our entire findings are due to chance. The histograms of the maximum anisotropy detected in the MC samples for every scaling relation, together with the results from the real samples, are displayed in Fig. 4.12.

Our sample

For the $L_X - T$ relation, we find that there is a 1.6% probability ($p = 0.016$) to observe a $\geq 2.8\sigma$ anisotropy within an isotropic Universe, using our methodology. One sees that the statistical significance of the two methods does not vary significantly.

For the $Y_{SZ} - T$ relation, the chance to randomly observe a $\geq 4.1\sigma$ anisotropy in an isotropic Universe is $p = 0.011$. This is significantly more probable than implied by standard analysis and demonstrates how apparent anisotropies might be present due to noise and cosmic variance. Nevertheless, the probability of such results to occur randomly is still quite low. If we consider the probability that the observed $L_X - T$ and $Y_{SZ} - T$ anisotropies emerge simultaneously for a simulated sample, then the probability dramatically drops to $p = 0.001$. On top of that, one needs to consider the direction agreement of the anisotropies of the real samples, which is within 10°. Out of the 10000 isotropic MC samples, only one exhibits this level of anisotropy for both scaling relations and within such a narrow cone ($p = 10^{-4}$). It is important to stress again that the correlation between the L_X and Y_{SZ} values has been taken into account as explained before.

For the $L_{BCG} - T$ relation, a $\geq 1.9\sigma$ anisotropy is detected for 42% of the samples, mostly due to the large scatter. Although this result alone is consistent with isotropy, when combined with the $L_X - T$ and $Y_{SZ} - T$ results, it returns $p = 4.2 \times 10^{-4}$, without accounting for the three similar anisotropy directions. When this is also included, one obtains $p = 3.5 \times 10^{-6}$.[14].

To sum up, from our sample alone, there is a 1 in $\sim$ 286000 probability that an observer would obtain our results due to statistical noise, cosmic variance, or scatter correlation between L_X, Y_{SZ}, and L_{BCG}.

4.8.3 Joint probability

Before we assess the overall probability of our results considering ACC as well, we wish to test ACC alone. For the $L_{bol} - T$ relation, the observed anisotropy amplitude is detected in the isotropic samples with $p = 0.26$, much less rare than implied by the default methods and consistent with isotropy. The observed behavior of the $Y_{SZ} - T$ relation yields $p = 0.055$ alone, more statistical significant than $L_{bol} - T$.

[14]Here we find the maximum angular distance θ among the most anisotropic directions of the three scaling relations. We then see how often all three directions lie within θ. This is done for all simulated samples. We then multiply this probability with the probability which comes purely from the amplitude of the anisotropies (i.e., $p = 4.2 \times 10^{-4}$).

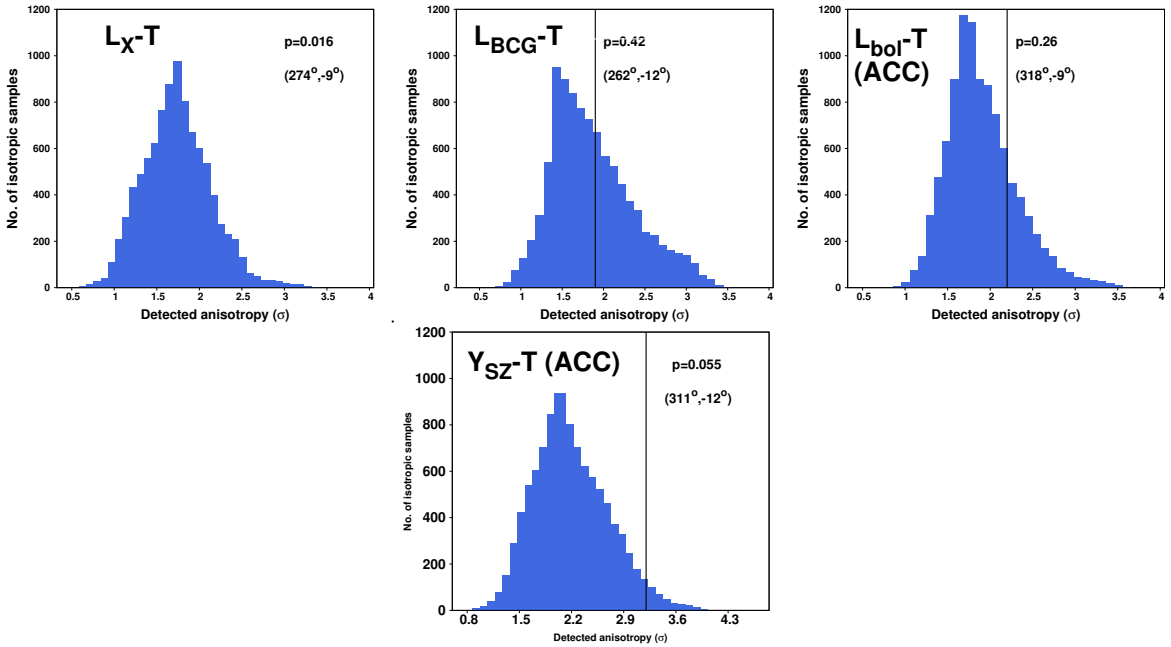

Figure 4.12: Histograms of the statistical significance of the maximum anisotropy as detected in 10,000 isotropic MC simulations for the $L_X - T$, $Y_{SZ} - T$, $L_{BCG} - T$, $L_{bol} - T$ (ACC), and $Y_{SZ} - T$ (ACC) scaling relations. The vertical black line represents the results from the real data, with the $p-$value and the direction also shown.

The joint probability to observe such anisotropies simultaneously in a sample is $p = 0.028$. If they were also to be separated by only $< 8^\circ$ as in the real data, then the probability significantly drops to $p = 0.003$. One sees that there are strong indications of an existing anisotropy from the ACC alone, although not enough to completely exclude the scenario of a random event.

Since the two samples are completely independent, the overall probability of our results is given by multiplying the distinct probabilities from the two samples. This yields $p = 1.2 \times 10^{-8}$. Furthermore, one needs to account for the agreement in the anisotropy direction between our sample and ACC. The maximum angular separation between the results of the two samples, for any two scaling relations, is 50°. Since the two samples are independent, one would expect a uniform distribution in the angular separation of their simulated maximum anisotropy directions. Thus, a $\leq 50^\circ$ separation would have a $\sim 28\%$ chance to occur.

Finally, combining all the available information, we find that our results are practically impossible to occur randomly within an isotropic Universe without an underlying physical cause, since the probability for this to happen is $p = 3.4 \times 10^{-9}$.[15]

4.9 Discussion and conclusions

The study of the (an)isotropic behavior of galaxy cluster scaling relations opens a very promising window for testing the cosmological principle. Galaxy cluster samples are much more spatially uniform than SNIa ones, and they extent to much larger scales than the galaxy samples which are used to study BFs. They can also be observed in several wavelengths and allow us to measure many different properties of

[15] Even if one completely ignores the directions of the anisotropies and only consider the amplitudes, the probability still is $p = 2.5 \times 10^{-5}$.

them. This provides us with plenty of nearly independent tests that trace cosmological phenomena, and that can be carried out with the same sample of objects. This has been accomplished in this work.

4.9.1 Systematics are not the reason of the consistent anisotropies

The $L_X - T$ anisotropy toward $(l, b) \sim (280^\circ, -15^\circ)$ that was originally observed in M20, could in principle be due to uncalibrated X-ray effects, such as excess X-ray absorption toward this sky direction. With our new data and analysis strategy, especially from the $L_X - Y_{SZ}$ relation which shows no signs of extra X-ray absorption toward the region in question, we can now decisively exclude this possibility. The lack of excess X-ray absorption effects toward that region is further confirmed by the analysis of ACC, and by the $L_X - L_{BCG}$ relation of our sample. The comparison between the X-ray-determined N_{Htot} and the W13-based N_{Htot} also does not indicate such an effect. Furthermore, the same anisotropies persist in scaling relations that are insensitive to unaccounted X-ray absorption, such as $Y_{SZ} - T$ and $L_{BCG} - T$. Thus, one sees that this is not the reason for the observed anisotropy.

Another possible solution to the observed anisotropies was the existence of biases related to the sample or the followed methodology, such as selection and archival biases, the effect of the Zone of Avoidance gap, etc. Our current results clearly exclude these possibilities as well. We showed that the Malmquist bias is more likely to underestimate the observed anisotropies rather than explain them. Also, it would not have such a strong effect for $Y_{SZ} - T$, $L_{BCG} - T$, and the ACC sample (which is not flux-limited). It was also shown that the fraction of morphologically relaxed and disturbed clusters does not spatially vary strongly enough to have any effect in the apparent anisotropy of the $L_X - T$ relation. Even if it did, this would have no strong effect on the $Y_{SZ} - T$ anisotropies, or the results from the other samples. Finally, by using isotropic simulated data we showed that the ZoA gap does not affect the amplitude of the anisotropies, while it has a very small effect in the direction of the latter. Even when we adjust our methodology to minimize the effects of this gap, the results are the same.

Finally, the isotropic MC simulations verify the very high ($> 5\sigma$) statistical significance of the observed anisotropies, when all the cluster scaling relations that are sensitive to cosmological phenomena are combined.

4.9.2 Cosmological phenomena behind the tension

The only obvious remaining explanations for the persisting cluster scaling relation anisotropies are two. The first one is a spatial variation of H_0 at a 9% level, due to a primordial anisotropy or new physics at $z \lesssim 0.2$ scales. The second one is a BF motion of ~ 1000 km/s extending to $\gtrsim 500$ Mpc scales. Both of these scenarios are in tension with ΛCDM and the generally adopted isotropic assumption. The results for every scaling relation that traces such phenomena are summarized in Tables 4.3 and 4.4. In Fig. 4.13, the amplitude and directions of the detected BFs are plotted, for different redshift bins.

Unfortunately, these two explanations are not distinguishable with the current data sets and more high$-z$ clusters are needed. The upcoming eRASS catalogs will provide us with thousands of such clusters. These distant objects will be of crucial importance when applying the techniques presented in this work, since we will be able to tell if, and at which scale, the cluster behavior converges to isotropy. The kSZ effect, which is caused by the peculiar motion of clusters in the CMB frame, can also be utilized to differentiate cosmological anisotropies from BFs. The limited number of clusters in our sample, together with the low redshifts and the large angular cluster sizes, did not allow us to extract useful information for this effect by stacking filtered kSZ maps of objects that presumably move toward a common direction. The reason for this lies in the large power of the primary CMB anisotropies at the scales that are relevant to our sample, as well as the limited angular resolution and sensitivity provided by

Table 4.3: Maximum anisotropy direction for every scaling relation, together with the needed H_0 relative variation in order to fully explain the anisotropy. The statistical significances derived by the default Bootstrap method and by the MC isotropic simulations are also displayed. The MC $p-$values account for both the amplitude of the anisotropies, and the agreement in their directions. The Gaussian σ values that correspond to the $p-$values are also displayed, for easier comparison.

Scaling relation	Max. anisot. direction (l, b)	H_0 variation (%)	Bootsrap significance (σ)	MC $p-$value (σ)
		Our sample		
$L_X - T$	$(274^{\circ}{}^{+43^{\circ}}_{-41^{\circ}}, -9^{\circ}{}^{+33^{\circ}}_{-31^{\circ}})$	$8.7 \pm 3.1\%$	2.8σ	$p = 0.016$ (2.4σ)
$Y_{SZ} - T$	$(268^{\circ}{}^{+34^{\circ}}_{-31^{\circ}}, -16^{\circ}{}^{+29^{\circ}}_{-30^{\circ}})$	$14.0 \pm 3.4\%$	4.1σ	$p = 0.011$ (2.6σ)
$L_{BCG} - T$	$(257^{\circ}{}^{+58^{\circ}}_{-49^{\circ}}, -12^{\circ}{}^{+38^{\circ}}_{-40^{\circ}})$	$9.1 \pm 4.8\%$	1.9σ	$p = 0.420$ (0.8σ)
		Our sample+ACC		
$L_X - T$	$(284^{\circ}{}^{+31^{\circ}}_{-12^{\circ}}, -4^{\circ}{}^{+7^{\circ}}_{-23^{\circ}})$	$9.3 \pm 3.1\%$	3.0σ	$p = 8.8 \times 10^{-4}$ (3.3σ)
$Y_{SZ} - T$	$(276^{\circ}{}^{+29^{\circ}}_{-23^{\circ}}, -14^{\circ}{}^{+19^{\circ}}_{-21^{\circ}})$	$13.3 \pm 3.1\%$	4.3σ	$p = 1.9 \times 10^{-4}$ (3.8σ)
All combined	$(\mathbf{273}^{\circ}{}^{+\mathbf{42}^{\circ}}_{-\mathbf{38}^{\circ}}, \mathbf{-11}^{\circ}{}^{+\mathbf{27}^{\circ}}_{-\mathbf{27}^{\circ}})$	$\mathbf{9.0 \pm 1.7\%}$	$\mathbf{5.4\sigma}$	$\mathbf{p = 3.4 \times 10^{-9}}$ (5.9σ)

Planck. Next-generation SZ instruments will significantly improve over *Planck's* sensitivity and angular resolution and allow for direct measurements of BFs using the kSZ effect.

Anisotropic Hubble expansion

In the case of an anisotropic Hubble expansion, a primordial anisotropy that extends to very large scales might be present. Such an anisotropy might correlate with the CMB dipole, if the latter is not purely of kinematic origin. Many claims for the detection of such cosmological anisotropies have been made recently[16]. Fosalba et al. (2020) found highly statistically significant anisotropies in the cosmological parameter constraints from the CMB using *Planck*, toward a region consistent with our results. Secrest et al. (2020) also found a large-scale anisotropy on the matter distribution, rejecting cosmic isotropy and the solely kinematic interpretation of the CMB dipole at a $\sim 4\sigma$ level. If their result was caused only due to our local motion within the matter rest frame, this would correspond to a ~ 900 km/s velocity, similar with our BF results.

Similar large-scale anisotropies in the distribution of high$-z$ radio and infrared sources have also been found (e.g., Tiwari et al., 2015; Colin et al., 2017; C. A. P. Bengaly et al., 2018; Rameez et al., 2018; Siewert et al., 2020), usually implying a $\sim 600 - 1500$ km/s motion compared to the matter rest frame. In other words, there are very strong indications that the matter rest frame differs from the CMB one, which is assumed to be the ultimately isotropic one. If true, this would have crucial implications on the standard model of cosmology. On the other hand, results that do not show any strong evidence for departure for statistical isotropy have also been presented (e.g., Andrade et al., 2019; C. A. P. Bengaly et al., 2019). Future eRASS catalogs will also shed more light on this question since they will provide previously unmatched catalogs of millions of X-ray point sources, tracing the matter distribution out to very large

[16]The existing literature is too large to be fully included here, therefore we focus only on the most recent results, or on results that were not already mentioned in M20. We direct the reader there for many additional studies that find consistent results with this work.

Table 4.4: Best-fit bulk flows for every scaling relation, method, and redshift bin that was considered in this work. MR and MA methods are explained in Sect. 4.3.2.

Scaling relation (method)	Redshift bin	Amplitude (km/s)	Direction (l, b)	Redshift bin	Amplitude (km/s)	Direction (l, b)
		Our sample				
$L_X - T$ (MR)	$z < 0.06$	1160 ± 420	$(318^{\circ}{}^{+37^{\circ}}_{-37^{\circ}}, -5^{\circ}{}^{+24^{\circ}}_{-23^{\circ}})$	$z < 0.1$	1140 ± 400	$(322^{\circ}{}^{+34^{\circ}}_{-33^{\circ}}, -13^{\circ}{}^{+23^{\circ}}_{-22^{\circ}})$
	$0.06 < z < 0.12$	1280 ± 440	$(262^{\circ}{}^{+54^{\circ}}_{-50^{\circ}}, +2^{\circ}{}^{+24^{\circ}}_{-28^{\circ}})$	$z < 0.16$	1090 ± 370	$(309^{\circ}{}^{+34^{\circ}}_{-31^{\circ}}, -20^{\circ}{}^{+21^{\circ}}_{-20^{\circ}})$
	$0.12 < z < 0.3$	1210 ± 670	$(253^{\circ}{}^{+61^{\circ}}_{-60^{\circ}}, -18^{\circ}{}^{+33^{\circ}}_{-29^{\circ}})$	$z < 0.25$	1050 ± 330	$(311^{\circ}{}^{+32^{\circ}}_{-31^{\circ}}, -18^{\circ}{}^{+19^{\circ}}_{-19^{\circ}})$
	All	1080 ± 330	$(313^{\circ}{}^{+33^{\circ}}_{-35^{\circ}}, -17^{\circ}{}^{+20^{\circ}}_{-21^{\circ}})$			
$L_X - T$ (MA)	$z < 0.09$	730 ± 320	$(268^{\circ}{}^{+32^{\circ}}_{-30^{\circ}}, -5^{\circ}{}^{+24^{\circ}}_{-22^{\circ}})$	$z < 0.16$	710 ± 290	$(278^{\circ}{}^{+29^{\circ}}_{-28^{\circ}}, -12^{\circ}{}^{+23^{\circ}}_{-22^{\circ}})$
	$z > 0.067$	690 ± 340	$(293^{\circ}{}^{+38^{\circ}}_{-40^{\circ}}, -12^{\circ}{}^{+27^{\circ}}_{-27^{\circ}})$	$z < 0.25$	670 ± 160	$(291^{\circ}{}^{+26^{\circ}}_{-27^{\circ}}, -21^{\circ}{}^{+21^{\circ}}_{-21^{\circ}})$
	All	650 ± 280	$(298^{\circ}{}^{+25^{\circ}}_{-25^{\circ}}, -21^{\circ}{}^{+19^{\circ}}_{-18^{\circ}})$			
$Y_{SZ} - T$ (MR)	$z < 0.07$	1110 ± 420	$(254^{\circ}{}^{+45^{\circ}}_{-40^{\circ}}, -17^{\circ}{}^{+19^{\circ}}_{-19^{\circ}})$	$z < 0.1$	1080 ± 400	$(257^{\circ}{}^{+25^{\circ}}_{-24^{\circ}}, -28^{\circ}{}^{+25^{\circ}}_{-21^{\circ}})$
	$0.07 < z < 0.12$	920 ± 540	$(312^{\circ}{}^{+59^{\circ}}_{-62^{\circ}}, -34^{\circ}{}^{+32^{\circ}}_{-29^{\circ}})$	$z < 0.16$	1050 ± 390	$(265^{\circ}{}^{+34^{\circ}}_{-31^{\circ}}, -27^{\circ}{}^{+24^{\circ}}_{-21^{\circ}})$
	$0.12 < z < 0.3$	1280 ± 780	$(321^{\circ}{}^{+75^{\circ}}_{-103^{\circ}}, -42^{\circ}{}^{+45^{\circ}}_{-29^{\circ}})$	$z < 0.25$	1020 ± 390	$(267^{\circ}{}^{+32^{\circ}}_{-31^{\circ}}, -27^{\circ}{}^{+22^{\circ}}_{-22^{\circ}})$
	All	1030 ± 370	$(263^{\circ}{}^{+33^{\circ}}_{-35^{\circ}}, -22^{\circ}{}^{+20^{\circ}}_{-21^{\circ}})$			
$Y_{SZ} - T$ (MA)	$z < 0.09$	1270 ± 370	$(254^{\circ}{}^{+22^{\circ}}_{-22^{\circ}}, -28^{\circ}{}^{+14^{\circ}}_{-18^{\circ}})$	$z < 0.16$	1170 ± 360	$(270^{\circ}{}^{+25^{\circ}}_{-23^{\circ}}, -30^{\circ}{}^{+24^{\circ}}_{-19^{\circ}})$
	$z > 0.09$	820 ± 430	$(242^{\circ}{}^{+94^{\circ}}_{-79^{\circ}}, -13^{\circ}{}^{+20^{\circ}}_{-24^{\circ}})$	$z < 0.25$	1080 ± 330	$(264^{\circ}{}^{+24^{\circ}}_{-23^{\circ}}, -23^{\circ}{}^{+22^{\circ}}_{-23^{\circ}})$
	All	1040 ± 310	$(267^{\circ}{}^{+23^{\circ}}_{-21^{\circ}}, -28^{\circ}{}^{+17^{\circ}}_{-15^{\circ}})$			
$L_{BCG} - T$ (MR)	$0.03 < z < 0.15$	620 ± 400	$(293^{\circ}{}^{+50^{\circ}}_{-51^{\circ}}, +2^{\circ}{}^{+29^{\circ}}_{-30^{\circ}})$			
$L_{BCG} - T$ (MA)	$0.03 < z < 0.15$	650 ± 370	$(261^{\circ}{}^{+47^{\circ}}_{-52^{\circ}}, -25^{\circ}{}^{+30^{\circ}}_{-22^{\circ}})$			
			ACC			
$L_{bol} - T$ (MR)	$z < 0.2$	1020 ± 630	$(277^{\circ}{}^{+66^{\circ}}_{-59^{\circ}}, +2^{\circ}{}^{+29^{\circ}}_{-31^{\circ}})$	$z < 0.35$	920 ± 540	$(244^{\circ}{}^{+69^{\circ}}_{-52^{\circ}}, +20^{\circ}{}^{+24^{\circ}}_{-33^{\circ}})$
	All	940 ± 450	$(254^{\circ}{}^{+60^{\circ}}_{-44^{\circ}}, +18^{\circ}{}^{+24^{\circ}}_{-30^{\circ}})$			
$L_{bol} - T$ (MA)	All	890 ± 440	$(324^{\circ}{}^{+39^{\circ}}_{-51^{\circ}}, -3^{\circ}{}^{+32^{\circ}}_{-33^{\circ}})$			
$Y_{SZ} - T$ (MR)	$z < 0.2$	1080 ± 620	$(281^{\circ}{}^{+61^{\circ}}_{-52^{\circ}}, -7^{\circ}{}^{+39^{\circ}}_{-37^{\circ}})$	$z < 0.35$	970 ± 490	$(264^{\circ}{}^{+59^{\circ}}_{-52^{\circ}}, +6^{\circ}{}^{+27^{\circ}}_{-29^{\circ}})$
	All	980 ± 420	$(268^{\circ}{}^{+45^{\circ}}_{-39^{\circ}}, +6^{\circ}{}^{+29^{\circ}}_{-29^{\circ}})$			
$Y_{SZ} - T$ (MA)	All	910 ± 410	$(273^{\circ}{}^{+43^{\circ}}_{-35^{\circ}}, -11^{\circ}{}^{+21^{\circ}}_{-20^{\circ}})$			

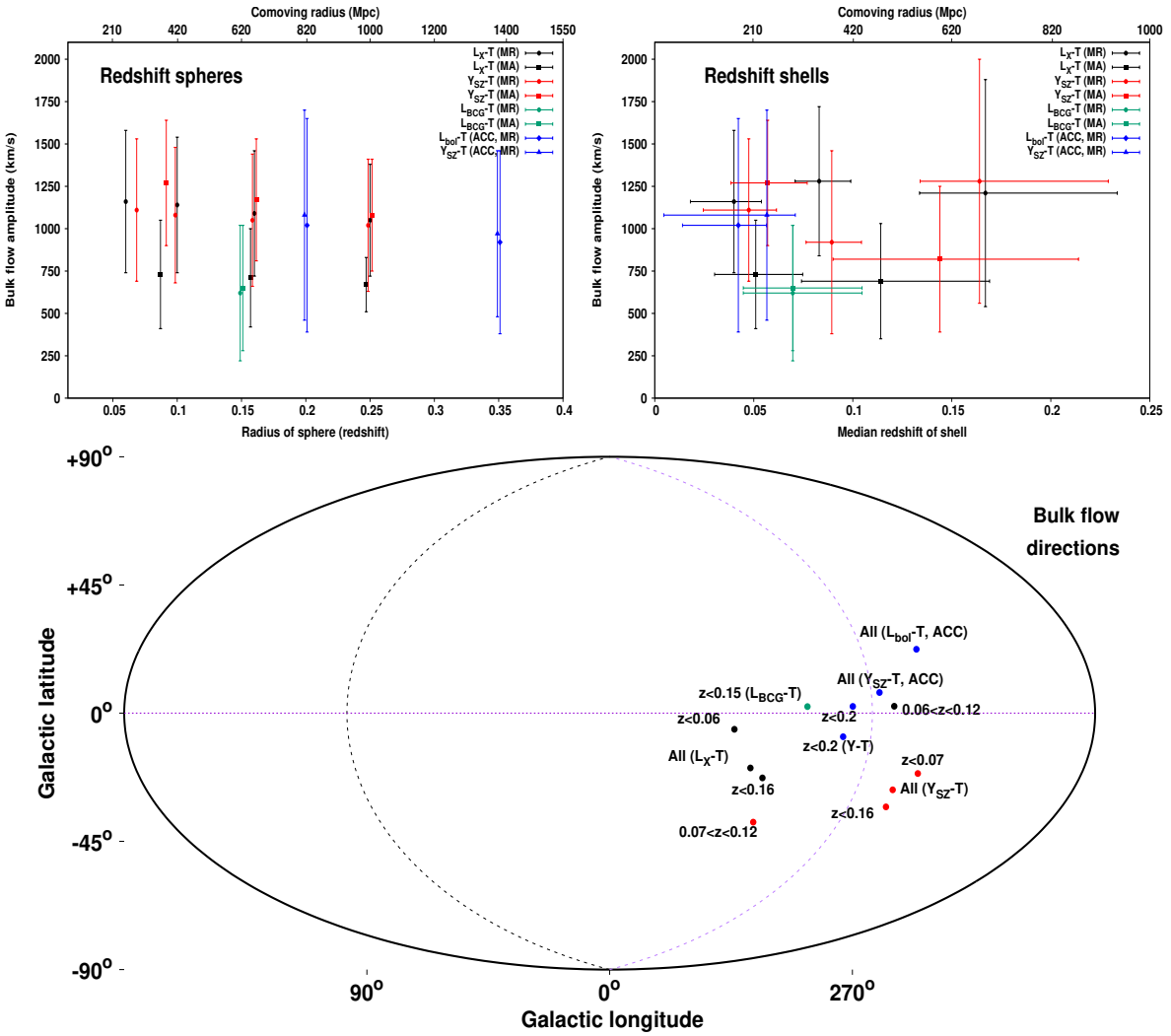

Figure 4.13: *Top left*: Bulk flow amplitude and its 68.3% uncertainty as a function of the redshift radius of the used spherical volumes (or the comoving distance radius). Circles and squares correspond to the MR and MA methods respectively. Black, red, and green points correspond to the $L_{\rm X} - T$, $Y_{\rm SZ} - T$, and $L_{\rm BCG} - T$ relations respectively. Blue diamonds and triangles correspond to the ACC $L_{\rm bol} - T$ and $Y_{\rm SZ} - T$ relations respectively. Results above $z \gtrsim 0.16$ are expected to be dominated by more local clusters and thus being overestimated. *Top right*: Bulk flow amplitude and its 68.3% uncertainty as a function of the median redshift of each shell (or the comoving distance), together with the standard deviation of the redshift distribution. The color coding is the same as before. Data points with both the same color and shape, are independent to each other. *Bottom*: Examples of bulk flow directions as found for different redshift bins and methods. The color coding is the same as before. All directions agree with each other within 1σ.

scales.

In addition, much work has been done on testing the isotropy using SNIa. Colin et al. (2019) detect a 3.9σ anisotropy in the deceleration parameter (toward a consistent direction with our results) using a maximum-likelihood analysis. In contrast, Soltis et al. (2019) find no evidence of departure from isotropy using a novel nonparametric methodology. Except for different SNIa samples, the two papers also follow different approaches in the treatment of the data. Many other studies (e.g., Chang et al., 2015; Deng et al., 2018; Sun et al., 2019; Zhao et al., 2019; Salehi et al., 2020; Hu et al., 2020) also used SNIa combined with other probes, identifying an anisotropic direction in impressive agreement with our results. The statistical significance of their findings however is marginally consistent with an isotropic Universe. They also argue that the main problem of such SNIa studies is still the highly inhomogeneous distribution of the data across the sky, while the effect of peculiar velocity corrections has also been studied (e.g., Huterer, 2020; Mohayaee et al., 2020). Finally, other kinds of nonlocal tensions with the cosmological principle have been also observed (Horvath et al., 2020; Shamir, 2020).

Large scale bulk flows

The consistent observation of cluster anisotropies across several scaling relations could hint to the existence of large BFs that by far exceed the BF scales predicted by ΛCDM. In Fig. 4.13, one sees that a > 700 km/s motion is consistently detected wrt the CMB rest frame, with no signs of fading at $\gtrsim 500$ Mpc. The observed BF amplitude of spherical volumes of much larger radius might be overestimated since clusters at lower distances are expected to dominate the BF signal. However, this plays no role for the iterative redshift shells results at $z > 0.12$, which seem to hint that the large BF might indeed persist farther (with a small statistical significance of $\sim 2\sigma$). More high$-z$ clusters are necessary to derive safe conclusions at these scales.

ΛCDM predict negligible BF amplitudes at scales of $\gtrsim 250$ Mpc. Flow motions of similar, large amplitudes have been reported in the past for galaxy clusters (e.g., Lauer et al., 1994; M. J. Hudson et al., 1999; Kashlinsky et al., 2008; Kashlinsky et al., 2010; Atrio-Barandela et al., 2015), while Osborne et al. (2011), Planck Collaboration et al. (2014) and and Mody et al. (2012) fail to see any large scale BFs in the CMB kSZ data. Studies using thousands of galaxies, consistently detect a BF toward the same direction with us, but with a ~ 4 times smaller amplitude. However, it also seems to extend to scales larger than ~ 300 Mpc, up to where the galaxy surveys are usable. For instance, Watkins et al. (2009) and Magoulas et al. (2016) found a ~ 400 km/s BF at $\sim 100 - 150h^{-1}$ Mpc scales toward $(l, b) \sim (295^{\circ}, +10^{\circ})$, which is moderately discrepant with the standard cosmological model. Carrick et al. (2015) and Boruah et al. (2020) found a ~ 170 km/s BF toward $(l, b) \sim (303^{\circ}, +3^{\circ})$ that extends to $z > 0.067$, but not particularly inconsistent with the standard expectations. Lavaux et al. (2013) used the kSZ effect on galaxy halos and found a BF of ~ 285 km/s for $200h^{-1}$ Mpc scales. Watkins et al. (2015) also found a good agreement with ΛCDM at small scales, but a moderate disagreement at larger ones. Furthermore, Peery et al. (2018) find only a 2% chance for their detected BF at scales $150h^{-1}$ Mpc to occur within ΛCDM. Studies have tried to constrain the BF with SNIa data as well, which extend to much larger scales, but are highly inhomogeneous (Colin et al., 2011; Feindt et al., 2013; Appleby et al., 2015; Mathews et al., 2016; Salehi et al., 2020, and references therein) find similar results to the galaxy surveys, where mild BFs extend to larger-than-expected scales. However, they again stress the limitations of current SNIa samples for such studies and that conclusive answers cannot be given. Other studies have stressed that the usual Newtonian treatment of peculiar velocity fields can significantly underestimate the inferred bulk flows (e.g., Tsagas et al., 2020; Tsaprazi et al., 2019). From all that it is evident that it is still not quite clear if the detected BF motions are entirely in agreement with the standard model, and out to what scale the BF persists.

Substantial, local matter inhomogeneities such as local voids or overdensities, could contribute to

giving rise to unexpected large BFs. If we are located away from the void center, this could cause the apparent expansion rate to be lower toward the more matter-dominated side. There have been claims for the existence of such large voids (or overdensities) that could create outflows out to ~ 400 Mpc scales (Keenan et al., 2012; Rubart et al., 2014; J. R. Whitbourn et al., 2014; Shanks et al., 2019; Shanks et al., 2019; Tully et al., 2019; Böhringer et al., 2020; Kazantzidis et al., 2020; Haslbauer et al., 2020, and references therein), and their effects on the measured H_0 have been studied. These scales are close to the median distance distribution of our cluster samples, and thus could indeed affect our results. The predicted H_0 variation due to these voids is slightly lower than the one we observe, but generally agrees. Of course, the fact that they offer a possible (at least partial) explanation for the local cluster anisotropies, does not alleviate the problem, since the existence of such large voids is in direct disagreement with the ΛCDM.

4.10 Summary

In this work, we applied a scrutinized test for the isotropy of the local Universe. We studied the anisotropy of 10 galaxy cluster scaling relations, utilizing observations in X-rays, infrared, and submillimeter. Using the $L_{\rm X}-T$, $Y_{\rm SZ}-T$, and $L_{\rm BCG}-T$ scaling relations of eeHIFLUGCS, and combining with the completely independent ACC sample, we detected a $\sim 5.5\sigma$ anisotropy toward $(l,b) \sim (280^{\circ}{}^{+35^{\circ}}_{-35^{\circ}}, -15^{\circ}{}^{+20^{\circ}}_{-20^{\circ}})$. This high statistical significance is further confirmed by applying our methods to isotropic Monte Carlo simulated samples. Considering the low median redshift of the cluster data ($z \sim 0.1$), this direction agrees with a plethora of past studies of several probes. We robustly showed that our data do not suffer from unknown X-ray absorption issues, and our results do not originate from any kind of known biases. Moreover, it would be extremely difficult for any "typical" bias to simultaneously explain the similar anisotropic results across nearly independent scaling relations, in different wavebands.

If the observed anisotropies were the result of an anisotropic expansion rate, one would need a $\sim 9\%$ variation of H_0 to reconcile with the observations. Alternatively, one would need a bulk flow motion of ~ 900 km/s, possibly extending beyond 500 Mpc, to explain the obtained cluster anisotropies. Due to the low redshift range of our samples, these two phenomena are currently inseparable for a typical observer. However, both of these scenarios are in tension with the standard assumptions in ΛCDM. Since these are currently the only available explanations for our observations, we are faced with a severe problem that needs to be solved. The future eRASS catalogs will help us understand these anisotropies better, and determine if there is a scale of convergence with isotropy, or if this anomaly extends to much larger scales.

4.11 Appendix A: Additional details on cluster measurements

Details on the $Y_{\rm SZ}$ measurement

The MMFs algorithms are applied to the *Planck* data in steps that are analogous to the ones presented by A16 (Sect. 2.1). Fields with a size of $10^{\circ} \times 10^{\circ}$ are extracted around each cluster at each of the *Planck* High Frequency Instrument (HFI) bands. The Low Frequency Instrument (LFI) channels are excluded because of their low spatial resolution and lower sensitivity. The six *Planck* HFI maps for each cluster are then processed with a MMF, which filters and combines them into a single map. The needed spectrum of the tSZ effect has been computed for both the nonrelativistic case as well as with relativistic corrections as explained later. In all cases, the instrumental impact on the shape of the spectral energy distribution

(SED) has been taken into account by computing the bandpass-corrected spectra (see Eq. 13, Eq. A1, and Table A1 in Erler et al. 2018).

Applying the filters and coadding the filtered maps yields a map of the deconvolved central Comptonization parameter $y_0^{\rm MMF}$ in each pixel of the map. Using the normalized cluster template, the value of $y_0^{\rm MMF}$ is converted to Y_{5R500} by

$$Y_{5R500}\,[\mathrm{arcmin}^2] = y_0^{\rm MMF} 2\pi \int_0^{5\theta_{500}} \mathrm{d}\theta\, y(\theta)\,\theta, \tag{4.10}$$

where $y_0^{\rm MMF}$ is the value of the y-parameter through the central l.o.s. that has been derived using MMFs, $y(\theta)$ is the y-parameter profile of the cluster that has been normalised to unity, and θ is the radial angular coordinate in the plane of the sky, and θ_{500} being the apparent R_{500} in arcmin.

A total of four different Y_{5R500} values are extracted for every cluster. The first value is obtained via a MMF approach using the nonrelativistic spectrum of the tSZ effect. This method is identical to the one used by the *Planck* Collaboration. The second value is obtained via a MMF approach using the relativistic spectrum of the tSZ effect computed using the M20 estimates for T. When the latter is not available, T is calculated through the $L_{\rm X} - T$ relation found in M20, where $L_{\rm X}$ is given by MCXC, after it has been corrected for the X-ray absorption based on the Willingale et al. (2013) values (following the same procedure as in M20). The third value is obtained via a constrained MMF approach (CMMF, E19) using the nonrelativistic spectrum of the tSZ effect and the spectrum of the kSZ effect. The latter is used to remove any bias introduced by the kSZ effect. The fourth and last value is obtained identically to the third value, but using a relativistic spectrum of the tSZ effect.

The four Y_{5R500} values do not differ significantly to each other ($< 7.2\%$), and any selection for the default Y_{5R500} used in this work results in the same conclusions with only minimal numerical fluctuations. We choose as the default Y_{5R500} the result of the fourth approach, where a CMMF approach is followed as described in E19, correcting for relativistic effects and attempting to remove any kSZ bias. The change in the Y_{5R500} values due to the removal of the kSZ effect is usually much smaller than the 1σ uncertainties of the central values. This has nearly no effect in any BF detection from our analysis, since the major contribution of BFs to $Y_{\rm SZ}$ comes from D_A and the (biased) redshift-distance conversion.

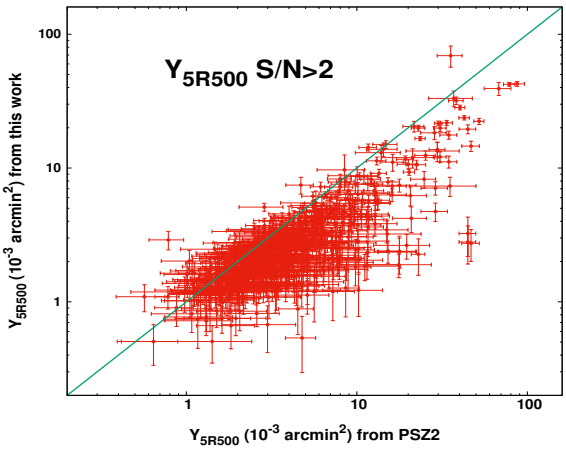

Figure 4.14: Comparison between the default Y_{5R500} values we use in this work based on the method of E19 and the Y_{5R500} values as given in the PSZ2 catalog for the 566 clusters in common. The equality line is displayed in green.

Comparison with the PSZ2 values

In the left panel of Fig. 4.14 we compare the values of our default Y_{5R500} with the ones from PSZ2 for 566 common clusters[17]. One can see there is a linear relation between the two which demonstrates the robustness of our method. Nevertheless, a systematic offset from the values reported by the *Planck* Collaboration is observed, especially in higher Y_{5R500} values. This partially arises from the fact that A16 estimate the size of clusters directly from the SZ data by mapping the significance of the obtained values for Y_{5R500} as a function of MMF filter templates of different cluster size, parameterized through the scale radius $\theta_s = \theta_{500}/c_{500}$, where c_{500} is the cluster's concentration parameter. However, for the vast majority of clusters, the $\theta_s - Y_{5R500}$ plane is left largely unconstrained, for which reason the *Planck* Collaboration employs an XMM-Newton derived $\theta - Y_{5R500}$ prior to break the degeneracy between the two parameters (e.g. Fig. 16 of A16). Additionally, small differences in the adopted centers might contribute to the observed scatter as well[18]. Although the data employed here are identical and our filtering is based on the same MMF technique as used by A16, differences in the reported values for Y_{5R500} can therefore still appear. The comparison does not significantly change with the use of Y_{5R500} values based on the other three E19 approaches we described in Appendix 4.11.

Details on obtaining the near infrared BCG luminosity L_{BCG}

The main criteria for a galaxy to be selected as the BCG were the following. Firstly, it must be the brightest in the *r*-band of the optical regime or *Ks* and *W1* in 2MASS and WISE of the NIR domain. Secondly, it should be located within a distance of R_{500} from the X-ray center of the cluster. Both of these values are taken by the MCXC catalog. Thirdly, the BCG's redshift must be within a certain range Δz of the cluster redshift. If the BCG redshift was estimated via photometric measurements, then $\Delta z \leq 0.02$, whilst the allowed redshift difference for spectroscopic redshifts was $\Delta z \leq 0.01$. If multiple BCG candidates were suggested for one cluster, the following criteria were considered. The BCG should possess a rather extended envelope and it should be selected by optical surveys over NIRs.

Two different corrections took place before selecting the BCG of every cluster. The galaxy magnitudes were corrected for galactic extinction, using the Schlegel maps (Schlegel et al., 1998) and assuming an extinction law (Fitzpatrick, 1999) with R_V= 3.1. The photometric magnitudes were also corrected to the rest frame of individual galaxies by applying an appropriate k-correction. The k-correction code provided by Chilingarian et al. (2011) was used for all data except for WISE, as the coefficients for WISE filters are not included in this program. For WISE galaxies, we instead used the k-correction code from Blanton (Blanton et al., 2007).

Details on the X-ray determined $N_{\mathrm{H,Xray}}$

To determine $N_{\mathrm{H,Xray}}$, we used the exact same spectral fitting procedure as described in M20, when the X-ray redshift was fitted. This time the $N_{\mathrm{H,Xray}}$ is left free to vary instead. Its value was linked between the spectra from the $0 - 0.2\ R_{500}$ region and the $0.2 - 0.5\ R_{500}$ region. The redshift is kept fixed at its M20 value, while the temperature, metallicity and normalization values are left free to vary for each region separately. We used the 0.7-7.0 keV range to fit the spectra (to be consistent with the results from M20). The Asplund et al. (2009) abundance table was used for the fits.

We were able to constrain $N_{\mathrm{H,Xray}}$ for 213 out of 237 Chandra clusters and 27 out of 76 XMM-Newton clusters. When we performed the $N_{\mathrm{H,Xray}}$–N_{Htot} comparison, we saw that the data residuals compared

[17]The matching criteria were that the angular separation of the two given cluster centers should be $\leq 1.5^{\circ}$ and the redshift difference $\Delta z \leq 0.01$ between the two catalogs.

[18]The used SZ center is the position of the brightest pixel within a 15×15 arcmin^2 box centered around the X-ray peak.

to the best-fit model behaved strongly as a function of the $N_{\rm H,Xray}$ measurement uncertainty. Clusters with large statistical uncertainties were significantly downscattered, increasing the scatter of the relation. These were mostly low $N_{\rm H,Xray}$ clusters. The 0.7 keV cut removes most of the power for detecting $N_{\rm Htot}$ (which shows up more strongly at lower energies). So when the $N_{\rm Htot}$ effects are already small, a constraint is nearly impossible. To sufficiently restrict the noise, we excluded the 35% of the sample with the largest (average) uncertainties, leaving us with 156 clusters with an $N_{\rm H,Xray}$ measurement uncertainty of $< 25\%$. Although these cuts were chosen arbitrarily, they took place strictly before any anisotropy test, to avoid any confirmation bias.

4.12 Appendix B: ACC results

In this section, we only use the ACC sample to study the anisotropic behavior of the $L_{\rm bol} - Y_{\rm SZ}$, $L_{\rm bol} - T$, and $Y_{\rm SZ} - T$ relations. Due to the much smaller number of clusters, we consider a $\theta = 90^\circ$ scanning cones for all scaling relations, so at least 35 clusters lie within each cone.

The $L_{\rm X} - Y_{\rm SZ}$ relation

We study the $L_{\rm bol} - Y_{\rm SZ}$ relation for ACC alone. The results are shown in Fig. 4.15.

The maximum anisotropy is found toward $(l, b) = (24^\circ \pm 42^\circ, +22^\circ \pm 21^\circ)$ at a 2.3σ level. These 59 clusters are $26 \pm 11\%$ dimmer than the rest. This level of anisotropy can be considered marginally consistent with an isotropic $L_{\rm bol} - Y_{\rm SZ}$ relation. If however there was some extra X-ray absorption taking place toward that direction, it would correspond to an extra $N_{\rm Htot} \sim 7.9 \pm 3.4 \times 10^{20}/{\rm cm}^2$. This value is consistent with the $L_{\rm X} - Y_{\rm SZ}$ result of our sample within 1.1σ. The maximum anisotropy region however is located 90° away from the $L_{\rm X} - Y_{\rm SZ}$ direction. This could indicate that the normalization variation is due to statistical noise and does not reveal any unknown absorption. Alternatively, it could be attributed to the incapability of the $\theta = 90^\circ$ cones to accurately pinpoint the direction where the hidden X-ray absorption takes place, especially since the direction uncertainties are considerably large. Based on all the above, the case that the mild anisotropies seen in the ACC sample are due to chance cannot be excluded.

Finally, ACC further confirms our previous conclusion about the $L_{\rm X} - T$ anisotropies found in M20. There is no indication that they appear due to previously unaccounted X-ray effects, since the region toward $(l, b) \sim (300^\circ, -20^\circ)$ shows a completely consistent behavior with the rest of the sky.

The $L_{\rm bol} - T$ relation

For the $L_{\rm bol} - T$ relation of ACC, the maximum anisotropy is found toward $(l, b) = (318^\circ \pm 45^\circ, -9^\circ \pm 37^\circ)$, in a 2.2σ tension with the rest of the sky[19]. This region appears fainter than the rest by $\sim 32 \pm 13\%$ on average. Its behavior is almost identical to the results of M20, as seen in Fig. 4.15. However, the decreased statistical significance suggests that the $L_{\rm bol} - T$ relation for ACC alone is marginally consistent with isotropy. The angular separation between the most anisotropic regions of ACC and our sample is 40°, and well within the uncertainties.

Cosmological anisotropies and bulk flows

For ACC, one would need $H_0 = 61.3 \pm 4.2$ km/s/Mpc toward $(l, b) \sim (318^\circ, -9^\circ)$ and $H_0 = 72.2 \pm 2.4$ km/s/Mpc for the rest of the sky. The obtained H_0 value agrees within 1σ with the independent result

[19] In M20 we considered $\theta = 75^\circ$, because the slope was kept fixed, and fewer cluster per regions were needed to sufficiently determine the normalization. Here the slope is left free to vary.

from our sample.

For the BF explanation, applying the MR method to ACC, we find a BF of $u_{\mathbf{BF}}$= 940 ± 450 km/s toward $(l, b) = (254^\circ \pm 52^\circ, +18^\circ \pm 27^\circ)$. This direction is separated by 31° from the CMB dipole, and by 67° from the maximum anisotropy region, although this difference is within 1σ. Due to the limited number of data and the large scatter, we can only divide the sample into two independent redshift bins, $z < 0.2$ and $z > 0.2$. For the former we practically find the same BF as for the full sample, while for the latter we find no statistical significant evidence of a BF. However, the results are inconclusive due to the limited number of available clusters in this sample, and the subdominant effect BFs have at these redshifts compared to the intrinsic scatter.

For the MA method, we obtain $u_{\mathbf{BF}}$= 890 ± 440 km/s toward $(l, b) = (324^\circ \pm 45^\circ, -3^\circ \pm 32^\circ)$. This direction is more in agreement with the maximum anisotropy direction of ACC, while the BF amplitude is similar. The sample size is not sufficient to consider individual redshift bins that would provide different insights than the full sample.

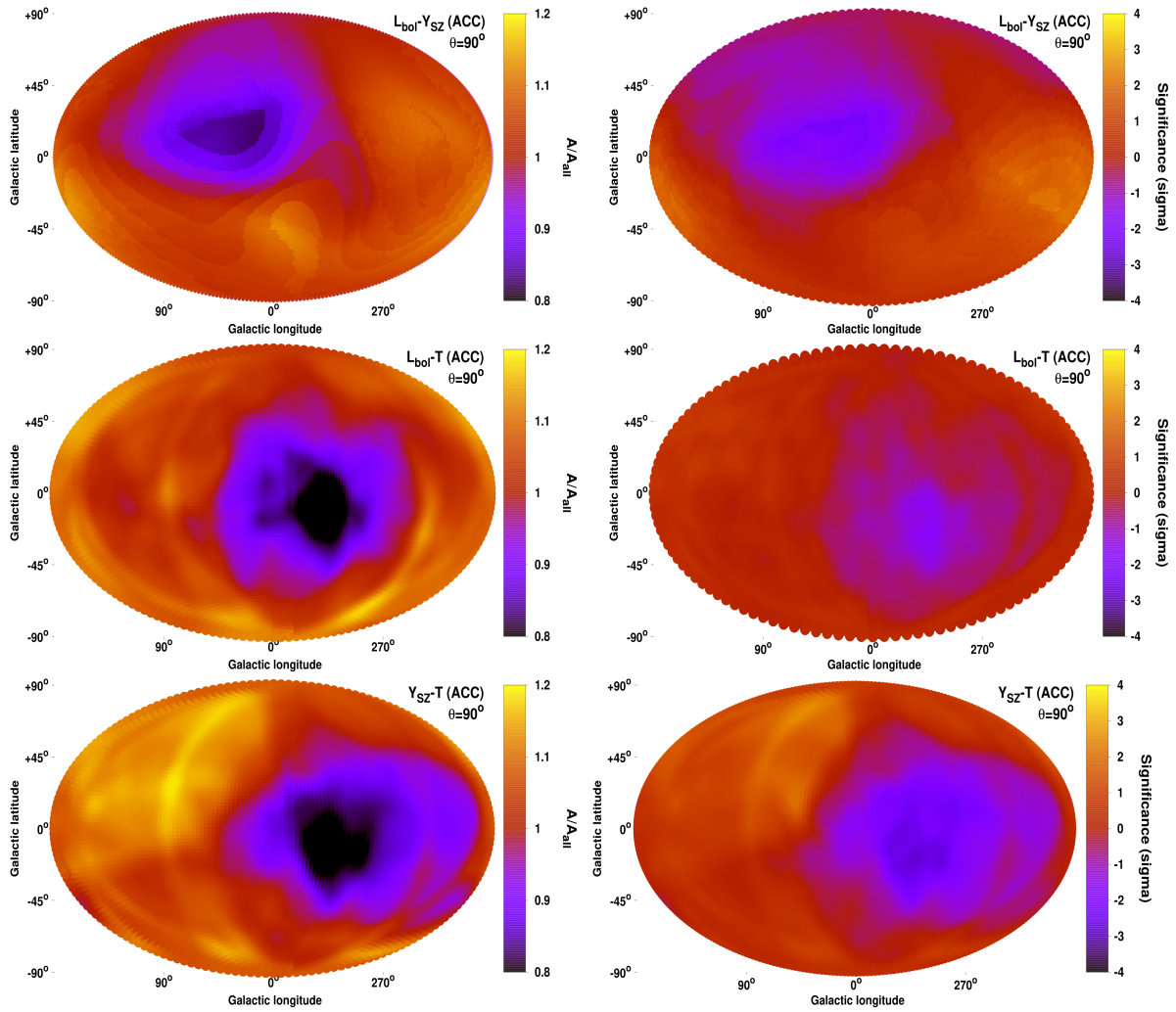

Figure 4.15: Normalization anisotropy maps and the respective statistical significance maps of the anisotropies for the $L_{\rm bol} - Y_{\rm SZ}$ (top), the $L_{\rm bol} - T$ (middle), and the $Y_{\rm SZ} - T$ (bottom) scaling relations for the ACC sample. The $L_{\rm bol} - Y_{\rm SZ}$ traces only unaccounted X-ray absorption effects, while the $L_{\rm X} - T$ and $Y_{\rm SZ} - T$ behavior mirrors cosmological anisotropies and BFs.

The $Y_{SZ} - T$ relation

We repeat the $Y_{SZ} - T$ anisotropy analysis with only the 113 ACC clusters with Y_{SZ} S/N> 2, with a median $z \sim 0.22$. The scatter is similar to our sample, but the limited number of clusters forces us to consider $\theta = 90^\circ$ cones. This way we ensure we have at least 35 clusters in each cone (which inevitably leads to large uncertainties). The normalization and sigma maps are displayed in Fig. 4.15. We find an anisotropy of 3.2σ toward $(l, b) = (311^\circ \pm 57^\circ, -12^\circ \pm 39^\circ)$, 42° away from the direction of our sample and well within the 1σ uncertainties. The relative difference of A_{YT} of this region compared to the rest of the sky is $35 \pm 11\%$. The direction is also identical to the one obtained with the $L_{bol} - T$ relation, with a larger statistical significance.

Cosmological anisotropies and bulk flows

In terms of H_0, one obtains $H_0 = 60.6 \pm 3.6$ km/s/Mpc toward the most anisotropic region, and $H_0 = 73.4 \pm 1.9$ km/s/Mpc for the opposite hemisphere. These values are consistent within $< 1.4\sigma$ with our sample's results, and with the joint $L_X - T$ analysis results.

For the BF scenario and the MR method, we obtain $u_{\mathbf{BF}} = 980 \pm 420$ km/s toward $(l, b) = (268^\circ \pm 42^\circ, +6^\circ \pm 29^\circ)$ for the full sample. Once again for ACC, the direction is close to the CMB dipole, but slightly shifted compared to the maximum anisotropy direction. The BF has its usual amplitude, even though the used sample has a large median $z \sim 0.22$. For $z < 0.2$ we obtain a similar BF as for the full sample. For $z > 0.2$, the BF points toward $(l, b) \sim (320^\circ, +5^\circ)$, however it is poorly constrained and not statistical significant.

For the MA method, we find $u_{\mathbf{BF}} = 910 \pm 440$ km/s toward $(l, b) = (273^\circ \pm 38^\circ, -11^\circ \pm 21^\circ)$ for the full sample, in agreement with the MR method.

Appendix C: Anisotropies in the other scaling relations

The $R - L_X$, $R - T$, $R - Y_{SZ}$, $R - L_{BCG}$, and $Y_{SZ} - L_{BCG}$ scaling relations cannot currently provide meaningful insights on the possible origin of the detected anisotropies. However, they may prove to be very useful for future tests with larger samples, and with a better characterization of the dynamical state of the clusters. Here we discuss their results, limitations, and future potential.

Anisotropies of the $R - L_X$, $R - T$, $R - Y_{SZ}$, and $R - L_{BCG}$ scaling relations

The scaling relations of the cluster effective radius are potentially very interesting, once the systematic biases are properly handled and the sample sizes are further increased. For the $R - L_X$, $R - Y_{SZ}$, and $R - L_{BCG}$ relations, both quantities depend on the cosmological parameters, but due to the rather flat slopes, the normalization weakly depends on the angular diameter distance ($A_{RX} \propto D_A^{(0.5-0.7)}$). Thus, a 15% spatial variation of H_0 would result in a $7 - 10\%$ variation of A_{RX}. Much smaller effects are expected due to BFs. This level of anisotropy would not be detectable over random noise combined with the mild, existing systematic issues. This is the most crucial limitation of these relations. Future samples, such as the eRASS catalogs, will dramatically increase the sample sizes, which will reduce the random noise and allow the detection of $\sim 10\%$ anisotropies.

For the $R - T$ relation, there is an $A_{RT} \propto D_A$ dependency. For the same underlying effect, $R - T$ will show half the normalization variation than $L_X - T$, $Y_{SZ} - T$ and $L_{BCG} - T$. Despite the weaker signal, it can still be a valuable test to detect cosmological anisotropies and BFs when applied to larger cluster samples, and when a more precise modelling of the systematics is feasible.

R is also rather insensitive to unaccounted X-ray absorption effects. The latter can only affect the determination of R_{500}, which is based on the absorption-affected flux. However, $L_X \propto R_{500}^{4.8}$, so a 20% bias in L_X would only cause a $< 4\%$ bias in R_{500}, which is negligible. To confirm this, we remeasure R for all clusters, after changing the input N_{Htot} by $\pm 50\%$. Almost all clusters (99.5% of the sample) show an R change of $< 2.5\%$.

The main systematic effect compromising the R scaling relations is the effect of the CC clusters on the measurements. This was already discussed in Sect. 4.4, and is more extensively discussed here. The directional behavior of these relations clearly correlates with the dynamical state of the clusters. The latter affects their surface brightness profiles, and consequently their half-light radii. For the $R - T$ relation, the relaxed systems appear to be $45 \pm 7\%$ "smaller" (lower normalization) than the disturbed ones. This constitutes a 6.5σ deviation (Fig. 4.16). It is clear then that the anisotropies possibly detected in these scaling relations will be entirely driven by the slightly inhomogeneous spatial distribution of such clusters, and not by cosmological phenomena. As discussed before, the R scaling relations (contrary to $L_X - T$ and $Y_{SZ} - T$) are not sensitive enough to cosmological effects, to overcome the bias coming from CC clusters.

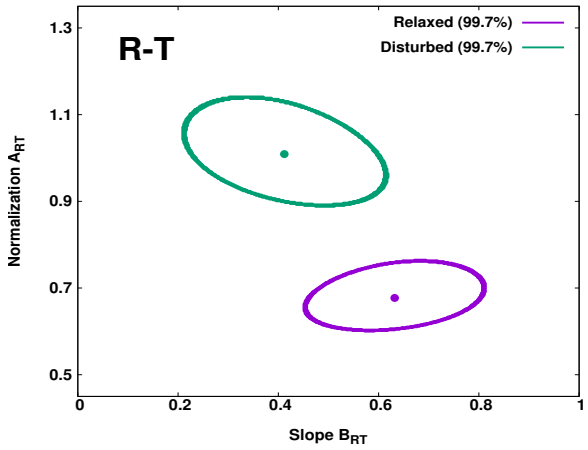

Figure 4.16: 3σ (99.7%) parameter space of the normalization and slope of the $R - T$ relation, for relaxed (purple) and disturbed (green) clusters.

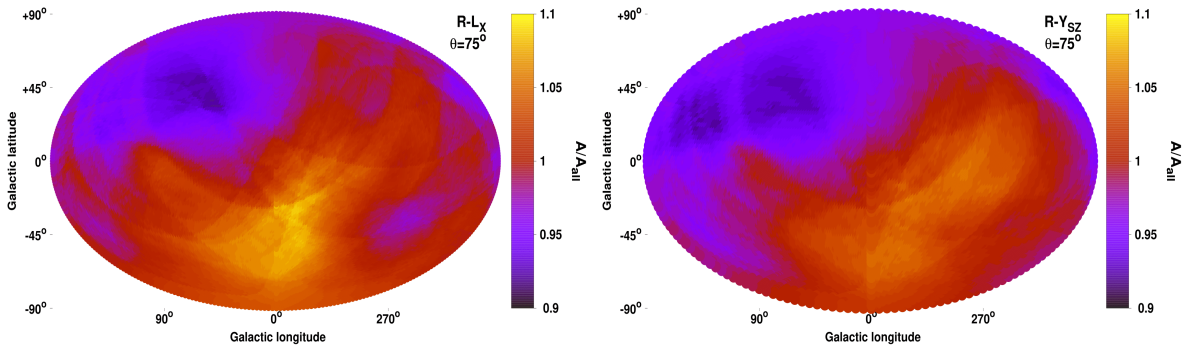

Figure 4.17: Normalization anisotropy map for $R - L_X$ (left) and $R - Y_{SZ}$ (right).

Indeed, when one attempts to scan the sky with a $\theta = 75^\circ$ cone, one obtains the same sky pattern for all four scaling relations. The normalization anisotropy maps for $R - L_X$ and $R - Y_{SZ}$ are displayed on

the top panel of Fig. 4.17. The map for $R - L_{\rm BCG}$ is not displayed since they are very similar to the other R maps. The smallest clusters are consistently found within 12° from $(l, b) \sim (64°, +32°)$. This direction strongly correlates with the region where the highest fraction of relaxed clusters in our sample is found, where there is also a lack of disturbed clusters, as can be seen by Fig. 4.8. The maximum anisotropy does not exceed 2.3σ for any relation, with a $\lesssim 14\%$ variation of A_{RX}. As such, the effect of this bias is not extremely strong, but sufficient to dominate over the effect of the possible cosmological anisotropies and BFs.

Calibration of $R - T$ anisotropies for dynamical state of clusters

To study the underlying cosmological effects, one would need larger samples to further smooth out the sky distribution of different dynamical types of clusters. Also, one could attempt to calibrate the scaling relations for this systematic bias. This requires an observable proxy that effectively traces the existence of CC clusters. Unfortunately, such an observable is not currently available for our sample. Future work will soon provide a remarkable characterization of the core state of the eeHIFLUGCS clusters using numerous independent measurements. Proper calibration of the R relations will be then possible, followed by their application for the search of cosmological anisotropies.

For now, we use XBO as a proxy for relaxed clusters, as already discussed. We attempt to calibrate the $R-T$ relation and its anisotropy map. We create 10^5 randomly drawn bootstrap subsamples (same process as in M20), independent of direction. We investigate the correlation between the A_{RT} and the median XBO for every subsample. The results are shown in Fig. 4.18. We then calibrate the A_{RT} anisotropy map based on the median XBO of every sky region and the observed correlation between the two. Although the induced uncertainties due to this calibration are too large to allow for any meaningful conclusions, this offers a useful example for potential future applications of the R relations. Finally, the behavior of the apparent $R - T$ anisotropies after this correction is applied is very interesting. The previously anisotropic region now becomes milder. The $(l, b) \sim (260°, -10°)$ direction starts showing a lower A_{RT} behavior, consistent with the previous results and the scenario of a cosmological anisotropy or a large BF.

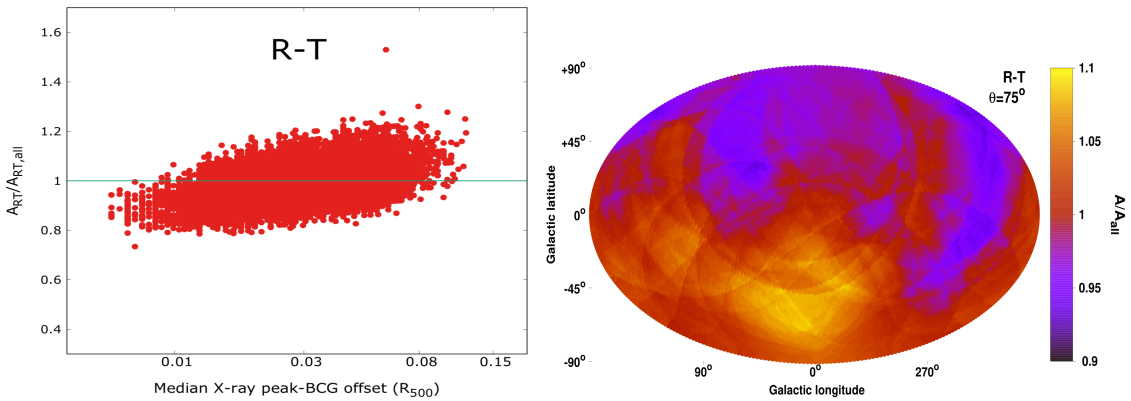

Figure 4.18: *Top*: Correlation between the best-fit normalization A_{RT} (over the full sample's best-fit value) and the median XBO for every of the 10^5 bootstrap subsamples. *Bottom*: A_{RT} anisotropy map after calibrating for the existing correlation with the XBO.

The $Y_{SZ} - L_{BCG}$ relation

Both quantities of this relation are unaffected by absorption effects due to the infrared and submillimeter wavelengths, while they depend on the cosmological parameters in the same manner. Accounting for the overall best-fit slope, a very weak dependance of the normalization on the angular diameter distance remains ($A_{YL_{\rm LBCG}} \sim D_A^{0.26}$). In detail, a 15% variation in H_0 would only lead to a $< 3\%$ variation in $A_{YL_{\rm LBCG}}$. Similarly, a 1000 km/s BF at $z = 0.05$ would only cause a 0.5% change in $A_{YL_{\rm LBCG}}$. It is clear then that only sample-related biases can create observable anisotropies in this scaling relation.

Due to the large scatter and the limited number of clusters, we consider $\theta = 90^\circ$ cones to scan the sky. The anisotropy of the $Y_{\rm SZ} - L_{\rm BCG}$ normalization is displayed in Fig. 4.19. The relation shows a $\sim 30\%$ variation mostly between the Northern and the Southern Galactic hemispheres, but with a negligible statistical significance of 1.4σ. The relation can be considered statistically isotropic, as expected, with no strong biases toward a direction. The normalization map is displayed in Fig. 4.19.

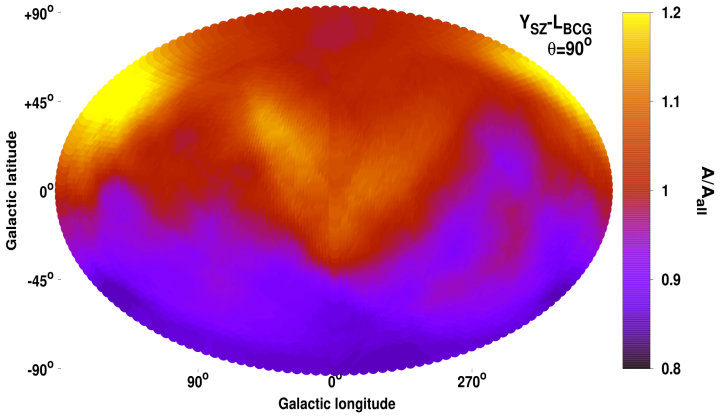

Figure 4.19: Normalization anisotropy map for the $Y_{\rm SZ} - L_{\rm BCG}$ relation. The statistical significance of the observed anisotropies is $\leq 1.4\sigma$, and thus the relation is statistically isotropic.

4.13 Appendix C: Scaling relations and anisotropies as functions of different selection cuts

In this section, we repeat the analysis for the $L_{\rm X} - Y_{\rm SZ}$, $Y_{\rm SZ} - T$, and $L_{\rm BCG} - T$ relations, for different $Y_{\rm SZ}$ S/N and redshift cuts. The summarized result is that our main conclusions remain unchanged.

The $L_X - Y_{SZ}$ relation

For the $L_{\rm X} - Y_{\rm SZ}$ relation, a lower $Y_{\rm SZ}$ threshold of S/N$\geq$ 4.5 was applied in the default analysis. This resulted in 460 clusters. If we consider two lower thresholds instead, namely S/N$\geq$ 2 and S/N$\geq$ 3, we have 1095 and 747 clusters respectively. The 3σ $L_{\rm X} - Y_{\rm SZ}$ contours for the three different cases are compared to Fig. 4.20. There is a $> 5\sigma$ shift in the best-fit $L_{\rm X} - Y_{\rm SZ}$ relation going from S/N$>$ 4.5 to S/N$>$ 2, while the scatter increases by $\sim 100\%$. The S/N$>$ 2 fit however, is dominated by several systematics. To begin with, the $L_{\rm X}$ residuals are strongly correlated with z, $N_{\rm Htot}$, and $Y_{\rm SZ}$, as can be seen in Fig. 4.21. These probably point toward biases in the X-ray selection process, and the need of a broken power law to describe $L_{\rm X} - Y_{\rm SZ}$. In the same figure, one can see that these systematic behaviors are not present for the S/N$>$ 4.5 case.

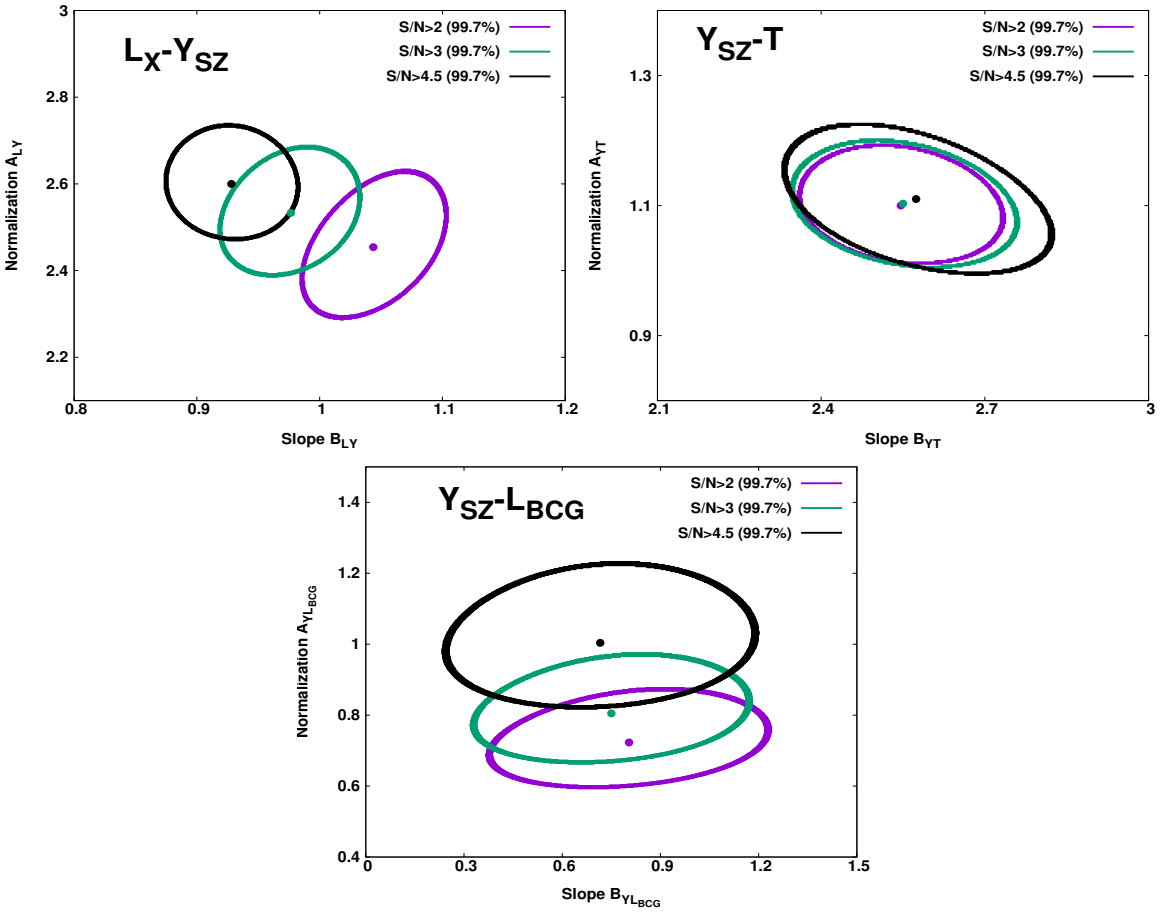

Figure 4.20: 3σ (99.7%) parameter space of the normalization and slope of the $L_{\rm X} - Y_{\rm SZ}$ (left), $Y_{\rm SZ} - T$ (middle), and $Y_{\rm SZ} - L_{\rm BCG}$ (right) relations, for S/N> 2 (purple), S/N> 3 (green), and S/N> 4.5 (black).

Despite these issues, when we scan the sky to detect $L_{\rm X} - Y_{\rm SZ}$ anisotropies, we get a similar map as for the default case. The anisotropy significance map (Fig. 4.22) illustrates that there are no excess X-ray absorption issues toward $(l, b) \sim (280^{\circ}, -15^{\circ})$ where the cosmological anisotropies are found. At the same time, the only anisotropic region again appears to be toward $(l, b) \sim (128^{\circ}, +21^{\circ})$, being $\sim 14\%$ fainter than the rest of the sky at a 2.5σ level, similar to the default case.

The $Y_{\rm SZ} - T$ relation

For the $Y_{\rm SZ} - T$ relation, we used a lower $Y_{\rm SZ}$ threshold of S/N$\geq$ 2 in the default analysis, resulting in 263 clusters. If we increase this lower threshold to S/N$\geq$ 3 or S/N$\geq$ 4.5, we are left with 242 and 190 clusters respectively. The best-fit $Y_{\rm SZ} - T$ does not change as a function of S/N, as can be seen in the middle panel of Fig. 4.20. The $Y_{\rm SZ}$ residuals remain independent of the cluster physical properties as well. When we repeat the anisotropy analysis for S/N$\geq$ 3 and for S/N$\geq$ 4.5, we obtain almost identical anisotropy results as for the default case. The A_{YT} variance map is displayed in Fig. 4.23. Thus, the observed anisotropies are independent of $Y_{\rm SZ}$ selection effects.

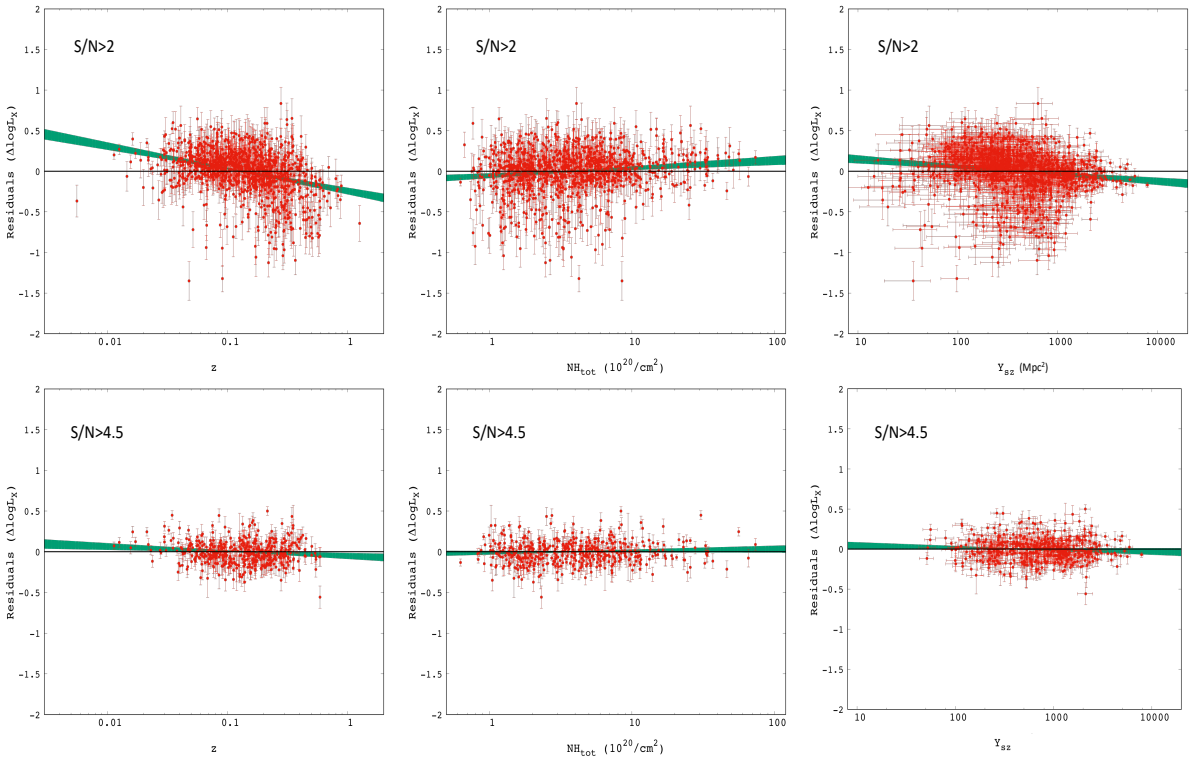

Figure 4.21: $L_{\rm X}$ residuals for the $L_{\rm X} - Y_{\rm SZ}$ relation for S/N> 2 (top) and S/N> 4.5 (bottom), as a function of z (left), $N_{\rm Htot}$ (middle), and $Y_{\rm SZ}$ (right). The green strips display the best-fit line with their 1σ uncertainties. It is evident that for S/N> 4.5, the slope is always consistent with zero, indicating no dependence of the residuals on the cluster physical properties.

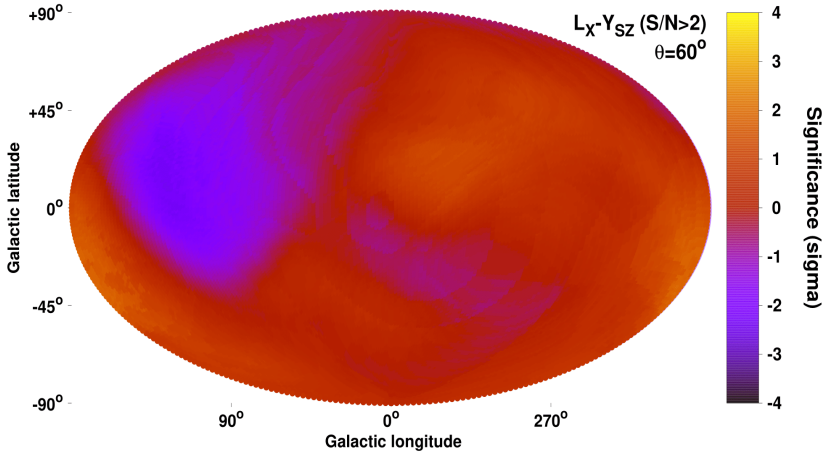

Figure 4.22: Statistical significance map of the $L_{\rm X} - Y_{\rm SZ}$ anisotropies for S/N> 2.

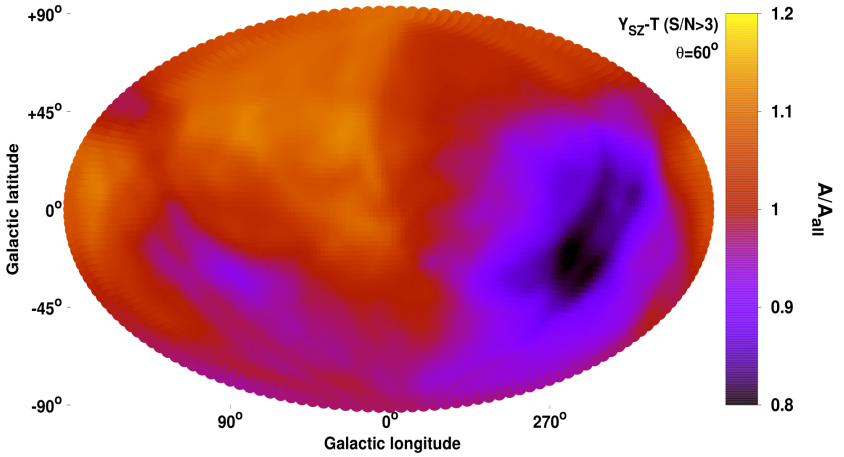

Figure 4.23: Normalization anisotropy map of the $Y_{\rm SZ} - T$ relation for S/N> 3.

The $Y_{\rm SZ} - T$ relation using the *Planck* values instead

To ensure that the observed $Y_{\rm SZ} - T$ anisotropies do not emerge due to some unknown directional bias in our own $Y_{\rm SZ}$ measurements, we repeat the analysis using the $Y_{\rm SZ}$ values from the PSZ2 catalog. Due to the higher $Y_{\rm SZ}$ S/N> 4.5 threshold that PSZ2 applied, 206 clusters were matched with our M20 sample. This S/N cut also leads to higher median T and $Y_{\rm SZ}$ compared to our default analysis. Thus, we adopt $C_Y = 85$ kpc^2 and $C_X = 6$ keV. For the best-fit parameters, we find $A_{YT} = 0.940 \pm 0.041$, $B_{YT} = 2.074 \pm 0.095$, $\sigma_{\rm int} = 0.184 \pm 0.019$, and $\sigma_{\rm int} = 0.232 \pm 0.024$. The scatter is $\sim 35\%$ larger than in our case (when $Y_{\rm SZ}$ S/N> 4.5), due to the different adopted R_{500} between the two independent analyses. This highlights the need to use our own measurement, where we increase the number of clusters, while decreasing the scatter. The slope differs by 2.2σ. The $Y_{\rm SZ} - T$ scaling relation is plotted in the left panel of Fig. 4.24.

Performing the $Y_{\rm SZ} - T$ sky scanning, one sees that we obtain roughly the same anisotropies with the PSZ2 $Y_{\rm SZ}$ values, as we did with our measurements. The A_{YT} map is shown in the right panel of Fig. 4.24. The maximum anisotropy is found toward $(l, b) = (254^{\circ}{}^{+32^{\circ}}_{-44^{\circ}}, -22^{\circ}{}^{+51^{\circ}}_{-29^{\circ}})$, with $H_0 = 64.6 \pm 2.5$ km/s, at a 2.9σ tension with the rest of the sky. This region is only 15° from the most anisotropic region as found in our default analysis, which demonstrates that the $Y_{\rm SZ} - T$ anisotropies are independent of the adopted $Y_{\rm SZ}$ catalog.

The $L_{\rm BCG} - T$ relation

For thel $L_{\rm BCG}$ scaling relations, we removed clusters at $z < 0.03$ since they appear systematically brighter than expected. We have also excluded all the $z > 0.15$ clusters, since the redshift evolution of $L_{\rm BCG}$ remains unknown. We applied these cuts to all $L_{\rm BCG}$ scaling relations in order to be consistent. However, these redshift issues are not as important in the $L_{\rm BCG} - T$ relation. One can see that in Fig. 4.25, where the $L_{\rm BCG}$ residuals are plotted as a function of z. Only the seven clusters with $z < 0.02$ are systematically upscattered, while $z > 0.15$ show the same behavior as the less distant clusters. Thus, we repeat our analysis using all the 259 clusters, regardless of their redshift. The best-fit $L_{\rm BCG} - T$ relation remains similar to the default analysis, with the parameter uncertainties being naturally smaller, due to the larger number of clusters. The anisotropic behavior of the relation remains the same as before. Interestingly, the statistical significance of the $L_{\rm BCG} - T$ relation rises from 1.9σ to 2.1σ. Both of these results are

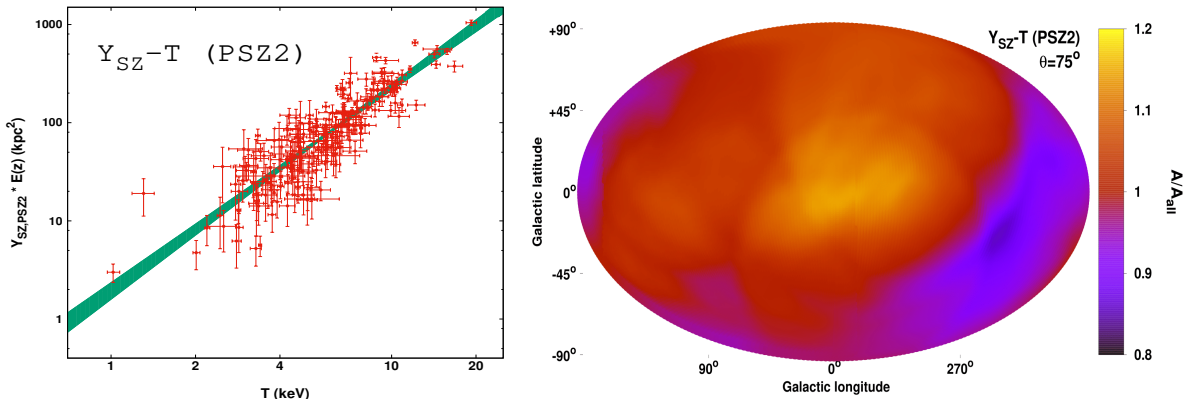

Figure 4.24: *Left*: The $Y_{SZ} - T$ relation when using the PSZ2 Y_{SZ} values, together with its 1σ best-fit function (green). *Right*: Normalization anisotropy map of the $Y_{SZ} - T$ relation when the PSZ2 values for Y_{SZ} are used.

displayed in Fig. 4.25.

4.14 Appendix D: More details about performed tests

ZoA of Avoidance bias

As discussed in Sect. 4.7.3, the ZoA gap does not introduce any significant bias to our results. Here we provide some plots related to that discussion. For simplicity, we only provide the relative images for the $L_X - T$ relation, since results from the other relations are similar. This is due to the fact that the used samples are simulated and isotropic, and that the cluster positions are the same across scaling relations. Thus, any effects come only from the applied cluster weighting during the sky scanning. We stress again that the observed anisotropies remain unaffected when this weighting is omitted, and the ZoA gap is invisible to the used algorithm, highlighting the lack of bias coming from ZoA in the real data.

In the top panel of Fig. 4.26, the galactic latitude of the most anisotropic region for every simulated sample is shown. As explained before, $\sim 43\%$ of these regions lie within ZoA, instead of the $\sim 33\%$ which would be the expectation if no bias was present. Here a nonflat distribution of the galactic latitudes is expected even in the completely bias-free case, since the sky area covered by each bin is not the same. Hence, the probability of the most anisotropic region to be located within each bin changes proportionally.

In the bottom panel of Fig. 4.26, we compare the relative difference of the observed anisotropy (in terms of σ) for two cases. The first is when the results from the analysis above are considered, without any data in the ZoA. The second is when we fill ZoA with simulated samples, as described in Sect. 4.7.3. As discussed there, the average maximum anisotropy signal is increased by $14 \pm 8\%$ when the ZoA clusters are excluded. This is mostly due to the different number of available data in the two cases.

Finally, in Fig. 4.27 the number of clusters within each cone with $\theta = 75^\circ$ is shown. As expected, close to the Galactic center fewer clusters are included in the cones, while the most clusters are found for the Galactic pole cones. The main anisotropic region of our analysis at $(l, b) \sim (280^\circ, -15^\circ)$ shows an average number of clusters.

MCMC fitting

In Sect. 4.8 we discussed the results obtained by the MCMC fitting. Here we provide some more details and plots about that test. Due to the high number of free parameters, we performed 2×10^7 iterations

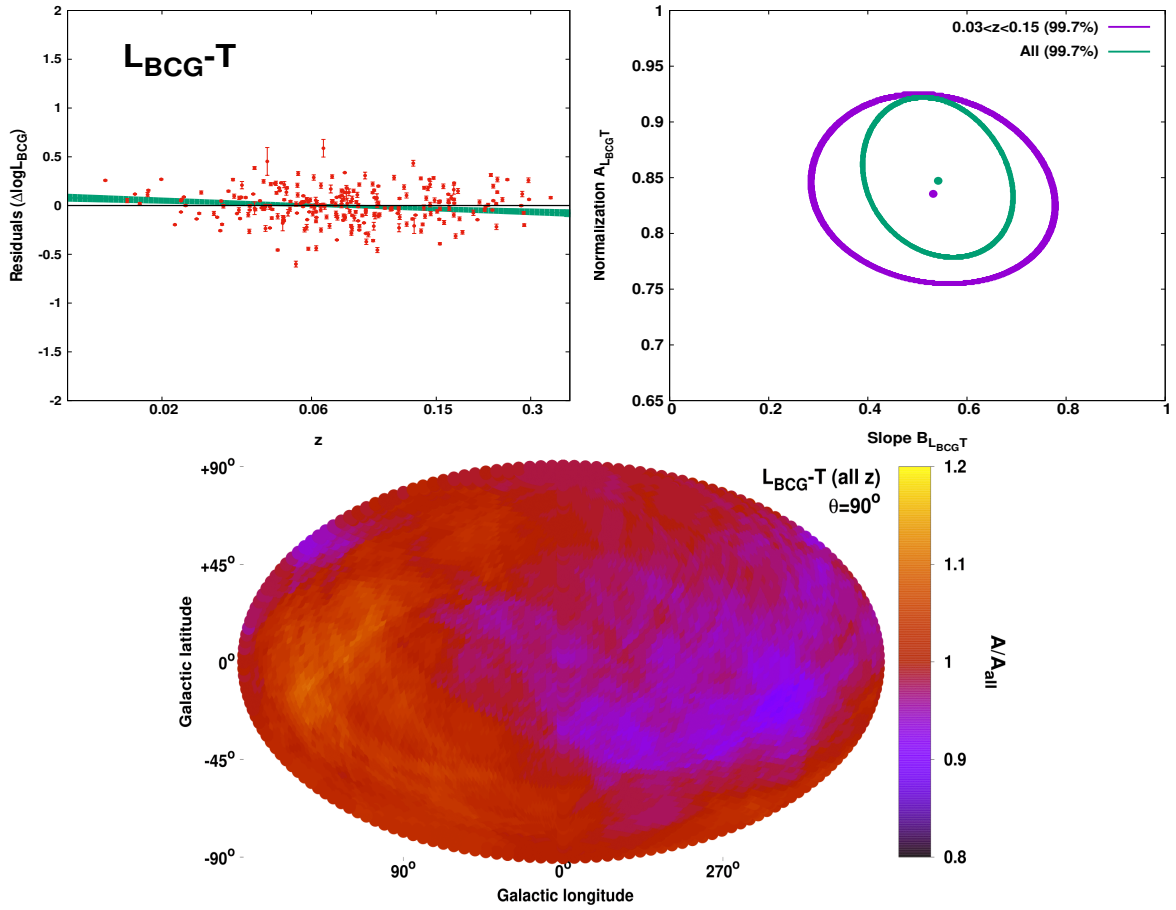

Figure 4.25: *Top left*: $L_{\rm BCG}$ residuals of the $L_{\rm BCG} - T$ fit, as a function of the BCG redshift. The green stripe corresponds to the best-fit function within 1σ. *Top right*: 3σ (99.7%) parameter space of the normalization and slope of the $L_{\rm BCG} - T$ relation, for all clusters (green), and for $0.03 < z < 0.15$ clusters (purple). *Bottom*: Normalization anisotropy map of the $L_{\rm BCG} - T$ relation when all clusters are considered independent of their redshift.

of the chain, with a burn in period of 10^4. A variable step size was used for every parameter, randomly drawn from the same Gaussian distribution with a zero mean, and a standard deviation $\sigma = 0.05$ of 0.05. Every 10^4 iterations, $\sigma = 0.5$ was used a single time, to fully explore the possibility of multiple likelihood maxima within the complicated parameter space. An acceptance rate of 18% was reached. The chain was run multiple times from varying initial positions and step size source distributions, to ensure that the same results were reached each time.

In Fig. 4.28, we plot the 3σ parameter space for u_z and u_T (redshift and temperature power indexes), which are the only two parameters with a significant impact on the best-fit normalization. As discussed before, their anticorrelation is strong, which generally cancels out any strong effects in the normalization (due to the flux-limited sample and the Eddington bias). The 3σ parameter space for u_{NH} and u_f ($N_{\rm Htot}$ and flux) is also plotted as a representative example for the rest of the free parameters. There is no significant effect from these cluster properties ($u_{NH} \sim u_f \sim 0$), and no correlation between them. This demonstrates that the rest of the cluster parameters do not induce any biases in the observed normalization of a cluster subsample.

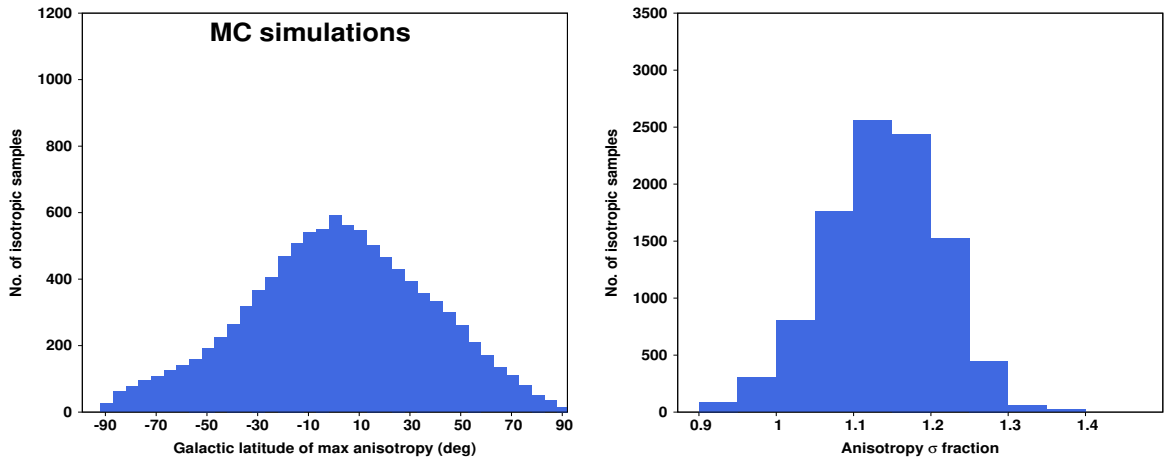

Figure 4.26: *Top*: Distribution of the galactic latitude of the most anisotropic regions as detected in the 10000 isotropic simulated samples for the $L_X - T$ relation. The distance weighting during the $L_X - T$ fitting was used here. Note that bins close to the ZoA cover a larger portion of the sky, and naturally more anisotropies are expected to be detected there even if no bias existed.

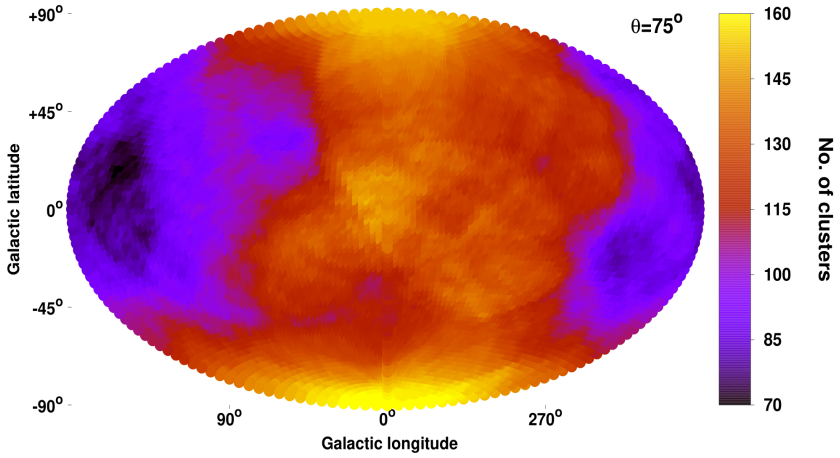

Figure 4.27: Number of clusters per $\theta = 75^{\circ}$ cone for the 313 clusters used in the $L_X - T$ relation.

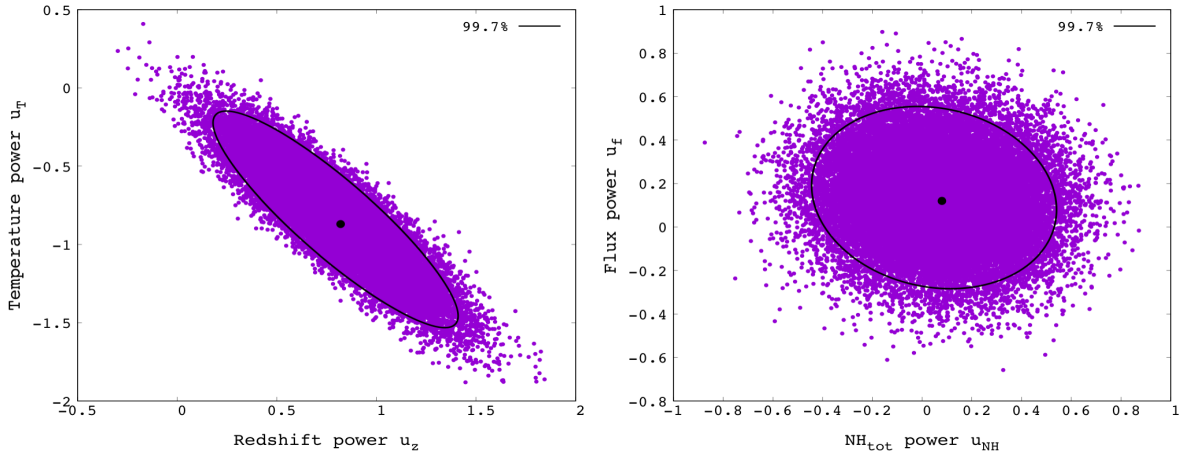

Figure 4.28: *Top*: Distribution of the galactic latitude of the most anisotropic regions as detected in the 10000 isotropic simulated samples for the $L_X - T$ relation. The distance weighting during the $L_X - T$ fitting was used here. Note that bins close to the ZoA cover a larger portion of the sky, and naturally more anisotropies are expected to be detected there even if no bias existed.

Sky fraction of Chandra and XMM-Newton clusters in our sample

In Fig. 4.29, we display the fraction of the clusters for which Chandra or XMM-Newton were used to determine T. Specifically, the fraction is defined as the Chandra clusters minus the XMM-Newton clusters over the sum. The results are discussed in Sect. 4.7.5.

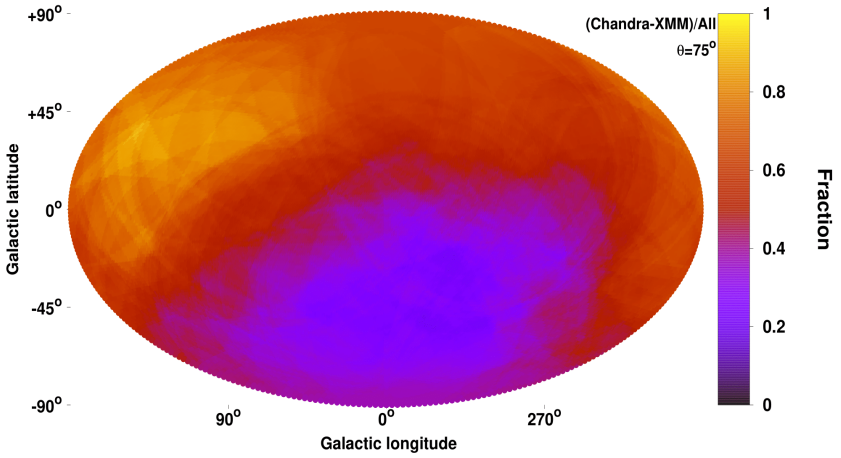

Figure 4.29: Spatial variation of fraction of Chandra clusters minus XMM-Newton clusters, over the sum.

Effects of bulk flows to adopted apparent R_{500}

If a BF is present, then the distance of a cluster is miscalculated. As a result, its L_X, and its mass M_{500}, its physical R_{500} (Mpc), and its apparent θ_{500} (arcmin) are also misinterpreted (see Piffaretti et al. 2011 and Sect. 2.4 of M20). Thus, the region within which we measure T, Y_{SZ}, and L_X, will also change, possibly yielding different results. This however is a negligible effect and not taken into account. In M20 (Appendix B), we showed that for H_0 anisotropies, θ_{500} remains practically unchanged. That is

because the opposite changes of R_{500} and D_A cancel each other out. Here, we test if a BF can cause significant changes in the adopted θ_{500} and how this would affect our used parameter values. We combine the $L_{\rm X}\sim E(z)^{7/3}M_{500}^{1.64}$ relation of M. Arnaud et al. (2010). the fact that $M_{500}\sim R_{500}^3\,H_0^2E(z)^2$, and that $D_L=(1+z)^2D_A$. Then, θ_{500} reads as

$$\begin{aligned}\theta_{500}=\frac{R_{500}}{D_A}&\sim\frac{1}{D_A}\left(\frac{M_{500}}{E(z)^2}\right)^{1/3}\sim\frac{1}{D_A}\frac{L_{\rm X}^{0.203}}{E(z)^{1.14}}\\&\sim\frac{1}{D_A}\frac{D_L^{0.406}}{E(z)^{1.14}}\sim\frac{(1+z)^{0.812}}{D_A^{0.592}E(z)^{1.14}}.\end{aligned}\tag{4.11}$$

We typically find BFs of $\sim$ 1000 km/s. For clusters at $z=0.05$, this would cause a $\lesssim 6\%$ change in θ_{500}. For $z=0.1$, this change would be $\lesssim 2\%$. For T, the percent changes are roughly the same as in θ_{500} (see Appendix B in M20). Therefore, for the BF case we considered, and for low-z clusters, we expect a $\lesssim 6\%$ bias. As an example, let us estimate how this would affect the anisotropies of the $L_{\rm X}-T$ relation. If clusters appear less luminous (or closer) than expected due to a BF (as for the main anisotropic region of our results), this would mean that the distance is underestimated, hence θ_{500} is slightly overestimated. Thus, the measured T is actually slightly underestimated, since it was measured in an annulus further from the center than planned, where clusters are generally cooler. If we indeed measured the correct, higher T, then these clusters would appear even fainter than before compared to the expectations. Therefore, the observed anisotropies would be amplified. Consequently, any small bias that is introduced to θ_{500} due to an existing BF, would eventually suppress the BF signal, which is the opposite of what we would need to explain the anisotropies.

The $Y_{\rm SZ}$ measurements also suffer the same percent changes as θ_{500} (Fig. 4.30). One sees that for the same BF case as above, the employed MMF technique leads to a slight overestimation of $Y_{\rm SZ}$, which again suppress the BF signal. However, this effect is insignificant for two reasons. Firstly, due to the slope of the $Y_{\rm SZ}-T$ relation ($B_{YT}=2.546$), the changes of $Y_{\rm SZ}$ are less important than changes in T (which we already saw that can mildly smooth out the anisotropies). Secondly, the $Y_{\rm SZ}-T$ anisotropies are much larger than the $Y_{\rm SZ}$ changes due to a falsely assumed θ_{500}.

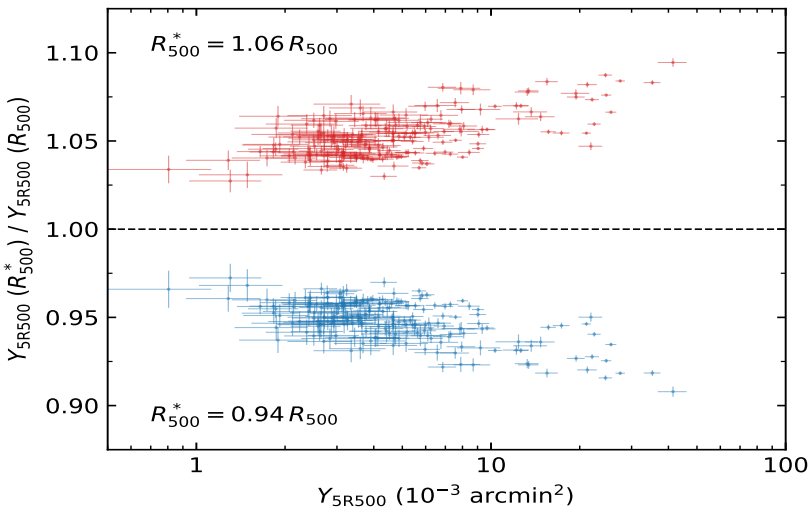

Figure 4.30: Relative change of the measured Y_{5R500} when the input R_{500} (and θ_{500}) is increased (red) or decreased (blue) by 6%.

Moreover, the measured T value goes into the measurement of Y_{SZ} when relativistic effects are considered. However, this dependance is very weak, since a 1 keV change in T would only lead to a $\sim 1\%$ change in Y_{SZ}, and thus a BF would practically not affect Y_{SZ} in that regard.

For the L_X measurements we cannot make quantitive predictions of the change they will suffer for a different θ_{500} input, since we did not conduct the measurements. However, we expect that L_X will remain almost unchanged, since only the outskirt area of the assumed cluster size will slightly change in case of a BF. The vast majority of X-ray cluster emission though comes from well within this area. Even if the change was not negligible, the same effect as for T and Y_{SZ} is expected, where the miscalculation of L_X actually makes us underestimate the BF signal rather than creating it.

It is evident that these changes are only minimal compared to the observed anisotropy amplitudes, not trivial to be accounted for (iterative Y_{SZ} and T measurements and BF estimations would be needed), opposite than explaining the anisotropies, and thus we ignore them.

CHAPTER 5

Conclusions and Outlook

The Cosmological Principle and galaxy cluster scaling relations

The premise that the expansion of the Universe is isotropic at large scales has played a crucial role in the development of the concordance cosmological model. The vast majority of extragalactic studies adopt this assumption and often base their conclusions on it, especially when data from across the entire sky are considered. The CP is so deeply imprinted in standard cosmology that a large fraction of the astronomical community falsely considers it a long-proven scientific fact. Even at local cosmic scales, where bulk flows might bias the distance estimation, most studies ignore the effects these motions might have on their results. For instance, galaxy cluster studies focusing on SCs or cluster count cosmology typically use heliocentric redshifts instead of CMB-frame redshifts, further amplifying any direction-dependent bias. If an anisotropy in the measured redshift-distance relation exists, especially at local scales, numerous past results might need revision. Thus, it is crucial to continuously scrutinize the assumption of cosmic isotropy and assess the effects that a possible deviation from it would have on our cosmological theories.

Although many studies exist that support the CP, a comparable amount of cosmological results reject it. Therefore, its validity remains a highly discussed topic. The recently introduced method to test the isotropy of the local Universe by employing galaxy cluster SCs, offers a novel, powerful tool with compelling prospects. If one has a cosmology-independent cluster measurement, such as the temperature T, one can study its correlation with a cosmology-dependent quantity, such as the X-ray luminosity $L_{\rm X}$ or the total integrated Compton parameter $Y_{\rm SZ}$. If the underlying redshift-distance relation spatially varies due to cosmological anisotropies or large bulk flows, then the relations between T and the other cluster quantities will vary in a similar way. It is of high significance that this strategy is independent of all previous isotropy studies, providing complementary results to other preexisting probes. Moreover, in contrast with other probes such as SNIa, galaxy clusters have the advantage that they can reveal information about their distance via multiple ways, such as their X-ray luminosity, size, SZ effect amplitude, and optical and infrared BCG luminosity. This allows for constructing SCs with different sensitivities on cosmology, bulk flows, or absorption issues and investigating different aspects of possible apparent anisotropies using a single cluster sample.

Summary and conclusions

In the first project of this thesis, I implemented the galaxy cluster X-ray luminosity-temperature relation $L_{\rm X} - T$ to study the isotropy of three independent cluster samples; our eeHIFLUGCS-based sample (referred to as M20 sample in the second project and hereafter), and the ACC and XCS-DR1 samples.

For the M20 sample, I found that the $L_X - T$ relation exhibits an apparent $\sim 30\%$[1] spatial variation in its normalization between the regions with the brightest and faintest clusters. Assuming that the intrinsic normalization of $L_X - T$ should be the same regardless of the direction, this result could be interpreted as a $\sim 15\%$ anisotropy of the Hubble constant, H_0. The apparently preferred axis was pinpointed towards $(l, b) \sim (280^\circ, -20^\circ)$, and the statistical significance of this tension reached $\sim 4\sigma$. Thus, it is highly improbable to be due to mere chance. When such an unexpected result is obtained, one needs to ensure that it is not caused by systematic biases or previously unknown absorption issues. The conducted analysis did not reveal any such issues since the anisotropy persists for several different cluster subsamples with different physical properties. Moreover, regions with opposite $L_X - T$ behavior seem to have a similar cluster distribution based on measurements such as temperature, redshift, metallicity, and hydrogen column density. When the ACC and XCS-DR1 samples are analyzed in the same fashion, similar anisotropies were observed. By performing a joint analysis of all 842 individual clusters from the three independent samples, I found that the observed H_0 anisotropy is boosted to a $\sim 5\sigma$ level, towards $(l, b) \sim (303^\circ, -27^\circ)$. Interestingly, numerous other studies that used independent probes detected similar anisotropies toward this part of the sky. All the above strongly portray the need to understand the physical mechanisms causing this effect. Even though the erratic $L_X - T$ behavior did not seem to originate from excess X-ray absorption issues or systematic biases, these scenarios could not be excluded until further tests were carried out.

In the second project of this thesis, I performed a more in-depth analysis of the cluster anisotropies, significantly improving our understanding of this apparent cosmological inconsistency. I mostly achieved that in three ways; by studying the directional behavior of nine more galaxy cluster SCs, quantifying the amplitude and scale of the bulk flow that could explain these findings, and performing isotropic Monte Carlo simulations to better assess the statistical significance of my results and validate the robustness of the used methodology. Additionally to L_X and T, I also make use of three more cluster measurements, independent from each other and depending on the assumed cosmological model. These quantities are Y_{SZ}, the X-ray half-light radius R, and the infrared luminosity of the cluster BCGs, L_{BCG}. The Y_{SZ} values of the ACC sample are also measured and used. The SCs that include R unfortunately suffer from certain systematics that cannot be solved currently, but they are expected to provide valuable insights on the cluster anisotropies in the future. The L_{BCG} SCs, although not a standalone test due to their high scatter, offer a complementary consistency check for the main SCs. The greatest improvement in the anisotropy searching compared to the first project comes from the $L_X - Y_{SZ}$ and $Y_{SZ} - T$ relations, for the reasons discussed below. This project's conclusions add to the ones from the first project, and thus, they compose the overall conclusions of this thesis. The main results are summarized below:

No excess X-ray absorption found

The $L_X - Y_{SZ}$ relation can effectively trace previously unknown absorption effects due to the strong dependence of L_X on such effects, the insensitivity of Y_{SZ} to Galactic absorption issues, and the fact that $L_X - Y_{SZ}$ is unaffected by any cosmological anisotropies or bulk flows (since these effects similarly affect both L_X and Y_{SZ}). Hence, any significant deviation from statistical isotropy should mostly come from excess X-ray absorption issues. The relation also exhibits a low scatter and has many available clusters (573 individual objects), making it an excellent tool for discovering such absorption biases. I found that there are no signs of excess X-ray absorption toward $(l, b) \sim (280^\circ, -20^\circ)$, or any region close by. This is further confirmed by using the $L_X - L_{BCG}$ relation in a similar manner. Furthermore, I used the X-ray-determined N_{Htot} and compared it with the one I applied during the entire analysis. A systematic

[1] This is an average number, since the exact variation amplitude slightly varies depending on the chosen scanning cone sizes and some other conditions explained in Chapters 3 and 4.

offset of this ratio toward one sky region could also reveal previously unaccounted X-ray absorption issues. Once again, no such issues were found toward $(l, b) \sim (280^{\circ}, -20^{\circ})$. Therefore, the scenario of previously unknown absorption issues as the cause of the $L_{\rm X} - T$ anisotropies is strongly disfavored. A marginal signal for some excess absorption is found toward the opposite sky direction, which would further amplify the observed $L_{\rm X} - T$ anisotropy. However, the statistical significance is small, and the effect can be attributed to chance.

Apparent anisotropy in the expansion rate

The directional behavior of the $Y_{\rm SZ} - T$ relation constitutes a nearly absorption-free test of cosmic isotropy. It also shows a lower scatter than the $L_{\rm X} - T$ relation, which makes it ideal for such a study. Repeating the anisotropy searching with $Y_{\rm SZ} - T$, I found that it exhibits almost the same behavior as $L_{\rm X} - T$. Namely, it shows a $\sim 14\%$ H_0 anisotropy toward $(l, b) \sim (270^{\circ}, -15^{\circ})$ for both the M20 and ACC samples. The statistical significance of the anisotropy is 4.3σ, following a more conservative approach than in the first project. The $L_{\rm BCG} - T$ relation supports these findings as well. When all results from $L_{\rm X} - T$, $Y_{\rm SZ} - T$, and $L_{\rm BCG} - T$ are combined for both M20 and ACC, H_0 is found to variate by $9 \pm 1.7\%$, with the most anisotropic direction being $(l, b) = (273^{\circ}{}^{+42^{\circ}}_{-38^{\circ}}, -11^{\circ}{}^{+27^{\circ}}_{-27^{\circ}})$. The statistical significance of the anisotropy boosts up to 5.4σ. No past study has reached such a high statistical significance for the observed anisotropy in the local Universe. The sky map displaying the overall H_0 spatial variation is shown in Fig. 4.7, while Table 4.3 gives the exact numerical results in detail.

Large bulk flows

The vast majority of used clusters lie at $z \lesssim 0.2$. As a result, one cannot distinguish between an H_0 anisotropy or large-scale, strong bulk flows. Thus, I quantified the amplitude and scale of such a flow motion that would explain the apparent cluster anisotropies. I found that a bulk flow of ~ 900 km/s seems to exist, that extends out to at least ~ 500 Mpc, toward $(l, b) \sim (275^{\circ}, -10^{\circ})$ (average from different methods, samples, and SCs). Different SCs agree on their detected bulk flow motion. The same holds for the M20 and ACC samples. The detected bulk flow does not seem to fade away up to the scales that the used cluster samples extend, although it is slightly more statistically significant for scales below $z < 0.12$ (~ 500 Mpc). The overall results for the bulk flow analysis are summarized in Table 4.4, while they are visualized in Fig. 4.13. Such large bulk flows contradict the CP since they require large mater inhomogeneities in the local Universe. Until more high$-z$ are obtained, it is not clear which of the two effects is the origin of the observed anisotropies.

Further confirming the existence of the anisotropies

I conclusively showed that the cluster anisotropies observed across several SCs are not a product of the generally known biases through rigorous analysis. Specifically, I concluded that the Malmquist bias could not alleviate the tension between different sky regions, while the ZoA gap does not have any significant effect on the results. Furthermore, the correlation between the dynamical state of a cluster and its SC behavior has nearly no effect on the anisotropies, and the combination of possibly different cluster properties across sky regions cannot create an artificial anisotropic signal. Finally, I conducted Monte Carlo simulations, creating isotropic samples with the same properties as the real ones. Repeating the entire analysis on every sample, I confirmed the rarity with which the observed anisotropies can occur purely due to chance. I found a 1 in ~ 270 million parts chance for the observed anisotropies to appear in an isotropic Universe without any underlying physical phenomena.

This analysis strongly demonstrates that, at least at local scales of $z \sim 0.1 - 0.2$, there is a strong anisotropy in the redshift-distance relation. This anisotropy seems to strongly contradict ΛCDM at a statistically significant level. It is crucial to identify the cause of these findings since, depending on their origin, they can have a substantial effect on the late Universe cosmology.

Future prospects

The near future can be proven to be tremendously exciting for cosmic anisotropy studies using galaxy clusters. The large volume of forthcoming data will shed plenty of light on the exact reason for the cluster anisotropies and will conclusively confirm or reject the case of a spatially varying expansion rate or large-scale bulk flows. Two main strategies will help us achieve a decisive conclusion about the observed anisotropies in the future, and they are described below.

Decreased scatter of scaling relations

A crucial element for improving cosmic anisotropy constraints from galaxy cluster SCs is to make them more precise, i.e., to reduce their scatter. Currently, $L_{\rm X} - T$ and $Y_{\rm SZ} - T$ exhibit a slightly lower scatter than other probes, such as quasars or the Tully-Fischer relation. However, they are still disadvantageous compared to the very low scatter that the SNIa distance moduli show. The use of cluster morphological parameters shows a promising future potential for reducing the cluster SCs scatter and alleviate their biases. As discussed, the dynamical state of clusters often correlates with their scatter in certain SCs. By measuring the cluster morphological parameters, one can include them in the SCs in such a way that the final scatter is decreased. Moreover, this will enable us to use SCs which were strongly biased in the past (such as the X-ray half-light radius SCs), providing us with new valuable information about the observed anisotropies. Overall, the inclusion of the morphological parameters in the SCs will help us pinpoint the anisotropies and evaluate their characteristics and nature significantly better.

More clusters, especially at large distances

The second pivotal development that will provide more conclusive answers on the origin of the observed anisotropies is the increase of the cluster sample sizes. This will be achieved by the upcoming eRASS samples. After the completion of the 4-year all-sky survey, thousands of reliable cluster temperatures and tens of thousands X-ray luminosities will be provided. Many of these clusters will be detected for the first time, and other cluster properties, such as $Y_{\rm SZ}$, will also become available. It is essential to detect the cluster anisotropies using new, independent cluster samples. Another critical factor is the future availability of more clusters beyond $z \gtrsim 0.2$ (~ 800 Mpc) that eRASS will provide. By utilizing these clusters, the anisotropies will be traced out to greater distances. Consequently, one will assess if there is a cosmic scale at which the anisotropies gradually fade away. This is of utter importance to understand if the findings of this work are caused by large bulk flows in the local Universe or by a primordial anisotropy in the expansion rate, which extends to the entire observable Universe.

Final remarks

I demonstrate how galaxy cluster scaling relations can probe cosmic isotropy. The findings of this thesis suggest that the local Universe appears to be anisotropic, either due to a nonuniform expansion rate or due to unexpectedly large bulk flows. Both scenarios contradict the standard cosmological model. The

exact origin of the anisotropies remains to be identified in future work. This answer could profoundly alter the way we understand the cosmos.

Bibliography

Abbott, T. et al. (2018). *The Dark Energy Survey: Data Release 1*. The Astrophysical Journal Supplement Series **239** 18 (cit. on p. 120).

Akrami, Y. et al. (2014). *Power Asymmetry in WMAP and Planck Temperature Sky Maps as Measured by a Local Variance Estimator*. Astrophysical Journal, Letters **784** L42. arXiv: 1402.0870 (cit. on p. 50).

Akritas, M. G. and M. A. Bershady (1996). *Linear Regression for Astronomical Data with Measurement Errors and Intrinsic Scatter*. Astrophysical Journal **470** 706. eprint: astro-ph/9605002 (cit. on p. 61).

Allen, S. W., A. E. Evrard and A. B. Mantz (2011). *Cosmological Parameters from Observations of Galaxy Clusters*. Annual Review of Astron and Astrophys **49** 409. arXiv: 1103.4829 [astro-ph.CO] (cit. on pp. 21, 116).

Alpher, R. A., H. Bethe and G. Gamow (1948). *The Origin of Chemical Elements*. Physical Review **73** 803 (cit. on p. 6).

Aluri, P. K. and P. Jain (2012). *Parity asymmetry in the CMBR temperature power spectrum*. Monthly Notices of the RAS **419** 3378. arXiv: 1108.5894 [astro-ph.CO] (cit. on p. 50).

Amendola, L. and S. Tsujikawa (2010). *Dark Energy: Theory and Observations* (cit. on p. 14).

Andrade, U., C. A. P. Bengaly, J. S. Alcaniz et al. (2019). *Revisiting the statistical isotropy of GRB sky distribution*. arXiv e-prints arXiv:1905.08864. arXiv: 1905.08864 [astro-ph.CO] (cit. on pp. 51, 117, 154).

Andrade, U., C. A. P. Bengaly, B. Santos et al. (2018). *A Model-independent Test of Cosmic Isotropy with Low-z Pantheon Supernovae*. Astrophysical Journal **865** 119. arXiv: 1806.06990 [astro-ph.CO] (cit. on p. 51).

Antoniou, I. and L. Perivolaropoulos (2010). *Searching for a cosmological preferred axis: Union2 data analysis and comparison with other probes*. Journal of Cosmology and Astroparticle Physics **12** 012. arXiv: 1007.4347 (cit. on p. 51).

Appleby, S., A. Shafieloo and A. Johnson (2015). *Probing Bulk Flow with Nearby SNe Ia Data*. Astrophysical Journal **801** 76. arXiv: 1410.5562 (cit. on pp. 51, 117, 157).

Aprile, E. et al. (2018). *Dark Matter Search Results from a One Ton-Year Exposure of XENON1T*. Physical Review Letters **121** 111302. arXiv: 1805.12562 [astro-ph.CO] (cit. on p. 11).

Arnaud, K. A. (1996). "XSPEC: The First Ten Years". *Astronomical Data Analysis Software and Systems V*. Ed. by G. H. Jacoby and J. Barnes. Vol. 101. Astronomical Society of the Pacific Conference Series 17 (cit. on pp. 44, 54, 120).

Arnaud, M. et al. (2010). *The universal galaxy cluster pressure profile from a representative sample of nearby systems (REXCESS) and the Y_{SZ} - M_{500} relation*. Astronomy and Astrophysics **517** A92. arXiv: 0910.1234 [astro-ph.CO] (cit. on pp. 58, 105, 174).

Asplund, M. et al. (2009). *The Chemical Composition of the Sun*. Annual Review of Astron and Astrophys **47** 481. arXiv: 0909.0948 [astro-ph.SR] (cit. on pp. 26, 44, 59, 60, 160).

Atrio-Barandela, F. et al. (2015). *Probing the Dark Flow Signal in WMAP 9 -Year and Planck Cosmic Microwave Background Maps*. Astrophysical Journal **810** 143. arXiv: 1411.4180 (cit. on pp. 51, 157).

Bahcall, N. A. and R. Cen (1992). *Galaxy Clusters and Cold Dark Matter: A Low-Density Unbiased Universe?* Astrophysical Journal, Letters **398** L81 (cit. on p. 8).

Bailey, M. E., S. V. M. Clube and W. M. Napier (1986). *The origin of comets*. Vistas in Astronomy **29** 53 (cit. on p. 2).

Baumgartner, W. H. and R. F. Mushotzky (2006). *Oxygen Abundances in the Milky Way Using X-Ray Absorption Measurements toward Galaxy Clusters*. Astrophysical Journal **639** 929. eprint: astro-ph/0509614 (cit. on p. 56).

Beltrán Jiménez, J., V. Salzano and R. Lazkoz (2015). *Anisotropic expansion and SNIa: An open issue*. Physics Letters B **741** 168. arXiv: 1402.1760 [astro-ph.CO] (cit. on p. 51).

Bender, A. N. et al. (2016). *Galaxy cluster scaling relations measured with APEX-SZ.* Monthly Notices of the RAS **460** 3432. arXiv: 1404.7103 [astro-ph.CO] (cit. on p. 127).

Bengaly Jr., C. A. P., A. Bernui and J. S. Alcaniz (2015). *Probing Cosmological Isotropy with Type Ia Supernovae*. Astrophysical Journal **808** 39. arXiv: 1503.01413 (cit. on p. 51).

Bengaly, C. A. P., R. Maartens, N. r. Randriamiarinarivo et al. (2019). *Testing the Cosmological Principle in the radio sky*. arXiv e-prints arXiv:1905.12378. arXiv: 1905.12378 [astro-ph.CO] (cit. on pp. 51, 154).

Bengaly, C. A. P., R. Maartens and M. G. Santos (2018). *Probing the Cosmological Principle in the counts of radio galaxies at different frequencies*. Journal of Cosmology and Astro-Particle Physics **2018** 031. arXiv: 1710.08804 [astro-ph.CO] (cit. on pp. 51, 117, 154).

Bengaly C. A. P., J. et al. (2017). *Is there evidence for anomalous dipole anisotropy in the large-scale structure?* Monthly Notices of the RAS **464** 768. arXiv: 1606.06751 [astro-ph.CO] (cit. on p. 93).

Bennett, C. L., R. S. Hill et al. (2011). *Seven-year Wilkinson Microwave Anisotropy Probe (WMAP) Observations: Are There Cosmic Microwave Background Anomalies?* Astrophysical Journals **192** 17. arXiv: 1001.4758 [astro-ph.CO] (cit. on p. 50).

Bennett, C. L., D. Larson et al. (2013). *Nine-year Wilkinson Microwave Anisotropy Probe (WMAP) Observations: Final Maps and Results*. Astrophysical Journals **208** 20. arXiv: 1212.5225 (cit. on p. 50).

Bertin, E. and S. Arnouts (1996). *SExtractor: Software for source extraction.* **117** 393 (cit. on p. 41).

Bertone, G. and D. Hooper (2018). *History of dark matter*. Reviews of Modern Physics **90** 045002. arXiv: 1605.04909 [astro-ph.CO] (cit. on p. 6).

Betoule, M. et al. (2014). *Improved cosmological constraints from a joint analysis of the SDSS-II and SNLS supernova samples*. Astronomy and Astrophysics **568** A22. arXiv: 1401.4064 [astro-ph.CO] (cit. on p. 137).

Bharadwaj, V., T. H. Reiprich, L. Lovisari et al. (2015). *Extending the L_X - T relation from clusters to groups. Impact of cool core nature, AGN feedback, and selection effects*. Astronomy and Astrophysics **573** A75. arXiv: 1410.5428 (cit. on pp. 51, 143).

Bharadwaj, V., T. H. Reiprich, G. Schellenberger et al. (2014). *Intracluster medium cooling, AGN feedback, and brightest cluster galaxy properties of galaxy groups. Five properties where groups differ from clusters*. Astronomy and Astrophysics **572** A46. arXiv: 1402.0868 [astro-ph.CO] (cit. on pp. 120, 126, 130).

Blake, C. and J. Wall (2002). *A velocity dipole in the distribution of radio galaxies*. Nature **416** 150. eprint: astro-ph/0203385 (cit. on p. 51).

Blanton, M. R. and S. Roweis (2007). *K-corrections and filter transformations in the ultraviolet, optical, and near-infrared*. The Astronomical Journal **133** 734 (cit. on p. 160).

Bleem, L. E. et al. (2015). *Galaxy Clusters Discovered via the Sunyaev-Zel'dovich Effect in the 2500-Square-Degree SPT-SZ Survey*. Astrophysical Journals **216** 27. arXiv: 1409.0850 [astro-ph.CO] (cit. on p. 119).

Böhringer, H., P. Schuecker, L. Guzzo et al. (2004). *The ROSAT-ESO Flux Limited X-ray (REFLEX) Galaxy cluster survey. V. The cluster catalogue*. Astronomy and Astrophysics **425** 367. arXiv: astro-ph/0405546 [astro-ph] (cit. on p. 53).

Böhringer, H., P. Schuecker, G. W. Pratt et al. (2007). *The representative XMM-Newton cluster structure survey (REXCESS) of an X-ray luminosity selected galaxy cluster sample*. Astronomy and Astrophysics **469** 363. arXiv: astro-ph/0703553 [astro-ph] (cit. on p. 57).

Böhringer, H., W. Voges et al. (2000). *The Northern ROSAT All-Sky (NORAS) Galaxy Cluster Survey. I. X-Ray Properties of Clusters Detected as Extended X-Ray Sources*. Astrophysical Journals **129** 435. eprint: astro-ph/0003219 (cit. on p. 53).

Böhringer, H., G. Chon and C. A. Collins (2020). *Observational evidence for a local underdensity in the Universe and its effect on the measurement of the Hubble constant*. Astronomy and Astrophysics **633** A19. arXiv: 1907.12402 [astro-ph.CO] (cit. on p. 158).

Böhringer, H. and N. Werner (2010). *X-ray spectroscopy of galaxy clusters: studying astrophysical processes in the largest celestial laboratories*. Astronomy and Astrophysicsr **18** 127 (cit. on p. 25).

Boissier, S. and N. Prantzos (1999). *Chemo-spectrophotometric evolution of spiral galaxies - I. The model and the Milky Way*. Monthly Notices of the RAS **307** 857. eprint: astro-ph/9902148 (cit. on p. 78).

Bolejko, K., M. A. Nazer and D. L. Wiltshire (2016). *Differential cosmic expansion and the Hubble flow anisotropy*. Journal of Cosmology and Astroparticle Physics **2016** 035. arXiv: 1512.07364 [astro-ph.CO] (cit. on p. 117).

Bondi, H. and T. Gold (1948). *The Steady-State Theory of the Expanding Universe*. Monthly Notices of the RAS **108** 252 (cit. on p. 6).

Borm, K. et al. (2014). *Constraining galaxy cluster temperatures and redshifts with eROSITA survey data*. Astronomy and Astrophysics **567** A65. arXiv: 1404.5312 (cit. on pp. 52, 91).

Boruah, S. S., M. J. Hudson and G. Lavaux (2020). *Cosmic flows in the nearby Universe: new peculiar velocities from SNe and cosmological constraints*. Monthly Notices of the RAS **498** 2703. arXiv: 1912.09383 [astro-ph.CO] (cit. on p. 157).

Briel, U. G. et al. (1996). *The ROSAT Users' Handbook* (cit. on p. 32).

Cai, Y.-C. et al. (2014). *A Possible Cold Imprint of Voids on the Microwave Background Radiation*. Astrophysical Journal **786** 110. arXiv: 1301.6136 [astro-ph.CO] (cit. on p. 50).

Carrick, J. et al. (2015). *Cosmological parameters from the comparison of peculiar velocities with predictions from the 2M++ density field*. Monthly Notices of the RAS **450** 317. arXiv: 1504.04627 [astro-ph.CO] (cit. on pp. 93, 117, 136, 137, 157).

Carter, J. A. and A. M. Read (2007). *The XMM-Newton EPIC background and the production of background blank sky event files*. Astronomy and Astrophysics **464** 1155. arXiv: astro-ph/0701209 [astro-ph] (cit. on p. 37).

Chang, Z. and H.-N. Lin (2015). *Comparison between hemisphere comparison method and dipole-fitting method in tracing the anisotropic expansion of the Universe use the Union2 data set*. Monthly Notices of the RAS **446** 2952. arXiv: 1411.1466 [astro-ph.CO] (cit. on p. 157).

Chen, Y. et al. (2007). *Statistics of X-ray observables for the cooling-core and non-cooling core galaxy clusters*. Astronomy and Astrophysics **466** 805. arXiv: astro-ph/0702482 [astro-ph] (cit. on p. 64).

Chilingarian, I. V. and I. Y. Zolotukhin (2011). *A universal ultraviolet–optical colour–colour–magnitude relation of galaxies*. Monthly Notices of the Royal Astronomical Society **419** 1727 (cit. on p. 160).

Chluba, J. et al. (2012). *A fast and accurate method for computing the Sunyaev-Zel'dovich signal of hot galaxy clusters*. MNRAS **426** 510. arXiv: 1205.5778 (cit. on p. 119).

Choudhury, S., A. Subramaniam and A. A. Cole (2016). *Photometric metallicity map of the Large Magellanic Cloud*. Monthly Notices of the RAS **455** 1855. arXiv: 1510.05769 [astro-ph.GA] (cit. on p. 80).

Colin, J., R. Mohayaee, M. Rameez et al. (2018). *Apparent cosmic acceleration due to local bulk flow*. arXiv e-prints arXiv:1808.04597. arXiv: 1808.04597 [astro-ph.CO] (cit. on p. 51).

Colin, J., R. Mohayaee, M. Rameez et al. (2017). *High-redshift radio galaxies and divergence from the CMB dipole*. Monthly Notices of the RAS **471** 1045. arXiv: 1703.09376 [astro-ph.CO] (cit. on pp. 51, 154).

– (2019). *Evidence for anisotropy of cosmic acceleration*. Astronomy and Astrophysics **631** L13. arXiv: 1808.04597 [astro-ph.CO] (cit. on pp. 117, 157).

Colin, J., R. Mohayaee, S. Sarkar et al. (2011). *Probing the anisotropic local Universe and beyond with SNe Ia data*. Monthly Notices of the RAS **414** 264. arXiv: 1011.6292 [astro-ph.CO] (cit. on pp. 51, 93, 117, 157).

Condon, J. J. (1988). "Radio sources and cosmology". *Galactic and Extragalactic Radio Astronomy*. Ed. by K. I. Kellermann and G. L. Verschuur 641 (cit. on p. 51).

Courtois, H. M. et al. (2013). *Cosmography of the Local Universe*. Astronomical Journal **146** 69. arXiv: 1306.0091 [astro-ph.CO] (cit. on p. 17).

Davis, M. et al. (1985). *The evolution of large-scale structure in a universe dominated by cold dark matter*. Astrophysical Journal **292** 371 (cit. on p. 8).

De Luca, A. and S. Molendi (2004). *The 2-8 keV cosmic X-ray background spectrum as observed with XMM-Newton*. Astronomy and Astrophysics **419** 837. arXiv: astro-ph/0311538 [astro-ph] (cit. on pp. 38, 39, 45).

De Martino, I. and F. Atrio-Barandela (2016). *SZ/X-ray scaling relations using X-ray data and Planck Nominal maps*. Monthly Notices of the RAS **461** 3222. arXiv: 1606.04983 [astro-ph.CO] (cit. on p. 126).

de Sitter, W. (1916a). *Einstein's theory of gravitation and its astronomical consequences*. Monthly Notices of the RAS **76** 699 (cit. on p. 4).

– (1916b). *On Einstein's theory of gravitation and its astronomical consequences. Second paper*. Monthly Notices of the RAS **77** 155 (cit. on p. 4).

– (1917). *Einstein's theory of gravitation and its astronomical consequences. Third paper*. Monthly Notices of the RAS **78** 3 (cit. on p. 4).

Deng, H.-K. and H. Wei (2018). *Null signal for the cosmic anisotropy in the Pantheon supernovae data*. European Physical Journal C **78** 755. arXiv: 1806.02773 [astro-ph.CO] (cit. on p. 157).

Di Valentino, E., A. Melchiorri and J. Silk (2020). *Planck evidence for a closed Universe and a possible crisis for cosmology*. Nature Astronomy **4** 196. arXiv: 1911.02087 [astro-ph.CO] (cit. on p. 12).

Dickey, J. M. and F. J. Lockman (1990). *H I in the Galaxy*. Annual Review of Astron and Astrophys **28** 215 (cit. on p. 56).

Dicks, D. R. (1971). *Early Greek astronomy to Aristotle* (cit. on p. 2).

D'Onghia, E. and A. J. Fox (2016). *The Magellanic Stream: Circumnavigating the Galaxy*. Annual Review of Astronomy and Astrophysics **54** 363. arXiv: 1511.05853 [astro-ph.GA] (cit. on p. 80).

Douspis, M., L. Salvati and N. Aghanim (2019). *On the tension between Large Scale Structures and Cosmic Microwave Background*. arXiv e-prints arXiv:1901.05289. arXiv: 1901.05289 [astro-ph.CO] (cit. on p. 8).

Ebrahimpour, L. et al. (2018). *The XMM Cluster Survey: joint modelling of the $L_X - T$ scaling relation for clusters and groups of galaxies*. arXiv e-prints arXiv:1805.03465. arXiv: 1805.03465 [astro-ph.CO] (cit. on p. 51).

Eckert, D., S. Molendi and S. Paltani (2011). *The cool-core bias in X-ray galaxy cluster samples. I. Method and application to HIFLUGCS*. Astronomy and Astrophysics **526** A79. arXiv: 1011.3302 [astro-ph.CO] (cit. on p. 145).

Eckmiller, H. J., D. S. Hudson and T. H. Reiprich (2011). *Testing the low-mass end of X-ray scaling relations with a sample of Chandra galaxy groups*. Astronomy and Astrophysics **535** A105. arXiv: 1109.6498 (cit. on p. 64).

Efstathiou, G., J. R. Bond and S. D. M. White (1992). *COBE background radiation anisotropies and large-scale structure in the universe*. Monthly Notices of the RAS **258** 1P (cit. on pp. 8, 50).

Efstathiou, G. and S. Gratton (2020). *The evidence for a spatially flat Universe*. Monthly Notices of the RAS **496** L91. arXiv: 2002.06892 [astro-ph.CO] (cit. on p. 12).

Einstein, A. (1916). *Die Grundlage der allgemeinen Relativitätstheorie*. Annalen der Physik **354** 769 (cit. on p. 4).

Eriksen, H. K. et al. (2004). *Asymmetries in the Cosmic Microwave Background Anisotropy Field*. Astrophysical Journal **605** 14. eprint: astro-ph/0307507 (cit. on p. 50).

Erler, J., K. Basu et al. (2018). *Planck's view on the spectrum of the Sunyaev-Zeldovich effect*. Monthly Notices of the RAS **476** 3360. arXiv: 1709.01187 [astro-ph.CO] (cit. on pp. 29, 159).

Erler, J., M. E. Ramos-Ceja et al. (2019). *Introducing constrained matched filters for improved separation of point sources from galaxy clusters*. Monthly Notices of the RAS **484** 1988. arXiv: 1809.06446 [astro-ph.IM] (cit. on p. 119).

Ettori, S., L. Lovisari and M. Sereno (2020). *From "universal" profiles to "universal" scaling laws in X-ray galaxy clusters*. arXiv e-prints arXiv:2010.04192. arXiv: 2010.04192 [astro-ph.CO] (cit. on pp. 126, 127).

Feindt, U. et al. (2013). *Measuring cosmic bulk flows with Type Ia supernovae from the Nearby Supernova Factory*. Astronomy and Astrophysics **560** A90. arXiv: 1310.4184 [astro-ph.CO] (cit. on pp. 93, 117, 157).

Fitzpatrick, E. L. (1999). *Correcting for the effects of interstellar extinction*. Publications of the Astronomical Society of the Pacific **111** 63 (cit. on p. 160).

Fixsen, D. J. et al. (1996). *The Cosmic Microwave Background Spectrum from the Full COBE FIRAS Data Set*. Astrophysical Journal **473** 576. eprint: astro-ph/9605054 (cit. on p. 50).

Fosalba, P. and E. Gaztanaga (2020). *Explaining Cosmological Anisotropy: Evidence for Causal Horizons from CMB data*. arXiv e-prints arXiv:2011.00910. arXiv: 2011.00910 [astro-ph.CO] (cit. on pp. 117, 154).

Freeth, T. et al. (2008). *Calendars with Olympiad display and eclipse prediction on the Antikythera Mechanism*. Nature **454** 614 (cit. on p. 3).

Friedmann, A. (1922). *Über die Krümmung des Raumes*. Zeitschrift fur Physik **10** 377 (cit. on p. 4).

Furnell, K. E. et al. (2018). *Exploring relations between BCG and cluster properties in the SPectroscopic IDentification of eROSITA Sources survey from 0.05 <z < 0.3*. Monthly Notices of the RAS **478** 4952. arXiv: 1804.02868 [astro-ph.GA] (cit. on p. 126).

Gamow, G. (1946). *Expanding Universe and the Origin of Elements*. Physical Review **70** 572 (cit. on p. 6).

Giles, P. A. et al. (2016). *The XXL Survey. III. Luminosity-temperature relation of the bright cluster sample*. Astronomy and Astrophysics **592** A3. arXiv: 1512.03833 [astro-ph.CO] (cit. on p. 51).

Giodini, S. et al. (2013). *Scaling Relations for Galaxy Clusters: Properties and Evolution*. Space Science Reviews **177** 247. arXiv: 1305.3286 (cit. on pp. 21, 28).

Guth, A. H. (1981). *Inflationary universe: A possible solution to the horizon and flatness problems*. Physical Review D **23** 347 (cit. on p. 7).

Hanson, D. and A. Lewis (2009). *Estimators for CMB statistical anisotropy*. Physical Review D **80** 063004. arXiv: 0908.0963 [astro-ph.CO] (cit. on p. 50).

Haslbauer, M., I. Banik and P. Kroupa (2020). *The KBC void and Hubble tension contradict ΛCDM on a Gpc scale - Milgromian dynamics as a possible solution*. Monthly Notices of the RAS **499** 2845. arXiv: 2009.11292 [astro-ph.CO] (cit. on p. 158).

Hasselfield, M. et al. (2013). *The Atacama Cosmology Telescope: Sunyaev-Zel'dovich selected galaxy clusters at 148 GHz from three seasons of data*. Journal of Cosmology and Astroparticle Physics **2013** 008. arXiv: 1301.0816 [astro-ph.CO] (cit. on p. 119).

Heath, T. L. (1932). *Greek astronomy* (cit. on p. 2).

Heath, T. L. and Aristarchus of Samos (1913). *Aristarchus of Samos, the ancient Copernicus; a history of Greek astronomy to Aristarchus, together With Aristarchus's Treatise on the sizes and distances of the sun and moon* (cit. on p. 3).

Hilton, M. et al. (2012). *The XMM Cluster Survey: evidence for energy injection at high redshift from evolution of the X-ray luminosity-temperature relation*. Monthly Notices of the RAS **424** 2086. arXiv: 1205.5570 (cit. on p. 51).

Hoffman, Y., H. M. Courtois and R. B. Tully (2015). *Cosmic bulk flow and the local motion from Cosmicflows-2*. Monthly Notices of the RAS **449** 4494. arXiv: 1503.05422 [astro-ph.CO] (cit. on p. 117).

Horner, D. J. (2001). *X-ray scaling laws for galaxy clusters and groups*. PhD thesis: University of Maryland College Park (cit. on pp. 52, 121).

Horvath, I. et al. (2020). *The clustering of gamma-ray bursts in the Hercules-Corona Borealis Great Wall: the largest structure in the Universe?* Monthly Notices of the RAS **498** 2544. arXiv: 2008.03679 [astro-ph.HE] (cit. on p. 157).

Hoyle, F. (1948). *A New Model for the Expanding Universe*. Monthly Notices of the RAS **108** 372 (cit. on p. 6).

Hu, J. P., Y. Y. Wang and F. Y. Wang (2020). *Testing cosmic anisotropy with Pantheon sample and quasars at high redshifts*. Astronomy and Astrophysics **643** A93. arXiv: 2008.12439 [astro-ph.CO] (cit. on pp. 117, 157).

Hubble, E. P. (1929). *A spiral nebula as a stellar system, Messier 31.* Astrophysical Journal **69** 103 (cit. on p. 5).

Hubble, E. (1929). *A Relation between Distance and Radial Velocity among Extra-Galactic Nebulae*. Proceedings of the National Academy of Science **15** 168 (cit. on p. 5).

Huchra, J. P. (1992). *The Hubble Constant*. Science **256** 321 (cit. on p. 8).

Hudson, D. S. et al. (2010). *What is a cool-core cluster? a detailed analysis of the cores of the X-ray flux-limited HIFLUGCS cluster sample*. Astronomy and Astrophysics **513** A37. arXiv: 0911.0409 [astro-ph.CO] (cit. on pp. 31, 58, 127, 143, 145).

Hudson, M. J., R. J. Smith, J. R. Lucey and E. Branchini (2004). *Streaming motions of galaxy clusters within 12 000 km s^{-1}- V. The peculiar velocity field*. Monthly Notices of the RAS **352** 61. arXiv: astro-ph/0404386 [astro-ph] (cit. on p. 117).

Hudson, M. J., R. J. Smith, J. R. Lucey, D. J. Schlegel et al. (1999). *A Large-scale Bulk Flow of Galaxy Clusters*. Astrophysical Journal, Letters **512** L79. arXiv: astro-ph/9901001 [astro-ph] (cit. on p. 157).

Huterer, D. (2020). *Specific Effect of Peculiar Velocities on Dark-energy Constraints from Type Ia Supernovae*. Astrophysical Journal, Letters **904** L28. arXiv: 2010.05765 [astro-ph.CO] (cit. on p. 157).

Itoh, N., Y. Kohyama and S. Nozawa (1998). *Relativistic Corrections to the Sunyaev-Zeldovich Effect for Clusters of Galaxies*. ApJ **502** 7. arXiv: astro-ph/9712289 (cit. on p. 119).

Jansen, F. et al. (2001). *XMM-Newton observatory. I. The spacecraft and operations*. Astronomy and Astrophysics **365** L1 (cit. on pp. 33, 53).

Javanmardi, B. and P. Kroupa (2017). *Anisotropy in the all-sky distribution of galaxy morphological types*. Astronomy and Astrophysics **597** A120. arXiv: 1609.06719 (cit. on p. 51).

Javanmardi, B., C. Porciani et al. (2015). *Probing the Isotropy of Cosmic Acceleration Traced By Type Ia Supernovae*. Astrophysical Journal **810** 47. arXiv: 1507.07560 (cit. on p. 51).

Jungman, G., M. Kamionkowski and K. Griest (1996). *Supersymmetric dark matter*. Physics Reports **267** 195. arXiv: hep-ph/9506380 [hep-ph] (cit. on p. 11).

Kaastra, J. S. et al. (2008). *Thermal Radiation Processes*. Space Science Reviews **134** 155. arXiv: 0801.1011 [astro-ph] (cit. on p. 25).

Kaiser, N. (1986). *Evolution and clustering of rich clusters*. Monthly Notices of the RAS **222** 323 (cit. on pp. 28, 51, 116).

Kaiser, N., H. Aussel et al. (2002). "Pan-STARRS: a large synoptic survey telescope array". *Survey and Other Telescope Technologies and Discoveries*. Vol. 4836. International Society for Optics and Photonics 154 (cit. on p. 120).

Kaiser, N., W. Burgett et al. (2010). "The Pan-STARRS wide-field optical/NIR imaging survey". *Ground-based and Airborne Telescopes III*. Vol. 7733. International Society for Optics and Photonics 77330E (cit. on p. 120).

Kalberla, P. M. W. et al. (2005). *The Leiden/Argentine/Bonn (LAB) Survey of Galactic HI. Final data release of the combined LDS and IAR surveys with improved stray-radiation corrections*. Astronomy and Astrophysics **440** 775. arXiv: astro-ph/0504140 [astro-ph] (cit. on pp. 26, 56).

Kalus, B. et al. (2013). *Constraints on anisotropic cosmic expansion from supernovae*. Astronomy and Astrophysics **553** A56. arXiv: 1212.3691 [astro-ph.CO] (cit. on pp. 51, 93).

Kashlinsky, A., F. Atrio-Barandela and H. Ebeling (2011). *Measuring the Dark Flow with Public X-ray Cluster Data*. Astrophysical Journal **732** 1. arXiv: 1012.3214 (cit. on p. 51).

Kashlinsky, A., F. Atrio-Barandela, H. Ebeling et al. (2010). *A New Measurement of the Bulk Flow of X-Ray Luminous Clusters of Galaxies*. Astrophysical Journal, Letters **712** L81. arXiv: 0910.4958 [astro-ph.CO] (cit. on pp. 51, 117, 157).

Kashlinsky, A., F. Atrio-Barandela, D. Kocevski et al. (2008). *A Measurement of Large-Scale Peculiar Velocities of Clusters of Galaxies: Results and Cosmological Implications*. Astrophysical Journal, Letters **686** L49. arXiv: 0809.3734 (cit. on pp. 51, 117, 157).

Kazantzidis, L. and L. Perivolaropoulos (2020). *Hints of a local matter underdensity or modified gravity in the low z Pantheon data*. Physical Review D **102** 023520. arXiv: 2004.02155 [astro-ph.CO] (cit. on p. 158).

Keenan, R. C. et al. (2012). *Testing for a Large Local Void by Investigating the Near-infrared Galaxy Luminosity Function*. Astrophysical Journal **754** 131. arXiv: 1207.1588 [astro-ph.CO] (cit. on p. 158).

Kim, J. and P. Naselsky (2010). *Anomalous Parity Asymmetry of the Wilkinson Microwave Anisotropy Probe Power Spectrum Data at Low Multipoles*. Astrophysical Journal **714** L265. arXiv: 1001.4613 [astro-ph.CO] (cit. on p. 50).

Kofman, L. A., N. Y. Gnedin and N. A. Bahcall (1993). *Cosmological Constant, COBE Cosmic Microwave Background Anisotropy, and Large-Scale Clustering*. Astrophysical Journal **413** 1 (cit. on p. 8).

Kogut, A. et al. (1993). *Dipole Anisotropy in the COBE Differential Microwave Radiometers First-Year Sky Maps*. Astrophysical Journal **419** 1. eprint: astro-ph/9312056 (cit. on p. 50).

Kolata, J. J. (2015). *Elementary Cosmology: From Aristotle's Universe to the Big Bang and Beyond* (cit. on p. 3).

Kravtsov, A. V. and S. Borgani (2012). *Formation of Galaxy Clusters*. Annual Review of Astron and Astrophys **50** 353. arXiv: 1205.5556 [astro-ph.CO] (cit. on p. 21).

Krupp, E. C. (1994). *Echoes of the ancient skies. The astronomy of lost civilizations.* (Cit. on p. 1).

Kuntz, K. D. and S. L. Snowden (2008). *The EPIC-MOS particle-induced background spectra*. Astronomy and Astrophysics **478** 575 (cit. on pp. 37, 41, 42, 59).

Lauer, T. R. and M. Postman (1994). *The Motion of the Local Group with Respect to the 15,000 Kilometer per Second Abell Cluster Inertial Frame*. Astrophysical Journal **425** 418 (cit. on pp. 117, 157).

Lavaux, G., N. Afshordi and M. J. Hudson (2013). *First measurement of the bulk flow of nearby galaxies using the cosmic microwave background*. Monthly Notices of the RAS **430** 1617. arXiv: 1207.1721 [astro-ph.CO] (cit. on p. 157).

Leavitt, H. S. and E. C. Pickering (1912). *Periods of 25 Variable Stars in the Small Magellanic Cloud.* Harvard College Observatory Circular **173** 1 (cit. on p. 5).

Lemaıtre, G. (1927). *Un Univers homogène de masse constante et de rayon croissant rendant compte de la vitesse radiale des nébuleuses extra-galactiques*. Annales de la Société Scientifique de Bruxelles **47** 49 (cit. on p. 6).

– (1931a). *Expansion of the universe, A homogeneous universe of constant mass and increasing radius accounting for the radial velocity of extra-galactic nebulae*. Monthly Notices of the RAS **91** 483 (cit. on p. 4).

– (1931b). *The Beginning of the World from the Point of View of Quantum Theory.* Nature **127** 706 (cit. on p. 6).

Li, M. et al. (2012). *Bulk Flow of Halos in ΛCDM Simulation*. Astrophysical Journal **761** 151. arXiv: 1207.5338 [astro-ph.CO] (cit. on p. 136).

Lin, H.-N. et al. (2016). *Testing the isotropy of the Universe by using the JLA compilation of Type Ia supernovae*. Monthly Notices of the RAS **456** 1881. arXiv: 1504.03428 [astro-ph.CO] (cit. on p. 51).

Linde, A. D. (1982). *A new inflationary universe scenario: A possible solution of the horizon, flatness, homogeneity, isotropy and primordial monopole problems*. Physics Letters B **108** 389 (cit. on p. 7).

Lopes, P. A. A. et al. (2018). *Optical substructure and BCG offsets of Sunyaev-Zel'dovich and X-ray-selected galaxy clusters*. Monthly Notices of the RAS **478** 5473. arXiv: 1805.09631 [astro-ph.CO] (cit. on pp. 127, 143).

Lovisari, L. and T. H. Reiprich (2019). *The non-uniformity of galaxy cluster metallicity profiles*. Monthly Notices of the RAS **483** 540. arXiv: 1811.05987 [astro-ph.CO] (cit. on pp. 78, 79).

Lovisari, L., T. H. Reiprich and G. Schellenberger (2015). *Scaling properties of a complete X-ray selected galaxy group sample*. Astronomy and Astrophysics **573** A118. arXiv: 1409.3845 (cit. on pp. 51, 64, 70).

Lovisari, L., G. Schellenberger et al. (2020). *X-Ray Scaling Relations for a Representative Sample of Planck-selected Clusters Observed with XMM-Newton*. Astrophysical Journal **892** 102. arXiv: 2002.11740 [astro-ph.CO] (cit. on pp. 125, 143).

Magoulas, C. et al. (2016). "Measuring the cosmic bulk flow with 6dFGSv". *The Zeldovich Universe: Genesis and Growth of the Cosmic Web*. Ed. by R. van de Weygaert et al. Vol. 308 336 (cit. on p. 157).

Manolopoulou, M. et al. (2020). *Environmental dependence of X-ray and optical properties of galaxy clusters*. Monthly Notices of the RAS. arXiv: 2010.12671 [astro-ph.CO] (cit. on p. 143).

Mantz, A. B. et al. (2015). *Weighing the giants - IV. Cosmology and neutrino mass*. Monthly Notices of the RAS **446** 2205. arXiv: 1407.4516 [astro-ph.CO] (cit. on p. 12).

Mariano, A. and L. Perivolaropoulos (2012). *Is there correlation between fine structure and dark energy cosmic dipoles?* Physical Review D **86** 083517. arXiv: 1206.4055 [astro-ph.CO] (cit. on pp. 51, 93).

Markevitch, M. (1998). *The L_X-T Relation and Temperature Function for Nearby Clusters Revisited*. Astrophysical Journal **504** 27. eprint: astro-ph/9802059 (cit. on p. 90).

Marsh, D. J. E. (2016). *Axion cosmology*. Physics Reports **643** 1. arXiv: 1510.07633 [astro-ph.CO] (cit. on p. 11).

Mathews, G. J. et al. (2016). *Detectability of Cosmic Dark Flow in the Type Ia Supernova Redshift?Distance Relation*. Astrophysical Journal **827** 60. arXiv: 1412.1529 [astro-ph.CO] (cit. on p. 157).

Maughan, B. J. (2007). *The L_X-Y_X Relation: Using Galaxy Cluster X-Ray Luminosity as a Robust, Low-Scatter Mass Proxy*. Astrophysical Journal **668** 772. arXiv: astro-ph/0703504 [astro-ph] (cit. on pp. 61, 122, 143).

Maughan, B. J. et al. (2012). *Self-similar scaling and evolution in the galaxy cluster X-ray luminosity-temperature relation*. Monthly Notices of the RAS **421** 1583. arXiv: 1108.1200 (cit. on pp. 51, 61, 90, 143).

McCammon, D. et al. (2002). *A High Spectral Resolution Observation of the Soft X-Ray Diffuse Background with Thermal Detectors*. Astrophysical Journal **576** 188. arXiv: astro-ph/0205012 [astro-ph] (cit. on p. 45).

McConnachie, A. W. (2012a). *The Observed Properties of Dwarf Galaxies in and around the Local Group*. The Astronomical Journal **144** 4. arXiv: 1204.1562 [astro-ph.CO] (cit. on p. 78).

– (2012b). *The Observed Properties of Dwarf Galaxies in and around the Local Group*. Astronomical Journal **144** 4. arXiv: 1204.1562 [astro-ph.CO] (cit. on p. 80).

McNamara, B. R. and P. E. J. Nulsen (2007). *Heating Hot Atmospheres with Active Galactic Nuclei*. Annual Review of Astron and Astrophys **45** 117. arXiv: 0709.2152 [astro-ph] (cit. on p. 31).

Mehrtens, N. et al. (2012). *The XMM Cluster Survey: optical analysis methodology and the first data release*. Monthly Notices of the RAS **423** 1024. arXiv: 1106.3056 (cit. on p. 52).

Mernier, F. et al. (2015). *Abundance and temperature distributions in the hot intra-cluster gas of Abell 4059*. Astronomy and Astrophysics **575** A37. arXiv: 1412.5369 [astro-ph.HE] (cit. on p. 38).

Migkas, K. and M. Plionis (2016). *Testing the isotropy of the Hubble expansion*. Revista Mexicana de Astronomia y Astrofisica **52** 133. arXiv: 1602.02310 (cit. on p. 51).

Migkas, K., G. Schellenberger et al. (2020). *Probing cosmic isotropy with a new X-ray galaxy cluster sample through the L_X-T scaling relation*. Astronomy and Astrophysics **636** A15. arXiv: 2004.03305 [astro-ph.CO] (cit. on p. 116).

Migkas, K. and T. H. Reiprich (2018). *Anisotropy of the galaxy cluster X-ray luminosity-temperature relation*. Astronomy and Astrophysics **611** A50. arXiv: 1711.02539 [astro-ph.CO] (cit. on pp. 51, 95, 116).

Mittal, R., A. Hicks et al. (2011). *The L_X - T_{vir} relation in galaxy clusters: effects of radiative cooling and AGN heating*. Astronomy and Astrophysics **532** A133. arXiv: 1106.5185 (cit. on pp. 51, 72, 143, 145).

Mittal, R., D. S. Hudson et al. (2009). *AGN heating and ICM cooling in the HIFLUGCS sample of galaxy clusters*. Astronomy and Astrophysics **501** 835. arXiv: 0810.0797 [astro-ph] (cit. on p. 126).

Mody, K. and A. Hajian (2012). *One Thousand and One Clusters: Measuring the Bulk Flow with the Planck ESZ and X-Ray-selected Galaxy Cluster Catalogs*. Astrophysical Journal **758** 4. arXiv: 1202.1339 [astro-ph.CO] (cit. on p. 157).

Mohayaee, R., M. Rameez and S. Sarkar (2020). *The impact of peculiar velocities on supernova cosmology*. arXiv e-prints arXiv:2003.10420. arXiv: 2003.10420 [astro-ph.CO] (cit. on p. 157).

Mohr, J. J. and A. E. Evrard (1997). *An X-Ray Size-Temperature Relation for Galaxy Clusters: Observation and Simulation*. Astrophysical Journal **491** 38. arXiv: astro-ph/9707184 [astro-ph] (cit. on p. 130).

Mohr, J. J., E. D. Reese et al. (2000). *The X-Ray Size-Temperature Relation for Intermediate-Redshift Galaxy Clusters*. Astrophysical Journal **544** 109. arXiv: astro-ph/0004242 [astro-ph] (cit. on p. 130).

Morandi, A., S. Ettori and L. Moscardini (2007). *X-ray and Sunyaev-Zel'dovich scaling relations in galaxy clusters*. Monthly Notices of the RAS **379** 518. arXiv: 0704.2678 [astro-ph] (cit. on pp. 126, 127).

Mörtsell, E. and S. Dhawan (2018). *Does the Hubble constant tension call for new physics?* Journal of Cosmology and Astroparticle Physics **2018** 025. arXiv: 1801.07260 [astro-ph.CO] (cit. on p. 8).

Nagai, D., A. V. Kravtsov and A. Vikhlinin (2007). *Effects of Galaxy Formation on Thermodynamics of the Intracluster Medium*. Astrophysical Journal **668** 1. arXiv: astro-ph/0703661 [astro-ph] (cit. on p. 118).

Nagarajan, A. et al. (2019). *Weak-lensing mass calibration of the Sunyaev-Zel'dovich effect using APEX-SZ galaxy clusters*. Monthly Notices of the RAS **488** 1728. arXiv: 1804.03671 [astro-ph.CO] (cit. on pp. 126, 149).

Osborne, S. J. et al. (2011). *Measuring the Galaxy Cluster Bulk Flow from WMAP Data*. Astrophysical Journal **737** 98. arXiv: 1011.2781 (cit. on pp. 117, 157).

Pacaud, F., M. Pierre, C. Adami et al. (2007). *The XMM-LSS survey: the Class 1 cluster sample over the initial 5 deg^2 and its cosmological modelling*. Monthly Notices of the RAS **382** 1289. arXiv: 0709.1950 (cit. on p. 51).

Pacaud, F., M. Pierre, A. Refregier et al. (2006). *The XMM Large-Scale Structure survey: the X-ray pipeline and survey selection function*. **372** 578. arXiv: astro-ph/0607177 [astro-ph] (cit. on p. 41).

Parker, R. A. (1974). *Ancient Egyptian Astronomy*. Philosophical Transactions of the Royal Society of London Series A **276** 51 (cit. on p. 1).

Pavlidou, V. et al. (2020). *Turnaround density as a probe of the cosmological constant*. Astronomy and Astrophysics **638** L8. arXiv: 2004.04395 [astro-ph.CO] (cit. on p. 23).

Peebles, P. J. E. (1984). *Tests of cosmological models constrained by inflation*. Astrophysical Journal **284** 439 (cit. on p. 8).

Peery, S., R. Watkins and H. A. Feldman (2018). *Easily interpretable bulk flows: continuing tension with the standard cosmological model*. Monthly Notices of the RAS **481** 1368. arXiv: 1808.07772 [astro-ph.CO] (cit. on pp. 117, 123, 157).

Penzias, A. A. and R. W. Wilson (1965). *A Measurement of Excess Antenna Temperature at 4080 Mc/s.* Astrophysical Journal **142** 419 (cit. on p. 6).

Perlmutter, S. et al. (1999). *Measurements of Ω and Λ from 42 High-Redshift Supernovae*. Astrophysical Journal **517** 565. arXiv: astro-ph/9812133 [astro-ph] (cit. on pp. 7, 8).

Piffaretti, R. et al. (2011). *The MCXC: a meta-catalogue of x-ray detected clusters of galaxies*. Astronomy and Astrophysics **534** A109. arXiv: 1007.1916 (cit. on pp. 52, 57, 118, 173).

Planck Collaboration, P. A. R. Ade, N. Aghanim, Y. Akrami et al. (2016). *Planck 2015 results. XVI. Isotropy and statistics of the CMB*. Astronomy and Astrophysics **594** A16. arXiv: 1506.07135 (cit. on p. 50).

Planck Collaboration, P. A. R. Ade, N. Aghanim, M. I. R. Alves et al. (2014). *Planck 2013 results. I. Overview of products and scientific results*. Astronomy and Astrophysics **571** A1. arXiv: 1303.5062 [astro-ph.CO] (cit. on p. 19).

Planck Collaboration, P. A. R. Ade, N. Aghanim, C. Armitage-Caplan et al. (2014). *Planck 2013 results. XXIII. Isotropy and statistics of the CMB*. Astronomy and Astrophysics **571** A23. arXiv: 1303.5083 [astro-ph.CO] (cit. on p. 50).

Planck Collaboration, P. A. R. Ade, N. Aghanim, M. Arnaud, M. Ashdown, J. Aumont, C. Baccigalupi, A. Balbi, A. J. Banday, R. B. Barreiro, M. Bartelmann et al. (2011). *Planck early results. XI. Calibration of the local galaxy cluster Sunyaev-Zeldovich scaling relations*. Astronomy and Astrophysics **536** A11. arXiv: 1101.2026 [astro-ph.CO] (cit. on pp. 126, 127).

Planck Collaboration, P. A. R. Ade, N. Aghanim, M. Arnaud, M. Ashdown, J. Aumont, C. Baccigalupi, A. Balbi, A. J. Banday, R. B. Barreiro, E. Battaner et al. (2014). *Planck intermediate results. XIII. Constraints on peculiar velocities*. Astronomy and Astrophysics **561** A97. arXiv: 1303.5090 (cit. on p. 157).

Planck Collaboration, P. A. R. Ade, N. Aghanim, M. Arnaud, M. Ashdown, J. Aumont, C. Baccigalupi, A. J. Banday et al. (2016). *Planck 2015 results. XXVII. The second Planck catalogue of Sunyaev-Zeldovich sources*. Astronomy and Astrophysics **594** A27. arXiv: 1502.01598 (cit. on p. 119).

Planck Collaboration, N. Aghanim, Y. Akrami et al. (2020). *Planck 2018 results. VI. Cosmological parameters*. Astronomy and Astrophysics **641** A6. arXiv: 1807.06209 [astro-ph.CO] (cit. on pp. 12, 19).

Planck Collaboration, N. Aghanim, M. Arnaud et al. (2011). *Planck early results. X. Statistical analysis of Sunyaev-Zeldovich scaling relations for X-ray galaxy clusters*. Astronomy and Astrophysics **536** A10. arXiv: 1101.2043 [astro-ph.CO] (cit. on p. 126).

Plionis, M. and I. Georgantopoulos (1999). *The ROSAT X-ray background dipole*. Monthly Notices of the RAS **306** 112. eprint: astro-ph/9812391 (cit. on p. 51).

Pratt, C. T. and J. N. Bregman (2020). *SZ Scaling Relations of Galaxy Groups and Clusters Near the North Ecliptic Pole*. Astrophysical Journal **890** 156. arXiv: 2001.07802 [astro-ph.CO] (cit. on p. 126).

Pratt, G. W., M. Arnaud et al. (2019). *The Galaxy Cluster Mass Scale and Its Impact on Cosmological Constraints from the Cluster Population*. **215** 25. arXiv: 1902.10837 [astro-ph.CO] (cit. on p. 8).

Pratt, G. W., J. H. Croston et al. (2009). *Galaxy cluster X-ray luminosity scaling relations from a representative local sample (REXCESS)*. Astronomy and Astrophysics **498** 361. arXiv: 0809.3784 (cit. on pp. 51, 90, 104, 105, 143).

Predehl, P. et al. (2016). "eROSITA on SRG". *Space Telescopes and Instrumentation 2016: Ultraviolet to Gamma Ray*. Vol. 9905. 99051K (cit. on p. 52).

Pritychenko, B. (2015). *A Nuclear Data Approach for the Hubble Constant Measurements*. arXiv e-prints arXiv:1506.02978. arXiv: 1506.02978 [astro-ph.CO] (cit. on p. 5).

Qin, F. et al. (2019). *Bulk flow and shear in the local Universe: 2MTF and COSMICFLOWS-3*. Monthly Notices of the RAS **482** 1920. arXiv: 1811.00822 [astro-ph.CO] (cit. on pp. 117, 136).

Rameez, M. (2019). *Concerns about the reliability of publicly available SNe Ia data*. arXiv e-prints arXiv:1905.00221. arXiv: 1905.00221 [astro-ph.CO] (cit. on p. 51).

Rameez, M. et al. (2018). *The dipole anisotropy of AllWISE galaxies*. Monthly Notices of the RAS **477** 1772. arXiv: 1712.03444 [astro-ph.CO] (cit. on pp. 51, 154).

Ramos-Ceja, M. E. et al. (2019). *Projection effects in galaxy cluster samples: insights from X-ray redshifts*. Astronomy and Astrophysics **626** A48. arXiv: 1904.10275 [astro-ph.GA] (cit. on p. 53).

Read, A. M. and T. J. Ponman (2003). *The XMM-Newton EPIC background: Production of background maps and event files*. **409** 395. arXiv: astro-ph/0304147 [astro-ph] (cit. on p. 37).

Reichert, A. et al. (2011). *Observational constraints on the redshift evolution of X-ray scaling relations of galaxy clusters out to z 1.5*. Astronomy and Astrophysics **535** A4. arXiv: 1109.3708 [astro-ph.CO] (cit. on pp. 51, 52, 57, 121).

Reiprich, T. H. (2017). *Follow-up of eROSITA and Euclid Galaxy Clusters with XMM-Newton*. Astronomische Nachrichten **338** 349. arXiv: 1701.04216 (cit. on pp. 53, 116).

Reiprich, T. H. and H. Böhringer (2002). *The Mass Function of an X-Ray Flux-limited Sample of Galaxy Clusters*. Astrophysical Journal **567** 716. eprint: astro-ph/0111285 (cit. on pp. 16, 143).

Reiprich, T. H., K. Basu et al. (2013). *Outskirts of Galaxy Clusters*. Space Science Reviews **177** 195. arXiv: 1303.3286 [astro-ph.CO] (cit. on pp. 21, 25).

Riess, A. G. (2019). *The expansion of the Universe is faster than expected*. Nature Reviews Physics **2** 10. arXiv: 2001.03624 [astro-ph.CO] (cit. on p. 10).

Riess, A. G. et al. (1998). *Observational Evidence from Supernovae for an Accelerating Universe and a Cosmological Constant*. Astronomical Journal **116** 1009. arXiv: astro-ph/9805201 [astro-ph] (cit. on p. 8).

Řıpa, J. and A. Shafieloo (2017). *Testing the Isotropic Universe Using the Gamma-Ray Burst Data of Fermi/GBM*. Astrophysical Journal **851** 15. arXiv: 1706.03556 [astro-ph.HE] (cit. on p. 51).

Robertson, A., R. Massey and V. Eke (2017). *What does the Bullet Cluster tell us about self-interacting dark matter?* Monthly Notices of the RAS **465** 569. arXiv: 1605.04307 [astro-ph.CO] (cit. on pp. 4, 23).

Rosati, P., S. Borgani and C. Norman (2002). *The Evolution of X-ray Clusters of Galaxies*. Annual Review of Astron and Astrophys **40** 539. arXiv: astro-ph/0209035 [astro-ph] (cit. on p. 21).

Rossetti, M. et al. (2016). *Measuring the dynamical state of Planck SZ-selected clusters: X-ray peak - BCG offset*. Monthly Notices of the RAS **457** 4515. arXiv: 1512.00410 [astro-ph.CO] (cit. on pp. 127, 143).

Rubart, M. and D. J. Schwarz (2013). *Cosmic radio dipole from NVSS and WENSS*. Astronomy and Astrophysics **555** A117. arXiv: 1301.5559 [astro-ph.CO] (cit. on p. 51).

Rubart, M., D. Bacon and D. J. Schwarz (2014). *Impact of local structure on the cosmic radio dipole*. Astronomy and Astrophysics **565** A111. arXiv: 1402.0376 [astro-ph.CO] (cit. on p. 158).

Rubin, V. C., J. Ford W. K. and N. Thonnard (1978). *Extended rotation curves of high-luminosity spiral galaxies. IV. Systematic dynamical properties, Sa -> Sc.* Astrophysical Journal, Letters **225** L107 (cit. on p. 7).

Ruggles, C. L. N. (2005). *Ancient astronomy : an encyclopedia of cosmologies and myth* (cit. on p. 1).

Salehi, A., H. Farajollahi et al. (2020). *Are Type Ia supernova powerful tool to detect anisotropic expansion of the Universe?* The European Physical Journal C **80** 753. URL: https://doi.org/10.1140/epjc/s10052-020-8269-z (cit. on pp. 117, 157).

Salehi, A., M. Yarahmadi and S. Fathi (2020). *The cosmological bulk flow in QCDM model: (In)consistency with ΛCDM*. arXiv e-prints arXiv:2001.01743. arXiv: 2001.01743 [astro-ph.CO] (cit. on p. 157).

Sarazin, C. L. (1986). *X-ray emission from clusters of galaxies*. Reviews of Modern Physics **58** 1 (cit. on p. 21).

Sarkar, S., B. Pandey and R. Khatri (2019). *Testing isotropy in the Universe using photometric and spectroscopic data from the SDSS*. Monthly Notices of the RAS **483** 2453. arXiv: 1810.07410 [astro-ph.CO] (cit. on p. 51).

Schellenberger, G. and T. H. Reiprich (2017). *HICOSMO - cosmology with a complete sample of galaxy clusters - I. Data analysis, sample selection and luminosity-mass scaling relation*. Monthly Notices of the RAS **469** 3738. arXiv: 1705.05842 [astro-ph.CO] (cit. on p. 59).

Schellenberger, G., T. H. Reiprich et al. (2015). *XMM-Newton and Chandra cross-calibration using HIFLUGCS galaxy clusters . Systematic temperature differences and cosmological impact*. Astronomy and Astrophysics **575** A30. arXiv: 1404.7130 (cit. on pp. 16, 56, 134, 148).

Schlegel, D. J., D. P. Finkbeiner and M. Davis (1998). *Maps of dust infrared emission for use in estimation of reddening and cosmic microwave background radiation foregrounds*. The Astrophysical Journal **500** 525 (cit. on p. 160).

Schönrich, R. and P. J. McMillan (2017). *Understanding inverse metallicity gradients in galactic discs as a consequence of inside-out formation*. Monthly Notices of the RAS **467** 1154. arXiv: 1605.02338 [astro-ph.GA] (cit. on p. 78).

Schuecker, P. (2005). *New Cosmology with Clusters of Galaxies*. Reviews in Modern Astronomy **18** 76. arXiv: astro-ph/0502234 [astro-ph] (cit. on p. 21).

Schwarz, D. J. and B. Weinhorst (2007). *(An)isotropy of the Hubble diagram: comparing hemispheres*. Astronomy and Astrophysics **474** 717. arXiv: 0706.0165 (cit. on pp. 51, 93).

Schwarz, D. J., C. J. Copi et al. (2016). *CMB anomalies after Planck*. Classical and Quantum Gravity **33** 184001. arXiv: 1510.07929 [astro-ph.CO] (cit. on p. 50).

Scrimgeour, M. I. et al. (2016). *The 6dF Galaxy Survey: bulk flows on 50-70 h^{-1} Mpc scales*. Monthly Notices of the RAS **455** 386. arXiv: 1511.06930 [astro-ph.CO] (cit. on p. 117).

Secrest, N. et al. (2020). *A Test of the Cosmological Principle with Quasars*. arXiv e-prints arXiv:2009.14826. arXiv: 2009.14826 [astro-ph.CO] (cit. on pp. 117, 154).

Shafer, R. A. and A. C. Fabian (1983). "The (an)isotropy of the X-ray sky". *Early Evolution of the Universe and its Present Structure*. Ed. by G. O. Abell and G. Chincarini. Vol. 104. IAU Symposium 333 (cit. on p. 51).

Shamir, L. (2020). *Galaxy spin direction distribution in HST and SDSS show similar large-scale asymmetry*. arXiv e-prints arXiv:2011.03723. arXiv: 2011.03723 [astro-ph.CO] (cit. on p. 157).

Shanks, T., L. M. Hogarth and N. Metcalfe (2019). *Gaia Cepheid parallaxes and 'Local Hole' relieve H_0 tension*. Monthly Notices of the RAS **484** L64. arXiv: 1810.02595 [astro-ph.CO] (cit. on p. 158).

Shanks, T., L. M. Hogarth, N. Metcalfe and J. Whitbourn (2019). *Local Hole revisited: evidence for bulk motions and self-consistent outflow*. Monthly Notices of the RAS **490** 4715. arXiv: 1909.01878 [astro-ph.CO] (cit. on p. 158).

Shanks, T., N. Metcalfe et al. (2015). *The VLT survey telescope ATLAS*. Monthly Notices of the Royal Astronomical Society **451** 4238 (cit. on p. 120).

Siewert, T. M., M. Schmidt-Rubart and D. J. Schwarz (2020). *The Cosmic Radio Dipole: Estimators and Frequency Dependence*. arXiv e-prints arXiv:2010.08366. arXiv: 2010.08366 [astro-ph.CO] (cit. on p. 154).

Singal, A. K. (2011). *Large Peculiar Motion of the Solar System from the Dipole Anisotropy in Sky Brightness due to Distant Radio Sources*. Astrophysical Journal, Letters **742** L23. arXiv: 1110.6260 [astro-ph.CO] (cit. on p. 51).

Skrutskie, M. et al. (2006). *The two micron all sky survey (2MASS)*. The Astronomical Journal **131** 1163 (cit. on p. 120).

Slipher, V. M. (1917). *Nebulae*. Proceedings of the American Philosophical Society **56** 403 (cit. on p. 5).

Snowden, S. L., M. R. Collier and K. D. Kuntz (2004). *XMM-Newton Observation of Solar Wind Charge Exchange Emission*. Astrophysical Journal **610** 1182. arXiv: astro-ph/0404354 [astro-ph] (cit. on p. 38).

Snowden, S. L., R. Egger et al. (1997). *ROSAT Survey Diffuse X-Ray Background Maps. II.* Astrophysical Journal **485** 125 (cit. on p. 60).

Soltis, J. et al. (2019). *Percent-Level Test of Isotropic Expansion Using Type Ia Supernovae*. Physical Review Letters **122** 091301. arXiv: 1902.07189 [astro-ph.CO] (cit. on pp. 117, 157).

Spandagos, E. (2004). *Astronomy of the Ancient Greeks* (cit. on p. 2).

Spina, L. et al. (2017). *The Gaia-ESO Survey: the present-day radial metallicity distribution of the Galactic disc probed by pre-main-sequence clusters*. Astronomy and Astrophysics **601** A70. arXiv: 1702.03461 [astro-ph.SR] (cit. on p. 78).

Springel, V. et al. (2005). *Simulations of the formation, evolution and clustering of galaxies and quasars*. Nature **435** 629. arXiv: astro-ph/0504097 [astro-ph] (cit. on p. 15).

Stark, A. A. et al. (1992). *The Bell Laboratories H I survey*. Astrophysical Journals **79** 77 (cit. on p. 56).
Starobinsky, A. A. (1982). *Dynamics of phase transition in the new inflationary universe scenario and generation of perturbations*. Physics Letters B **117** 175 (cit. on p. 7).
Steele, J. M. (2015). *Babylonian Observational and Predictive Astronomy* 1855 (cit. on p. 2).
Stephenson, F. R., K. K. C. Yau and H. Hunger (1985). *Records of Halley's comet on Babylonian tablets*. Nature **314** 587 (cit. on p. 2).
Sun, Z. Q. and F. Y. Wang (2018). *Testing the anisotropy of cosmic acceleration from Pantheon supernovae sample*. Monthly Notices of the Royal Astronomical Society **478** 5153. ISSN: 0035-8711. eprint: http://oup.prod.sis.lan/mnras/article-pdf/478/4/5153/25102137/sty1391.pdf. URL: https://doi.org/10.1093/mnras/sty1391 (cit. on p. 51).
Sun, Z. Q. and F. Y. Wang (2019). *Probing the isotropy of cosmic acceleration using different supernova samples*. European Physical Journal C **79** 783. arXiv: 1804.05191 [astro-ph.CO] (cit. on p. 157).
Sunyaev, R. A. and Y. B. Zeldovich (1970). *The Spectrum of Primordial Radiation, its Distortions and their Significance*. Comments on Astrophysics and Space Physics **2** 66 (cit. on p. 27).
– (1972). *The Observations of Relic Radiation as a Test of the Nature of X-Ray Radiation from the Clusters of Galaxies*. Comments on Astrophysics and Space Physics **4** 173 (cit. on p. 27).
Sweatman, M. B. and A. Coombs (2018). *Decoding European Palaeolithic art: Extremely ancient knowledge of precession of the equinoxes*. arXiv e-prints arXiv:1806.00046. arXiv: 1806.00046 [physics.hist-ph] (cit. on p. 1).
Tanaka, Y., H. Inoue and S. S. Holt (1994). *The X-ray astronomy satellite ASCA*. Publications of the ASJ **46** L37 (cit. on p. 34).
Taton, R. (1989). *Planetary astronomy from the renaissance to the rise of astrophysics. Part A: TYCHO Brahe to Newton* (cit. on p. 4).
Tauber, J. A. et al. (2010). *Planck pre-launch status: The Planck mission*. Astronomy and Astrophysics **520** A1 (cit. on p. 34).
Tegmark, M., A. de Oliveira-Costa and A. J. Hamilton (2003). *High resolution foreground cleaned CMB map from WMAP*. Physical Review D **68** 123523. eprint: astro-ph/0302496 (cit. on p. 50).
Tiwari, P. et al. (2015). *Dipole anisotropy in sky brightness and source count distribution in radio NVSS data*. Astroparticle Physics **61** 1. arXiv: 1307.1947 [astro-ph.CO] (cit. on pp. 51, 154).
Tsagas, C. G. and K. Filippou (2020). *Large-scale peculiar velocity fields: Newtonian vs relativistic treatment*. arXiv e-prints arXiv:2003.01186. arXiv: 2003.01186 [gr-qc] (cit. on p. 157).
Tsaprazi, E. and C. G. Tsagas (2019). *Relativistic approach to the kinematics of large-scale peculiar motions*. arXiv e-prints arXiv:1906.05164. arXiv: 1906.05164 [astro-ph.CO] (cit. on p. 157).
Tully, R. B. et al. (2019). *Cosmicflows-3: Cosmography of the Local Void*. Astrophysical Journal **880** 24. arXiv: 1905.08329 [astro-ph.CO] (cit. on p. 158).
Verde, L. et al. (2001). *On galaxy cluster sizes and temperatures*. Monthly Notices of the RAS **321** L7. arXiv: astro-ph/0007426 [astro-ph] (cit. on p. 130).
Vielva, P. et al. (2004). *Detection of Non-Gaussianity in the Wilkinson Microwave Anisotropy Probe First-Year Data Using Spherical Wavelets*. Astrophysical Journal **609** 22. arXiv: astro-ph/0310273 [astro-ph] (cit. on p. 50).
Vikhlinin, A., R. A. Burenin et al. (2009). *Chandra Cluster Cosmology Project. II. Samples and X-Ray Data Reduction*. Astrophysical Journal **692** 1033. arXiv: 0805.2207 [astro-ph] (cit. on p. 146).
Vikhlinin, A., L. van Speybroeck et al. (2002). *Evolution of the Cluster X-Ray Scaling Relations since z 0.4*. Astrophysical Journal, Letters **578** L107. eprint: astro-ph/0207445 (cit. on p. 51).
Voges, W. et al. (1999). *The ROSAT all-sky survey bright source catalogue*. Astronomy and Astrophysics **349** 389. arXiv: astro-ph/9909315 [astro-ph] (cit. on p. 53).

Walker, A. G. (1937). *On Milne's Theory of World-Structure*. Proceedings of the London Mathematical Society **42** 90 (cit. on p. 4).

Wang, Y.-Y. and F. Y. Wang (2018). *Testing the isotropy of the Universe with Type Ia supernovae in a model-independent way*. Monthly Notices of the RAS **474** 3516. arXiv: 1711.05974 [astro-ph.CO] (cit. on p. 51).

Watkins, R. and H. A. Feldman (2015). *Large-scale bulk flows from the Cosmicflows-2 catalogue*. Monthly Notices of the RAS **447** 132. arXiv: 1407.6940 [astro-ph.CO] (cit. on pp. 117, 157).

Watkins, R., H. A. Feldman and M. J. Hudson (2009). *Consistently large cosmic flows on scales of 100 hâ1 Mpc: a challenge for the standard ÎCDM cosmology*. Monthly Notices of the Royal Astronomical Society **392** 743. eprint: /oup/backfile/Content_public/Journal/mnras/392/2/10.1111/j.1365-2966.2008.14089.x/2/mnras0392-0743.pdf. URL: +%20http://dx.doi.org/10.1111/j.1365-2966.2008.14089.x (cit. on pp. 51, 157).

Webb, J. K. et al. (2011). *Indications of a Spatial Variation of the Fine Structure Constant*. Physical Review Letters **107** 191101. arXiv: 1008.3907 [astro-ph.CO] (cit. on p. 93).

Weinberg, S. (1972). *Gravitation and Cosmology: Principles and Applications of the General Theory of Relativity* (cit. on p. 14).

Weisskopf, M. C. et al. (2000). "Chandra X-ray Observatory (CXO): overview". *X-Ray Optics, Instruments, and Missions III*. Ed. by J. E. Truemper and B. Aschenbach. Vol. 4012. 2. eprint: astro-ph/0004127 (cit. on pp. 33, 53).

Whitbourn, J. R. and T. Shanks (2014). *The local hole revealed by galaxy counts and redshifts*. Monthly Notices of the RAS **437** 2146. arXiv: 1307.4405 [astro-ph.CO] (cit. on p. 158).

White, S. D. M. et al. (1993). *The baryon content of galaxy clusters: a challenge to cosmological orthodoxy*. **366** 429 (cit. on p. 8).

Willingale, R. et al. (2013). *Calibration of X-ray absorption in our Galaxy*. Monthly Notices of the RAS **431** 394. arXiv: 1303.0843 [astro-ph.HE] (cit. on pp. 26, 45, 56, 120, 159).

Willson, M. A. G. (1970). *Radio observations of the cluster of galaxies in Coma Berenices - the 5C4 survey.* Monthly Notices of the RAS **151** 1 (cit. on p. 23).

Wilms, J., A. Allen and R. McCray (2000). *On the Absorption of X-Rays in the Interstellar Medium*. Astrophysical Journal **542** 914. arXiv: astro-ph/0008425 [astro-ph] (cit. on p. 27).

Wright, E. L. (1979). *Distortion of the microwave background by a hot intergalactic medium.* ApJ **232** 348 (cit. on p. 119).

Wright, E. L. et al. (2010). *The Wide-field Infrared Survey Explorer (WISE): mission description and initial on-orbit performance*. The Astronomical Journal **140** 1868 (cit. on p. 120).

Yang, X., F. Y. Wang and Z. Chu (2014). *Searching for a preferred direction with Union2.1 data*. Monthly Notices of the RAS **437** 1840. arXiv: 1310.5211 [astro-ph.CO] (cit. on p. 93).

Yoon, M. et al. (2014). *Dipolar modulation in number counts of WISE-2MASS sources*. Monthly Notices of the RAS **445** L60. arXiv: 1406.1187 [astro-ph.CO] (cit. on pp. 51, 93).

York, D. G. et al. (2000). *The sloan digital sky survey: Technical summary*. The Astronomical Journal **120** 1579 (cit. on p. 120).

Zhang, Y. .-.-Y. et al. (2011). *HIFLUGCS: Galaxy cluster scaling relations between X-ray luminosity, gas mass, cluster radius, and velocity dispersion*. Astronomy and Astrophysics **526** A105. arXiv: 1011.3018 [astro-ph.CO] (cit. on p. 57).

Zhang, Y.-Y. et al. (2017). *HIFLUGCS: X-ray luminosity-dynamical mass relation and its implications for mass calibrations with the SPIDERS and 4MOST surveys*. Astronomy and Astrophysics **599** A138 (cit. on p. 143).

Zhao, D., Y. Zhou and Z. Chang (2019). *Anisotropy of the Universe via the Pantheon supernovae sample revisited*. Monthly Notices of the RAS **486** 5679. arXiv: 1903.12401 [astro-ph.CO] (cit. on p. 157).

Zitrin, A. et al. (2012). *Miscentring in galaxy clusters: dark matter to brightest cluster galaxy offsets in 10?000 Sloan Digital Sky Survey clusters*. Monthly Notices of the Royal Astronomical Society **426** 2944. ISSN: 0035-8711. eprint: https://academic.oup.com/mnras/article-pdf/426/4/2944/3309797/426-4-2944.pdf. URL: https://doi.org/10.1111/j.1365-2966.2012.21886.x (cit. on pp. 127, 143).

Zou, S. et al. (2016). *The X-ray luminosity-temperature relation of a complete sample of low-mass galaxy clusters*. Monthly Notices of the RAS **463** 820. arXiv: 1610.07674 (cit. on pp. 51, 61).

Zwicky, F. (1933). *Die Rotverschiebung von extragalaktischen Nebeln*. Helvetica Physica Acta **6** 110 (cit. on p. 7).

List of Figures

List of Tables

Acknowledgements

I owe the successful completion of my thesis, and the last 3 years in general, in two categories of people. The ones I interacted mainly professionally and my friends and family cycle. Let's start with the first category. First of all, I want to thank my supervisor, Thomas Reiprich, sincerely. He came up with the initial idea of this project back in 2016, when I started my internship in his group. Due to his very balanced guidance, I published my first paper on that topic already from the MSc thesis. Thomas left me enough room to develop my own ideas and methods while contributing significantly with his suggestions, ideas, and experience whenever I needed it. Moreover, a big thanks to him for allowing me to pursue this exciting research project instead of other more predictable but more "safe" PhD topics. Not many supervisors operate like that. I do not have anything that I would like him to do differently as a supervisor with no intention to flatter him. He also created a very warm and comfortable environment for me to work in, and I really enjoyed our collaboration. I also want to thank Florian Pacaud for his numerous valuable suggestions and for being so helpful overall. His XMM-Newton pipeline allowed me to obtain the data needed for this entire project. Miriam Ramos-Ceja was also a big help during my first year, guiding me through data reduction and cluster spectral analysis. Furthermore, I want to thank Gerrit Schellenberger and Lorenzo Lovisari for all the fruitful discussions we had and because their expertise helped me improve my work significantly. Gerrit also provided a crucial part of the used data in this project. The same goes for Jens Erler. I was lucky to have such good collaborators. I also thank Nhan Nguyen for providing useful data as well. Of course, I really enjoyed sharing an office with Chaoli and being in the same group with all the students who passed by during these 3 years. A big thanks to Cristiano Porciani and John Antoniadis, who were happy to join my TAC meetings and gave me great feedback on my work progress. John was the one that gave us the idea of the press release for the first project, which led to a great deal of exposure for my work in the largest science media, and many invited seminars for me.

A person's work is inseparably connected with their personal lives. Without some people, I would not be able to enjoy my time here so much or even have the opportunity to be here. Of course, I thank these people in person and in more important aspects of life than the acknowledgments section of my thesis. So I'll keep it short. First and foremost, I thank my life partner, Eftychia, for being my other half and going through everything together. I thank my parents, which they made so many sacrifices for me to be here and whom I miss. It's not easy for them to be apart from me for so long for several reasons, but they are the biggest supporters of me being here anyway. I also thank all my true friends that we shared so many great moments all these years, David, Thanos, Christos, George, and Chatzistratis. Moreover, I really want to thank all the Blazing Suns team members, which gave me back an essential aspect of my life, basketball. Thanks, guys. Last but not least, I want to thank all the people back home at Filyro, that I enjoy so much being with them during my time in Greece. Shoutout to the Paidiki crew! I really appreciate all of these people, and I genuinely value their impact on me, and subsequently, on my work.

Finally, I want to thank the International Max Planck Research School (IMPRS) for Astronomy and Astrophysics at the Universities of Bonn and Cologne, and the Bonn-Cologne Graduate School for Physics and Astronomy (BCGS). They financially supported the travel expenses that allowed me to

participate in international conferences, which eventually helped progress my work significantly and travel to many places to present my work in seminars. IMPRS and AIfA also paid my salary for these 3 years, for which I am of course, truly grateful!

List of Publications

First author papers, refereed

I **Migkas, Konstantinos**, Pacaud, Florian, Schellenberger, Gerrit, Erler, Jens, Nguyen, Nhan, Reiprich, Thomas H., Ramos-Ceja, Miriam E. & Lovisari, Lorenzo — 2021, A&A, 649, A151 — Cosmological implications of the anisotropy of ten multiwavelength galaxy cluster scaling relations — DOI: 10.1051/0004-6361/202140296

II **Migkas, Konstantinos**, Schellenberger, Gerrit, Reiprich, Thomas H., Pacaud, Florian, Ramos-Ceja, Miriam E. & Lovisari, Lorenzo — 2020, A&A, 636, A15 — Probing cosmic isotropy with a new X-ray galaxy cluster sample through the $L_{\rm X} - T$ scaling relation — DOI: 10.1051/0004-6361/201936602

III **Migkas, Konstantinos** & Reiprich, Thomas H. — 2018, A&A 611, A50 — Anisotropy of the galaxy cluster X-ray luminosity-temperature relation — DOI: 10.1051/0004-6361/201731222

IV **Migkas, Konstantinos** & Plionis, Manolis — 2016, RMXAA, 52, 133 — Testing the isotropy of the Hubble expansion — DOI: 10.1051/0004-6361/201731222

Second-or-later author papers, refereed

i Reiprich, Thomas H., (27 authors), **Migkas, Konstantinos**, (18 authors) — 2020, accepted in A&A — The Abell 3391/95 galaxy cluster system. A 15 Mpc intergalactic medium emission filament, a warm gas bridge, infalling matter clumps, and (re-) accelerated plasma discovered by combining SRG/eROSITA data with ASKAP/EMU and DECam data — DOI: 10.1051/0004-6361/202039590

ii Ramos-Ceja, Miriam E., Pacaud, Florian, Reiprich, Thomas H., **Migkas, Konstantinos**, Lovisari, Lorenzo & Schelleberger, Gerrit — 2019, A&A 626, A48 — Projection effects in galaxy cluster samples: insights from X-ray redshifts — DOI: 10.1051/0004-6361/201935111